Durham E-Theses

A new theory for the diffuse gamma - ray background

Strong, A. W.

How to cite:

Strong, A. W. (1975) *A new theory for the diffuse gamma - ray background*, Durham theses, Durham University. Available at Durham E-Theses Online: http://etheses.dur.ac.uk/8146/

Use policy

A NEW THEORY FOR THE DIFFUSE GAMMA - RAY BACKGROUND

BY

A.W. STRONG,

M.A., M.SC., F.R.A.S.

A THESIS SUBMITTED TO THE

UNIVERSITY OF DURHAM FOR

THE DEGREE OF DOCTOR OF PHILOSOPHY.

JUNE, 1975.

TO MY PARENTS

ABSTRACT

A study is made of a model for the diffuse gamma-ray background in which cosmic-ray interactions with the microwave radiation at early epochs initiate an electron-photon cascade whose end product is the presently observed gamma-ray spectrum. Cosmic-ray protons (at least those with energies above 10^{12} eV) are assumed to be of extragalactic origin, and the shape of the cosmic-ray spectrum is assumed to be determined in part by the energy losses on the microwave background, so that the gamma-ray and cosmic-ray spectra can be related.

Strong evolution of the cosmic-ray sources is required at a rate which can be determined from the observed cosmic-ray spectrum. The model parameters required to give the observed spectrum are obtained, and the resulting model used to compute the gamma-ray spectra expected, using both analytical and numerical approaches.

It is found that the predicted gamma-ray spectrum in the range 10^5 - 10^8 eV shows remarkably good agreement with the observations. However a detailed assessment of the model indicates a possible discrepancy with observation above 10^7 eV, although confirmation of experimental results must be awaited before the theory can be rejected.

PREFACE

The work presented in this thesis was carried out while the author was a research student under the supervision of Prof. A.W. Wolfendale in the Physics Department of the University of Durham, between October 1971 and September 1973. Since October 1973 the author has been a Research Assistant in the same Department.

In 1972, 1973 and 1975 visits were made to the Institute of Nuclear Research in Lodz, Poland, to work with Dr. J. Wdowczyk. Some of the work reported here was carried out in collaboration with Dr. Wdowczyk, but most of the research and all calculations were the work of the author.

The results obtained in this thesis have been reported in the following papers:

Strong, Wolfendale and Wdowczyk, Nature 241, 109 (1973)

Strong, Wdowczyk and Wolfendale, Proc. 13th Int. Conf. Cosmic Rays, Denver, 1, 27 (1973)

" " " J. Phys. A. 7, 120 (1974)

Strong and Wdowczyk, Proc. 14th Int. Conf. Cosmic Rays, Munich, (1975)

Strong, submitted to Mon. Not. Roy. Astr. Soc. (1975)

CONTENTS

Chapter 9   <u>Review</u> <u>of</u> <u>Observational</u> <u>data</u> <u>on</u> <u>the</u> <u>Gamma-Ray</u> <u>Back-</u>
<u>ground</u> <u>and</u> <u>comparison</u> <u>with</u> <u>the</u> <u>models</u>.

9.1 Introduction.

9.2 Gamma-Ray astronomy techniques.

9.3 Gamma-Ray experiments from Balloon altitudes.

9.4 Gamma-Ray Observations from spacecraft.

9.5 Review of experimental data on the X-ray Background.

9.6 Comparison of models with experimental data.

9.7 Conclusions.

Chapter 1.   A Review of Observational and Theoretical Aspects of the Origin of Cosmic-Rays and the Diffuse Gamma- Ray Background.

1.1 Introduction.

In the quest for an understanding of the physical processes occurring in the Universe, the unification of apparently unrelated observational data is an important way of simplifying the problem, and may lead to greater insight into the evolution of physical systems and of the Universe as a whole. This thesis is concerned with an attempt at such a synthesis, to relate the primary cosmic-ray spectrum observed at the Earth, the diffuse gamma-ray background, and, indirectly, the fact that powerful radio sources appear to have been much more numerous in the early history of the Universe.

The theory developed here involves the following assumptions:
a) the primary cosmic-ray spectrum is of extragalactic origin at least above about 10^{12} eV, b) the shape of the primary spectrum can be related to interactions with the blackbody background radiation at early epochs, (c) that the sources of cosmic-rays (CR) were much more numerous in the past, evolving in a manner similar to that of powerful radio sources, (d) the gamma-ray spectrum is the end product of an electron-photon cascade initiated by the interactions with the blackbody radiation, and proceeding via further electromagnetic interactions with this and other radiation fields in extragalactic space. The derivation of this spectrum is the main subject of later Chapters, the object being to compare the predicted spectrum with the observational data.

To provide the framework and context against which this theory has been developed, it is necessary to review current ideas on cosmic-ray

origin, the gamma-ray background and radio-source evolution. The
following sections discuss these topics in turn.

1.2 Observational facts about Cosmic-rays.

The main observational data which can be used in arguing about CR
origin (with reference particularly to the question of Galactic or
extra-Galactic origin) will now be briefly summarized. The existence of
a highly isotropic flux of extraterrestrial relativistic particles with
energies ranging from less than 100 MeV up to more than 10^{20} eV has been
established using techniques ranging from direct observation from space-
craft at low energies to extensive air-showers for energies above 10^{14} eV.
A survey of the experimental data is given in the appendix to Chapter 2;
for the present section the important features are:

(a) The overall energy density is about 1 eV cm^{-3} , mainly in the form of
nucleons below 10 GeV. About one percent of the energy is in the form of
electrons.

(b) The spectral shape is of the form $j(E) = AE^{-\gamma}$, with $\gamma \sim 2.5$ up
to about 10^{15} eV, beyond which a steepening to $\gamma \sim 3$, approximately, occurs.
A power-law dependence continuing up to the highest observed energies is
consistent with the data.

(c) The flux is extemely isotropic, both at low and high energies. Below
10^{11} eV, the CR are isotropized by the interplanetary magnetic field,
but above this energy the angular distribution should begin to reflect
that beyond the Solar-System. The muon telescope experiment of Elliot (1974)
gives an anisotropy $\delta = (I_{max} - I_{min})/(I_{max} + I_{min}) < 2 \ 10^{-4}$ for a median
energy 1.5 10^{11} eV, which implies a velocity of streaming past the Sun
less than 50 km s^{-1}. At the high energy end of the spectrum ($> 10^{19}$ eV),
where deflections by the Galactic field become small, no significant
departures from isotropy appear to have been found to date, although some
results of marginal significance have been claimed (Bell et al. 1973,

Krasilnikov et al. 1974, Hillas and Ouldridge (1975), Kiraly and White
1975). Further discussion of this point is given in Sec 1.3 .

(d) Data on the chemical composition at energies between 100MeV and 100
GeV, in particular the ratio of 'primary' nuclei (C,N,O etc) to 'daughter '
nuclei (Li,Be,B etc, which cannot be primary since they are destroyed
rapidly in stellar interiors), can be used to obtain the path-length in
grams $\lambda = \rho c \tau$, where ρ = density of the interstellar medium and τ =
mean lifetime of CR in the Galaxy (see for example Meyer 1974). There is
good evidence for a decrease of λ with increasing energy, the mean value
being about 5 gm cm^{-2} (Shapiro and Silberberg 1970). The ratio of pos-
itrons to electrons can also be used to obtain a similar value for λ
(Fanselow et al. 1969). Another important result is the increase in the
number of Fe nuclei relative to C,N,O with increasing energy, above
a few GeV (Ormes et al. 1973).

(e) The lifetime of CR in the Galaxy follows from λ provided we know
ρ , and inserting the typical Galactic density of 1 H atom cm^{-3} gives
$\tau \sim 10^6$ years. However, it is uncertain how much of the path length is
traversed in sources, and it is possible that CR are excluded from the
denser clouds, so that this estimate may be wrong. A direct determination
of the CR lifetime is required, and the decay of Be^{10} (half-life 1.6 10^6
years) is a possible 'clock', since its abundance relative to other
secondaries will be higher for small τ than for large τ . Extensive study
of the Be/B ratio (which includes Be^7 and Be^9) has been made (O'Dell et
al. 1973 ; Shapiro and Silberberg 1970), giving $\tau < 3{-}10 \; 10^6$ years.
However, the validity of this result has been questioned by Raisbeck and
Yiou (1973) on the basis of the inaccuracy in our knowledge of production
cross-sections, and they claim that the isotopic abundance of Be^{10} must
be determined for a reliable result.

(f) The overall abundance distribution of elements in CR at a few GeV per nucleon shows strong similarities to the Solar System abundances (see e.g. review by Rasmussen 1975). In particular, the alpha-particle nuclei C,N,O,Ne,Mg,Si etc. show similar abundance ratios. The main differences are (i) an underabundance of H and He (normalized to the C,N,O group), (ii) a lower even-Z to odd-Z ratio, (iii) an over-abundanceof the elements Li, Be, B and the sub-iron group (Z = 19 - 25). Of these (ii) and (iii) are mainly attributable to propagation effects in the interstellar medium. The 'source' composition and path-length distribution required to fit the observed abundances has been extensively studied. Shapiro and Silberberg (1974) find that a function of the form $dN/d\lambda = (1 - \exp(-2.8\lambda^2))\exp(-0.23\lambda)$ fits a wide array of observed abundances, and the resulting source abundances are then generally well correlated with Solar-System abundances (Fig 1, from Shapiro and Silberberg 1974). A decrease of the ratio of CR to Solar-system abundances with increasing first ionization potential has been pointed out by Casse and Goret (1973) and by Havnes (1973). The possible interpretation of this is discussed in Sec 1.3.

1.3 Galactic Theories of CR origin.

Galactic origin for the bulk of CR has been championed chiefly by Ginzburg (1964, 1970 and refs. therein). It should be pointed out at once that the CR electrons must be Galactic on account of their short ($\sim 10^8$ years) lifetime in the microwave background radiation, so that only the nucleon component need be discussed here. A general problem which arises for Galactic models is that if CR propagate by 3-D diffusion and are confined to the Galactic disc for 10^6 years, then an anisotropy greater than that observed is expected (Speller et al. 1972). Ginzburg and Syrovatskii (1964) developed a model in which
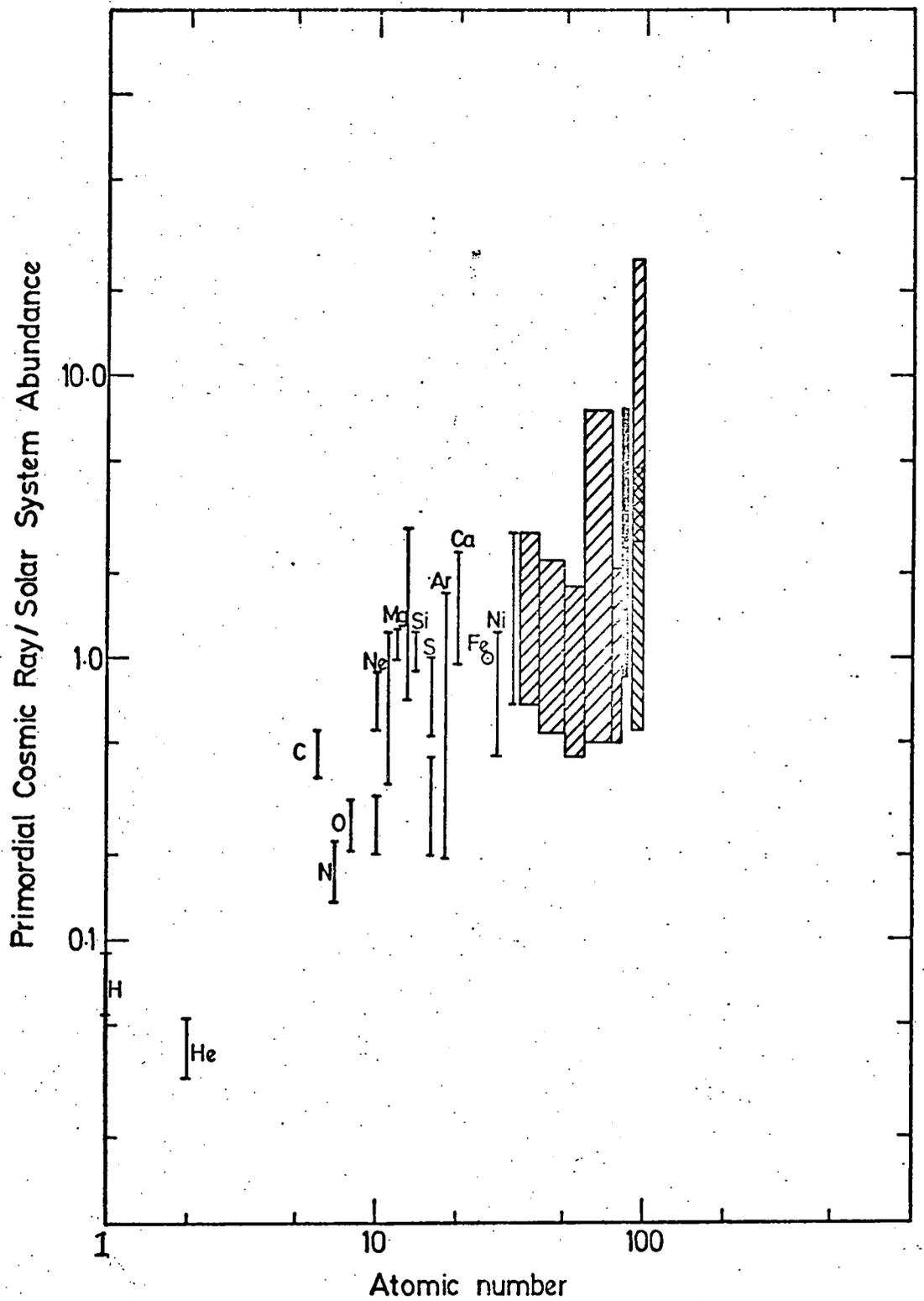
Fig 1-1

Ratio of elemental abundances of cosmic-rays at sources to those for the Sun and meteorites. (The values are normalized to unity at Iron). From Shapiro and Silberberg (1974).

most of the lifetime is spent in a spherical 'halo' around the Galaxy; in this case $\tau \sim 10^8$ years and $\rho \sim 10^{-2}$ cm^{-3}, and the anisotropy limits can be satisfied. However, the evidence for such a halo is equivocal, and has not been observed in normal external spiral Galaxies (Lang and Terzian 1968). Also, the Be/B ratio suggests that $\tau < 10^7$ years (see Sec 1.2(e)). However, it now seems likely that particles diffuse in 1-D along stochastically wandering field lines (Jones 1971), and that the probability of observing a low anisotropy in this case, although still small, is no more unlikely than any other value. Taking into account the random nature of sources (assumed to be supernovae) in space and time, Dickinson and Osborne (1974) showed that the probability of observing $\delta \sim 10^{-4}$ is typically a few percent, so that an 'accidental' low value cannot be ruled out.

The most likely sources of CR in the Galaxy are supernovae (orig- inally suggested by Baade and Zwicky, 1934), their remnants, possibly in association with pulsars, or pulsars themselves. A Galactic volume of 4.10^{66} cm^3 (assuming a disc radius 15 kpc and thickness 1 kpc), filled with CR to a density of 1 eV cm^{-3} requires about 6.10^{54} ergs in CR, so that if $\tau \sim 10^6$ years, we require 6.10^{48} erg yr^{-1} injected. Taking a supernova rate of 1 per 50 years (Ilovaisky and Lequeux 1972), we need about 3.10^{50} ergs per supernova. This is of the same order as the energy content of supernova remnants on the basis of their sychrotron emission if we assume the local ratio of electrons to protons, viz. about 1% . Perhaps the most convincing evidence is the recent observation of the Vela SNR as a gamma-ray source (Thompson et al. 1974); if interpreted as the effect of pion-decay following CR - gas interactions, a total CR content of about 10^{51} ergs may be required, and if typical of other supernova remnants, this is more than adequate to supply the Galaxy at the observed level. Another important clue is provided by the chemical composition of CR. Nucleosynthetic calculations (Schramm and Arnett 1973)

indicate that the explosions of massive stars ($> 8M_\odot$), the probable nature of Type II supernovae, can produce the observed abundance ratios. The C^{12} detonation model of Arnett (1969), which involves less massive stars, appears to be ruled out as the principal source of Galactic CR, since it burns the bulk of its C and O to the iron peak elements.

The difference in spectral shape between iron nuclei ($\gamma = 2.0 \pm .14$) and the lighter elements ($\gamma = 2.4 - 2.8$) (Ormes et al. 1973) may be a result of interstellar propagation (Webber et al. 1973, Audouze and Cesarsky 1973, Meneguzzi 1973), but may alternatively reflect a difference in the source for Fe nuclei (Balasubramanyan et al. 1973). Because the surface of neutron stars is believed to consist principally of iron, Ramaty et al. (1973) suggest that pulsars are the source of the iron nuclei.

Colgate and Johnson (1960) examined the acceleration of particles in supernova shock-waves. The underlying mechanism is the deposition of nearly all the energy of a supernova in the expanding shell, the velocity of which increases as it propagates into the lower density surrounding medium. Relativistic velocities can be reached and a maximum particle energy of 10^{13} eV (or 10^{17} eV if plasma oscillation shocks are considered) can be produced, with a spectral index $\gamma \sim 3$. For a 10^{-4} mass fraction ejected from a 10 $M_\odot$ star, the energy available is $\sim 2 \cdot 10^{51}$ ergs, adequate to maintain the Galactic flux (Colgate and White, 1963, 1966). Later calculations (Colgate et al 1972, Colgate and McKee 1972) gave a spectrum $\gamma \sim 3.1$ and energies up to 10^{14} eV.

Possible evidence against such a shock-wave mechanism is provided by the decrease in cosmic-ray abundances relative to the Solar-System abundances with increasing first ionization potential: this suggests that an electromagnetic rather than a hydrodynamic process is at work (Cassé and Goret 1973 ; Havnes 1971, 1973).

Turning to the possibility of accelerating CR in pulsars, the most important evidence comes from the observation that the spectrum of the Crab nebula is of power-law form from radio frequencies up to the X - ray region, strongly indicating a synchrotron origin. The very high energy loss rates for the electrons involved, which have energies up to about 10^{13} eV, implies continuous injection of particles. The pulsar NP 0532 at the centre of the Crab nebula seems a likely source for these electrons, and indeed the slowing - down rate of the Crab pulsar shows that its energy loss is approximately equal to the required energy input for relativistic particles. The acceleration may occur via the low frequency electromagnetic waves generated by the pulsar (Gunn and Ostriker, 1971, Ostriker and Gunn, 1971). The dynamics of the expanding supernova remnant may be governed by the pressure of relativistic particles which fill the cavity left by the shock-wave as it sweeps up the interstellar medium (Ostriker and Gunn 1971). According to the theory of acceleration by electromagnetic waves (Gunn and Ostriker, 1971), the energy reached depends on the parameter $\nu = eB/mc\Omega$, where B is the magnetic field and Ω is the frequency of the wave. In the immediate vicinity of the pulsar, where B $\sim 10^{12}$ gauss, the energies expected are 10^{18} - 10^{23} eV during the early stages; when Ω has fallen to values small enough to give 1 GeV particles, most of the pulsar energy has already been lost (Gunn and Ostriker 1969; Kulsrud, Ostriker and Gunn 1972). Such a mechanism may explain the highest energy end of the spectrum and a spectral index of $\gamma = 2.5$ is predicted (Gunn and Ostriker 1969). For the low energy end, it is necessary to consider regions much farther from the pulsar, where B is smaller, and a possible site is the expanding supernova shell. Using the model for a supernova remnant developed by Ostriker and Gunn (1971) , Kulsrud et al. (1972) showed that particle energies of 10^9 - 10^{16} eV, with spectral index $\gamma \sim 2$, could be produced. Although more energy goes into electrons than protons, most of this is lost by synchrotron radiation. The total energy injected in relativistic particles was 10^{48} - $10^{49.5}$ ergs.

At the high energy end of the spectrum, where the deflections of CR in the Galactic magnetic field become progressively smaller, there is the possibility of distinguishing Galactic sources as anisotropies in the angular distribution. A uniform distribution of sources in the Galaxy should also lead to anisotropies on account of the different path-lengths through the Galaxy in different directions; this has been considered by Karakula et al (1972) and Osborne et al (1973) using various field configurations and data on arrival directions of CR above 10^{17} eV from the Haverah Park and Sydney (SUGAR) arrays. These authors conclude that a large fraction of the particles at these energies must be of extragalactic origin, unless they are predominantly iron nuclei.

The most recent analysis of the isotropy of arrival directions has been made by Kiraly and White (1975), using data from five air-shower arrays, a total of 119 events above 10^{19} eV. The distribution of arrival directions is shown in Fig 2. An analysis by Krasilnikov et al. (1974) suggested a significant 1st harmonic amplitude centred at R.A. 13h , with a chance probability of 2.6%. This is in contrast to the analysis of 87 showers above $1.5 \ 10^{19}$ eV by Linsley and Watson (1974), who concluded that the distribution was essentially isotropic; the difference was made apparently by the addition of 20 showers from the Yakutsk array and 12 from Haverah Park. A tentative identification of the excess with the Virgo cluster was made by Krasilnikov et al (1974). A different interpretation in terms of Galactic centre sources has been given by Hillas and Ould-ridge (1975): the 13 h peak is centred on $1 = 0^{\circ}$ (1 = Galactic longitude) but lies south of the Galactic plane, and the authors suggested that this could be the effect of deflection by a field along the spiral arms (though Kiraly et al. (1975) point out that the field direction would have to be oppositely directed to that observed locally).   Kiraly and White (1975)
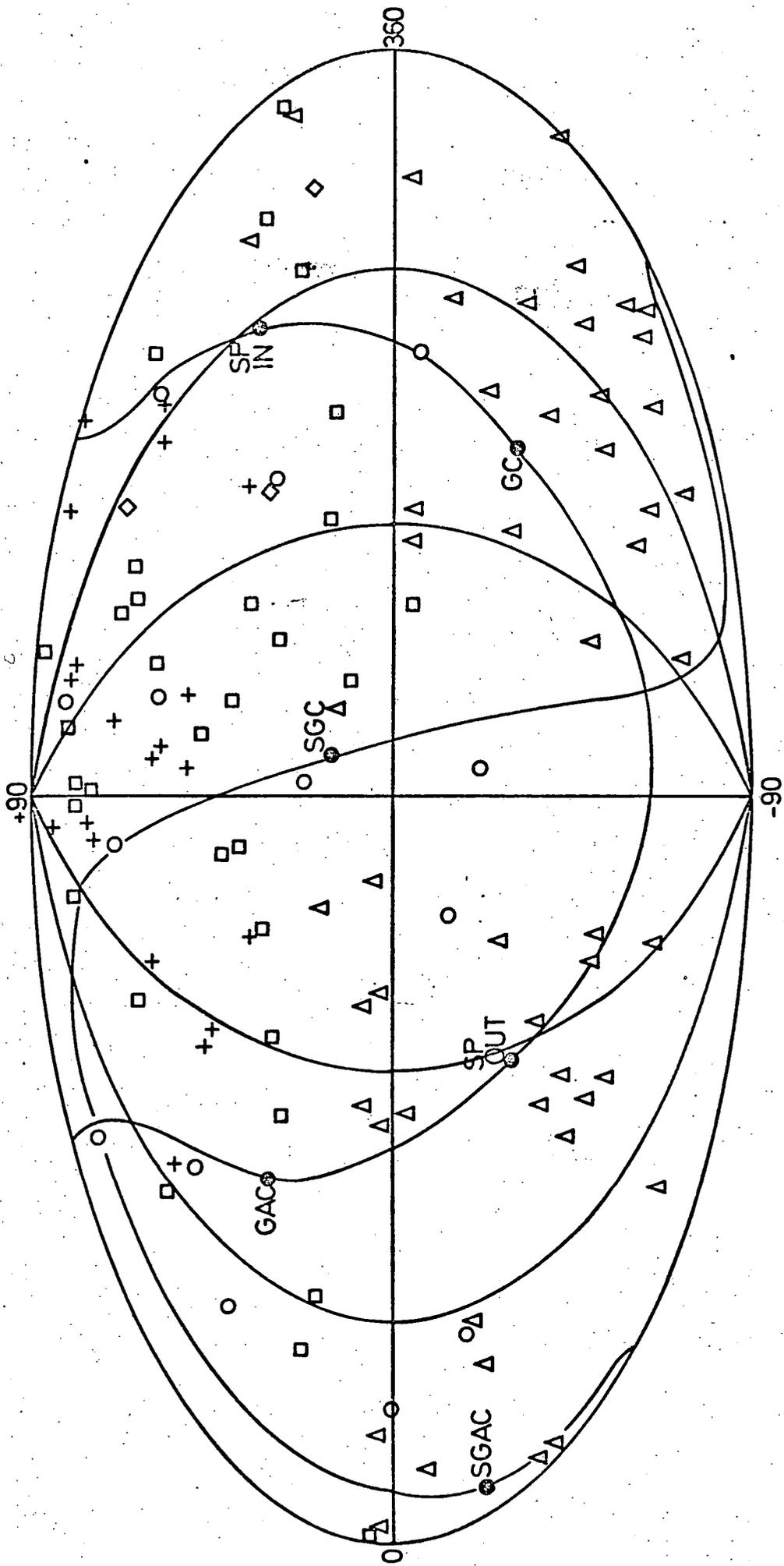
Fig 1-2   Aitoff equal area projection of arrival directions for 119 EAS with primary energy above 10¹⁹ eV. Celestial Co-ordinates. Galactic and supergalactic equators shown as solid lines. From Kiraly and White (1975). Code for EAS arrays: ◇ Cornell, □ Haverah Park, △ Sydney, ○ Volcano Ranch, + Yakutsk.

Table 1-1   Properties of main classes of Galaxy

Type	Description	Example	Number Density Mpc^{-3}	Luminosity (ergs s^{-1}) Radio	I.R.	Optical	X-ray
Spiral Sa - Sc Elliptical E0 - E6	Normal Hubble types 90% S 10% E	M31 M32	10^{-2}	10^{38}	10^{42}	10^{43-44}	10^{39}
Radio Galaxies	Often double, centred on giant Ellipticals	Cyg A	10^{-10} $10^{-8.5}$ 10^{-7} $10^{-5.5}$	10^{45} 10^{44} 10^{43} 10^{42}			10^{42}(Cyg A) $- 10^{46}$(Her A)
Seyferts	Small stellar nucleus. Broad emission lines.	NGC 1275	10^{-4}	10^{39} (NGC4151) 10^{42} (NGC1275)	10^{45} -10^{46}		10^{42}(4151) $- 10^{44}$(1275)
QSO's	Stellar appearance. UV,IR excess Large redshift Broad emission lines	3C273	$10^{-8.5}$ 10^{-7} 10^{-6}	10^{45}		10^{46} 10^{45} 10^{44}	10^{45-46} (3C273)

used Monte Carlo techniques to determine the significance of the suggested peaks, and found that such distributions can be generated by chance with quite high probability. It therefore appears that we must await further statistics before conclusions can be drawn from arrival directions.

If CR are of Galactic origin, then it is possible that the increase in slope at $3 \ 10^{15}$ eV is related to an energy dependent mean free path above this energy. Bell et al (1974) used the observed distribution of radii of neutral hydrogen clouds (1 - 100 pc) and their associated magnetic fields to predict this energy dependence, and find a good fit to the spectrum up to about 10^{17} eV. The model predicts lifetimes of only $\sim 3 \ 10^5$ years for CR below 10^{15} eV, a value which would only be consistent with the traversal of 5 gm cm^{-2} of matter if most of this is traversed in the sources themselves.

1.4 Extragalactic Cosmic Rays.

The possibility of a Universe filled with CR protons to a density of 1 eV cm^{-3} , equal to that in the Galaxy, was originally put forward by Burbidge (1962), the most extensive discussion being in Brecher and Burbidge (1972). The principal objections to such a hypothesis were originally thought to be connected with the energy requirements - the mean density of the Universe is about 10^{-10} ergs cm^{-3} (if we include the observed, luminous matter only, i.e. a density of $\sim 10^{-7}$ atoms cm^{-3}), so that a CR density of $\sim 10^{-12}$ ergs cm^{-3} requires very efficient conversion to high-energy particles. A contribution of 10^{63} ergs per normal Galaxy is required. Table 1 summarizes the properties of the main types of Galaxy which populate the Universe. The most obvious candidates for sources of CR are the powerful radio sources such as M87, which are known

to contain a minimum of 10^{58} - 10^{60} ergs in relativistic particles (the estimates depend on the assumed proton to electron ratio). If we imagine that all galaxies go through a phase of strong radio emission, then since the density of galaxies is 10^{-75} cm^{-3}, we find an average CR density of only 10^{-17} to 10^{-15} ergs cm^{-3}, much less than that required. Brecher and Burbidge (1972) pointed out that since the energy calculated in this way is that for equipartition between field and particles, it is possible that much higher particle fluxes (and hence much lower fields) are present. Seyfert galaxies are another possible CR source; typical Seyferts emit 10^{45-46} ergs s^{-1} in the infra-red, corresponding to a total output of 10^{60-61} ergs if their lifetime is 10^8 years, which is the value suggested by the fact that about 1% of all galaxies are Seyferts and assuming all galaxies go through a Seyfert stage. The IR radiation probably originates in CR electrons via synchtrotron or Inverse Compton processes; a proton to electron ratio of 100 would then give the required output of CR protons.

A classic test for extragalactic origin of CR protons is provided by the interactions with the intergalactic medium, which will result in the production of π^o-decay gamma-rays. The rate of production of gamma-rays above 100 MeV for the local CR spectrum has been calculated by Stecker (1973) to be $q(> 100\text{MeV}) = 1.3 \ 10^{-25}$ s^{-1} per H atom, where corrections for the presence of He nuclei in the CR and the gas are included. Neglecting redshift effects (which introduce factors of order unity), the expected γ-ray flux from the intergalactic medium is

$$j(> 100\text{MeV}) = \frac{1.3 \ 10^{-25}}{4\pi} \ cH_o^{-1} \ n_{IGM} \left(\frac{w_{EG}}{w_G}\right) \sim 10^2 n_{IGM} \frac{w_{EG}}{w_G}$$
$$\text{cm}^{-2} \ \text{s}^{-1} \ \text{sr}^{-1}$$

where n_{ISM} is the extragalactic gas density, and w_{EG} and w_G are the

Fig 1-3

The latitude distribution of Galactic gamma-rays (> 100MeV) averaged over the regions l= 90-150°, 160-170° and 200-260°, as predicted on extragalactic (upper curves) and Galactic (lower curves) models of Cosmic Ray origin. For comparison, the distribution observed by Fichtel et al. (1974) for the same regions is shown. Only neutral Hydrogen gas is included. The extragalactic model assumes uniform CR intensity; the Galactic model assumes a CR variation of the form exp -(R-10)/2.44. (R in kpc), which is an approximation to the distribution of mass density and also the surface density of supernova remnants. Solid lines: no allowance for detector resolution, dashed lines: Gaussian response with $\sigma = 3°$ assumed (an approximation to that of SAS-II, Fichtel et al. 1974). From Dodds et al.(1975).

compared with the observational results from SAS-2 (Fichtel et al. 1974).
It is possible that this provides the first conclusive evidence against
extragalactic CR at energies of a few GeV.

For the very high energy CR, an important test of origin is
provided by the onset of photomeson production by interactions with
the blackbody radiation, the threshold for which is $\sim 5 \; 10^{19}$ eV. The
attenuation length rapidly falls to $\sim 10^{26}$ cm at 10^{20} eV, so that
we would not expect to observe CR of this energy from 'cosmological'
distances ($\sim 10^{28}$ cm). The apparent absence of any cutoff in the
primary spectrum above 10^{19} eV is often interpreted as conclusive
evidence against the extragalactic origin of such particles,but Strong
et al. (1974a) have shown that the data is at present consistent with
a production spectrum of the form $E^{-2.75}$ (differential) at all energies.
Fig 4 shows the expected spectrum for a model in which we take an
expanding cosmology with $H_o = 50$ km s^{-1} Mpc^{-1} and $q_o = 0$,
the normalization being at 10^{12} eV. The large statistical and system-
atic errors at 10^{20} eV inherent in the data preclude the elimination
of such a model at present. In Chapter 2, we consider in detail a model
with sources evolving with epoch, and show that it too may be consistent
with observation.

It was pointed out by Strong et al. (1974b) that if CR production
is proportional to the density of galaxies, then the local super-
cluster will dominate at 10^{20} eV, since the photomeson cutoff does not
significantly attenuate CR from the supercluster. Taking a supercluster
radius of 20 Mpc and a density of galaxies in the supercluster 25 times
the average density of the Universe, it is found that such relatively
local sources contribute about 10% of all CR below 10^{19} eV, but eventually
dominate at higher energies. Fig 5 shows a possible spectrum from such a
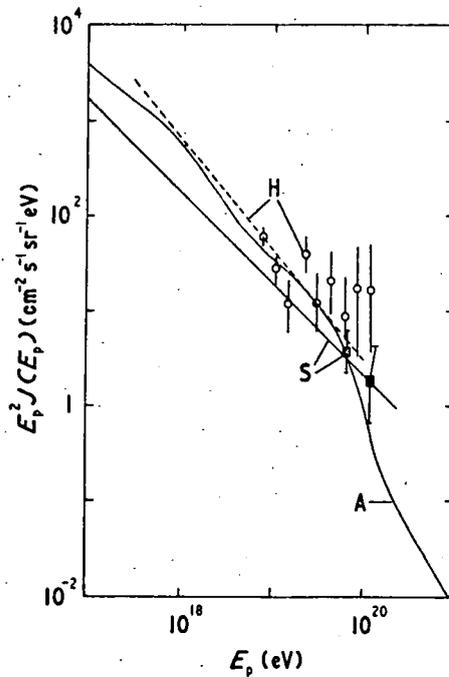
Fig 1-4   Comparison of expected form of a power-law CR spectrum, attenuated by pair-production and photomeson production, with experimental data from Haverah Park (H) and Sydney (S) arrays. Production spectrum of form $E^{-2.75}$ is assumed, and normalized to data at 10^{12} eV. CR production rate assumed uniform in expanding Universe with $H_O = 50$ km s^{-1}Mpc^{-1}. Present day blackbody radiation temperature $T = 2.7$ K. From Strong et al. (1974a)
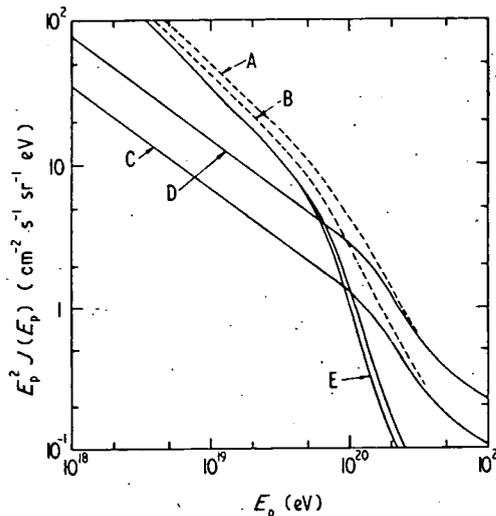
Fig 1-5   Proton spectrum expected for extragalactic origin assuming source density proportional to density of Galaxies. Curve E shows the contribution from Universal CR (static Universe case), C and D the supercluster contributions taking a supercluster fraction of 6% and 13% respectively. The total spectra are shown as curves A and B. From Strong et al. (1974b)

'supercluster enhancement' model. It can be seen that the photomeson cutoff may be very much less than for the usual extragalactic models.

A more restricted type of extragalactic model involves production and confinement within the local supercluster (SC). The local SC is centred on the Virgo cluster of galaxies at about 18 Mpc distant (de Vaucouleurs, 1970), which contains about 10^4 galaxies and also the powerful radio source M87. Brecher and Burbidge (1972) suggested that since diffusion out of superclusters is probably a slow process, taking 10^{9-10} years, a SC confinement model is more reasonable and at the same time reduces the energy requirements by a factor of about 100.

If CR do fill the Universe at the local energy density, then we would expect them to be isotropic at all energies. On the basis of the low anisotropy at 10^{11}-10^{12} eV, Elliot (1974) has suggested that extragalactic sources predominate at least above these energies, with a possible change from extragalactic to Galactic origin at lower energies. Such a change may be supported by the apparent drop in the secondary to primary ratio between 10^{10} and 10^{11} eV.(see e.g. Meyer 1974). The evidence for anisotropy at the highest energies has been discussed above (Sec 1.3), and does not at present argue strongly for or against extra-Galactic origin.

1.5 The Gamma-ray Background.

The existence of an isotropic, diffuse flux of X-rays and gamma-rays is well established, and the experimental data relating to the spectrum is reviewed in Chapter 9 as a prelude to comparison with the theory developed in preceding chapters. As in the case of the CR spectrum, attention is now directed towards the main features of current observations and theory of origin.

Fig 6 shows a compilation of the data above 10 keV taken from Ch. 9. It is worth noting at once that a power-law of the form $E^{-2.1}$ provides a rough fit to the whole spectrum from 10 keV to 30 MeV, although individual experiments give evidence of deviations particularly in the 10 MeV region, where an excess may be present. Above 30 MeV, the SAS-2 data indicate a steeper spectrum, roughly E^{-3}.

It is possible that the X-ray part of the spectrum (1-100 keV) is due to intergalactic plasma at temperatures of $10^7 - 10^8$ K and densities of the order of the critical density ($\sim 10^{-5}$ H atoms cm^{-3}) required to give a closed Universe (see e.g. Schwarz and Gursky, 1973). Such models can provide an adequate fit to the observed spectrum in this range. However the exponential cut-off with increasing energy precludes such a mechanism as an explanation of the gamma-ray part of the spectrum, which continues as a power-law up to much higher energies. For this reason the thermal models will not be discussed further here.

The existence of large energies in CR electrons in radio galaxies suggested one of the first possible mechanisms for the X- and gamma-ray backgrounds. Felten and Morrison (1963) proposed that the X-rays were generated by the inverse-Compton scattering (ICS) of starlight
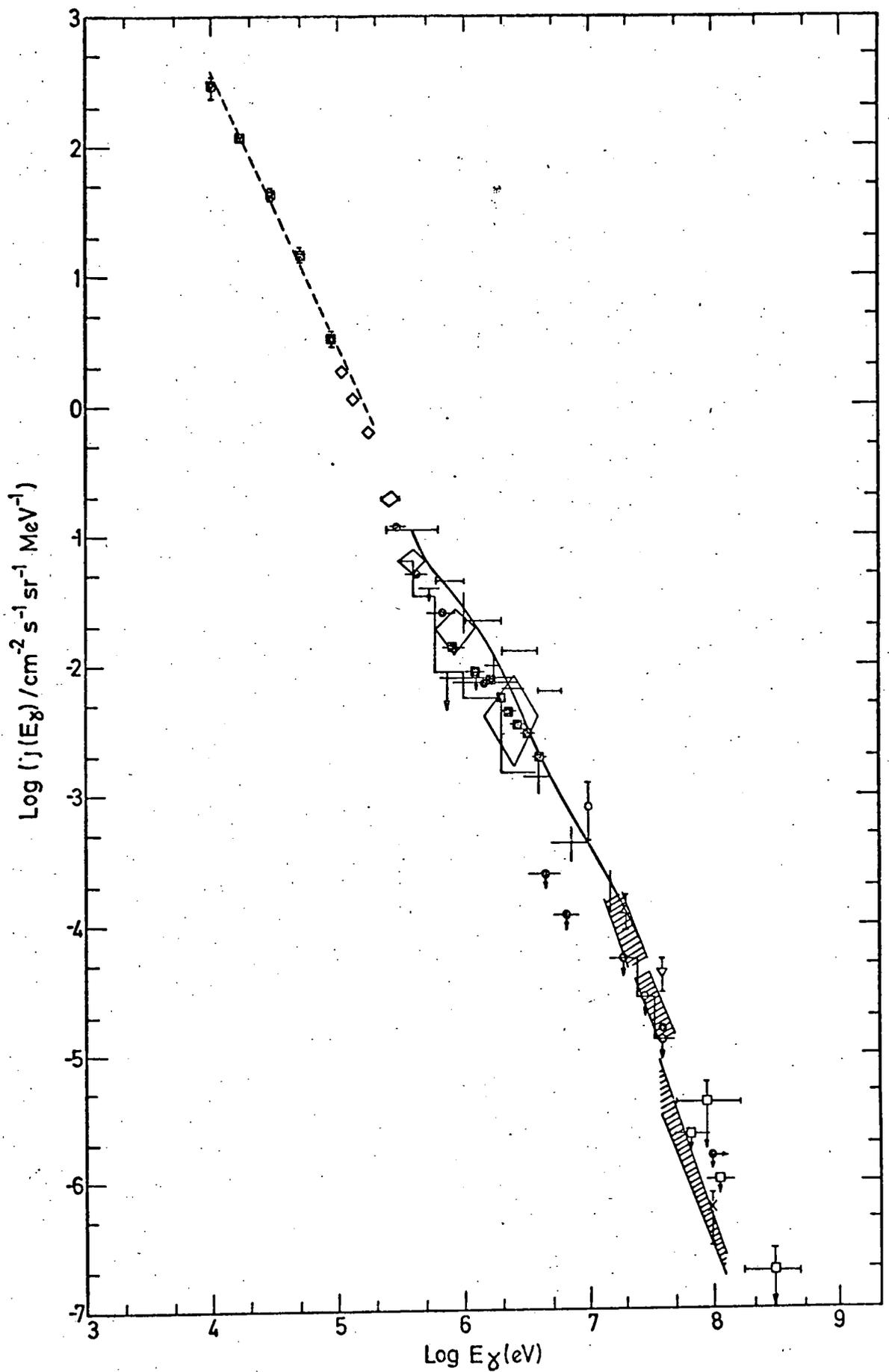
Fig 1-6 Compilation of data on the Gamma-Ray Background. A survey of the data and key to the experimental points is given in Chapter 9.

photons by relativistic electrons in intergalactic space. With the discovery of the microwave background, with its high photon density (400 cm^{-3} compared to perhaps 10^{-2} cm^{-3} for starlight), the role of ICS had to be re-assessed. Felten and Morrison (1966) suggested that electrons leaking out of radio galaxies could explain the X-ray background in this way. Although the intensity expected on the basis of energy-equipartition between particles and magnetic fields in radio sources was two orders of magnitude too small compared to the observed X-ray flux, the possibility that such equipartition is not valid cannot be excluded (see Sec 1.3). The _shape_ of the spectrum in this model agrees roughly with that observed; both synchrotron and ICS processes produce photon spectra of the form $j(E) \propto E^{-\frac{\gamma+1}{2}}$ for an electron spectrum with power law index γ. In the case of radio emission the spectrum is generally expressed in the form $I(\nu) \propto \nu^{-\alpha}$, (units of Watts Hz^{-1} sr^{-1}), so that $\alpha = (\gamma-1)/2$. Since many radio sources have $\alpha \sim 0.8$, the corresponding ICS X-ray spectrum should be of the form $E^{-1.8}$, which is quite close to that observed above 10 keV. This also implies $\gamma = 2.6$ for the electron spectrum, which is in good agreement with measurements of the local electron spectrum.

An attempt to overcome the energy problems mentioned above was made by Brecher and Morrison (1969), who showed that electron leaking out of _normal_ galaxies on a timescale of 10^6 years could provide the observed X- and gamma-ray fluxes by ICS. They also related the possible increase in the spectral index of the X-ray spectrum at 40 keV to that observed in the radio spectra of normal galaxies between 500 and 1500 MHz, the magnetic field required in this case being 4 μG and the electron energies a few GeV. Their model took into account the dispersion in the radio indices and spectral break energies of galaxies, and used an appropriate luminosity function for the radio intensities. The spectral shape predicted was of the form E^{-2} from about 40 keV up

to 10 MeV (corresponding to electron energies up to 50 GeV), and flattens slightly to $E^{-1.8}$ at higher energies in the absence of electron energy losses, which are expected to steepen the spectrum to $E^{-2.3}$ at 100 MeV. This type of spectrum is obviously compatible in a general way with the observations as shown in Fig 6. The ability of the model to account for the detailed shape of the X-ray region has been questioned by Cowsik and Kobetich (1972), although Brecher (1973) has argued that their criticisms are not consistent with the observed spectral shape of the radio fluxes from galaxies.

Other theories designed to account for the gamma-ray background have assumed a separate origin from the X-ray region. Stecker (1969a,b, 1971) proposed that π^{o}-decay gamma-rays from CR-gas interactions at high redshifts ($z \sim 100$) could explain the background. The π^{o}-decay spectrum has a peak at 70 MeV, which in this case will be redshifted back to ~ 1 MeV and can thus produce the excess at around this energy which some observations have shown. A comparison of this model with the data is shown in Fig 7. A good fit is obtained above 1 MeV. Unfortunately the maximum reshift for the proposed CR sources is an arbitrary parameter with no theoretical basis at present.

Another possible source of π^{o}-decay gamma rays is matter-antimatter annihilation at high redshifts, which is expected to occur on the boundaries of matter and antimatter regions in the Omnes baryon-symmetric cosmology (Omnes, 1969).Stecker et al.(1971) have shown that the spectral shape is essentially determined by absorption by Compton interactions with intergalactic gas, which cuts off the spectrum below 1 MeV, and by pair-production interactions with matter at higher energies. Fig 7 shows this model compared with the data; the fit is excellent, although it should be emphasized that the normalization is arbitrary.
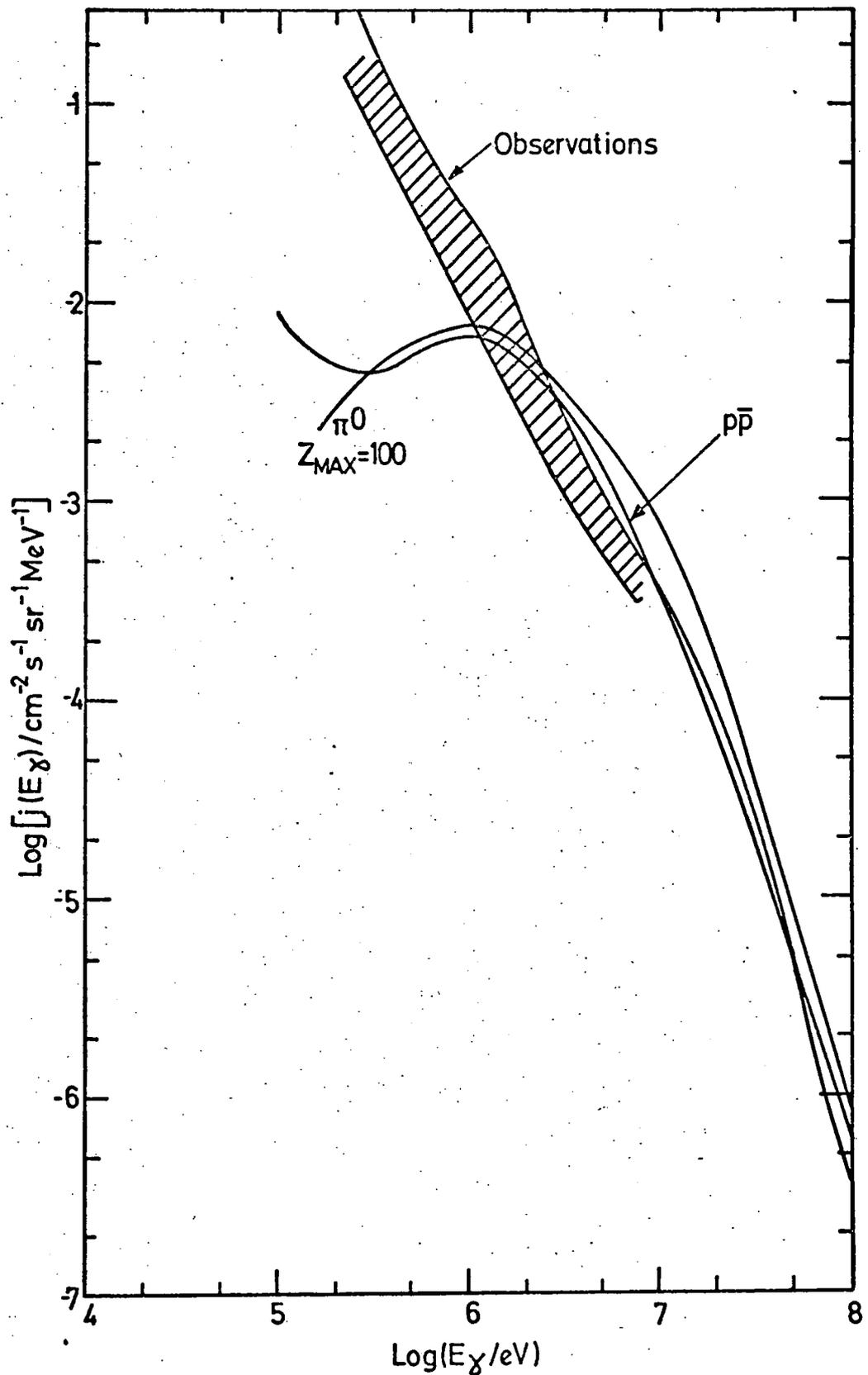
Fig 1-7 Comparison of two models for the gamma-ray background with a summary of the data in Fig 1-6. The models are 1) redshifted pion-decay spectrum from CR-gas interactions at early epochs (z ~100),   2) matter-antimatter annihilation in baryon-symmetric cosmology. Both theoretical spectra are from Stecker (1975).

1.6   The Evolution of Radio Sources and QSO 's.

The theory for the gamma-ray background developed in later Chapters involves extragalactic CR sources which are supposed to have been more numerous (or more powerful) in the past, on a cosmological time-scale. Although these sources are not here identified with any particular class of object, similar evolutionary trends are found in the powerful radio sources, which are known to be sources of relativistic electrons, and in the QSO 's. In this section, the evidence for such evolution will be reviewed.

Using the technique of radio source counts (described below), it was originally hoped that information on the cosmological parameters of the Universe could be obtained; however, it has become apparent that none of the standard cosmological models can reproduce the observed counts, and that they are dominated by evolutionary effects so large that only an accurate physical model of radio-galaxy development would allow the cosmological variations to be distinguished. For the more limited samples of objects which have optically measured redshifts, the lum-inosity-volume test can be applied, and as will be described later, this shows that evolution also occurs in the case of the radio-quiet QSO's.

Source Counts

Source counts determine the quantity $N(>S)$, the number of sources per steradian having a radio flux density greater than S.(The differ-ential form $N(S)$ is preferable given enough statistics, and this has been used by Longair (1974), but most earlier results are quoted in terms of $N(>S)$). For Euclidean space and a non-expanding cosmology, the exp-ected form $N_o(>S)$ for a uniformly distributed population of sources with luminosity function $\rho(P)$ (such that the number of sources per unit

volume between luminosity P and P+dP is $\rho(P)dP$), is easily derived.
A source of luminosity P is included in $N_o(S)$ provided $P/r^2 > S$, so
the number of such sources is $N(>S,P) = 4\pi/3 \; \rho(P)(P/S)^{3/2}$ per unit
volume. For the whole population of objects,

$$N(>S) = \frac{S^{-3/2}}{3} \int \rho(P) \; P^{3/2} dP$$

This is independent of $\rho(P)$ (except for a normalizing constant), so that
a knowledge of this function is not necessary in order to test the unif-
ormity of the source distribution in space.

More generally, when the cosmological model is taken into account,
a more complex form of $N(>S)$ is predicted, which depends on the spectrum
of the sources because of the redshifting of the radio flux and which
involves the modified inverse-square law of non-Euclidean space (see
e.g. the review by Longair, 1971). The expected shape of $N(>S)$ is
still independent of $\rho(P)$, provided that this is not itself a function
of redshift. For this reason, the counts are usually presented in the
form $N(>S)/N_o(>S)$. The important feature of such predicted source counts
is that without evolutionary effects all cosmological models predict
a less steep slope than in the Euclidean case.

Source counts are now available at frequencies from 178 to 5000MHz.
The most extensive is that of Pooley and Ryle (1968), the 5C survey at
408 MHz, which covers a flux range of 10^{-2} to 50 f.u. (1 f.u. = 10^{-26}
Watts m^{-2} Hz^{-1}.). Fig8 shows the form of N/N_o (from Longair, 1971). It
is clear that the slope of the curve is higher than the Euclidean value
(-1.5 on a log-log scale), and is more like -1.8 at high flux densities.
There is an excess of sources in the 0.1 - 10 f.u. range compared to the
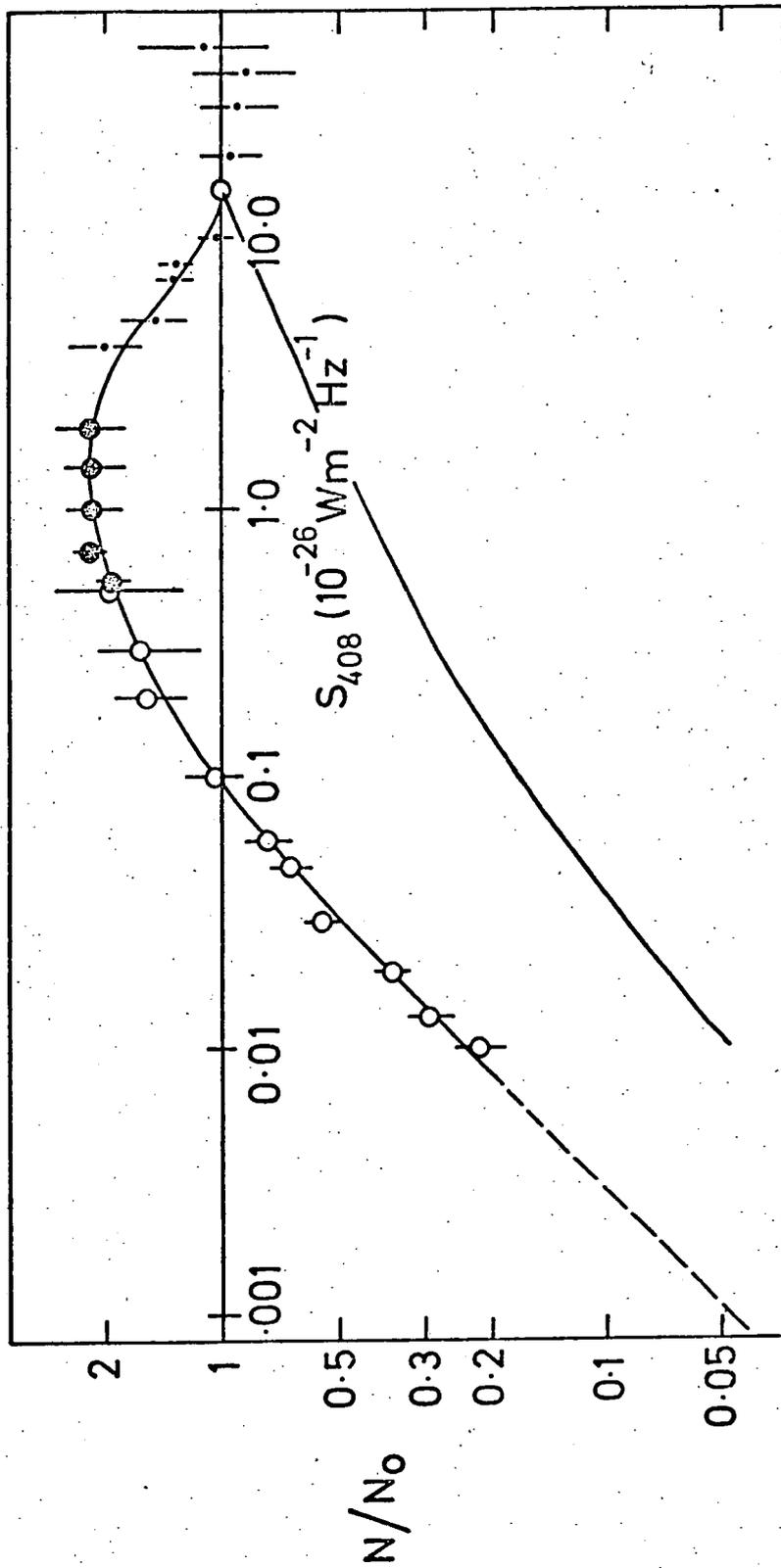
Fig 1-8

The log N ~ log S curve for the Cambridge 5C survey at 408 MHz.

From Longair (1971). The lower line shows the shape expected for

the case of a typical cosmological model without evolution.

Euclidean case. Fig 8 also shows the prediction for a typical cosmol-
ogical model with no source evolution (Longair 1971), which is clearly
in conflict with the observations. The counts at other frequencies have
been summarized by Longair (1974). At 178 MHz (the 3CR, 4C and North
Polar Surveys), 408 MHz (5C and Parkes surveys), and 1420 MHz (Wester-
bork, Greenbank, and Davis (1973) and Maslowski(1973) surveys) the
same feature of a steep slope at high flux densities is found. At
2700 MHz (Parkes) and 5000 MHz (Parkes and Greenbank) the distribution
is much flatter, and does not deviate significantly from the Euclidean
curve.

Longair (1966) showed that the 3CR (178 MHz) survey was consistent
with either density or luminosity evolution of the brightest sources,
with the form $\rho(z)$ (or $P(z)$) $\propto (1+z)^{\beta}$, up to a maximum redshift z_m. Here,
the density is defined relative to co-moving volumes, i.e. volumes which
expand with the Universe. For the case of density evolution, the best
model had $\beta = 5.7$ and $z_m = 4$. Models in which all radio sources evolve
were ruled out on the grounds that too many faint sources are predicted.
To obtain the rapid convergence below .25 f.u. shown by the 3CR counts,
it was necessary to restrict evolution to sources with luminosity more
than $10^{26.8}$ W Hz^{-1} sr^{-1} at 178 MHz, i.e. to the most powerful radio
sources. An independent restriction on the value of z_m is provided by
the radio background, which corresponds to a brightness temperature of
30 ± 7 K at 178 MHz (Bridle, 1967). Evolution of the form $(1+z)^6$ would
give an excess background if $z_m > 3$ (Longair 1971). However the source
counts do not in fact require a sharp cutoff at z_m - it is sufficient
that the source density does not continue to increase significantly
beyond z_m. Rowan-Robinson (1968) showed that evolution of the form
$\exp(\text{const.}(1 - \frac{1}{1 + z}))$ would fit the data equally well.

Luminosity - Volume Test.

The existence of a maximum redshift for evolution at $z \sim 3$ indicated by the source counts strongly suggests a connection with quasars, for which there appears to be a cutoff in the range $z = 2$ to 3, and this led Longair (1966) to suggest that the evolution of QSO's was responsible for the shape of the $N(>S)$ curve. To test this hypothesis requires $N(>S)$ for a sample of radio sources identified as QSO's but the number of such objects is too small for the source count method to be applicable. However, since the redshifts of QSO's is known, their spatial distribution can be determined (assuming cosmological origin of the redshifts), and this forms the basis of the 'luminosity-volume test' (Schmidt 1968).

This test was devised to overcome the selection effects which necessarily arise in the catalogues of QSO's. Samples of QSO's identified by optical searches (usually by looking for objects with a UV excess) have a single well defined limiting magnitude. However those QSO's discovered as a result of optical identifications of radio sources have a more complicated selection effect, since the source identification is limited first by the radio survey limit and second by the limit to which the optical identification can be made. The selection is further complicated by the varying ratio of optical to radio luminosity in QSO's. The luminosity-volume test overcomes this problem by calculating for each object the quantity V/V_m , the ratio of the volume V out to the source distance to the volume V_m corresponding to the maximum distance at which the source would be detected and identified as a QSO. For a uniform distribution of sources in Euclidean space, the mean value for this ratio for many sources, $\langle V/V_m \rangle$, is 0.5 , and larger values imply a concentration of sources at large z .

Schmidt (1968) applied the luminosity-volume test to 33 identified 3CR sources with $S(178 \text{ MHz}) > 9$ f.u. and $m_{vis} < 18.4$, and obtained $\langle V/V_m \rangle = 0.69$; only six of the sample had $V/V_m < 0.5$. The probability of the result occuring by chance was estimated to be only .01% (see also Rees and Schmidt 1971), and shows that QSO's are clustered towards the limits of their observable range. Schmidt (1972a) showed that density evolution of the form $\rho \propto (1+z)^6$, or alternatively $\rho \propto 10^{5\tau}$ (where τ = light travel time to the source in terms of the age of the Universe) up to $z_m = 2.5$ is consistent with the distribution of redshifts and luminosities of this sample. Pure luminosity evolution was ruled out because of the large numbers of optically identified QSO's at $m_{vis} = 19$ with $z > 2.5$ which would then be predicted.

Lynds and Wills (1972) applied the test to 31 QSO's in the 4C catalogue and obtained $\langle V/V_m \rangle = 0.67 \pm 0.05$, in good agreement with Schmidt's (1968) result. Fig 9 shows the histogram of values of V/V_m in this case.

It is of interest to see whether other classes of object apart from QSO's show evolutionary effects. Applying the luminosity-volume test to 25 radio galaxies with known redshifts, Schmidt (1972b) showed that there is little evidence for evolution ($\langle V/V_m \rangle = 0.53 \pm 0.06$), but the maximum redshift measured was only 0.25. Schmidt also attempted to separate the radio galaxies from the QSO's in the 5C survey at 408 MHz (Pooley and Ryle 1968) by subtracting the expected contribution from QSO's according to the evolutionary schemes obtained previously in Schmidt (1970) and Schmidt (1972a), taking a ratio of QSO's to radio galaxies of 0.2 . The source-count method was then applied to the remaining sources, and strong evolution, similar to that suggested by Longair (1966), was found. On the other hand Schmidt found that the sharp changeover from no evolution to strong evolution at $P(178 \text{ MHz}) = 10^{26.8} \text{ W Hz}^{-1} \text{ sr}^{-1}$ could not account for the steep slope of $N(>S)$ without overestimating the number
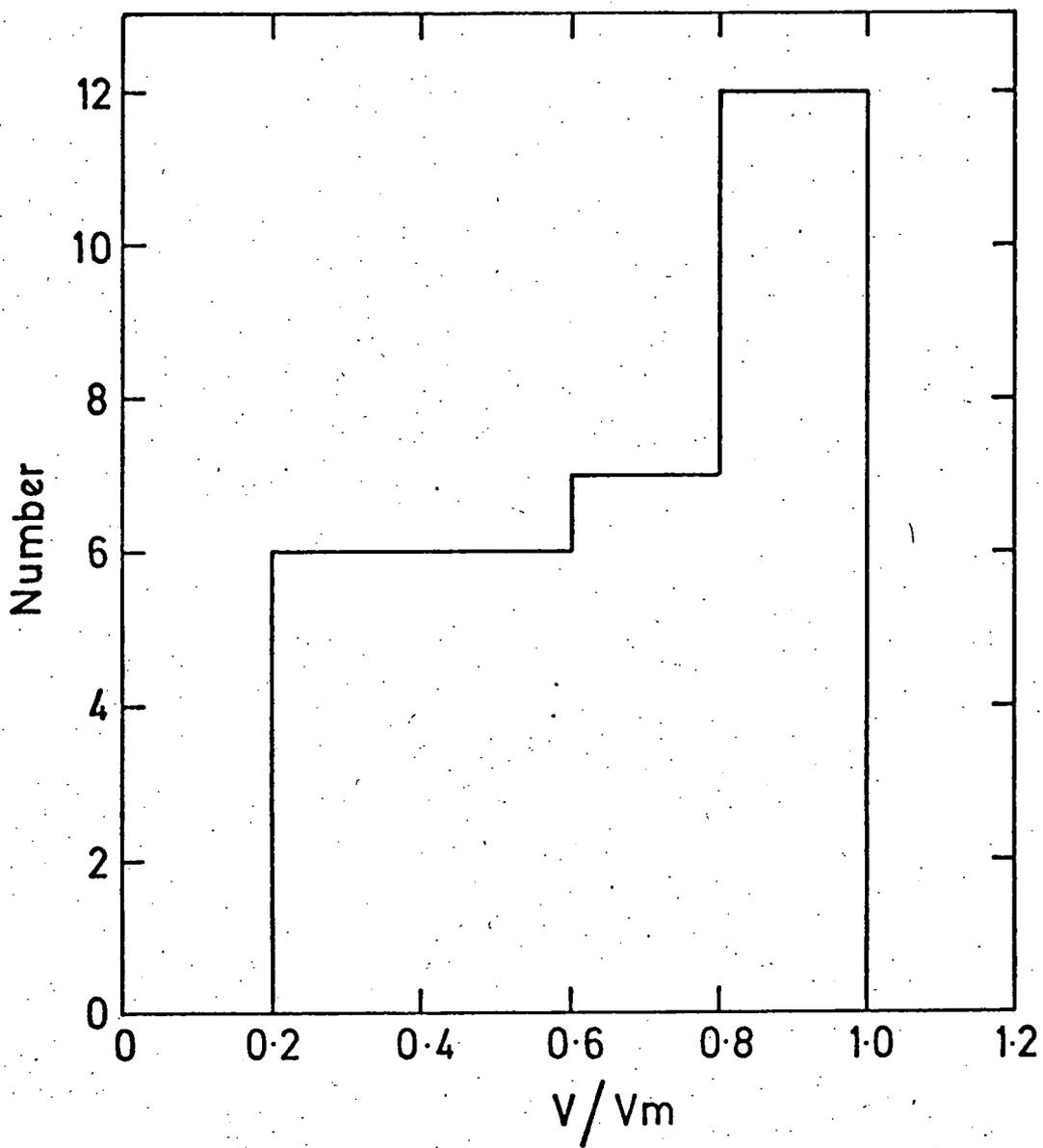
<u>Fig 1-9</u> Distribution of V/V_m for 31 QSO's in the 4C catalogue

(Lynds and Wills, 1972). The mean value is $\langle V/V_m \rangle = .67 \pm .05$

of faint sources.

The luminosity-volume test has been applied to samples of optically selected QSO's complete down to magnitude 18 by Schmidt (1970). A similar evolutionary law to that for the radio QSO's was found.

In conclusion, there is now evidence for the rapid evolution of various types of powerful sources of radiation, and, as discussed in Sec 1.4, such objects must also be sources of energetic particles. This provides some justification for the assumption of evolution in cosmic-ray sources necessary for the theory developed in later chapters.

1.7 Introductory description of the new model for the Gamma-Ray Background.

The model for the gamma-ray background uses a model for the shape of the primary proton component of cosmic-rays suggested by Hillas (1968). In the Hillas model, it is supposed that CR primaries are of extragalactic origin (in the 'Universal' sense), and that the shape of the spectrum is related to the interactions with the blackbody radiation at high redshifts. As an introduction to the more detailed treatment in later Chapters, a general description of the processes responsible for the CR and gamma-ray spectra in the present development of the model will now be given.

The spectrum of CR at production (only the proton component is considered) is taken to be a power law with spectral index γ; the total number of sources is supposed to increase in the past, according to a law of the type $(1 + z)^{\beta}$, up to a maximum z_m, where z is the cosmological redshift. This is similar to the evolution which seems to occur for powerful radio sources and QSO's, as discussed in Sec 1.6 .Protons lose energy by redshift after production, so that $E = E_o/(1+z)$, where E_o is the energy at production and E is the energy at the present time in the absence of other losses. In addition, other losses occur due to interactions with the blackbody radiation (radiation temperature 2.7 K, mean photon energy $6 \cdot 10^{-4}$ eV); the pair production process ($p + \gamma_{bb} \rightarrow p + e^+ + e^-$, denoted PC) has a threshold at $10^{18}/(1+z)$ eV, while photomeson production ($p + \gamma_{bb} \rightarrow p + \pi$) has a threshold at $5 \cdot 10^{19}/(1+z)$ eV. The PC process is considered to be the origin of the increase in spectral slope at about 10^{15} eV (the 'knee'); the position of the knee is determined by z_m and the change in slope by β. In Chapter

2 it is shown that the parameters z_m = 14.3 and β = 4.4 give a good fit to the primary spectrum in the range 10^{12} - 10^{19} eV.

The gamma-ray spectrum, which is the main subject of later chapters, is a consequence of a photon-electron cascade initiated by the PC electrons; the cascade proceeds via two electromagnetic processes - Inverse Compton Scattering ($e + \gamma_{bb} \rightarrow e + \gamma$), and pair-production ($\gamma + \gamma \rightarrow e^+ + e^-$), denoted by ICS and PP respectively. Initially both processes occur via the microwave radiation; for γ-ray energies below $10^{14}/(1+z)$ eV, PP cannot proceed in this way, but the presence of the starlight background (photon energy typically 1 eV) allows the process to continue down to energies near 10^{11} eV. Fig 1-10 showns schematically the typical energies and the associated processes which occur in the development of the cascade.

The model is examined in subsequent Chapters as follows. In Chapter 2, the primary spectrum is calculated for various parameters of the model, and compared with observations. The π^0-decay gamma-ray flux produced in low energy CR - gas interactions is also discussed here, since it sets important limits on the gas density allowed in the model if it is to account for all CR protons above GeV energies. Chapters 3, 4 and 5 are devoted to detailed examination of the PC, ICS and PP processes for use in the subsequent treatment of the gamma-ray spectrum in the model. Chapter 6 reviews observational and theoretical aspects of the various radiation fields which play an important role in the model. In Chapter 7, the gamma-ray spectrum is calculated using approximations which show that the model is potentially an explanation of the observed spectrum. Chapter 8 deals with a detailed numerical approach to the spectrum, using more real-

Summary of processes producing the gamma-ray spectrum

in the present model. γ_{bb} indicates microwave blackbody

photons, γ_s starlight photons. Typical energies of components

are shown.

COSMIC RAY SOURCES

p

p $10^{19}eV$

PC

p

e

e $10^{15}eV$

γ_{bb}

ICS

e

γ $10^{14}eV$

γ_{bb}

PP

γ_{bb}

e

e $10^{13}eV$

ICS

γ $10^{12}eV$

γ_{bb}

PP

γ_s

e

e $10^{10}eV$

ICS

γ $10^{8}eV$

γ_{bb}
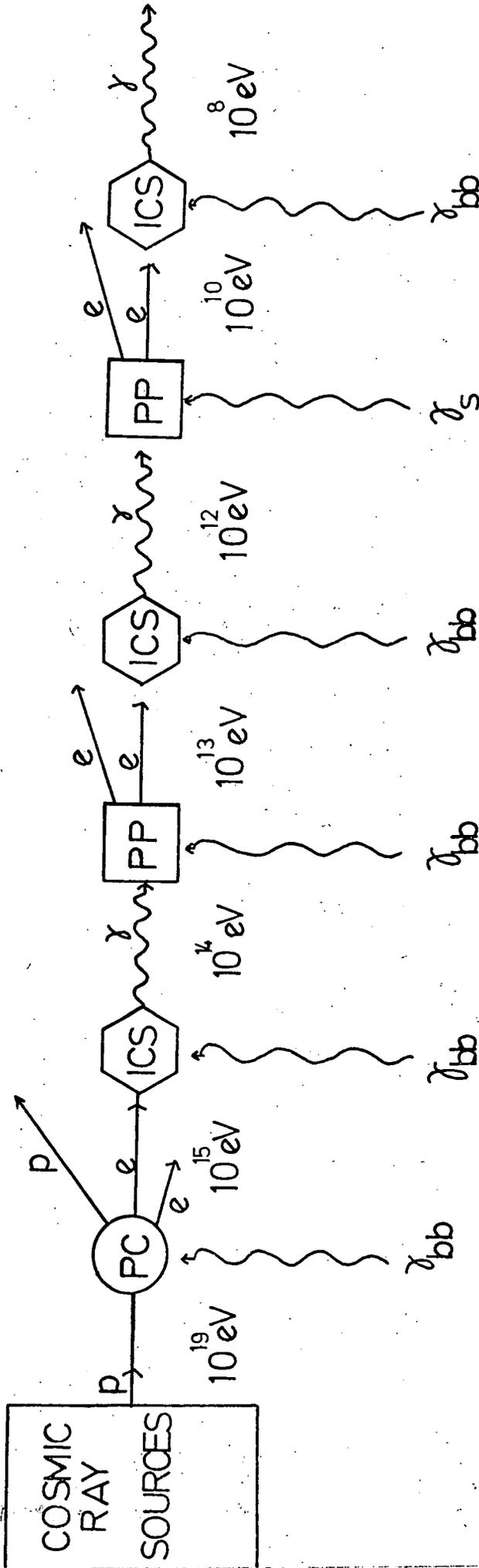
istic models for the starlight radiation fields. In Chapter 9, an extensive review of observational data on the gamma-ray background is made as a prelude to comparison with the data and an assessment of the viability of the model.

Chapter 1 References

Arnett W D , 1969, Astrophys. Sp.Sci 5, 180

Audouze J and Cesarsky C J, 1973, Nature 241, 98

Baade W and Zwicky F, 1934, Proc. Nat. Acad. Sci. 20 259

Balasubramanyan V K, Ormes J F, and Ramaty R, 1973, 13th Int. Conf.
    Cosmic Rays, Denver, 1, 163

Bell C J, Bray A D, Denehy B V, Goorevich L, Horton L, Loy J G,
    McCusker C B A, Nielsen P, Outhred A, Peak L S, Ulrichs J,
    Wilson L S, Winn M M., 1973, Proc. 13th Int. Conf. Cosmic Rays,
    Denver, 4, 2525

Bell M C, Kota J and Wolfendale A W., 1974, J. Phys A

Brecher K., 1973, Ap.J. 181, 255

Brecher K and Burbidge G R., 1972, Ap.J. 174, 253

Brecher K and Morrison P., 1969, Phys. Rev. Lett. 23, 802

Bridle A H., 1967, Mon. Not. Roy. Astr. Soc. 136, 219

Burbidge G R., 1962, Prog. Theor. Phys. 27, 999

Casse M and Goret P., 1973, Proc. 13th Int. Conf. Cosmic Rays,
    Denver, 1, 584

Colgate S A and Johnson H J, 1960, Phys. Rev. Lett. 5, 235

Colgate S A and McKee C R., 1973, Ap.J. 181, 903

Colgate S A, McKee C R, and Blevins B., 1972, Ap.J. 173, L87

Colgate S A and White R H, 1963, Proc. 8th Int. Conf. Cosmic Rays,
    Jaipur, 335.

Colgate S A and White R H., 1966, Ap.J. 143, 626

Cowsik R and Kobetich E J., 1972, Ap.J. 177, 585

Davis M M.,

Dickinson G J and Osborne J L., 1974, J.Phys. A. 7, 728

Dodds D, Strong A W and Wolfendale A W., 1975, Mon. Not. Roy. Astr.
    Soc., in the press.

Doroskhevich A G, Longair M S, and Zeldovich Ya B., 1970, Mon.
    Not. Roy. Astr. Soc., 147, 139

Elliot H., 1974, Phil. Trans. Roy. Soc. Lond. 277, 381

Fanselow J L, Hartman R C., Hildebrand R H and Meyer P., 1969,
    Ap.J. 158, 771

Felten J E and Morrison P., 1966, Ap. J. 146, 686

Fichtel C E, Hartman R C, Kniffen D A,Thompson D J, Bignami G F,
    Ogelman H, Ozel M F and Tumer T., 1974, GSFC Preprint X-662-74-304

Field G., 1972, Ann. Rev. Astr. Astrophys. 10, 227

Ginzberg V L, 1972, Nature Phys. Sci. 239, 8

Ginzberg V L, 1974, Phil. Trans. Roy. Soc. Lond. 277, 463

Ginzberg V L and Syrovatskii S I., 1964, 'The Origin of Cosmic Rays'.

Gunn J E and Ostriker J P., 1969, Phys. Rev. Lett. 22, 728

Gunn J E and Ostriker J P., 1971, Ap. 165, 523

Havnes O., 1971, Nature 221, 25

Havnes O., 1973, Astr. Astrophys. 24, 435

Hillas A M and Ouldridge M, 1975, Nature 253 609

Ilovaisky S A and Lequeux J., 1972, Astr. Astrophys. 20, 347

Jones F C., 1971, Proc. 12th Int. Conf. Cosmic Rays, Hobart, 1, 396

Karakula S, Osborne J L, Roberts E and Tkaczyk W., 1972, J. Phys. A.
    5, 904

Kiraly P and White M., 1975, preprint, submitted to J. Phys.

Kiraly P, Osborne J L, White M and Wolfendale A W., 1975, preprint,
    submitted to Nature.

Krasilnikov D D et al. , 1974, J. Phys. A. 7,L176

Kulsrud R M, Ostriker J P and Gunn J E., 1972, Phys. Rev. Lett. 28, 636

Lang K R and Terzian Y., Ap. Lett. 3, 29

Lingenfelter R E, Ramaty R and Fisk L A., 1971, Ap. Lett. 8, 93

Linsley J and Watson A A., 1974, Nature 249, 816

Longair M., 1966, Mon. Not. Roy. Astr. Soc. 133, 421

Longair M., 1970, Mon. Not. Roy. Astr. Soc. 150, 155

Longair M., 1971, Rep. Prog. Phys. 34, 1125

Longair M., 1974, in 'Confrontation of Cosmological Theories with

　　　Observational Data', IAU Symposium 63, 93

Longair M and Scheuer P A G., 1970, Mon. Not. Roy. Astr. Soc. 151, 45
Lynds R and Wills D., 1972, Ap. J. 172, 531
Maslowski ., 1973 Acta Astron. 22, 227

Meneguzzi M., Nature 271, 100 (1973)

Meyer, P., 1974, Phil. Trans. Roy. Soc. Lond. 277, 349

O'Dell F W, Shapiro M M, Silberberg R and Tsao C H., 1973, Proc. 13th

　　　Int. Conf. Cosmic Rays, Denver, 1, 490

Omnes R., 1969, Phys. Rev. Lett. 23, 38

Ormes J F, Balasubramanyan V K and Arens J F., 1973, Proc. 13th Int.

　　　Conf. Cosmic Rays, Denver, 1, 157

Osborne J L, Roberts E and Wolfendale A W., 1973, J. Phys. A. 7, 1767

Ostriker J P and Gunn J E., 1971, Ap. J. 164, L95

Pooley G G and Ryle M., 1968, Mon. Not. Roy. Astr. Soc. 139, 515

Raisbeck G and Yiou F., 1973, Proc. 13th Int. Conf. Cosmic Rays,

　　　Denver, 1, 494

Ramaty R, Balasubramanyan V K, and Ormes J F., 1973, Science 180, 731

Rasmussen I L., 1975, NATO Advanced Study Institute on 'Origin of

　　　Cosmic Rays', 97.

Rees M J and Schmidt M., 1971, Mon. Not. Roy. Astr. Soc. 154, 1

Rowan-Robinson M., 1968, Mon. Not. Roy. Astr. Soc. 138, 445

Sandage A and Lutyen ., 1969, Ap. J. 155, 913

Schmidt M., 1968, Ap. J. 151, 393

　　　　　　　1970,　"　　162, 371

　　　　　　　1972a　"　　176, 273

　　　　　　　1972b　"　　176, 289

　　　　　　　1972c　"　　176, 303

　　　　　　　1966　"　　146, 7

Schramm D N and Arnett W D., 1973, Proc. 13th Int. Conf. Cosmic Rays,

　　　Denver, 1, 646

Schwarz D and Gursky H., 1973, NASA SP-339, 15

Shapiro M M and Silberberg R., (1970) Ann. Rev. Nuc. Sci. 20, 323

Shapiro M M., 1974, Phil. Trans. Roy. Soc. Lond. 277, 319

Speller R, Thambyaphillai T and Elliot H., 1972, Nature 235, 25

Stecker F W., 1969a, Nature 222, 1157

        1969b Ap. J. 157, 507

        1971a 'Cosmic Gamma-Rays', Mono Book Corp, Baltimore, Md.

        1971b, Nature 229, 105

        1973, NASA SP-339, 211

        1975, NATO Advanced Study Institute 'The Origin of Cosmic

        Rays', 267

Stecker F W., Morgan D L and Bredekamp J H., 1971, Phys. Rev. Lett.

    27, 1469

Stecker F W, and Puget J L., 1972, Ap. J. 178, 57

Strong A W, Wdowczyk J and Wolfendale A W., 1974a, J. Phys. A. 7, 1489

                             1974b J. Phys. A. 7, 1767

Thompson D J, Bignami G F, Fichtel C E and Kniffen D A., 1974, Ap. J.

    190, L51

de Vaucouleurs G., 1970, Ap. J. 159, 435

Watson A A., 1975, NATO Advanced Study Institute 'Origin of Cosmic Rays',

    61

Webber W R, Lezniak J A, Kish J C and Damle S V., 1973, Nature 271, 97

Chapter 2.   The primary cosmic-ray spectrum on the Hillas model.

Introduction.

This chapter will be concerned with the calculation of the spectrum of

primary cosmic-rays in the Hillas model, and a comparison with recent experi-

mental data. Since the model draws on certain concepts of cosmology, a brief

summary of cosmological principles is given, in which the important parameters

are introduced. A general description of the methods for computing particle

spectra in evolving cosmological models is followed by their application to

the Hillas model, using both an analytical approximation, which gives useful

insight into the form of the spectrum, and also accurate numerical solutions.

A comparison with the data for energies above 10^{12} eV is then made. An estimate

of the energy lost to electron pairs in (γ, p) interactions is made on the basis

of the experimental and theoretical spectra, for use later in normalizing the

resulting gamma-ray spectrum. Finally, the gamma-ray flux resulting from inel-

astic collisions of cosmic-rays with intergalactic gas is calculated, placing

severe limits on the intergalactic gas density allowed in this model.

1.   Cosmological models.

The 'cosmological principle' that the Universe is, on a large enough scale,

homogeneous and isotropic, leads to the Robertson-Walker form of the line element

$$ds^2 = c^2 \, dt^2 - R^2(t) \, \frac{dr^2}{1-kr^2} + r^2(d\theta^2 + \sin^2\theta \, d\phi^2) \qquad (2.1)$$

where r, θ, ϕ, are spherical polar co-ordinates, and $k=+1$, 0, or -1 according as

space is open (hyperbolic), flat (Euclidean) or closed (spherical). $R(t)$ is

a dimensionless scale factor, and is the same at all points for the same cosmic

time, t. Substitution of (2.1) in the Einstein field equations gives the follow-

ing two equations for R :

$$\frac{3\dot{R}^2}{R^2} + \frac{3kc^2}{R^2} - \Lambda = 8\pi G\rho \qquad (2.2)$$

$$\frac{2\ddot{R}}{R} + \frac{\dot{R}^2}{R^2} + \frac{kc^2}{R^2} - \Lambda = -8\pi Gp/c^2$$

where ρ is the density and p the pressure. Λ is a constant of integration. We are interested in matter-dominated models in which the pressure is negligible (the Friedmann models). In this case equations (2.2) give

$$\frac{d}{dt}(\rho R^3) = 0 \qquad (2.3)$$

which is just conservation of matter.

Zero-pressure models can be parameterized and written in dimensionless form as follows (Stabell and Refsdahl, 1966):

Define $\quad q = -\frac{\ddot{R}}{RH^2} \quad , \quad \sigma = \frac{4\pi G\rho}{3 H^2} \quad , \quad H = \frac{\dot{R}}{R} \qquad (2.4)$

Then equations (2.2) become

$$= 3H^2(\sigma - q) = 3H_0^2(\sigma_0 - q_0)$$

$$kc^2 = H_0^2 R_0^2(3\sigma_0 - q_0 - 1)$$

$$\rho R^3 = \rho R_0^3$$

where subscript zero indicates present values, Substitution in (2.2) then gives

$$\frac{\dot{R}^2}{R_0^2} = 2\sigma_0 \frac{R_0}{R} + (\sigma_0 - q_0)\frac{R^2}{R_0^2} + q_0 + 1 - 3\sigma_0 \qquad (2.5)$$

The 'cosmological constant' Λ will be taken as zero, so that $\sigma_0 = q_0$. It is often convenient to use the redshift z as the independent variable, rather than t. R is related to z by

$$\frac{R}{R_0} = \frac{1}{1 + z} \qquad (2.6)$$

A photon emitted at time t with wavelength λ will have a wavelength λ, at a later time t_1 given by

$$\frac{R(t_1)}{R(t)} = \frac{\lambda'}{\lambda} = \frac{1 + z}{1 + z_1} \qquad (2.7)$$

where z and z_1 are the redshifts corresponding to t and t_1. The variation of z with t is given by (2.5) as

$$\frac{dt}{dz} = \frac{dt}{dR}\frac{dR}{dz} = H_0^{-1}/(1 + 2q_0 z)^{\frac{1}{2}}(1 + z)^2 \qquad (2.8)$$

2.2 Particle spectra in cosmological models.

In deriving particle spectra in an expanding cosmology, it is convenient to use the flux defined in terms of co-moving coordinates (i.e. coordinates expanding with the Universe), $j(E,z)$. This is related to the flux in proper coordinates $j_0(E,z)$ by

$$j(E,z) = j_0(E,z)(1 + z)^3 \qquad (2.9)$$

In this way the change of density due to the expansion is automatically allowed for, and need not be included in the equations for the flux. The development of the spectrum when there are no catastrophic or cascade type processes is described by the continuity equation in energy space:

$$\left.\frac{\partial j}{\partial z}\right)_E + \left.\frac{\partial}{\partial E}\right)_z \left[j\ \frac{db}{dE}\right] = G(E,z) \qquad (2.10)$$

where $b(E,z) = dE/dz$ and $G(E,z)$ is the source function defined as the flux of particles produced per unit energy range and redshift per unit of co-moving volume. Equation (2.10) can be solved by integrating along a contour in the (E,z) plane, this contour being the solution of $dE/dz = b(E,z)$ with initial condition $E(E_0, 0) = E_0$. Writing $j'(E_0, z) = j(E(E_0,z), z)$, so that

$$\left.\frac{\partial j'}{\partial z}\right)_{E_0} = \left.\frac{\partial j'}{\partial z}\right)_E + \left.\frac{\partial j'}{\partial E}\right)_z \left.\frac{\partial E}{\partial z}\right)_{E_0} \qquad (2.11)$$

Then equation (2.10) becomes

$$\left.\frac{\partial j'}{\partial z}\right)_{E_0} + j' \left.\frac{\partial b}{\partial E}\right)_z = G(E,z) \qquad (2.12)$$

Multiplying (2.12) by the integrating factor $\exp \int_0^z \frac{\partial b}{\partial E}\Big)_z dz'$ allows the solution to be written as

$$j'(z_m,E_0)\exp \int_0^{z_m} \frac{\partial b}{\partial E}\Big)_z dz' - j(0,E_0) = \int_0^{z_m} G(E,z')\exp \int_0^{z'} \frac{\partial b}{\partial E}\Big)_z dz''\ dz' \qquad (2.13)$$

where $E = E(E_0,z)$ and z_m is the maximum redshift from which particles are generated.

The integral spectrum can be calculated more simply using the integral source function $G(> E,z)$. Then

$$j(0, >E_0) = \int_0^{z_m} G(> E(E_0, z'), z')\ dz' \qquad (2.13a)$$

2.3 Solution of Energy-loss equation.

In the case of protons losing energy by interactions with the blackbody radiation, the important processes are pair-production and pion production. Pair-production is treated in detail in Chapter 3, and the calculated energy loss rates shown in Fig.3-5 are used in the present work. For pion production (i.e. the 'photomeson process'), the energy losses are taken form Stecker (1968). The inverse total attenuation lengths are plotted in fig 2-1, for a temperature $T_0 = 2.7K$. As explained in Ch.3 , the attenuation lengths at any other temperature can be obtained using the relation

$$\left[\frac{1}{E}\frac{dE}{dx}\right]^{-1} = \lambda(E, T) = \lambda\left(\frac{ET}{T_0}, T\right)\cdot\left(\frac{T}{T^0}\right)^3 \qquad (2.14)$$

where $T = T_0(1 + z)$.

Using (2.8) and (2.14), equation (2.11) becomes

$$\frac{dE}{dz} = \frac{cH_0^{-1}}{\lambda(E(1+z),T_0)} \cdot \frac{(1 + z)}{(1 + 2q_0 z)^{\frac{1}{2}}} + \frac{E}{(1 + z)} \qquad (2.15)$$

To solve this for $E(E_0, z)$ it is convenient to define $E_1 = E/(1 + z)$, since then

$$(1 + z)\frac{dE_1}{dz} = \frac{dE}{dz} - \frac{E}{(1 + z)}$$

and equation (2.15) becomes

$$\frac{dE_1}{dz} = \frac{cH_0^{-1}}{(E_1(1+z)^2, T_0)} \frac{(1 + z)}{(1 + 2q_0 z)^{\frac{1}{2}}} \qquad (2.15a)$$

In this way, the energy losses due to redshift are automatically included. Equation (2.15a) was solved numerically using a Runge-Kutta program.

2.4 Evaluation of $\left.\frac{\partial b}{\partial E}\right)_z$

It is useful to rewrite $\left.\partial b/\partial E\right|_z$ in the form

$$\left.\frac{\partial b}{\partial E}\right|_z = \left.\frac{\partial}{\partial E}\right|_z \frac{dE}{dz} = \left.\frac{\partial}{\partial E}\right|_z \left[E\left(\frac{1}{E}\frac{dE}{dz}\right)\right]$$

$$= \frac{1}{E}\frac{dE}{dz}\left[1 + \left.\frac{\partial}{\partial \ln E}\right|_z \ln \frac{1}{E}\frac{dE}{dz}\right]$$
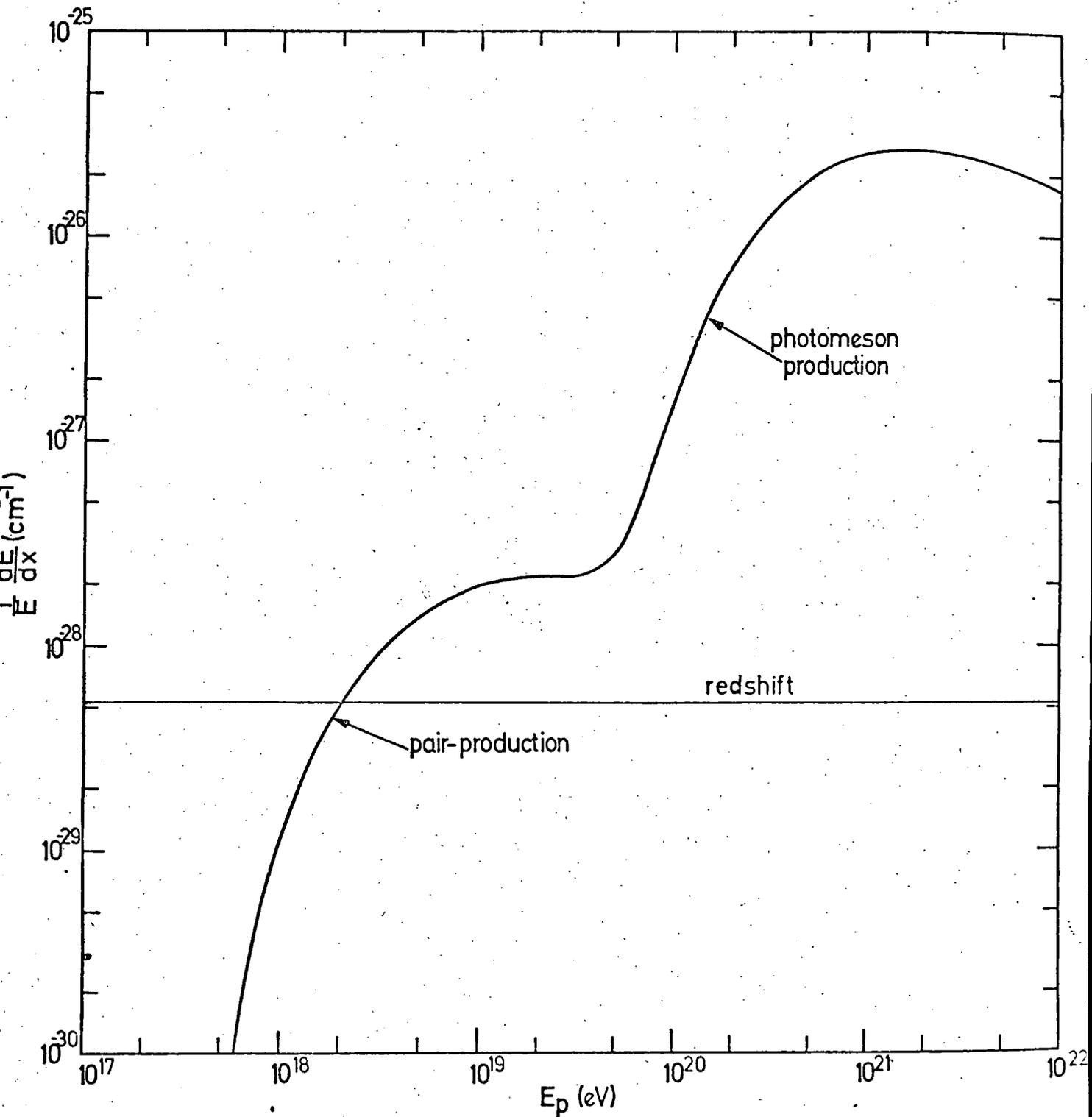
Fig 2-1

Energy losses for protons in a 2.7 K radiation field. The Inverse attenuation lengths are taken from Stecker (1968) for the photomeson production, and from Chapter 3 for pair-production. Redshift losses for z = 0 and H_o = 50 km s^{-1}Mpc^{-1} are also shown.

and

$$(1 + z_m) = \sqrt{(E_{th}/E_k)} \qquad (2.17)$$

In the energy region (ii), it is a good approximation to assume that contributions to the spectrum come only from $z < z_u$; above this redshift, energy losses increase rapidly, so the contribution from $z > z_u$ is small.

For energy losses by redshift only, $\partial b/\partial E|_z = 1/(1+z)$, and equation (2.13) becomes

$$j(0, E_0) = \int_0^{z_{max}} G(E_0(1+z), z)(1+z) \, dz \qquad (2.18)$$

where $z_{max} = z_m \qquad$ for $E_0 < E_k$

$\qquad\qquad = z_u \qquad$ for $E_0 > E_k$

We now consider the case where the production rate is assumed to follow a power law in (1+z), as in the models for radio source evolution discussed in Chapter 1. Then

$$G(E, z) = \frac{BH_0^{-1} (1+z)^{\beta} E^{-\gamma}}{(1+z)^2 (1+2q_0 z)^{\frac{1}{2}}} \qquad (2.19)$$

for a production rate of the form $B(1+z)^{\beta} E^{-\gamma}$, where B is a constant. Substitution in (2.18) gives

$$j(0, E_0) = BH_0^{-1} E_0^{-\gamma} \int_0^{z_{max}} \frac{(1+z)^{\beta - \gamma - 1}}{(1+2q_0 z)^{\frac{1}{2}}} dz \qquad (2.20)$$

For the case $q_0 = \frac{1}{2}$,

$$j(0, E_0) = \frac{BH_0^{-1} E_0^{-\gamma}}{\beta - \gamma - \frac{1}{2}} \left[(1+z_m)^{\beta - \gamma - \frac{1}{2}} -1 \right] \qquad E_0 < E_k$$

$$\qquad\qquad\qquad\qquad\qquad\qquad\qquad\qquad\qquad\qquad (2.21)$$

$$= \frac{BH_0^{-1} E_0^{-\gamma}}{\beta - \gamma - \frac{1}{2}} \left[(E_{th}/E_0)^{\frac{\beta - \gamma - \frac{1}{2}}{2}} -1 \right] \qquad E_0 > E_k$$

For $E_{th} > E_0$, i.e., just above the 'kink' in the spectrum, equation (2.21) shows that the increase in slope is, for $q_0 = \frac{1}{2}$,

$$\Delta\gamma = \frac{1}{2}(\beta - \gamma - \frac{1}{2})$$

Similarly, for $q_0 = 0$

$$\qquad\qquad\qquad\qquad\qquad\qquad\qquad\qquad (2.22)$$

$$\Delta\gamma = \frac{1}{2}(\beta - \gamma)$$

Hence if the spectrum is parameterized by γ, $\Delta\gamma$, and E_k , the model parameters β and z_m can be found.

Now since

$$\frac{1}{E}\frac{dE}{dz} = \lambda^{-1}\frac{dx}{dz} = \frac{\lambda^{-1} cH_0^{-1}}{(1+z)^2(1+2q_0z)^{\frac{1}{2}}}$$

we have

$$\left.\frac{\partial b}{\partial E}\right|_z = \frac{cH_0^{-1} \lambda^{-1}(E,z)}{(1+z)^2 (1+2q_0z)^{\frac{1}{2}}} \left[1 + \left.\frac{\partial}{\partial \ln E}\right|_z \ln\lambda^{-1}\right] \qquad (2.16)$$

The logarithmic gradient $\left.\partial/\partial\ln E\right|_z$ (λ^{-1}) was derived from Fig 2-1, and is shown

in Fig (2.2), for z = 0. The values for different z and energy E can be obtained

by reading this curve at E(1 + z). Hence to evaluate $\left.\partial b/\partial E\right|_z$, the value of

$E(E_0 ,z)$ is first obtained as described in Sec.2.3, and then the functions

given by Figs(2.1) and (2.2) are used to evaluate the expression of equation

(2.16).

2.5 <u>Analytical approximation for the proton spectrum in the Hillas model.</u>

A good understanding of the way in which the spectrum depends on the model

parameters can be obtained using a simple analytical approach. The spectrum can

be divided into three energy regions, characterized by

(i) energy loss by redshift only for all z up to z_m . $E_0 < E_k$

(ii) energy loss by redshift up to some z_u , after which the pair-prod-

uction losses begin to become dominant. $E_0 > E_k$

(iii) energy loss by pair-production and photomeson production are dominant

for all z.

Here, E_k is the energy at which the change in slope (the 'kink') in the prim-

ary spectrum is taken to occur. The value of z_u for a given E_0 is given approx-

imately by

$$E_0(1 + z) = E_{th} /(1 + z_u)$$

where E_{th} is the threshold energy for pair-production at z = 0, approximately

$7 \cdot 10^{17}$ eV. Hence

$$(1 + z_u) = \sqrt{(E_{th}/E_0)}$$
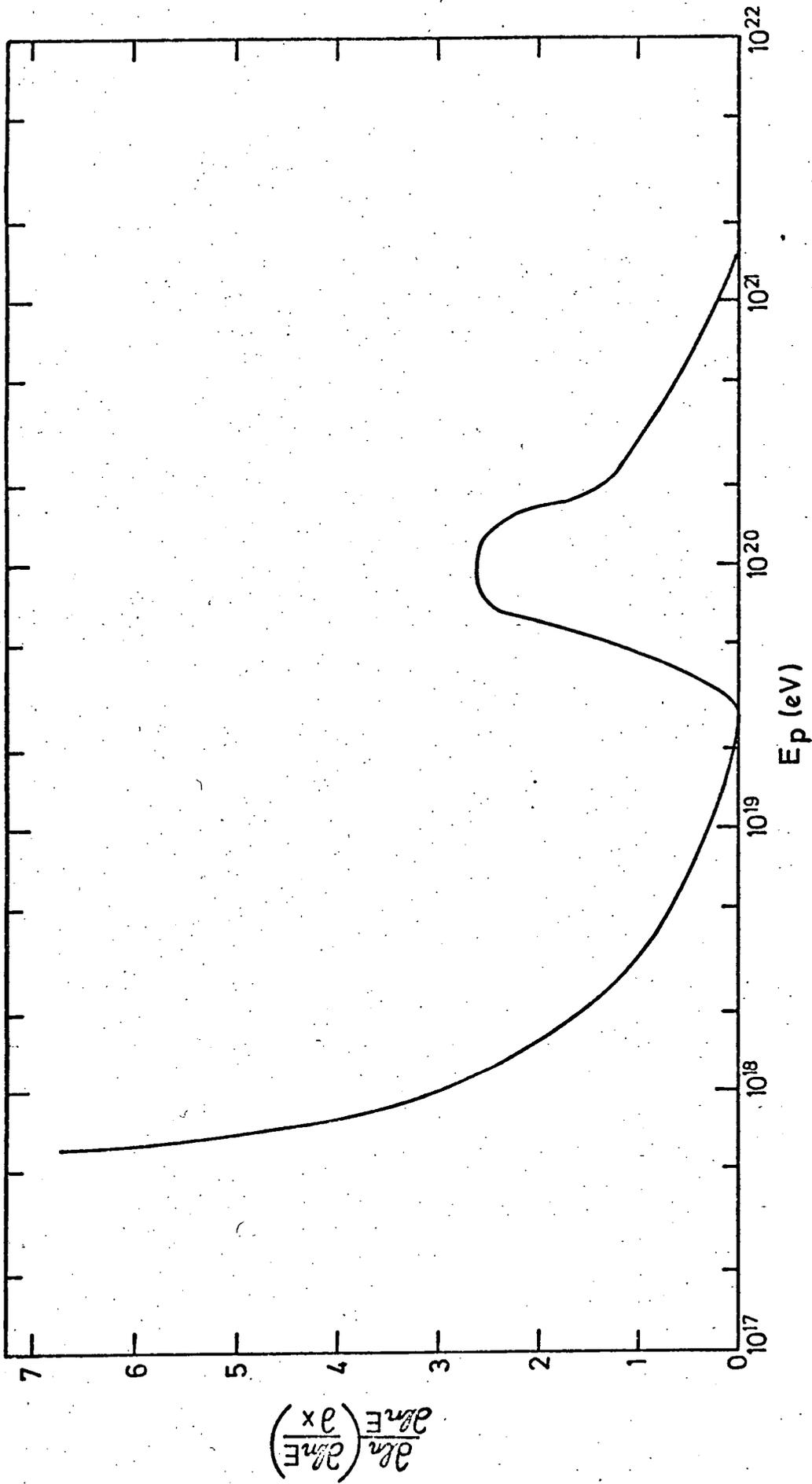
Fig 2-2   Logarithmic gradient of Inverse Attenuation Lengths for
protons on Blackbody radiation, based on Fig 2-1.

$$\frac{\partial \ln}{\partial \ln E}\left(\frac{\partial \ln E}{\partial x}\right)$$

E_p (eV)

2.6 Comparison with the experimental data.

The experimental data on the primary spectrum is discussed in the Appendix to this Chapter. The data, presented in integral form, are summarized in Fig 2-3. An estimate of the 'best' differential spectrum (from Hillas 1974) is shown in Fig 2-4.

The spectrum in Fig 2-3 is well represented by a power law of index $\gamma = 2.5$ for $E < 3.10^{15}$ eV, and $\gamma + \Delta\gamma = 3.2$ for $E > 3.10^{15}$ eV. This gives for the model, from equations (2.17) and (2.22)

$$1 + z_m = \sqrt{7.10^{17}/3.10^{15}} = 15.3 \qquad (2.23)$$

$$\text{and} \qquad \beta = 2(3.2 - 2.5) + 2.5 + 0.5 = 4.4 \quad (q_0 = \tfrac{1}{2}) \quad (2.24)$$

These values were used as the basis of the calculations for the model spectra using equations (2.13) and (2.13a). The model with parameters given above, and $H_0 = 50$ km s^{-1} Mpc^{-1} is taken as the 'standard' model.

In comparing the experimental data with the model, it must be pointed out that since only the proton component of the cosmic-rays is considered in the model, it is the proton spectrum data which should be used. However, the presence of extragalactic nuclei at energies below 10^{15} eV will not affect the spectrum of <u>nucleons</u> in the model, and it is the nucleon spectrum to which the data of Fig 2-3 refer. There is no experimental evidence for the presence of heavy nuclei above 10^{15} eV (the highest energy composition data being at 10^{12} eV, see Appendix to this Chapter), so that the assumption of pure proton composition above 10^{15} eV is not unreasonable.

The spectrum calculated for the 'standard model' defined above is shown in Fig 2-5, together with the experimental data of Fig 2-3. Normalization is to the data points in the $10^{12} - 10^{14}$ eV range (i.e. those from the work of Kempa (1973) assuming proton composition). Agreement is generally good
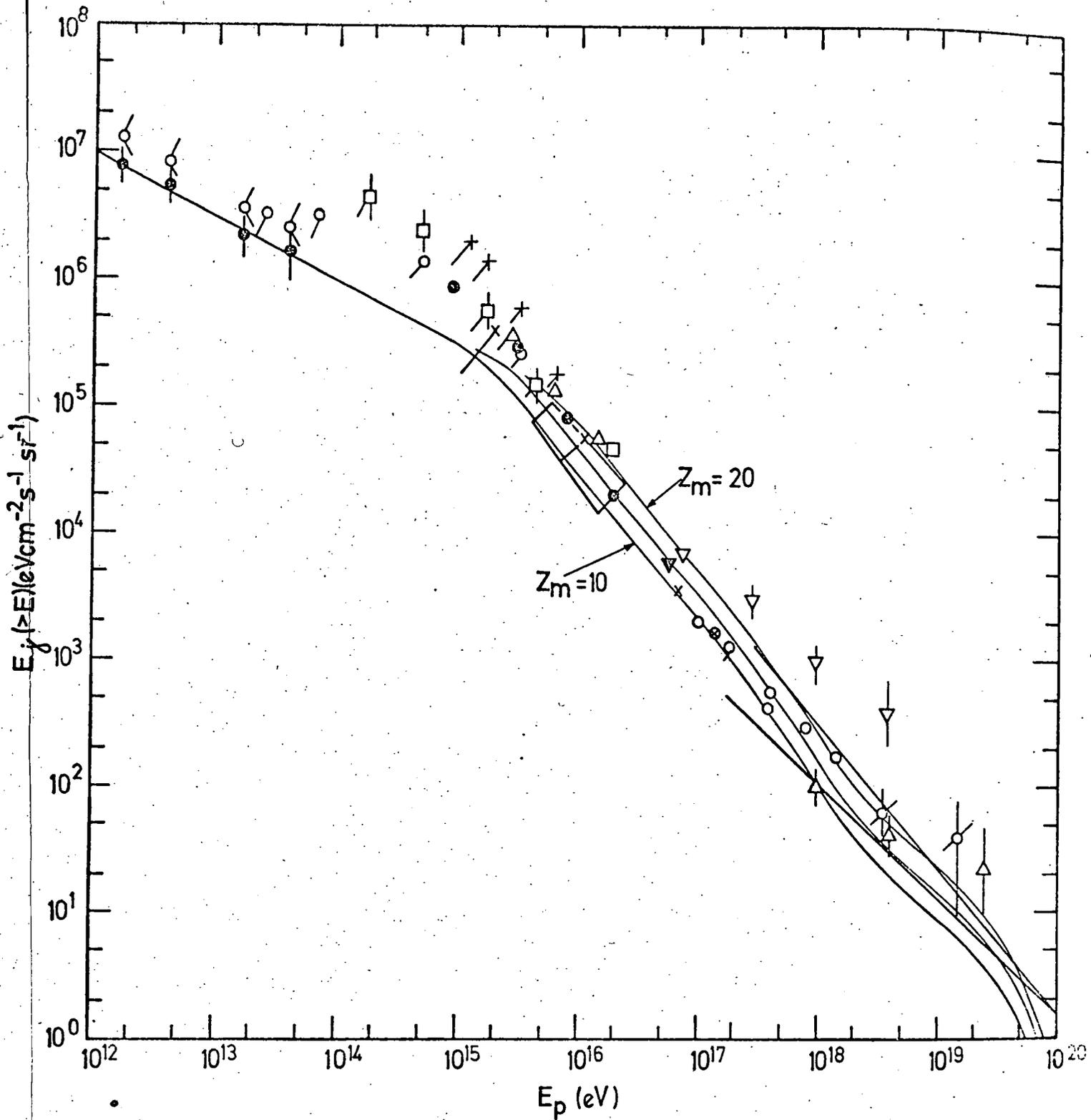
Fig 2-5

Comparison of experimental data with models with $H_o = 50$ km s^{-1}Mpc^{-1}, $\beta = 4.4$ and $z_m = 10$, 14.3 and 20.
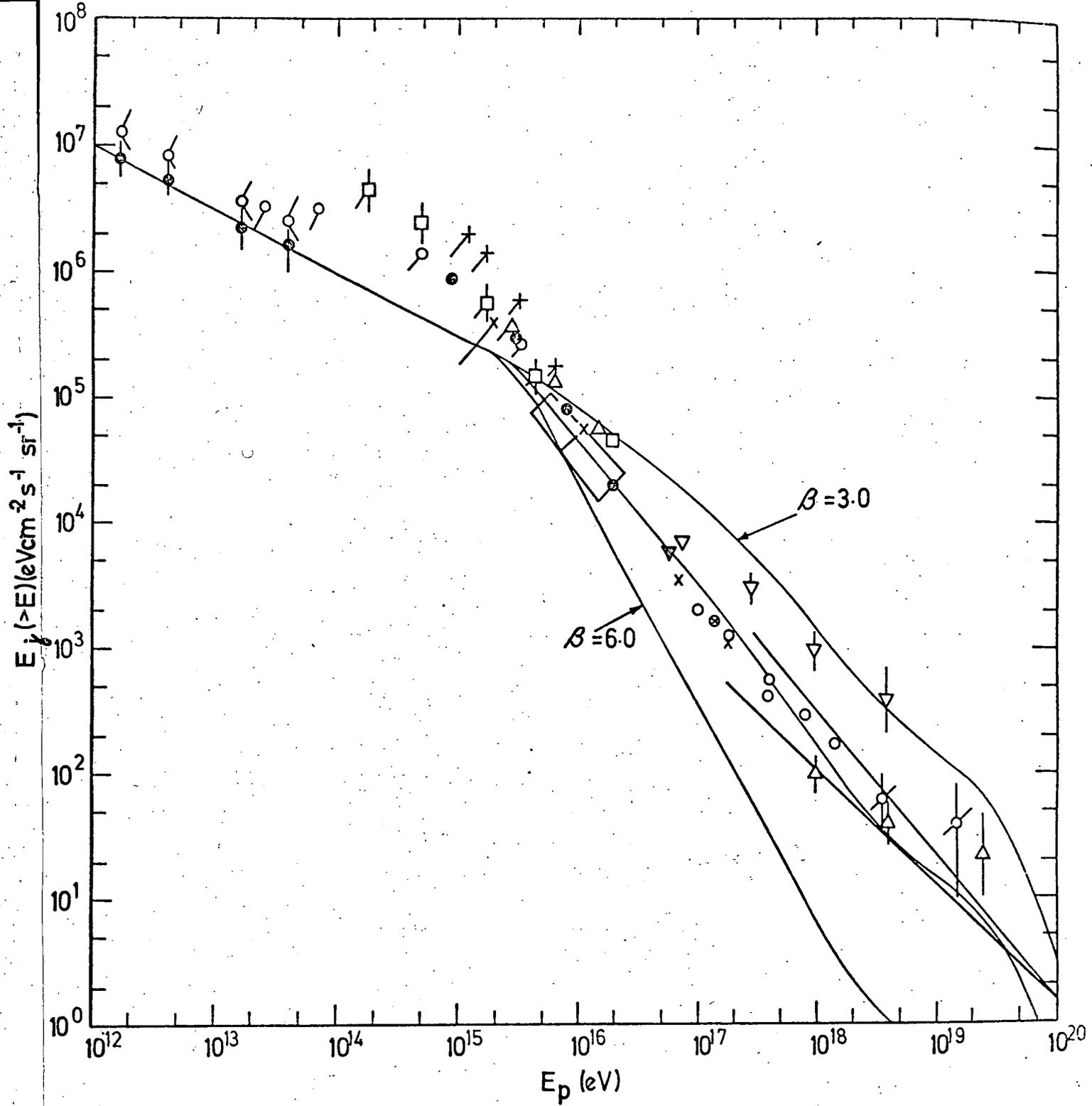
Fig 2-6

Comparison of experimental data with models with H_o = 50 km s^{-1} Mpc^{-1}, z_m = 14.3 and β = 3.0, 4.4 and 6.0.
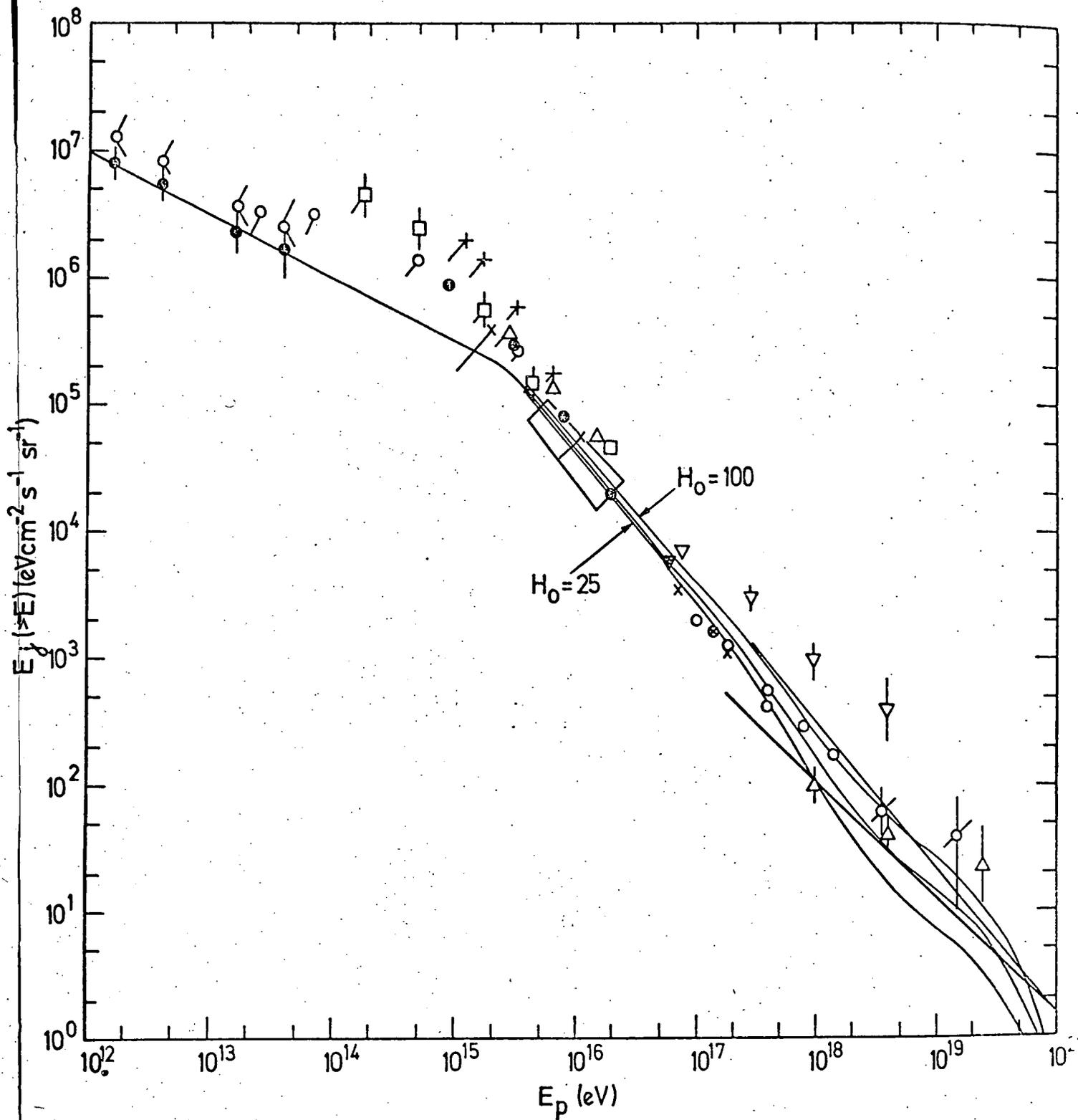
Fig 2-7

Comparison of experimental data with models with $\beta = 4.4$, $z_m = 14.3$, and $H_o = 25$, 50 and 100 km s^{-1} Mpc^{-1}.

the Hubble constant are roughly H_o = 25 - 100 km s^{-1}Mpc^{-1}, and the effect of
using these values in the standard model is shown in Fig 2-7. A decrease in
H_o clearly makes the fit at high energies worse, while H_o = 100 km s^{-1}Mpc^{-1},
by raising the high energy end of the spectrum by a factor of 2 relative to
the low energy end gives a rather better fit in the 10^{19} - 10^{20} eV range than
the standard model.

2.7. The energy range 10^{19} - 10^{20} eV

The presence of the photomeson cutoff is a problem in any 'universal'
model of cosmic-ray origin, and it is important to assess whether the present
model is consistent with the observations, taking into account the probable
experimental errors at the highest energies.

The differential spectra from the Haverah Park array (Edge et al.
1973) and the Sydney array (Bell et al. 1974) are shown in Fig 2-8. For
comparison, the differential spectrum, evaluated as described in Sec 2-2
is shown for the 'standard model'. The spectrum has been normalized to the
spectrum of nucleons in the 10^{12} - 10^{14} eV range, taking $E^2 j(E)$ = 1.5 10^6
cm^{-2}s^{-1}sr^{-1}eV at 10^{14} eV.

The standard model is consistent with the data in the range up to about
6.10^{19} eV. At higher energies, the predicted spectrum falls below the Haverah
Park data, but is still consistent with the Sydney points. In view of the
large errors, both statistical and systematic, which are still associated with
the highest energies, the photomeson cutoff does not at present give a conclusive
test of the theory. This is especially true of a steeply falling spectrum,
where errors in estimating the energy of events must lead to a flattening of
the experimental spectrum.
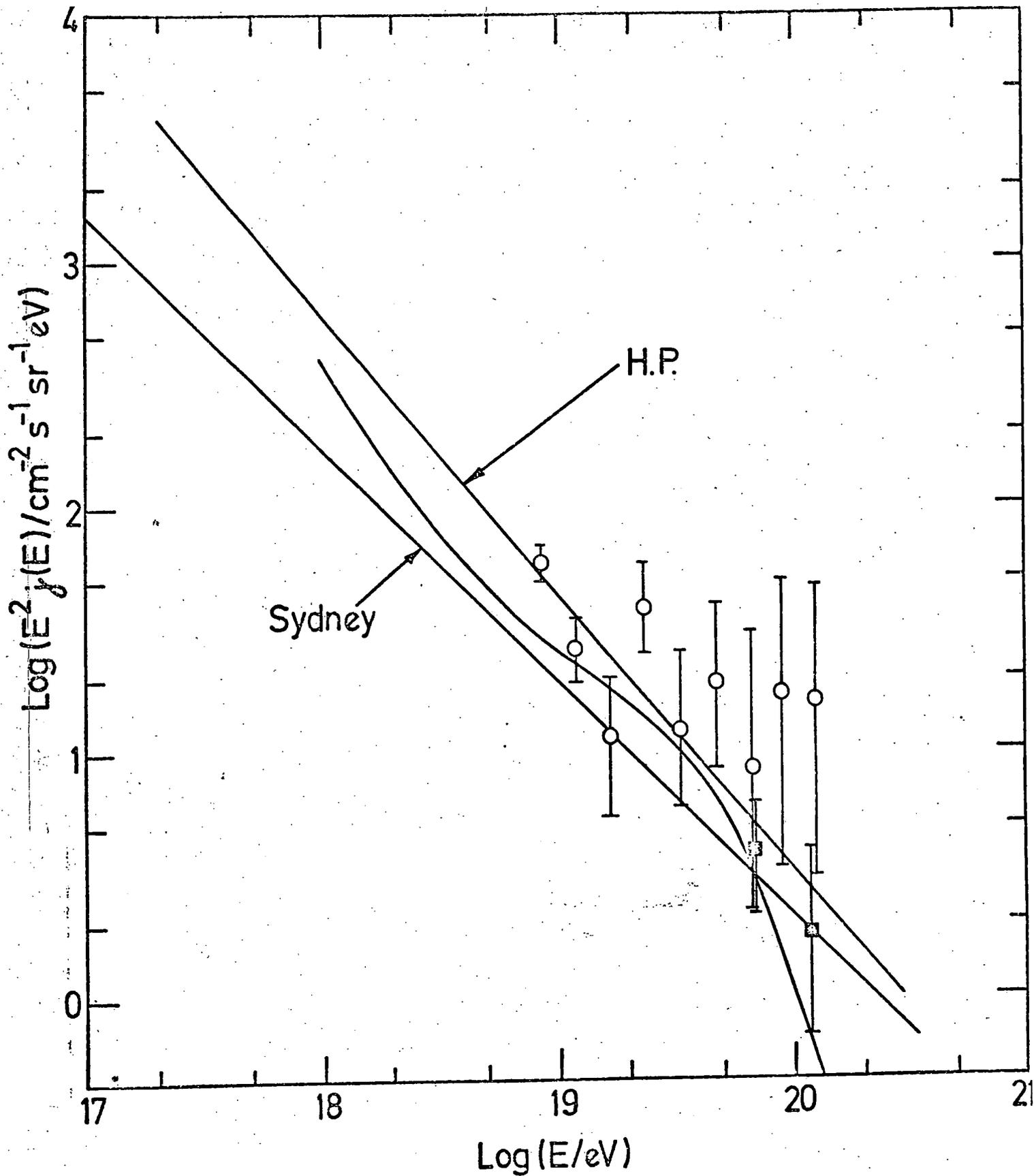
Fig 2-8

Differential primary spectrum in the range $10^{18} - 10^{20}$ eV for the 'standard model' compared with the data from the Sydney and Haverah Park experiments. Normalization is to nucleon spectrum at 10^{12} eV.

2-8 <u>Estimate of total energy in the γ-ray spectrum from (γ, p) interactions.</u>

The derivation of the γ-ray spectrum which results from the cascade initiated by electrons from (γ, p) interactions is described in Chapters 7 & 8. The normalization of this spectrum requires a knowledge of its total energy content, and this is best obtained by use of the primary spectrum studied in the preceding Sections. We note that since the redshift energy losses are independent of the form (protons, electrons or gamma-rays) in which the energy is carried, the difference in energy content between the 'unmodified' proton spectrum, which would be produced in the model in the absence of interactions with the blackbody background, and that which is actually produced when the interactions are included, is equal to the energy finally appearing in the gamma-ray spectrum.

This energy difference can be derived from the 'standard model' fit to the data, shown in Fig 2-5. For energies near E_k, this spectrum is adequately represented by the two power-law approximation described in Sec.2.8 . The energy content, expressed as a flux W, is given by

$$W = \int_{E_\ell}^{E_m} (Ej_0(E) - Ej(E)) \, dE \qquad (2.25)$$

where $j_0(E)$ is the unmodified spectrum with index γ and E_m is the highest energy contributing to electron pair-production. Since the spectrum of protons is steeply falling, it is sufficient here to assume $E_m \to \infty$. $j(E)$ has index γ for $E < E_k$ and $\gamma + \Delta\gamma$ for $E > E_k$. Then equation (2.25) leads to

$$W = E_k \, j(> E_k) \left[\frac{\gamma - 1}{\gamma - 2} - \frac{\gamma + \Delta\gamma - 1}{\gamma + \Delta\gamma - 2} \right] \qquad (2.26)$$

From the standard model spectrum of Fig. 2-5, $\gamma = 2.5$, and $\gamma + \Delta\gamma = 3.14$, giving $W = 1.1 \, E_k \, j(> E_k)$. Taking the model value at $E_k = 3.10^{15}$ eV, gives $W = 1.9 \, 10^5$ eV cm^{-2} s^{-1} sr^{-1}. The error on this value is determined by the uncertainty in the primary spectrum, which would allow a factor of about 2 in either direction in the normalization of the standard model. Hence we can take $W = (1 - 4).10^5$ eV cm^{-2} s^{-1} sr^{-1}.

2-9 Diffuse γ-ray flux from interactions with intergalactic gas.

If the Hillas model is taken to apply to all primary cosmic rays, including those of energies around a few GeV, then inelastic interactions with intergalactic gas, producing π^o-decay γ-rays, place severe observational limits on the density of such gas allowed in the model.

The γ-ray flux from this process can be calculated from

$$I(> E_\gamma) = c \iint j(E, z)n (1+z)^{-3} \sigma (> E_\gamma(1+z), E) \, dE \, dt \quad (2.27)$$

where n is the gas density at z, $j(E,z)$ is the proton flux (for proper lengths) at z, and $\sigma(> E_\gamma, E)$ is the cross-section for producing γ-rays above E_γ by protons of energy E. $j(E, z)$ is given by

$$j(E, z) = \int_z^{z_m} G\left[\frac{E(1+z')}{(1+z)}, z'\right] \left(\frac{1+z'}{1+z}\right)(1+z)^3 \frac{dt}{dz'} \, dz' \quad (2.28)$$

where the source function is given by equation (2.19). This integral can be evaluated to give

$$j(E, z) = j(E, 0) (1+z)^{2+\gamma} \quad \times \quad \frac{(1+z_m)^{\beta-\gamma-0.5} - (1+z)^{\beta-\gamma-0.5}}{(1+z_m)^{\beta-\gamma-0.5} - 1}$$

$$= j(E, 0) F(z) \quad (2.29)$$

Equation (2.27) can be written in the form (using $n = n_0(1+z)^3$)

$$I(> E_\gamma) = \frac{n_0 c}{4\pi} H_0^{-1} \int_0^{z_m} F(z) \, q(> E_\gamma (1+z)) \frac{dz}{(1+z)^{2.5}} \quad (2.30)$$

where $q(> E_\gamma)$ is the integral production rate of γ-rays per hydrogen atom of target gas, evaluated for the primary cosmic-ray spectrum. This function has been calculated by Cavallo and Gould (1971), and by Stecker (1970). The shapes of the function obtained by these authors are compared in Fig 2.9 . They differ only in small details , although there is some discrepancy in absolute magnitude. The most recent calculation (Stecker, 1973) gives $q(> 100 \text{ MeV}) = 1.3 \; 10^{-25}$ $\pm 0.2 \text{ s}^{-1}$, and this value is adopted here. (The calculation of q includes the effect of interactions of Helium nuclei both in the cosmic-rays and the gas; normal interstellar composition is assumed for the Helium; this will also hold for the intergalactic medium provided Helium is primordial).

$$\frac{q(>E_\gamma)}{q(>10\,\text{MeV})}$$

E_γ (MeV)

—— Stecker (1970)

- - - Cavallo and Gould (1971)

Fig 2-9
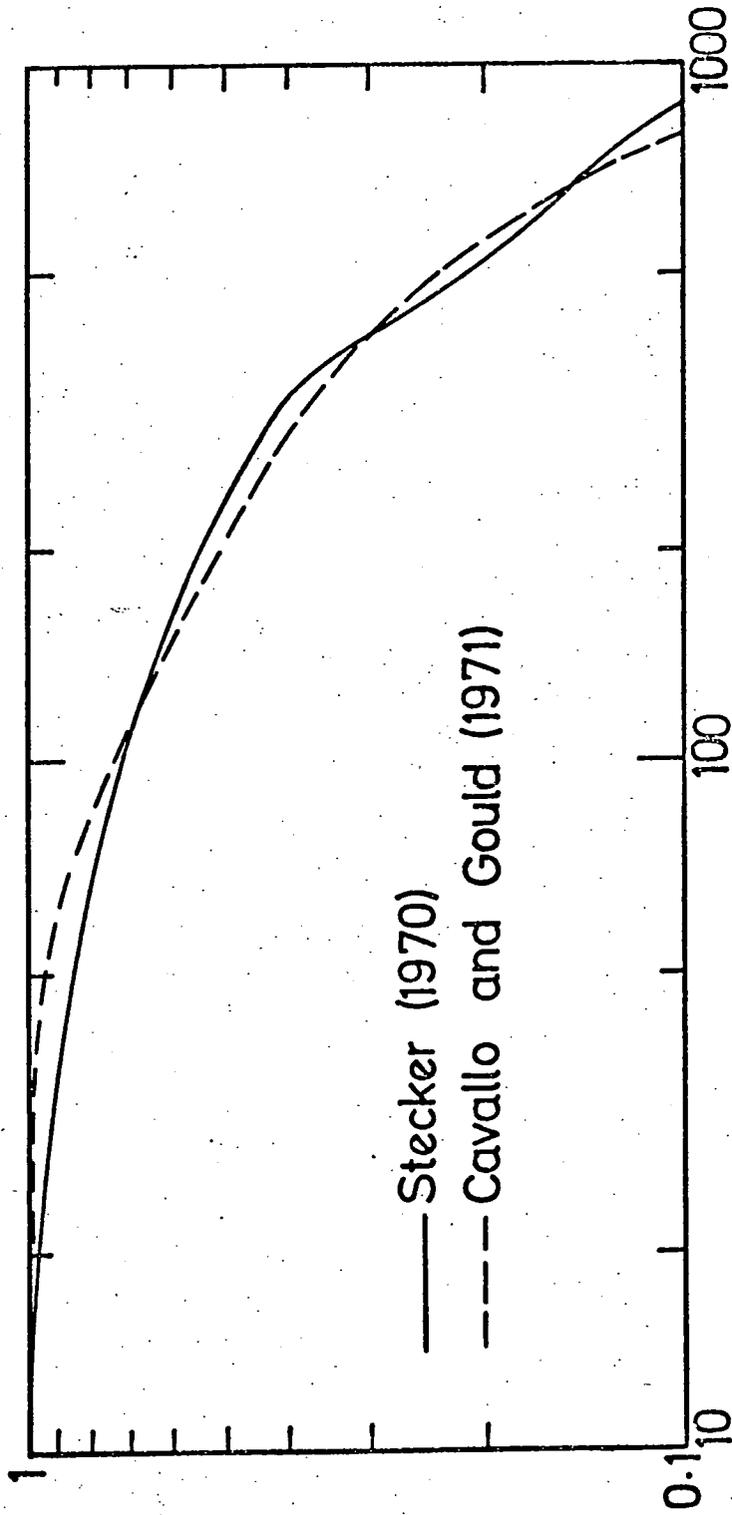
Comparison of integral production spectra of gamma-rays from cosmic-ray - gas interactions according to Stecker (1970, 1974) and Cavallo and Gould (1971). The curves are normalized to unity at 10 MeV.

The function under the integral in equation (2.30) is shown in Fig 2-10, for the parameters of the standard model. The main contribution comes from $z \sim 5$. Integrating under the curve and substituting in equation 2-30 gives

$$I_\gamma(> 100 \text{ MeV}) = 1.0 \ 10^4 \ n_o \ \text{cm}^{-2} \ \text{s}^{-1} \ \text{sr}^{-1} \qquad (2.31)$$

The experimental value given by the most recent analysis of the SAS - 2 data (see Chapter 9) is $I(> 100 \text{ MeV}) = 2 \ 10^{-5} \ \text{cm}^{-2} \ \text{s}^{-1} \ \text{sr}^{-1}$ (Fichtel et al. 1974). Hence the experimental value is violated if

$$n_o > 2 \ 10^{-5}/ \ 1.0 \ 10^4 = 2. \ 10^{-9} \ \text{cm}^{-3}$$

The significance of this limit has been discussed in Chapter 1.
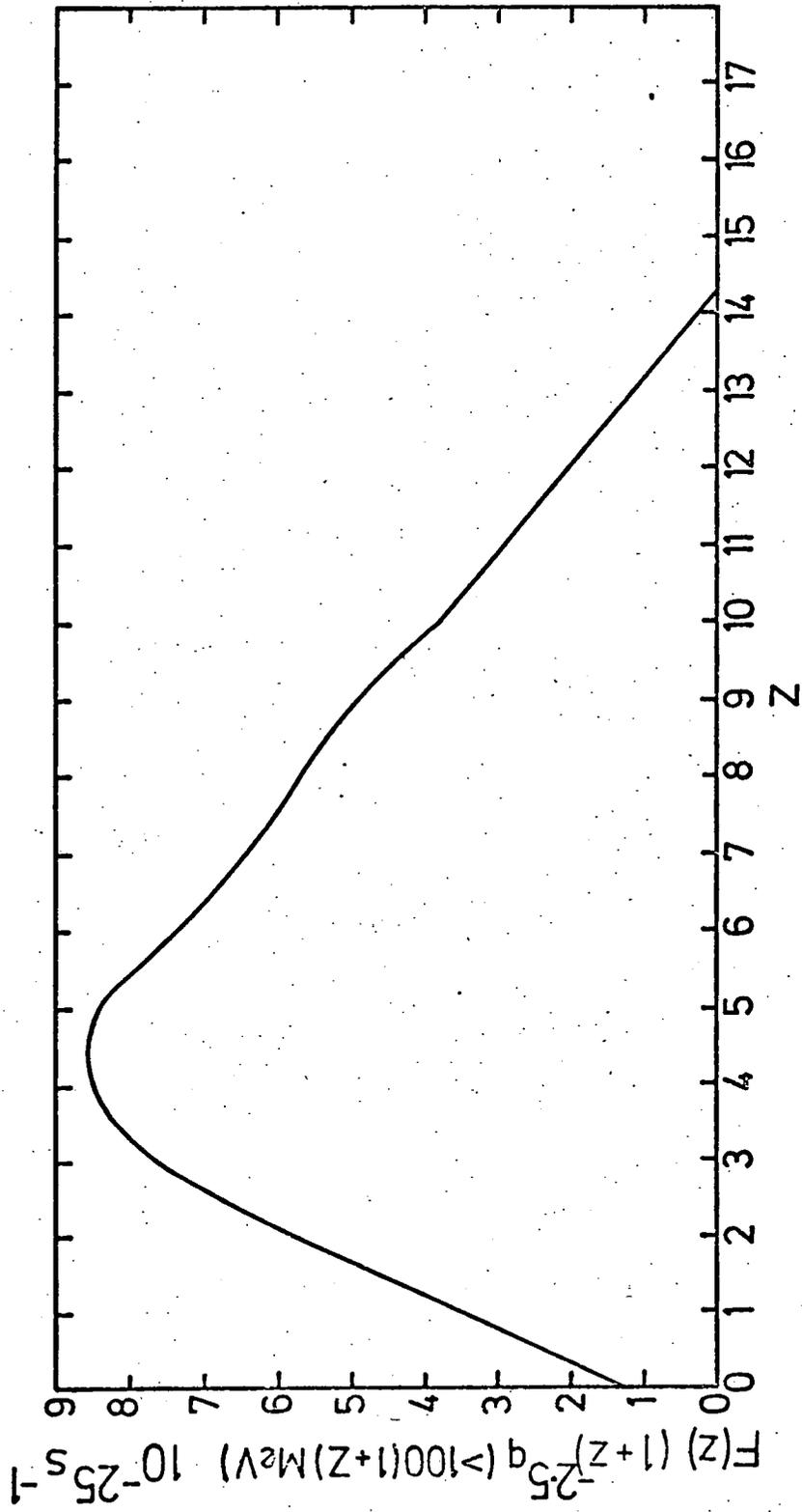
Fig 2-10

The form of the emission function of equation (2.30), showing the contribution from different redshifts to the presently observed gamma-ray spectrum from pion-decay.

Appendix : Summary of experimental data on the primary CR spectrum

above 10^{10} eV.

A large number of different techniques have been used to study

the primary CR spectrum, the principal ones involving direct detection

by balloon and satellite-borne experiments (mainly for energies below

10^{12} eV) and by study of extensive air-showers (EAS) which is applicable

to primary energies ablve 10^{14} eV. The satellite experiment of Grigorov

et al. (1971) is unique in extending the direct observational technique

to energies above 10^{12} eV.   The energy ranges 10^{10} - 10^{14} eV, 10^{14} -

10^{17} eV and $> 10^{17}$ eV will be considered separately.

10^{10} - 10^{14} eV

The data on the proton and He spectra from balloon and satellite

ionization-calorimeter experiments agree well up to 10^{12} eV. Fig A1

shows the spectra as determined by Ryan et al. (1972) and Webber (1973

and refs. therein) using balloons, and Grigorov (1971) using the PROTON

series of satellites. Ryan et al (1972) found a differential spectral

index γ = 2.75 ± .03 for protons (5 10^{10} - 2 10^{12} eV) and 2.77 ± .05 for

Alpha-particles (5 10^{10} - 5 10^{11} ev/nucleus). Grigorov et al. (1971)

claimed to find a steepening in the proton spectrum at 10^{12} eV, from

γ = 2.7 to   3.2, while the all-particle spectrum shows no such steep-

ening but rather a 35% drop in overall intensity at 10^{12} eV. These

results would imply a predoninance of heaviy nuclei at higher energies,

whcih however is in disagreement with studies of the ground level

μ^+ to μ^- ratio (Kempa et al. 1974 and refs therein).

The Goddard group has also obtained the iron spectrum in the 3 -

50 MeV range (Ramaty et al 1973), and a very flat spectrum with γ=
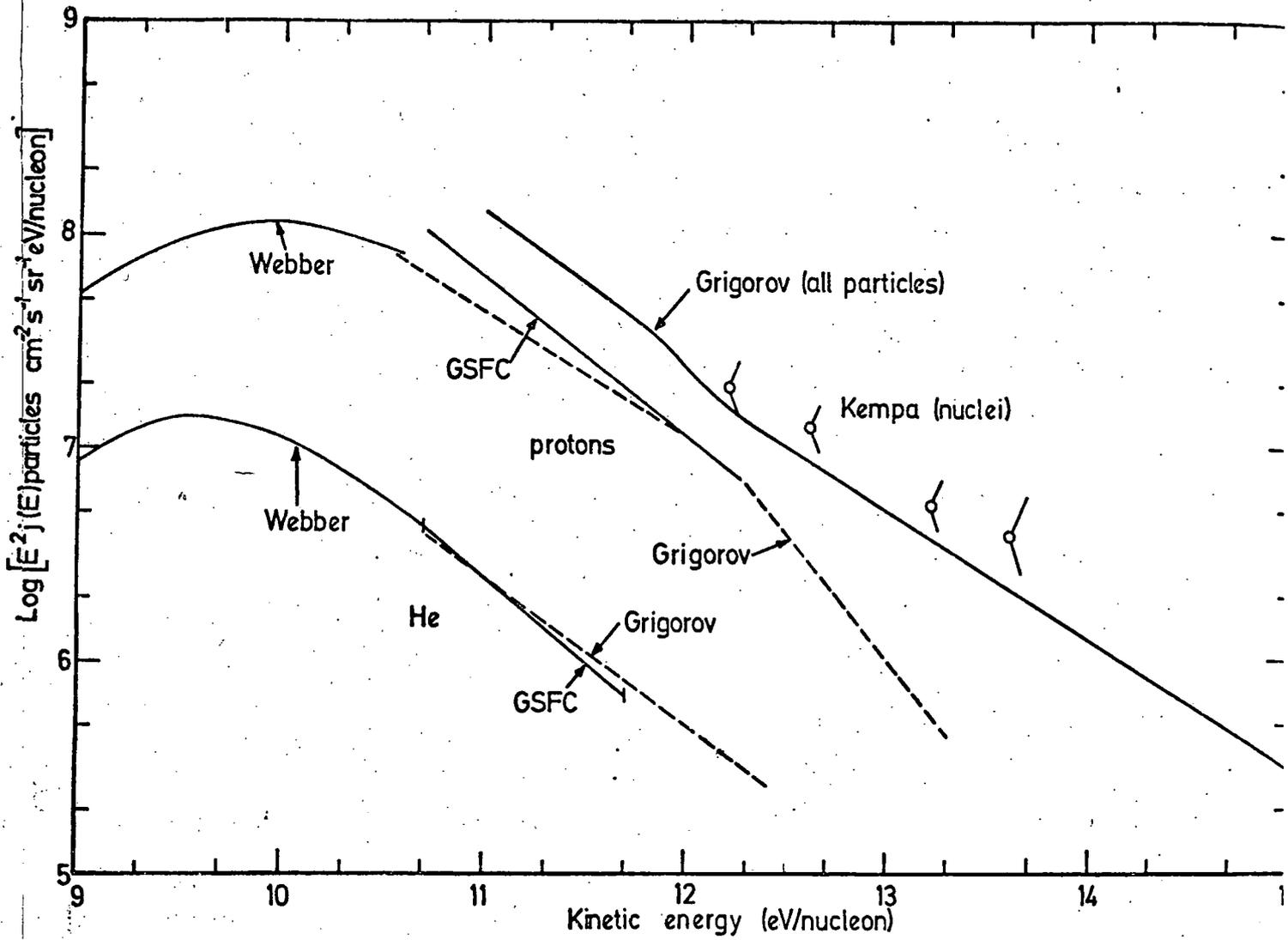
Fig A-1

Summary of data on the primary cosmic-ray spectrum between 10^9 and 10^{14} eV, from Webber (1973), GSFC (Ryan et al. 1972), Grigorov et al. (1971) and Kempa et al. (1974).

2.12 ± .13, compared with γ = 2.64 ± .04 for the C, N, O nuclei, was found.

It is possible to use information on the sea-level muon spectrum to derive the primary nucleon spectrum. Ramana-Murthy and Subramanian (1972) find that the data is consistent with the Feynman scaling hypothesis provided γ=2.67, which is close to the value found by direct methods. Using this exponent, the absolute flux of CR can be derived, and the results are roughly in agreement with the Grigorov et al. (1971) all-particle spectrum assuming composition as at 10^{10} eV. Elbert et al. (1973) use the muon spectrum to derive the nucleon spectrum up to 10^{15} eV, and the agreement with the PROTON results is good.

Another indirect technique is the study of the spectrum of nuclear active particles at various depths in the atmosphere. Kempa et al. (1974) used this method to obtain the nucleon spectrum in the range $6 \ 10^{11}$ - $4 \ 10^{13}$ eV. The spectrum is consistent with that of Grigorov et al. (1971), assuming 'normal composition' (the nucleon spectrum is converted to that for nuclei with normal composition (that at 10^{10} eV) by multiplying by 1.55).

10^{14} - 10^{17} eV.

Above 10^{14} eV, direct methods of observation are not possible owing to the low counting rates, and this region is exclusively studied at present by EAS. The maximimum of shower development for this energy range occurs at mountain altitudes ($\geqslant$ 3000 m), and many experiments have measured the electron component at such altitudes. The data have been summarized by Kempa et al (1974). The highest mountain labor-

atory is on Mt. Chacaltaya (5200 m), and experiments by Bradt et al.

(1965) and LaPointe et al .(1968) have determined the primary spectrum

in the range 10^{15} - 5 10^{16} eV. Other experiments have been located

in the Pamirs (3860 m ; Nikolskii et al. 1962), on Mt. Norikura

(2770 m; Miyake et al. 1962 and Kameda et al. 1960). The data from

these arrays, together with that from Moscow State University

(Kristiansen et al. 1972) have been used by Kempa et al (1974) to

obtain an estimate of the spectrum in the 10^{15}- 2. 10^{17} eV range,

using a uniform conversion from size to energy. The result is shown

in Fig A2. These authors point out that there is an apparent increase

in intensity above that expected from a power-law extrapolation of

the spectrum at lower energies.

The existence of a rather sharp change in slope (the 'knee')

at about 4. 10^{15} eV is most clearly shown in the electron size

spectra of showers. Fig A3, from Hillas (1974) compares the integral

size spectra at various altitudes with predictions based on a model

in which γ changes from 2.5 to 3.3 at 4.10^{15} eV (the primaries

were assumed to have A = 10). The fit to the data is good. Above

1.6 10^{16} eV, the spectrum appears to flatten to γ= 3.0, consistent

with that which prevails at higher energies (see below).

Results from the sea-level muon spectrum (which should give

a more accurate primary spectrum than electrons on account of the

slower attenuation in the atmosphere and hence smaller zenith-angle

dependence) are also reported by Kempa et al. (1974), and the results

for alternative multiplicity laws (no. of pions $\propto E^{\frac{1}{4}}$ and $E^{\frac{1}{2}}$) are

shown in Fig A2.

A summary of available EAS techniques for obtaining information
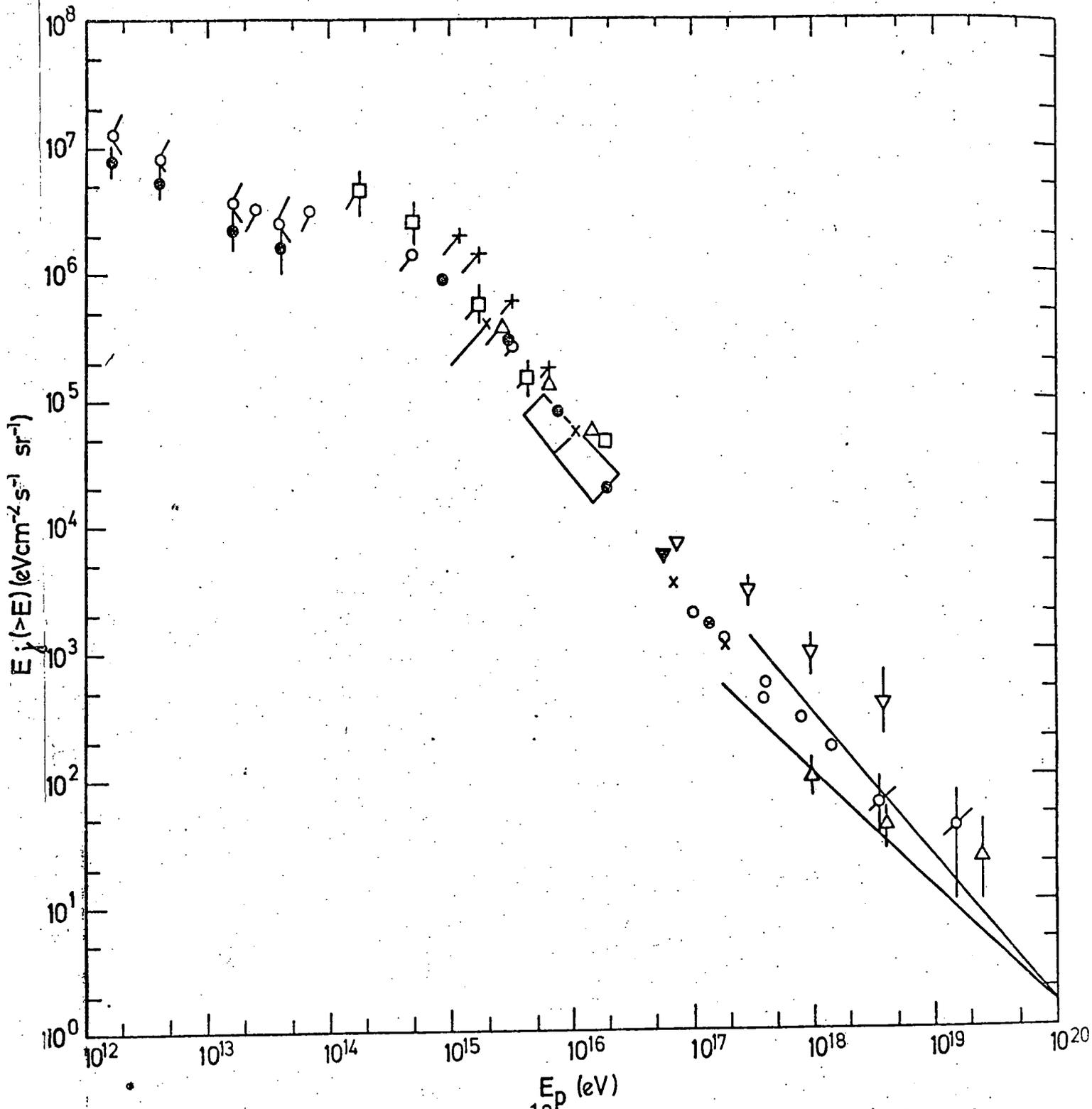
Fig A-2 The primary spectrum above 10^{12} eV, from Kempa et al. (1974). Particles are assumed to be protons.

Nikolskii (1962) ; Chudakov (see Nikolskii 1962); Bradt et al.(1965)
LaPointe et al. (1968); Kameda et al. (1960); Miyake et al.(1962)
Kristiansen et al. (1972); Lodz data, Olejniczak (1973);
Kempa (1973), nucleons; Kempa (1973), nuclei, composition as at 10^{10} eV
Aguirre et al. (1973); Krasilnikov (1973); Clark et al. (1963);
Linsley (1973); S - Sydney array, Bell et al. (1974); H- Haverah
Park array, Edge et al. (1973)
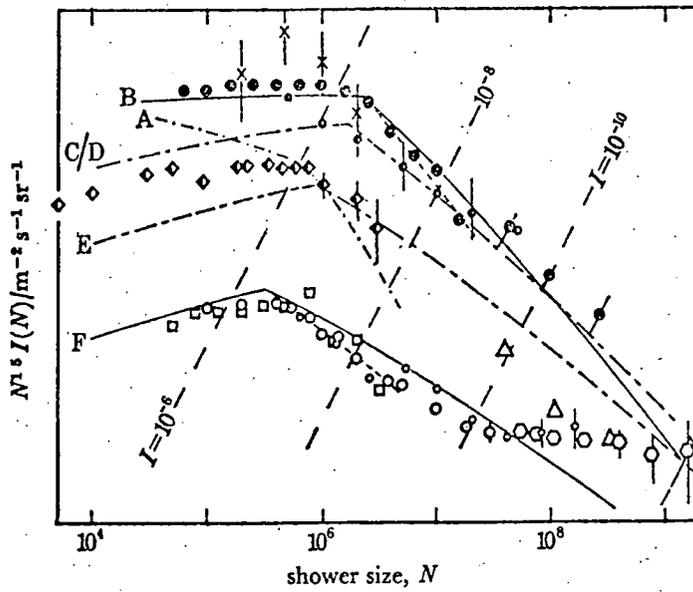
Fig A-3 Integral size spectrum of showers at various altitudes. For comparison, the expected size spectra for a power-law primary spectrum with differential exponent changing from -2.5 to -3.3 at $4 \cdot 10^{15}$ eV primary energy are shown. From Hillas (1974)
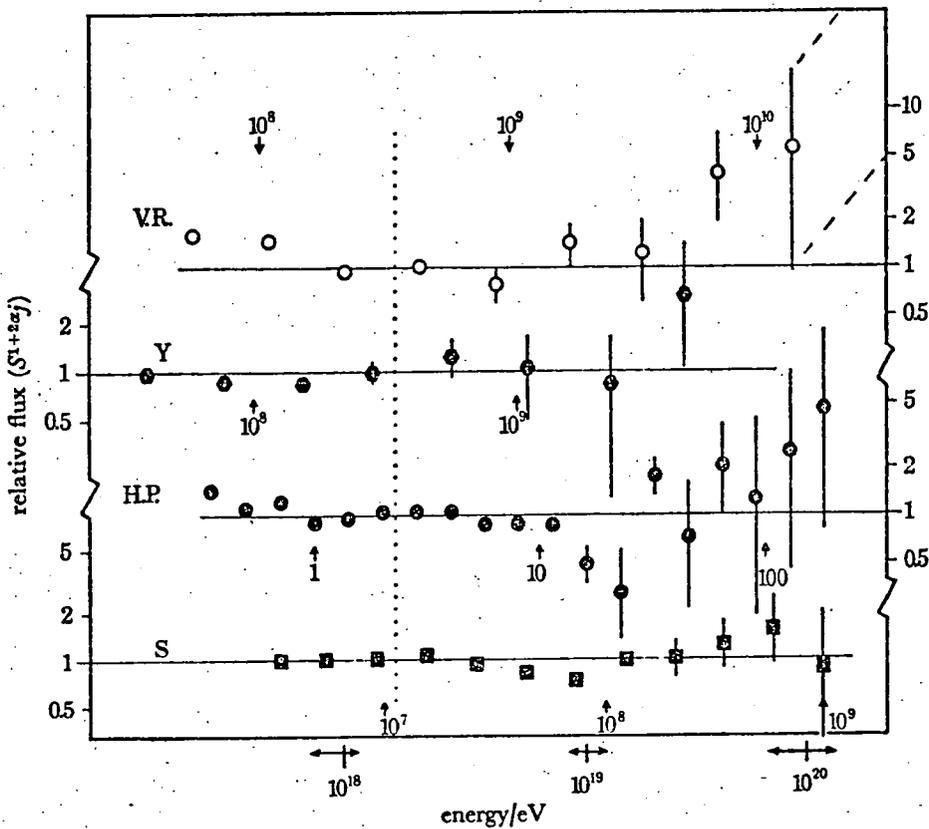
Fig A-4 Differential shower size spectra for energies above $3 \cdot 10^{17}$ eV, plotted to give a horizontal line for a primary spectrum E^{-3}. From Hillas, 1974. The size parameters S and values of α are:

Volcano Ranch (VR)	S=No. of electrons	$\alpha = .96$
Yakutsk (Y)	S=No. of electrons	$\alpha = .90$
Sydney (S)	S= No. of muons	$\alpha = 1.07$
Haverah Park (HP)	S= Cerenkov signal 600 m from axis	$\alpha = 1.04$

about the mass composition in this range has been given by Watson (1975).
The flattening of the CR spectrum relative to that at lower energies,
and the steep proton spectrum suggersted by Grigorov et al. (1971)
would indicate a dominance of heavy nuclei at about 10^{15} eV i.e. just
before the 'knee'. However, most of the data are consistent with a
mass compostion similar to that at 10^{10} eV (although uncertainty in the
nuclear physics at these energies is a major problem).

> 10^{17} eV

The information in this range is mainly from sea-level electron
and muon EAS measurements. The earliest results were from Volcano Ranch
(area 8 km^2; see Linsley 1973 for most recent report); the data are
being re-analysed at present. The measured parameter is here the
number of electrons in the shower at ground-level, and this is also
measured in the Yakutsk array (area 3.3km^2 ; Krasilnikov et al. 1973)
which also uses the Cerenkov light signal.

The muon component is measured at the Sydney (area 45 km^2; Bell
et al. 1974) and Haverah Park (12 km^2 ; Edge et al. 1973) arrays. The
spectral indices in the 10^{17} - 10^{19} eV range quoted in these papers are
γ = 2.96± .02 and γ = 3.17 ± .03 respectively. However, according to
Bell et al. (1974) the use of the same model to analyse the data leads
to almost identical primary spectra. A useful comparison of the four
experiments mentioned above is given by Hillas (1974), from which Fig A4
is taken. In each case, the quantity S used as a measure of the primary
energy is plotted in the form $j(S)S^{2\alpha+1}$ versus S. ($j(S)$ is the
differential flux with respect to S). The values of α for each exper-
iment come from model calculations, but are not very model dependent.
The resulting plots are consistent with $j(S)S^{2\alpha+1}$ = constant, which
is easily shown to follow from a spectrum $j(E) \propto E^{-3}$. However the

statistical errors become very large towards energies of 10^{20} eV, so that firm conclusions about the lack of a photomeson cutoff cannot be made at present (see Ch. 1 Sec 4 and Strong et al. 1974a,b for further discussion of this point).

At the present time there is no firm evidence relating to the mass composition above 10^{17} eV. Measurements on the fluctuations in arrival times of particles at large distance from the shower axis (Watson and Wilson 1974) may indicate mainly proton primaries at 10^{18} eV, but according to Hillas (1974) nuclei fragmenting in stages in the atmosphere might produce the same effect.

Chapter 2   References

Aguirre C et al. 1973, Proc. 13th Int Conf. Cosmic Rays, Denver, 4, 2598

Balasubramanyan V K and Ormes J F., 1973, Ap. J. 186, 109

Bell C J et al. 1974, J. Phys. A. 7, 990

Bradt H et al. 1965, Proc. 9th Int. Conf. Cosmic Rays, London, 715

Cavallo G and Gould R J., 1971, Nuov. Cim. 2B, 77

Chudakov A E et al., 1960, Proc. 6th Int. Conf. Cosmic Rays, Moscow, 2, 50

Comstock G M, Hsieh K C and Simpson J A., 1972, Ap. J. 173, 691

Edge D M et al. 1973, J. Phys. A. 6, 1612

Elbert J W, Keuffel J W, Lowe G H, Morrison J L and Mason G W., 1973, Proc. 13th Int. Conf. Cosmic Rays, Denver, 1, 213

Fichtel C E et al. 1974, GSFC Preprint X-662-74-304

Grigorov N L, Gubin Yu V, Rapoport I D, Savenko I A, Yakovlev B M, Akimov V V and Nesterov V E., 1971, Proc 12th Int. Conf. Cosmic Rays, Hobart, 5, 1746

Hillas A.M., 1968, Can. J. Phys. 46, S623
Hillas A M., 1974, Phil. Trans. Roy. Soc. Lond. 277, 413

Kameda T, Maeda T and Toyoda I, 1960, Proc. 6th Int. Conf. Cosmic Rays, Moscow, 2, 58.

Kempa J, Wdowczyk J and Wolfendale A W., 1974, J. Phys. A 7, 1213

Krasilnikov DD., 1973, Proc. 13th Int. Conf. Cosmic Rays, Denver, 2393

Kristiansen G B et al., 1972, Proc. 3rd European Symposium on EAS, Paris

LaPointe et al. 1968, Can. J. Phys. 45, S68

Linsley J, 1973, Proc. 13th Int. Conf. Cosmic Rays, Denver, 5, 3202

Miyake S et al., 1962, J. Phys. Soc. Japan, 17 A3 240

Nikolskii S I., 1962, Usp. Fiz. Nauk. 78, 365

Ormes J F and Webber W R., 1965, Proc. 9th Int. Conf. Cosmic Rays, London, 1, 349

Ramana Murthy P V and Subramanyan V K., 1972, Phys. Lett. 39B, 646

Ramaty R, Balasubramanyan V K and Ormes J F, 1973, Science 180, 731

Ryan M J et al., 1972, Phys. Rev. Lett 28, 985

Stabell R and Refsdahl S., 1966, Mon. Not. Roy. Astr. Soc. 132, 379

Stecker F W., 1968, Phys. Rev. Lett. 21, 1016

Stecker F W., 1973, NASA SP-339, 211

Watson A A, 1975, NATO Advanced Study Institute on Origin of Cosmic
    Rays, 61

Watson A A and Wilson J G., 1974, J. Phys. A 7, 1199

E j (>E) (eVcm^{-2} s^{-1} sr^{-1})

E_p (eV)

10^{12} 10^{13} 10^{14} 10^{15} 10^{16} 10^{17} 10^{18} 10^{19} 10^{20}

10^0 10^1 10^2 10^3 10^4 10^5 10^6 10^7 10^8
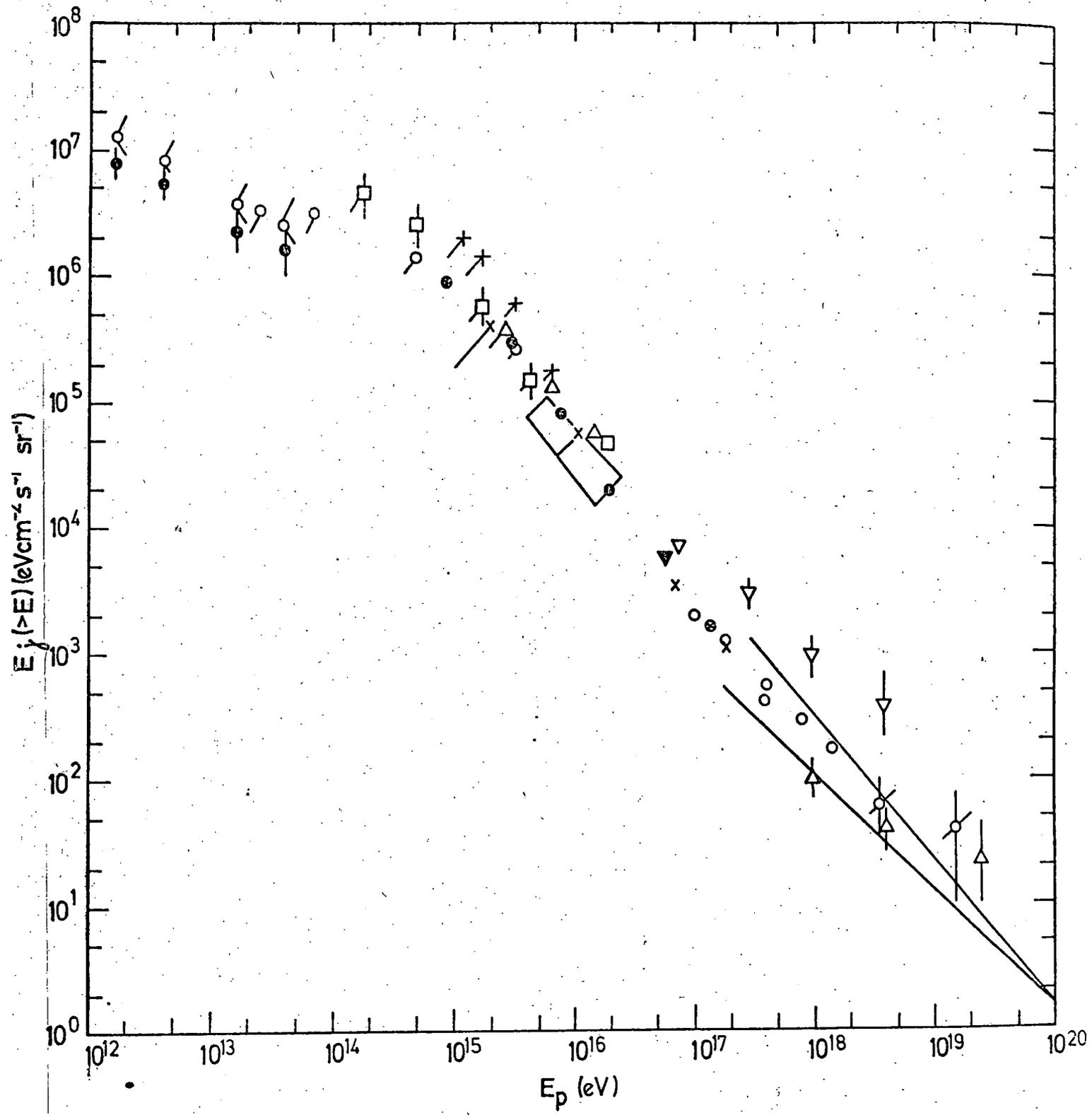
Fig 2-3

Experimental data on the primary cosmic-ray spectrum. The data are discussed in the Appendix to Chapter 2, and the key to experimental points is given in Fig A-2 of the Appendix.
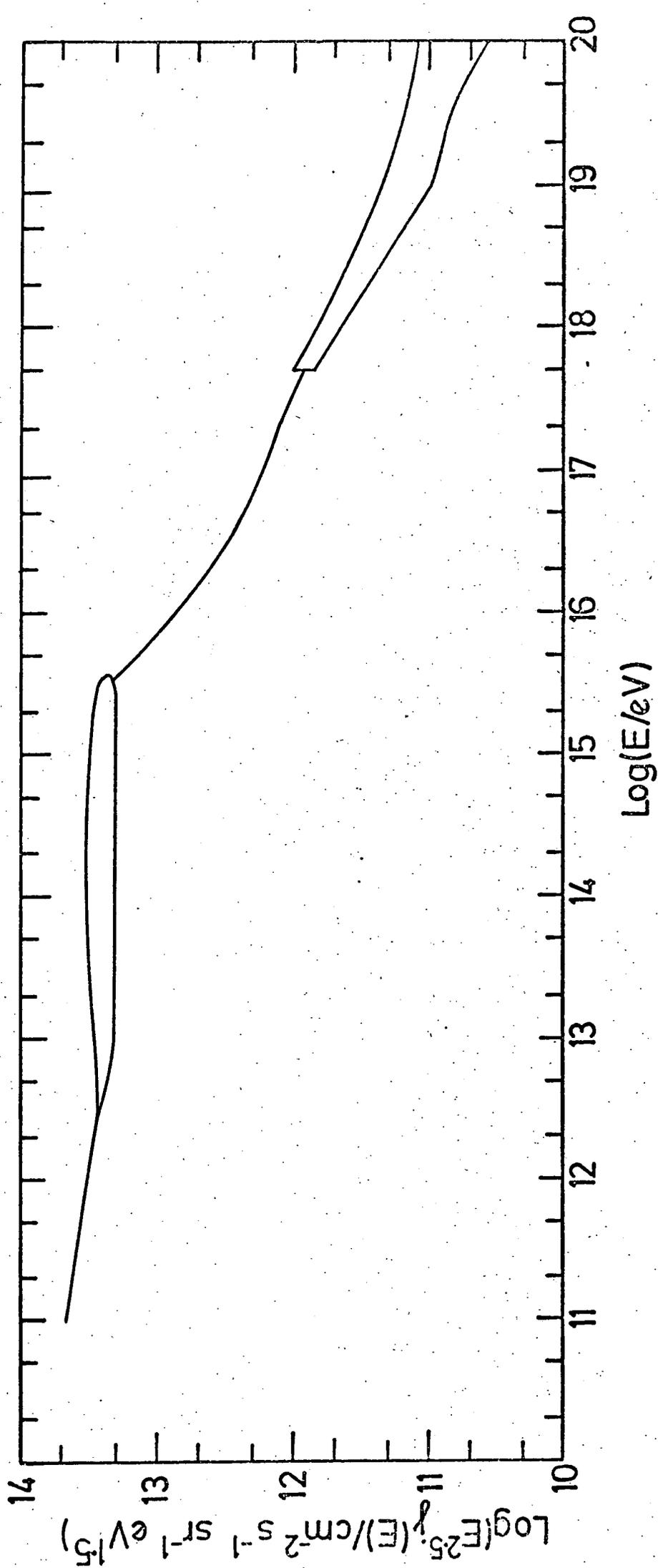
Fig 2-4

Estimate of the 'best' differential spectrum, from Hillas (1974).

up to about 4.10^{19} eV, where the photomeson cutoff sets in. A more detailed discussion of the high energy region is given later, using the differential spectrum. The model cannot account for the 'hump' in the spectrum which may exist in the 10^{14} - 10^{15} eV range. The existence of this feature is, however, a matter of controversy. (see Appendix for details). On the model, the spectral break at 3.10^{15} eV is quite sharp, a feature which also shows up in the electron size spectra of showers (see Appendix).

The effect of varying the model parameters from those of the standard model will now be considered.

(a) Variation of z_m.

This determines the position of the 'kink', as shown by equation (2.23). However, the uncertainty in E_k , and the fact that the threshold energy for pair-production is not sharply defined, allows some variation in this parameter. Fig 2-5 shows how the standard model is affected by changes of z_m to z_m = 10 and to z_m = 20. These extremes encompass roughly the range allowed by the data.

(b) Variation of β

The change in slope of the spectrum at E_k is determined by this parameter, but again some variation is allowed by the data. Fig 2-6 shows the consequence of taking β =3.0 and 6.0 as well as the standard 4.4. Agreement at the high energy end is clearly not possible for values of β less than 4.4 , while the maximum value consistent with the data is about 5.0.

(c) Variation of H_o.

From equation (2.21), the flux below E_k is inversely proportional to H_o in the model, while above 10^{19} eV, it is independent of H_o, since only contributions from small redshifts are significant. Hence an increase in H_o results in an overall flattening of the spectrum, although it does not produce any change in slope near E_k . The extreme experimental limits for

Chapter 3.   Pair - production by Cosmic - ray protons in a Blackbody
radiation field.

3.1 Introduction

The significance of the reaction $\gamma + p \rightarrow p + e^+ + e^-$ (referred to hereafter as PC), was first discussed by Feenberg and Primakoff (1948) who were concerned only with interactions with photons in the optical range. With the discovery of the microwave background radiation in 1965, Greisen (1966) pointed out that PC would result in some attenuation of extragalactic protons with energies above 10^{18} eV.

The threshold proton energy for this interaction is given roughly by the requirement that the photon energy in the proton frame must be at least two electron masses. Hence, for a head-on collision

$$2 \gamma \varepsilon > 2m_e$$

where ε is the laboratory photon energy. For a 2.7K radiation field, $\varepsilon = 2.7kT \sim 6.10^{-4}$ eV (see Sec 4.6) so that the threshold proton energy $E_{p,th}$ is given by

$$E_{p,th} = \left[5 \; 10^5 eV / 6 \; 10^{-4} eV \right] M_p = 10^{18} \; eV$$

For higher temperature radiation fields with $T = 2.7(1+z)$, the threshold is reduced to $10^{18}/(1+z)$.

The energy losses of protons by PC were treated in detail by Blumenthal (1970), using accurate expressions for the differential cross-sections. These results provide a useful check on the differential production rates of electrons from PC derived in this Chapter.

A rough estimate of the attenuation length λ_{pc} for PC may be made as follows. The interaction cross-section is roughly $\alpha r_o^2 = 6 \; 10^{-28} \; cm^2$, and each interaction has inelasticity $K \sim 2m_e/M_p \sim 10^{-3}$. The photon density for a 2.7K radiation field is 400 cm^{-3} (see Sec 4.6), so that

$$1/ \; K n_{ph} \sigma \sim 4 \; 10^{27} \; cm$$

Since λ_{pc} is of the same order as the Hubble radius, attenuation by PC is only

important on cosmological time-scales.

3.2 Differential reaction rates for PC.

Consider a collision between a high energy proton and a low energy photon, with the geometry shown in Fig 3-1. E_p and ε are the laboratory frame energies of the proton and photon respectively, and θ is the angle between their momenta in the laboratory frame. E'_+ and E'_- are the positron and electron energies in the proton frame, θ'_+ and θ'_- the angles made with the incident photon direction in the proton frame. Since $E_p \gg \varepsilon$, this direction is parallel, to a very good approximation, to the proton momentum. The proton-frame photon energy ε' is given by

$$\varepsilon' = \gamma \varepsilon (1 + \cos \theta) \qquad (3.1)$$

where $\gamma = E_p/M_p$.

The laboratory-frame energies of the electron and positron are given by

$$E_- = \gamma (E'_- - \beta \, p'_- \cos \theta_-)$$
$$E_+ = \gamma (E'_+ - \beta \, p'_+ \cos \theta_+) \qquad (3.2)$$

where p'_+ and p'_- are the proton-frame momenta of the positron and electron, and $\beta = (1 - 1/\gamma^2)^{\frac{1}{2}}$. (As usual in this type of problem, the recoil energy of the proton is neglected, since it is only about 10^{-3} ($=m_e/M_p$) of the electron-positron recoil energies).

For constant E'_+ , E'_-

$$dE'_\pm = - \gamma \beta \, p'_\pm \cos \theta'_\pm \qquad (3.3)$$

so that if we know the differential cross-section

$$\frac{d^2\sigma}{dE'_\pm \, d(\cos \theta'_\pm)} = f(E'_\pm , \theta'_\pm , \varepsilon')$$

we have

$$\frac{d^2\sigma}{dE'_\pm \, dE_\pm} = \frac{f(E'_\pm , \theta'_\pm, \varepsilon')}{\gamma \beta \, p'_\pm} \qquad (3.4)$$
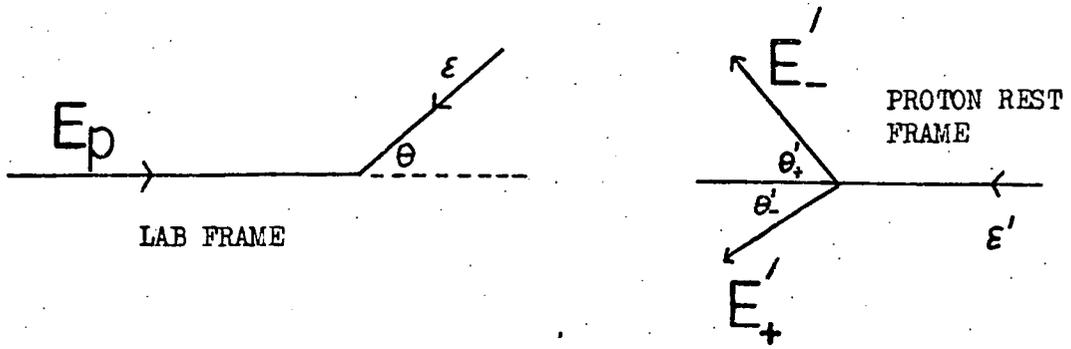
Fig 3-1.   Geometry of pair-creation in a proton-photon interaction,
illustrating notation used.
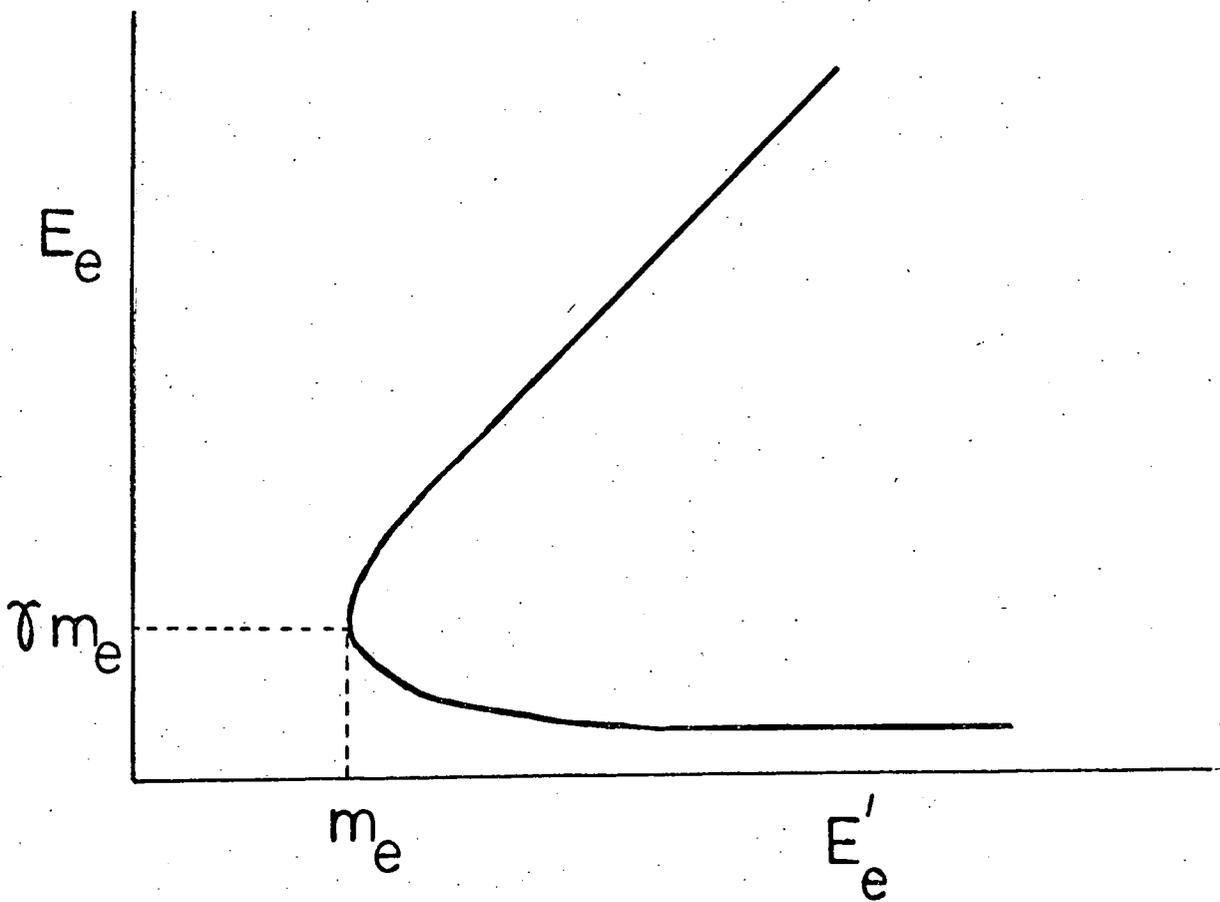
Fig 3-2. Maximum and minimum laboratory electron energies in PC
as a function of electron energy in proton frame (schematic).

For calculation of electron spectra from PC we require the function $g_{PC}(E_e , E_p)$ defined by

$$g_{PC}(E_e , E_p) = \frac{d}{dE_e} \langle \sigma n \rangle_{PC} (E_e , E_p) = 2 \int_{\varepsilon_l'}^{\infty} n(\varepsilon')d\varepsilon' \frac{f(E_e' ,\theta',\varepsilon')}{\gamma\beta p_e'} dE_e' \quad (3.5)$$

where E_+' and E_-' are replaced by E_e' since the process is symmetrical with respect to electrons and positrons to a good approximation (Blumenthal, 1970).

The limits of integration on E_e' can be obtained from (3.2). For the extreme values of E_e at $\cos\theta = \pm1$

$$E_e = \gamma(E_e' \pm p_e') \quad \text{(since } \beta = 1 \text{ effectively)} \quad (3.6)$$

The form of this function is shown in Fig 3-2. It is clear that $E_{e,max}'$ is limited only by the maximum available energy from the PC process, i.e.

$$E_{e,max}' = \varepsilon' - m_e \quad (3.7)$$

To obtain $E_{e,min}'$, equation (3.6) can be solved for E_e' to give

$$E_{e,min}' = \frac{m_e}{2} \left[\frac{1}{\gamma} \frac{E_e}{m_e} + \gamma \frac{m_e}{E_e} \right] \quad (3.8)$$

Another restriction is that $E_e' > m_e$; however the form of equation (3.8), which is symmetric in $E_e/\gamma m_e$ and its inverse, shows that this is always satisfied by the expression for $E_{e,min}'$.

The lower limit on ε' is that which allows production of an electron at rest together with one of energy $E_{e,min}'$, so

$$\varepsilon_l' = m_e \left[\frac{1}{\gamma} \frac{E_e}{m_e} + \gamma \frac{m_e}{E_e} \right] + m_e \quad (3.9)$$

3.3   The function $f(E_e' ,\theta_l',\varepsilon')$

The cross-section for PC after integrating over θ_+ has been given by Gluckstern and Hull (1953) as :

$$\frac{d^2\sigma}{dE_- \, d(\cos\theta_-)} = \frac{\alpha r_o^2 p_- p_+}{2k^3}\left[\; -4\sin^2\theta_-\;\frac{2E_-^2 + 1}{p_-^2 \Delta_-^4} \;+\; \frac{5E_-^2 - 2E_+E_- + 3}{p_-^2\,\Delta_-^2}\right.$$

$$+\;\frac{p_-^2 - k^2}{T^2\Delta_-^2} \;+\; \frac{2E_+}{p_-^2\,\Delta_-}$$

$$+\;\frac{Y}{p_-p_+}\left\{ 2E_-\sin^2\theta_-\;\frac{3k + p_-^2 E_+}{\Delta_-^4} \;+\; \frac{2E_-^2(E_-^2+E_+^2) - 7E_-^2 - 3E_+E_- - E_+^2 + 1}{\Delta_-^2}\right.$$

$$\left. +\; k\,\frac{(E_-^2 - E_-E_+ - 1)}{\Delta_-}\right\} \;-\; \frac{\delta_+^T}{p_+ T}\left\{\frac{2}{\Delta_-^2} \;-\; \frac{3k}{\Delta_-} \;-\; \frac{k(p_-^2 - k^2)}{T^2}\right\} \;-\; \left.\frac{2y_+}{\Delta_-}\right]$$

$$\text{(3.10)}$$

where $|k| = \varepsilon'/m_e$, $\Delta_-' = E_-' - p_-'\cos\theta_-'$, $T = |k - p_-|$,

k = photon momentum in proton frame ,

$$Y = 2/p_-^2 \ln\left[(E_+E_- + p_+p_- + 1)/k\right]$$
$$y_+ = p_+^{-1} \ln\left[(E_+ + p_+)/(E_+ - p_+)\right] \qquad\qquad \text{(3.11)}$$
$$\delta_+^T = \ln\left[(T + p_+)/(T - p_+)\right]$$

The quantities in equation (3.10) are all for the proton frame, the primes having

been dropped. Electron energies are in units of m_e .

We also have $\varepsilon' = E_+' + E_-'$ because the recoil energy of the proton is

neglected. Using equation (3.10), the integral (3.5) can be evaluated, but some

care is required in the integration over E_e' since terms in the denominator in

(3.10) approach zero in certain regions. Note that from eq.(3.2)

$$\Delta_-' = E_e'/\gamma\, m_e \qquad\qquad \text{(3.12)}$$

and that this is to be preferred to the expression involving a difference of two

terms given in eq.(3.11) , when Δ_-' is small. It is preferable to treat Δ_-' as the

primary variable, and use

$$\cos\theta_-' = (E_-' - \Delta_-')/p_-' \qquad\qquad \text{(3.13)}$$

Other terms involving differences can be expressed in terms of Δ_-' :-

$$p_+' = \sqrt{(\varepsilon' - E_-')^2 - m_e^2} \;=\; \sqrt{\varepsilon'^2 + p_-'^2 - 2\varepsilon' E_-'}$$

$$T = \sqrt{\varepsilon'^2 + p_-'^2 - 2\varepsilon' p_-' \cos \theta_-'}$$

$$T^2 - p_+'^2 = 2\varepsilon'(E_-' - p_-' \cos \theta_-') = 2\varepsilon' \Delta_-'$$

Hence

$$T^2 - p_+'^2 = 2\varepsilon' \Delta_-' / (T + p_+')$$

$$\zeta_+^T = \ln \frac{(T + p_+')^2}{2\varepsilon' \Delta_-'} \tag{3.14}$$

For large E_+' the denominator in the logarithmic term in y_+ becomes small,

and a better approximation is obtained using

$$E_+' - p_+' = (E_+'^2 - p_+'^2) / (E_+' + p_+') = m_e^2 / 2E_+' \qquad \text{for } E_+' \gg m_e$$

$$y_+ = (1/p_+') \ln (2E_+'^2 / m_e)^2 = (2/p_+') \ln 2E_+' \qquad \text{for } E_+' \gg m_e \tag{3.15}$$

3.4 Transformation of Planck spectrum to a moving frame.

We require the distribution $n(\varepsilon')$ seen by a highly relativistic

particle moving with respect to the blackbody radiation which is isotropic

for fundamental observers (i.e. observers at rest relative to the expanding

substratum). In such a highly relativistic frame the photon field becomes

a collimated beam along the direction of motion of the frame. The spectrum

$n(\varepsilon')$ is given by

$$n(\varepsilon') = \int_{\varepsilon_\ell}^{\varepsilon_u} n(\varepsilon) \, P(\varepsilon|\varepsilon') \, (1 + \cos \theta)$$

since the photon flux seen by the moving observer is proportional to the

relative velocity $c(1 + \cos \theta)$ between the observer and the photon in the

laboratory (i.e. fundamental observer) frame.

Using eq(3.1), we have for constant ε

$$d\varepsilon' = \gamma\varepsilon \, d(\cos \theta)$$

$$P(\varepsilon'|\varepsilon) \, d\varepsilon' = P(\cos \theta) \, d(\cos \theta)$$

$$P(\varepsilon'|\varepsilon) = 1/2\gamma\varepsilon$$

$$n(\varepsilon') = \int \frac{n(\varepsilon)}{2\gamma\varepsilon} \cdot \frac{\varepsilon'}{\gamma\varepsilon} \, d\varepsilon \tag{3.16}$$

From eq.(3.1) we have

$$\mathcal{E}_u = \infty$$

$$\mathcal{E}_\ell = \mathcal{E}'/2\gamma$$

The Planck spectrum has the form

$$n(\mathcal{E}) = (1/\pi^2\hbar^3 c^3) \, \mathcal{E}^2/(e^{\mathcal{E}/kT} - 1)$$

giving

$$n(\mathcal{E}') = \frac{\mathcal{E}'}{\pi^2\hbar^3 c^3} \cdot \frac{kT}{2\gamma^2} \int_{\mathcal{E}'/2\gamma kT}^{\infty} \frac{dx}{e^x - 1}$$

$$= \frac{1}{\pi^2\hbar^3 c^3} \, \frac{\mathcal{E}' kT}{2\gamma^2} \ln(1 - e^{-\mathcal{E}'/2\gamma kT})^{-1} \qquad (3.17)$$

3.5 Results of calculations for PC reaction rates.

Using equations (3.10) - (3.15) and (3.17), the double integration (3.5) was performed numerically for values of E_p and E_e over the range of interest for the Hillas model. Both inner and outer integrations were evaluated using Romberg routines. The resulting curves for $g_{PC}(E_e, E_p)$ are shown in Fig 3-3 for $E_p = 10^{18}$, 10^{19} and 10^{20} eV. The quantity $E_e^2 \, g_{PC}(E_e, E_p)$, which gives the energy in a logarithmic interval of E_e, is plotted in Fig 3-4.

For use in the calculations on the gamma-ray spectrum, a table of values of g_{PC} was constructed for $E_p = 6 \cdot 10^{17} - 10^{21}$ eV and $E_e = 10^{14} - 10^{18}$ eV. A routine for interpolating in the table allowed the value of g_{PC} to be evaluated rapidly for any E_p and E_e. The calculations were done for $T_o = 2.7K$, but the values for other T can be obtained as described below from the T_o values.

3.6 Derivation of $g_{PC}(E_e, E_p)$ for any T.

Given the function $g_{PC}(E_e, E_p, T_o)$ it is possible to obtain the function for different T as follows. From equations (3.5) - (3.9), (3.17), we have

$$g_{PC}(E_e, E_p, T) = \frac{kT}{\pi^2\hbar^3 c^3} \int_{\mathcal{E}_\ell(\frac{E_e}{E_p})/2\gamma kT}^{\infty} \frac{\mathcal{E}'}{2\gamma^3} \ln(1 - e^{-\mathcal{E}'/2\gamma kT})^{-1} d\mathcal{E}' \int_{E'_{e,min}(\frac{E_e}{E_p})}^{\mathcal{E}'-m_e} \frac{f(E'_e, E_e/E_p, \mathcal{E}')}{p'_e} dE'_e$$
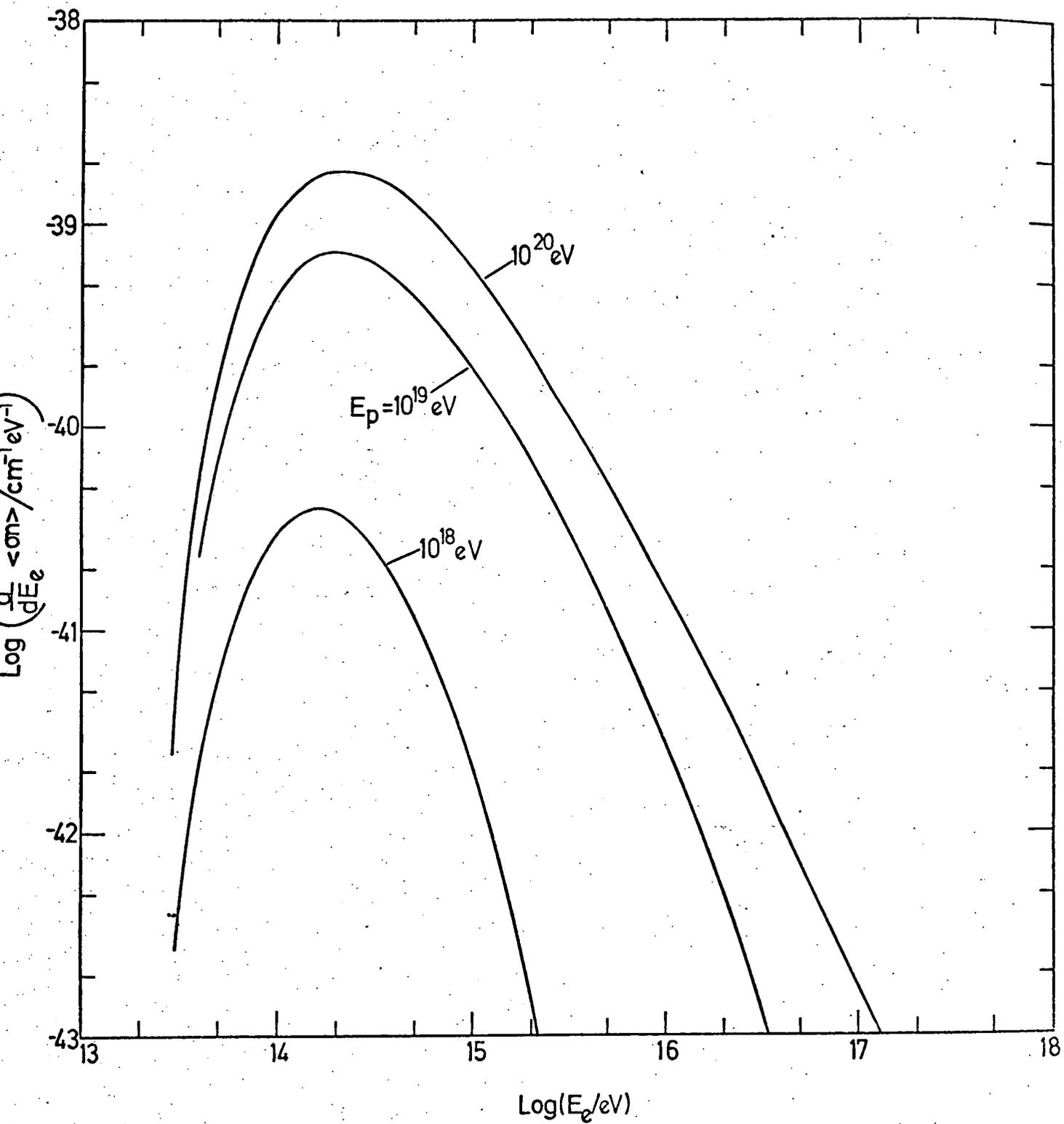
Fig 3-3

Differential reaction rates for the PC process for various proton energies, in a Blackbody radiation field with T = 2.7K.
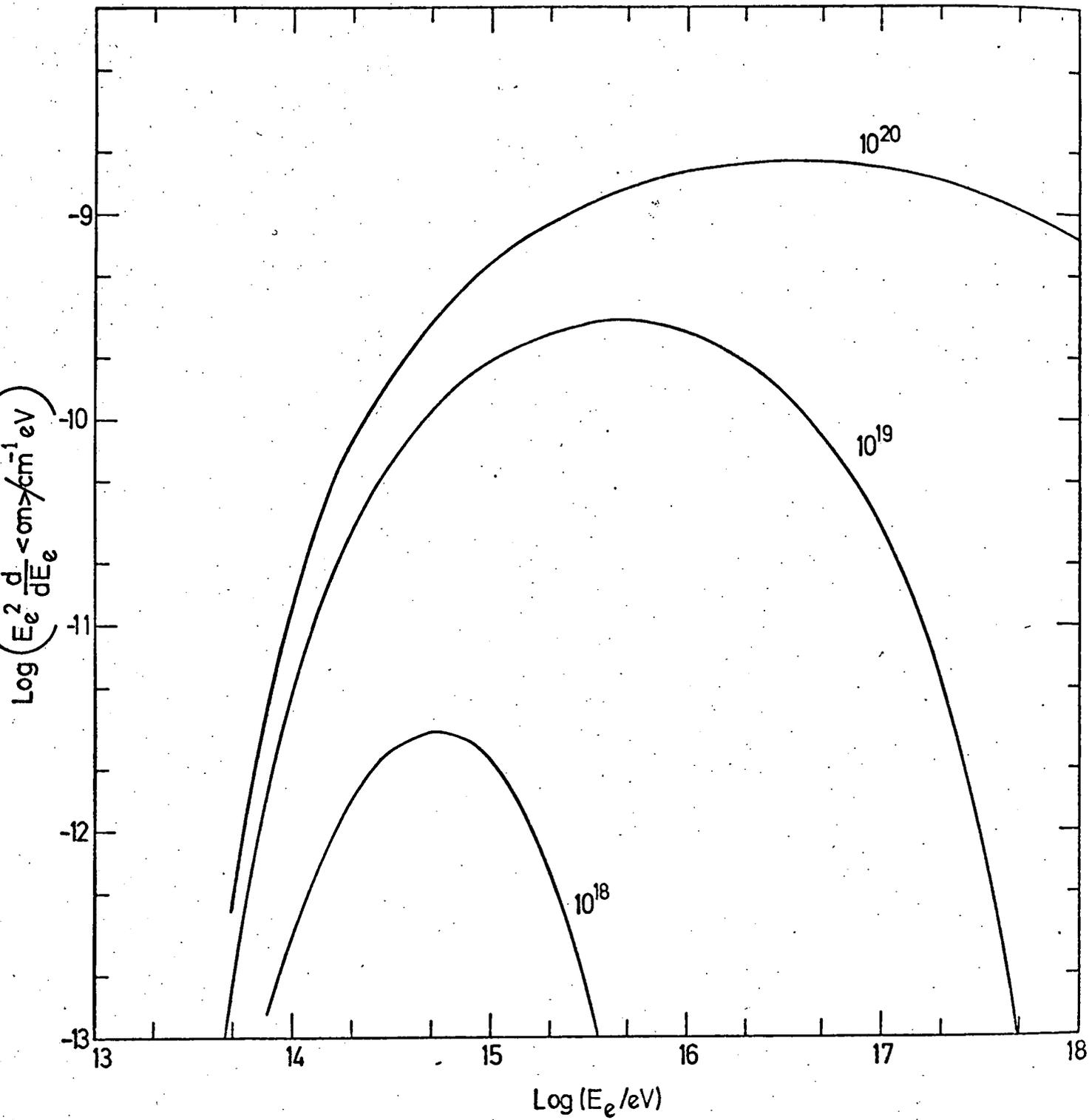
Fig 3-4

The reaction rates for PC from Fig 3-3 multiplied by E_e^2 to show the distribution of energy in electrons, as described in the text.

since $\theta' = \theta'(E_e' , E_e/E_p)$ from eq.(3.2).

Writing $x = \varepsilon'/2\gamma kT$ gives

$$g_{PC}(E_e , E_p , T) = kT \frac{(2\gamma kT)^2}{2\gamma^3} \int_{\varepsilon_\ell'(E_e/E_p)/2\gamma kT}^{\infty} x \ln(1 - e^{-x})^{-1} f'(E_e/E_p , 2\gamma kTx) \, dx$$

$$\propto T^4 F(E_e/E_p , E_p T) \tag{3.18}$$

Therefore

$$g_{PC}(E_e , E_p , T) = T^4/T_o^4 \, g_{PC}(E_p T/T_o , E_e T/T_o , T_o) \tag{3.19}$$

which can be obtained directly from the tabulated function $g_{PC}(E_e , E_p , T_o)$.

3.7 Attenuation lengths for protons for PC in a Planck radiation field.

The attenuation length $\lambda_{pc} = (1/E_p \, dE_p/dx)^{-1}$ can be calculated from g_{PC} since

$$\frac{dE_p}{dx} = \int_{2m_e}^{E_p - 2m_e} E_e \, g_{PC}(E_e , E_p) \, dE_e \tag{3.20}$$

The form of $_{PC}$ for T = 2.7K is shown in Fig 3-5. A useful check is obtained by comparing these results with those of Blumenthal (1970), and the agreement is found to be good.

The variation of λ_{pc} with T can be obtained from eq.(3.18) :

$$(1/E_p) \, dE_p/dx \propto E_p T/T \int_{2m_e}^{E_p - 2m_e} (E_e/E_p) \, T^4 F(E_e/E_p , E_p T) \, dE_e/E_p$$

$$= T^3 F'(E_p T) \tag{3.21}$$

In this integral, the contribution from the range of E_e near the upper limit is very small, so that the variation of λ_{pc} with this limit can be neglected.
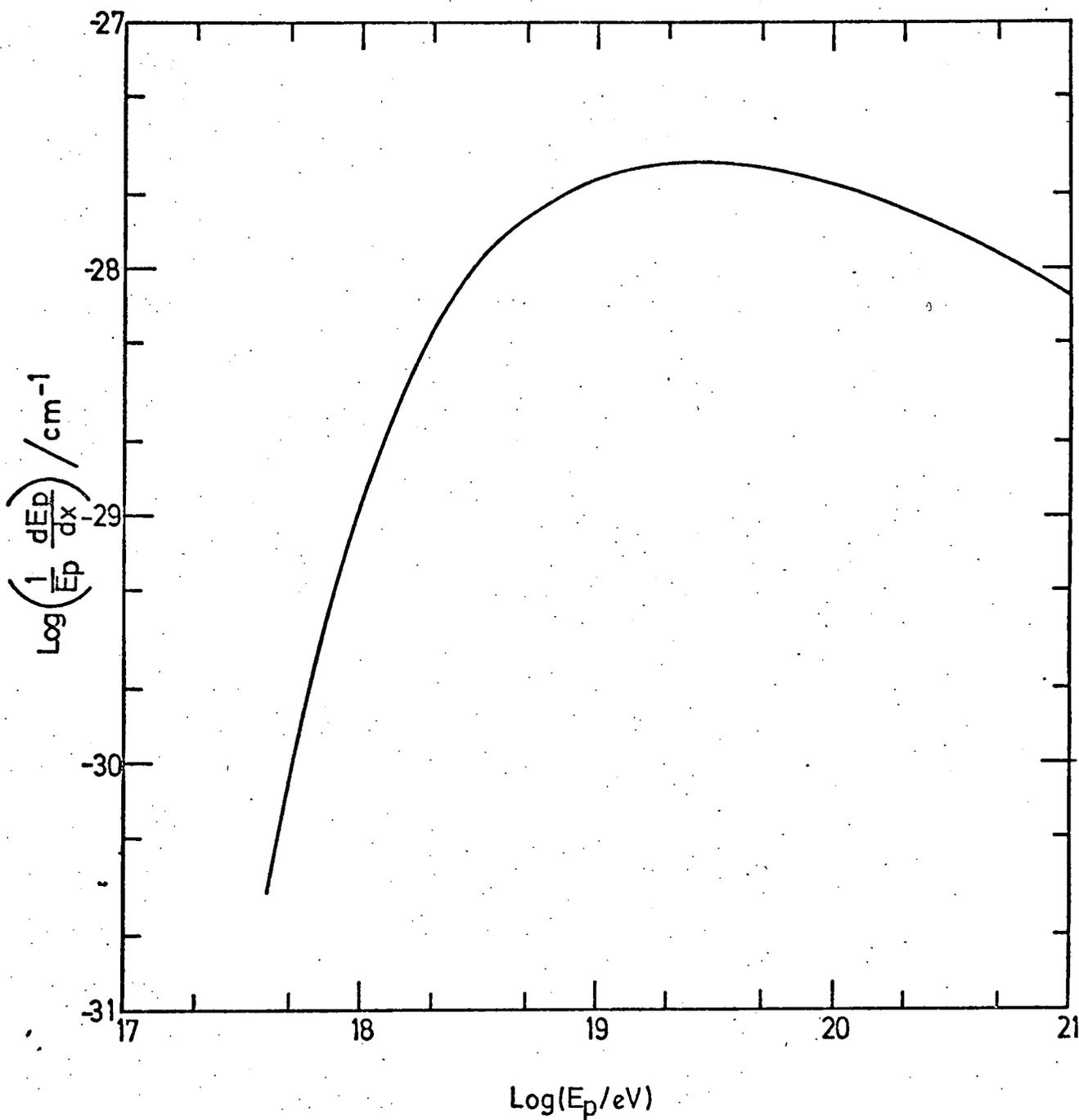
Fig 3-5

Inverse attenuation lengths for the PC process in a Blackbody

radiation field with T = 2.7 K.

Hence

$$\lambda_{pc}(E_p , T) = (T/T_o)^3 \lambda_{pc}(E_p T/T_o , T_o) \tag{3.22}$$

This form of λ_{pc} is as expected, since the density of photons is proportional to T^3, and the fractional energy loss per collision depends on $\varepsilon' (\sim \frac{k}{m_e} E_p T)$ from eqs.(3.1) and (3.2)

Chapter 3 References

Blumenthal G R., 1970, Phys. Rev. D, 1, 1596

Feenberg E and Primakoff H., 1948, Phys. Rev. 73, 449

Gluckstern R L and Hull M H., 1953, Phys. Rev. 90, 1030

Greisen K., 1966, Phys. Rev. Lett. 16, 748

Chapter 4. Inverse Compton Scattering on a Blackbody radiation field.

4.1 Introduction

The collision of a high energy electron with a low-energy photon, resulting in the transfer of energy to the photon, is known as Inverse Compton scattering (ICS), by analogy with Compton scattering, in which the photon transfers its energy to the electron.

This process was originally discussed by Feenberg and Primakoff (1948), in connection with the interactions of cosmic-ray electrons with starlight in the Galaxy and in extragalactic space. The possible significance of ICS in producing the X - ray and gamma-ray backgrounds, by scattering on the microwave background, was pointed out by Felten and Morrison (1963,1966), who give a useful account of the theory of ICS applied to astrophysical situations.

In the present Chapter, expressions are derived and evaluated for the differential reaction rates for ICS on a Planck radiation field, which are used in the calculation of the γ-ray spectrum in Chapters 7 and 8. Attenuation lengths and the mean energy transfer as a function of electron energy are computed from these expressions.

4.2 Kinematics of ICS.

Fig 4-1 shows the notation adopted here, with

E_e , $\underline{p}_e$	energy and momentum of electron before collision
E_{e1} , $\underline{p}_{e1}$	" " " after "
ε , $\underline{k}$	" " photon before "
E_γ , $\underline{k}_1$	" " " after "
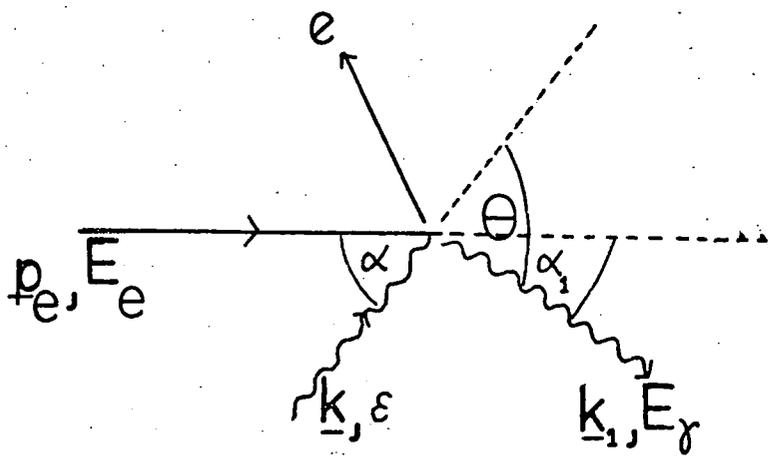
Fig 4-1. Geomety of Inverse Compton Scattering, illustrating notation used.

α angle between momenta of electron and photon initially

θ angle of deflection of photon

α_1 angle between incident electron momentum and outgoing photon momentum.

From conservation of 4-momentum :

$$\underline{p}_e + \underline{k} = \underline{p}_1 + \underline{k}_1$$

$$E_e + \varepsilon = E_{e1} + E_\gamma$$

Eliminating the energy and momentum of the outgoing electron :

$$-(\underline{p}_e + \underline{k} - \underline{k}_1)^2 + (E_e + \varepsilon - E_\gamma)^2 = m_e^2$$

i.e. $E_e\varepsilon - E_\gamma\varepsilon - E_e E_\gamma - \underline{p}_e\cdot\underline{k} + \underline{p}_e\cdot\underline{k}_1 + \underline{k}\cdot\underline{k}_1 = 0$

Writing $\beta = \underline{p}_e/E_e$ gives

$$E_e\varepsilon - E_\gamma\varepsilon - E_e E_\gamma - \beta E_e\varepsilon\cos\alpha + \beta E_e E_\gamma\cos\alpha_1 + \varepsilon E_\gamma\cos\theta = 0$$

i.e. $$\frac{E_\gamma}{\varepsilon} = \frac{1 - \beta\cos\alpha}{1 - \beta\cos\alpha_1 + \frac{\varepsilon}{E_e}(1 - \cos\theta)} \qquad (4.1)$$

In the special case of an electron at rest, $\beta = 0$ so that the usual Compton formula is obtained :

$$\frac{E'}{\varepsilon'} = \frac{1}{1 + \frac{\varepsilon'}{m_e}(1 - \cos\theta')} \qquad (4.2)$$

where dashes denote electron rest-frame quantities.

We require E_γ/E_e in terms of the electron-frame quantities. Using

$$E_\gamma = \gamma E'_\gamma (1 + \beta\cos\alpha_1')$$

gives

$$\frac{E_\gamma}{E_e} = \frac{\varepsilon'/m_e (1 + \beta\cos\alpha_1')}{1 + \frac{\varepsilon'}{m_e}(1 - \cos\theta')} \qquad (4.3)$$

In the case of interest for the present work, we always have $\gamma \gg 1$, so that α_1' is very small for all but a negligible fraction of the photons for an isotropic radiation photon distribution in the laboratory frame.

This can be seen as follows. If the components of photon momentum parallel and perpendicular to the electron momentum are denoted by $k_{\shortparallel}$, $k_{\perp}$, $k'_{\shortparallel}$ and $k'_{\perp}$ in the laboratory and electron frames respectively, then

$$k'_{\shortparallel} = \gamma (k_{\shortparallel} - \beta k) = \gamma k(\cos\alpha - \beta)$$

$$k'_{\perp} = k_{\perp} = k \sin\alpha$$

so that $\quad \tan\alpha' = \dfrac{k'_{\perp}}{k'_{\shortparallel}} = \dfrac{\sin\alpha}{\gamma(\cos\alpha - \beta)}$

In the laboratory frame, one half of the photons have $\alpha > 90^{\circ}$, and in the electron frame these electrons are contained in a cone of semi-angle α', where

$$\tan\alpha' = -1/\gamma\beta$$

Thus even for electrons of a few GeV, with $\gamma \sim 2000$, most of the photons have $\alpha' \sim 180^{\circ}$, i.e., the collision is head-on in the electron frame. In this case, $\alpha'_1 = \theta' - \alpha' = \theta' - 180^{\circ}$, so that $\cos\alpha'_1 = -\cos\theta'$, and equation (4.3) becomes

$$\frac{E_\gamma}{E_e} = \frac{\varepsilon'/m_e \quad (1 - \cos\theta')}{1 + \dfrac{\varepsilon'}{m_e}(1 - \cos\theta')} \qquad \text{for } \gamma \gg 1 \quad (4.4)$$

We can now distinguish high and low energy limits for eq.(4.4). Since

$$\varepsilon' = \gamma\varepsilon (1 - \beta \cos\alpha)$$

clearly $\quad E_\gamma/E_e \to 1 \quad$ for $\quad \gamma\varepsilon \gg m_e$

and $\quad E_\gamma \sim \gamma^2\varepsilon \quad$ for $\quad \gamma\varepsilon \ll m_e$

A Blackbody radiation field with T = 2.7K has $\varepsilon \sim 10^{-3}$ eV, so the changeover from low to high energy domains occurs at electron energies $\sim (5\ 10^5)^2/10^{-3} = 2.5\ 10^{14}$ eV. Above this energy, the electron transfers most of its energy to the photon - the process is catastrophic, while at lower energies, the energy losses become more continuous.

4.3 Differential reaction rates for ICS.

The differential cross-section for the Compton effect is given by the Klein-Nishina formula, summed over the initial and final polarizations states. In terms of electron-frame quantities, the result is (Jauch and Rohrlich, 1955):

$$\frac{d\sigma}{d\Omega'} = \frac{r_o^2}{2} \left(\frac{E'}{\varepsilon'}\right)^2 \left[\frac{\varepsilon'}{E'_\gamma} + \frac{E'_\gamma}{\varepsilon'} - \sin^2\theta'\right] \qquad (4.5)$$

where $r_o = e^2/mc^2$ and $d\Omega' = 2\pi\sin\theta'\, d\theta'$

It is convenient to write this expression in terms of the fractional energy transfer to the photon in the laboratory frame, $v = E_\gamma/E_e$. It follows from eqs. (4.2) and (4.4) that

$$\frac{E'}{\varepsilon'} = 1-v$$

and

$$\sin^2\theta' = 1 - \cos^2\theta' = \frac{2m_e}{\varepsilon'}\left(\frac{v}{1-v}\right) - \frac{m_e^2}{\varepsilon'^2}\left(\frac{v}{1-v}\right)^2$$

For constant ε', from eq.(4.4),

$$dv = \frac{dE_\gamma}{E_e} = \frac{\varepsilon'/m_e\;\sin\theta'}{\left[1 + \varepsilon'/m_e\;(1-\cos\theta')\right]^2} = \varepsilon'/m_e\;(1-v)^2\sin\theta'\, d\theta'$$

Hence from (4.5)

$$d\sigma = \pi r_o^2\,(m_e/\varepsilon')\left[\left(\frac{v}{1-v}\right)^2\frac{m_e^2}{\varepsilon'^2} - 2\left(\frac{v}{1-v}\right)\frac{m_e}{\varepsilon'} + (1-v) + \frac{1}{1-v}\right]\,dv \qquad (4.6)$$

for

$$0 \leqslant v < \frac{2\,\varepsilon'/m_e}{1 + 2\,\varepsilon'/m_e}$$

To obtain the differential reaction rate $g_{IC} = d/dE_\gamma <\sigma n>_{IC}(E_\gamma, E_e)$ we can use the expression for $n(\varepsilon')$ derived in Sec(3.4), eq. (3.17), to give

$$g_{IC}(E_\gamma, E_e) = \frac{\pi r_o^2}{\pi^2\hbar^3 c^3}\frac{kT}{2\gamma^3}\int_{\varepsilon'_{min}}^{\infty}\left[\left(\frac{v}{1-v}\right)^2\frac{m_e^2}{\varepsilon'^2} - 2\left(\frac{v}{1-v}\right)\frac{m_e}{\varepsilon'} + (1-v) + \frac{1}{1-v}\right] \cdot$$

$$\cdot \ln(1 - \exp(-\varepsilon'/2\gamma kT))^{-1}\, d\varepsilon' \qquad (4.7)$$

ε'_{min} is obtained using the upper limit for v for given ε' from eq.(4.6) :

$$\varepsilon'_{min} = \frac{m}{2}e\left(\frac{v}{1-v}\right) \qquad (4.8)$$

Equation (4.7) can be written in dimensionless form as follows :

Put $y = \varepsilon'/2\gamma kT$, $\qquad y_m = \frac{m}{2}e\left(\frac{v}{1-v}\right)\frac{m}{2E_e kT}$ $\qquad$ (4.9)

so that $\varepsilon' = \frac{y}{y_m}\frac{m}{2}e\left(\frac{v}{1-v}\right)$

Then

$$g_{IC}(E_\gamma ,E_e) = \frac{\pi r_o^2}{\pi^2 \hbar^3 c^3} \ (kT)^3 \cdot 16\frac{(1-v)}{v}\ y_m \ \left[\left(\tfrac{1}{2} + \frac{v^2}{4(1-v)}\right)\ I_1 - y_m I_2 + y_m^2 I_3\right]$$
$$(4.10)$$

where $\qquad I_1 = -\int\limits_{y_m}^{\infty}\ln(1 - e^{-y})\ dy$

$$I_2 = -\int\limits_{y_m}^{\infty}\frac{1}{y}\ln(1 - e^{-y})\ dy \qquad (4.11)$$

$$I_3 = -\int\limits_{y_m}^{\infty}\frac{1}{y^2}\ln(1 - e^{-y})\ dy$$

The functions $I_1 - I_3$ were evaluated numerically using a Romberg routine. Evaluating the constants in eqs. (4.9) and (4.10) gives

$$y_m = \frac{3.03\ 10^{15}}{E_e T}\ \frac{v}{4(1-v)} \qquad \text{for } E_e \text{ in eV}$$
$$(4.12)$$

$$\frac{\pi r_o^2 (kT)^3}{\pi^2 \hbar^3 c^3} = 2.08\ 10^{-24}\ T^3 \quad cm^{-1}$$

Approximations for y large and for y small.

For large y, the integrals I_{1-3} can be done analytically. Thus

$$I_1 \to \int\limits_{y_m}^{\infty}e^{-y}dy = e^{-y_m}$$

$$I_2 \to \int\limits_{y_m}^{\infty}y^{-1} e^{-y}dy \to \frac{e^{-y_m}}{y_m} \qquad (4.13)$$

$$I_3 \to \int\limits_{y_m}^{\infty}y^{-2}e^{-y}dy \to \frac{e^{-y_m}}{y_m^2}$$

Hence the terms in I_2 and I_3 in eq.(4.10) cancel for $y \gg 1$, and the reaction rate is given by

$$g_{IC}(E_\gamma, E_e) = 6.31 \; 10^{-9} \; \frac{T^2}{E_e} \left[2 + \frac{v^2}{1-v} \right] \; cm^{-1} \quad (4.14)$$

For small y, $-\ln(1-e^{-y}) \to -\ln(y)$, so that

$$I_1 \to -\ln(y) \; dy = y_m(1 - \ln y_m)$$

$$I_2 \to -y^{-1}\ln(y) \; dy = -\frac{(\ln y_m)^2}{2} \quad (4.15)$$

$$I_3 \to -y^{-2}\ln(y) \; dy = -\frac{1}{y_m}(1 + \ln y_m)$$

For $y_m < 0.1$, the integrals were evaluated using eqs. (4.15) over the range with $y < 0.1$, and then adding the contribution from $y > 0.1$. This gives

$$I_1 = -y_m(1 - \ln y_m) + 1.64$$

$$I_2 = \tfrac{1}{2}(\ln y_m)^2 + 0.659 \quad (4.16)$$

$$I_3 = -(1 + \ln y_m)/y_m + 2.07$$

The results of numerical evaluations of the ICS reaction rates are shown in Fig 4-2 for $E_e > 10^{15}$ eV and Fig 4-3 for $E_e < 10^{15}$ eV. In Fig 4-2, the quantity plotted is $g_{IC}(E_\gamma, E_e) \, v(1-v)$ against $(1-v)$ on a logarithmic scale. This gives a true indication of the distribution of energy in the scattered gamma-rays, since $dv = -(1-v) \, d(\ln(1-v))$, so that equal areas on the graph correspond to equal energies.[*] Similarly, in Fig 4-3, the quantity $g_{IC}(E_\gamma, E_e) \, v^2$ is plotted against v.

These graphs clearly demonstrate the energy regions discussed in Sec 4.2, viz., the high energy region $(E_e \gtrsim 10^{14} eV)$ in which the photon takes most of the energy, and the low energy region in which $E_\gamma \ll E_e$.

[*]After allowing for the logarithmic vertical scale of the graph.
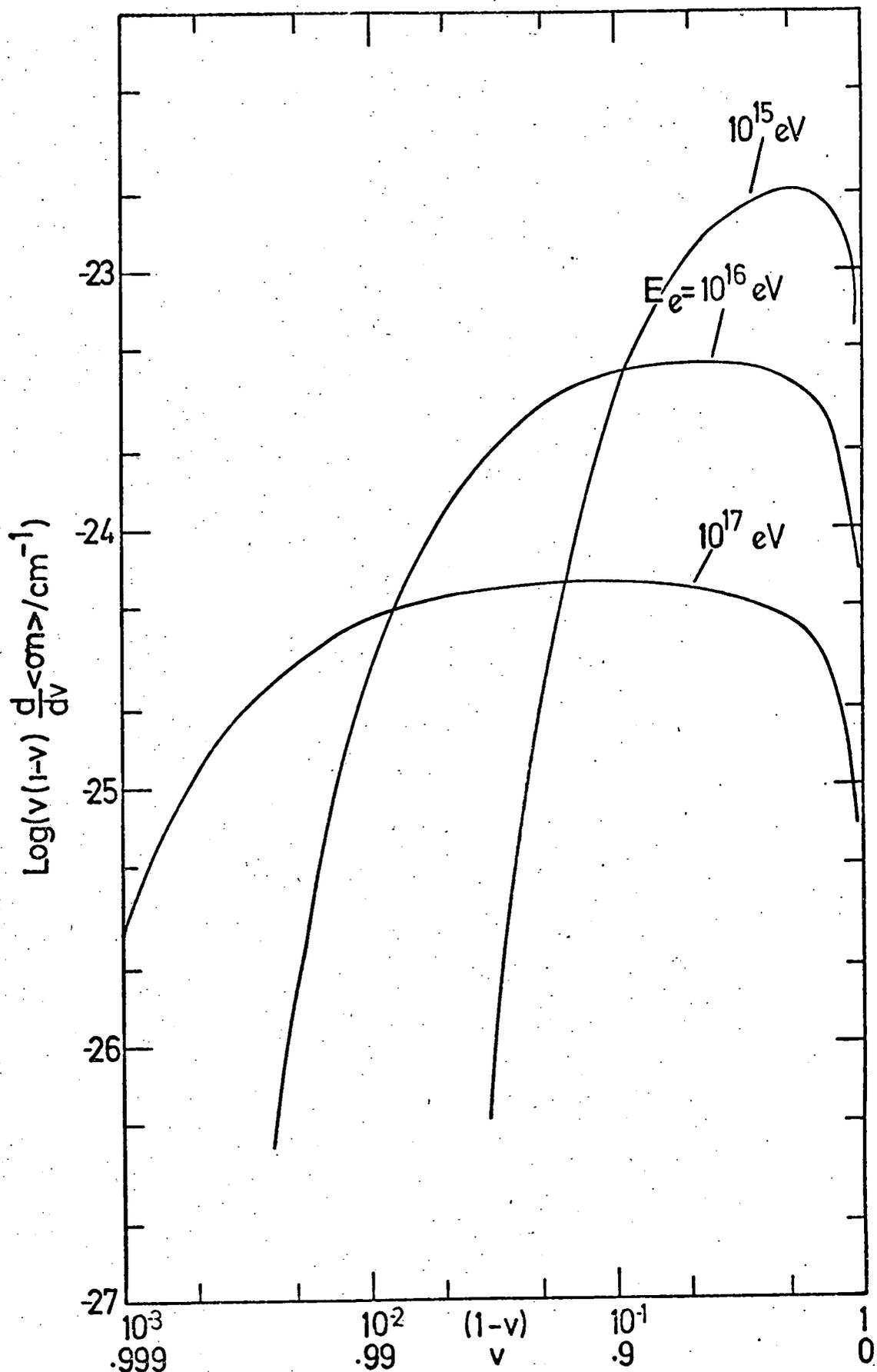
Fig 4-2

Differential reaction rates for ICS for $E_e \geqslant 10^{15}$

multiplied by $v(1-v)$ to show the energy distribution

of the scattered photons.
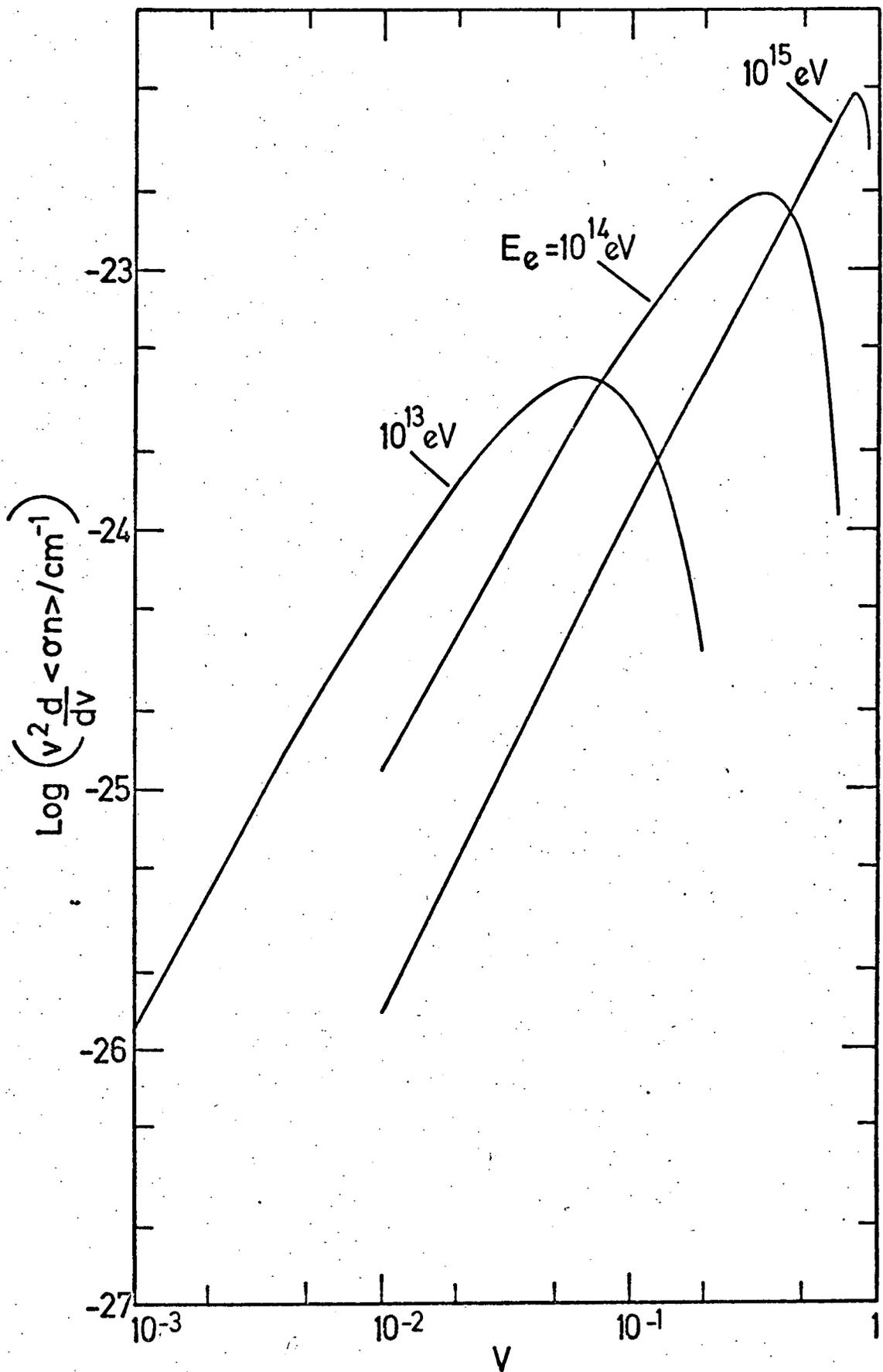
Fig 4-3

Differential reaction rates for ICS for $E_e \leqslant 10^{15}$ eV; in this plot multiplication by v^2 shows the energy distribution in the scattered photons.

4.4 The Gamma-ray spectrum for a unique target photon energy in ICS.

The differential cross-section in the form of eq.(4.6), and the electron-frame distribution of target photons, eq.(3.16), together give the following expression for the mean differential cross-section for an isotropic distribution of photons of energy ε :

$$\frac{d\bar{\sigma}}{dE_\gamma} = \int_{\frac{m_e}{2}\frac{v}{1-v}}^{2\gamma\varepsilon} d\sigma \, P(\varepsilon'|\varepsilon) \, d\varepsilon'$$

$$= \frac{\pi r_o^2}{2\gamma^2\varepsilon^2} \left(\frac{m_e}{E_e}\right) \int_{\frac{m_e}{2}\frac{v}{1-v}}^{2\gamma\varepsilon} \left[\left(\frac{v}{1-v}\right)^2 \left(\frac{m_e}{\varepsilon'}\right)^2 - 2\left(\frac{v}{1-v}\right)\frac{m_e}{\varepsilon'} + (1-v) + \frac{1}{1-v}\right] d\varepsilon'$$

$$= \frac{\pi r_o^2}{2\gamma^2\varepsilon^2} \frac{m_e^2}{E_e} \left[\frac{v(2-2v-v^2)}{2(1-v)^2} + 2\frac{v}{1-v}\ln\frac{m_e}{4\gamma\varepsilon}\frac{v}{1-v} - \left(\frac{v}{1-v}\right)^2 \frac{m_e}{2\gamma\varepsilon} \right.$$

$$\left. + 2\left(1-v + \frac{1}{1-v}\right)\frac{2\gamma\varepsilon}{m_e}\right] \tag{4.17}$$

The range of validity is given by eq.(4.4) as

$$0 \leqslant v \leqslant \frac{4\gamma\varepsilon/m_e}{1 + 4\gamma\varepsilon/m_e}$$

For $\gamma\varepsilon \ll m_e$, $v \sim 1$ so that eq.(4.17) can be approximated retaining only terms of first order in v. Putting $x = m_e v/4\gamma\varepsilon$ we get

$$\frac{d\bar{\sigma}}{dv} = 2\pi r_o^2 \frac{m_e}{\gamma\varepsilon} (1 + x - 2x^2 + 2x\ln x) \tag{4.18}$$

This agrees with the form given by Cowsik (1973)

The mean energy of the Compton scattered gamma-rays can be obtained from eq.(4.18) :

$$\bar{x} = \frac{\int_0^1 (1 + x - 2x^2 + 2x\ln x)x \, dx}{\int_0^1 (1 + x - 2x^2 + 2x\ln x) \, dx} = \frac{1}{3} \tag{4.19}$$

Therefore $\langle E_\gamma \rangle = 4/3 \, \gamma^2\varepsilon$, as given, for example, by Ginzburg and Syrovatskii (1964).

4.5 Total IC cross-sections for a unique target photon energy.

Integration of eq.(4.6) over v gives the total cross-section for ICS for given fixed ε'. The result is (see for example, Jauch and Rohrlich, 1955) :

$$\sigma(\varepsilon') = 2\pi r_0^2 \left[\frac{1+w}{w^3} \left(\frac{2w(1+w)}{1+2w} - \ln(1+2w) \right) + \frac{\ln(1+2w)}{2w} - \frac{(1+3w)}{(1+2w)^2} \right] \qquad (4.20)$$

where $w = \varepsilon'/m_e$.

For $\varepsilon' \to 0$, eq.(4.20) reduces to $\sigma = 8/3 \, \pi \, r_0^2$, the usual Thompson cross-section. For $\varepsilon' \gg m_e$,

$$\sigma \to 2\pi r_0^2 \left[\frac{1}{w} - \frac{\ln(1+2w)}{w^2} + \frac{\ln(1+2w)}{2w} - \frac{3}{4w} \right]$$

$$= \pi r_0^2 \frac{m_e}{\varepsilon'} \left[\ln \frac{2\varepsilon'}{m_e} + \frac{1}{2} \right] \qquad (4.21)$$

For an isotropic field of photons of energy ε, the average total cross section is obtained using (3.16) as

$$\sigma = \pi r_0^2 \int_0^{2\gamma\varepsilon} \frac{\varepsilon' d\varepsilon'}{2\gamma^2 \varepsilon^2} \frac{1}{\varepsilon'} \left(\ln \frac{2\varepsilon'}{m_e} + \frac{1}{2} \right) d\varepsilon'$$

$$= \frac{\pi r_0^2 m_e}{\gamma \varepsilon} \left[\ln \frac{4\gamma\varepsilon}{m_e} - \frac{1}{2} \right] \qquad (4.22)$$

This expression gives an approximate check on the results for the ICS interaction lengths on a blackbody radiation field derived in the next section.

4.6 Interaction lengths for ICS in a Blackbody radiation field.

The interaction length $\lambda_{ic}(E_e)$ is given by

$$\lambda_{ic}(E_e, T) = \overline{\sigma n}(E_e, T) = \int_0^\infty \sigma(\varepsilon') n(\varepsilon') d\varepsilon' \qquad (4.23)$$

where $\sigma(\varepsilon')$ is given by eq.(4.20) and $n(\varepsilon')$ by eq.(3.17). The results of a numerical evaluation of eq.(4.23) are shown in Fig 4-4, for T = 2.7K.

At low energies, the result is equal to $1/\sigma_T N$, where N is the number density of blackbody photons and $\sigma_T = 6.65 \; 10^{-25} \; cm^2$, the Thompson cross-section. N is given by

$$N = \frac{1}{\pi^2 \hbar^3 c^3} \int_0^\infty \frac{\epsilon^2 d\epsilon}{e^{\epsilon/kT} - 1} = \frac{(kT)^3}{\pi^2 \hbar^3 c^3} \int_0^\infty \frac{x^2 dx}{e^x - 1} = \frac{2.404(kT)^3}{\pi^2 \hbar^3 c^3}$$

$$= 20.3 \; T^3 \text{ photons } cm^{-3}.$$

For T = 2.7K, N = 400 cm^{-3}, so that $\lambda_{ICS} = (6.65 \; 10^{-25} \cdot 400)^{-1} = 3.76 \; 10^{22} cm.$

For the high energy limit, using eq.(4.22),

$$\lambda_{ICS} = \frac{1.535 \; 10^{13} \; E\epsilon}{\ln\left(\frac{4\gamma\epsilon}{m_e} - \frac{1}{2}\right) N} \qquad \text{for } \gamma\epsilon \gg m_e \qquad (4.24)$$

The mean energy for a blackbody distribution is given by

$$\bar{\epsilon} = \frac{kT \int_0^\infty \frac{x^3 dx}{e^x - 1}}{\int_0^\infty \frac{x^2 dx}{e^x - 1}} = \frac{\frac{\pi^4}{15} kT}{2.404} = 2.7kT \quad (4.25)$$

Using this value , and N = 400 cm^{-3} in eq.(4.24) gives the curve shown in in Fig 4-4 (marked 'approximate formula') . It agrees with the exact solution to about 10% at 10^{15} eV but rapidly diverges below this energy.

Using eqs.(4.23) and (3.17), and changing the variable of integration to $x = \epsilon'/2\gamma kT$, we find that $\lambda_{ICS}(E_e , T) \propto T^{-3} \times$ a function of $E_e T$.(cf. the case of the PC process, Sec 3.7). Therefore the function $\lambda_{ICS}(E_e , T_0)$ can be used to obtain λ_{ICS} for any other E_e and T.

4-7   Mean energy transfer in ICS on Blackbody radiation.

For approximate treatments of energy spectra from ICS, it is useful to use the quantity $\bar{v}_{ICS}$, the mean fractional energy transfer to the photon, weighted according to the appropriate   reaction rate:

$$\bar{v}_{ICS} = \frac{1}{E_e} \frac{\int_0^{E_e} E_\gamma g_{IC}(E_\gamma , E_e) \, dE_\gamma}{\int_0^{E_e} g_{IC}(E_\gamma , E_e) \, dE_\gamma} \qquad (4.26)$$

This expression was evaluated numerically, using eq.(4.7) for g_{IC}.

Log(λ_{ICS}/cm)

Log(E_e/eV)

Exact calculation

Approximate formula
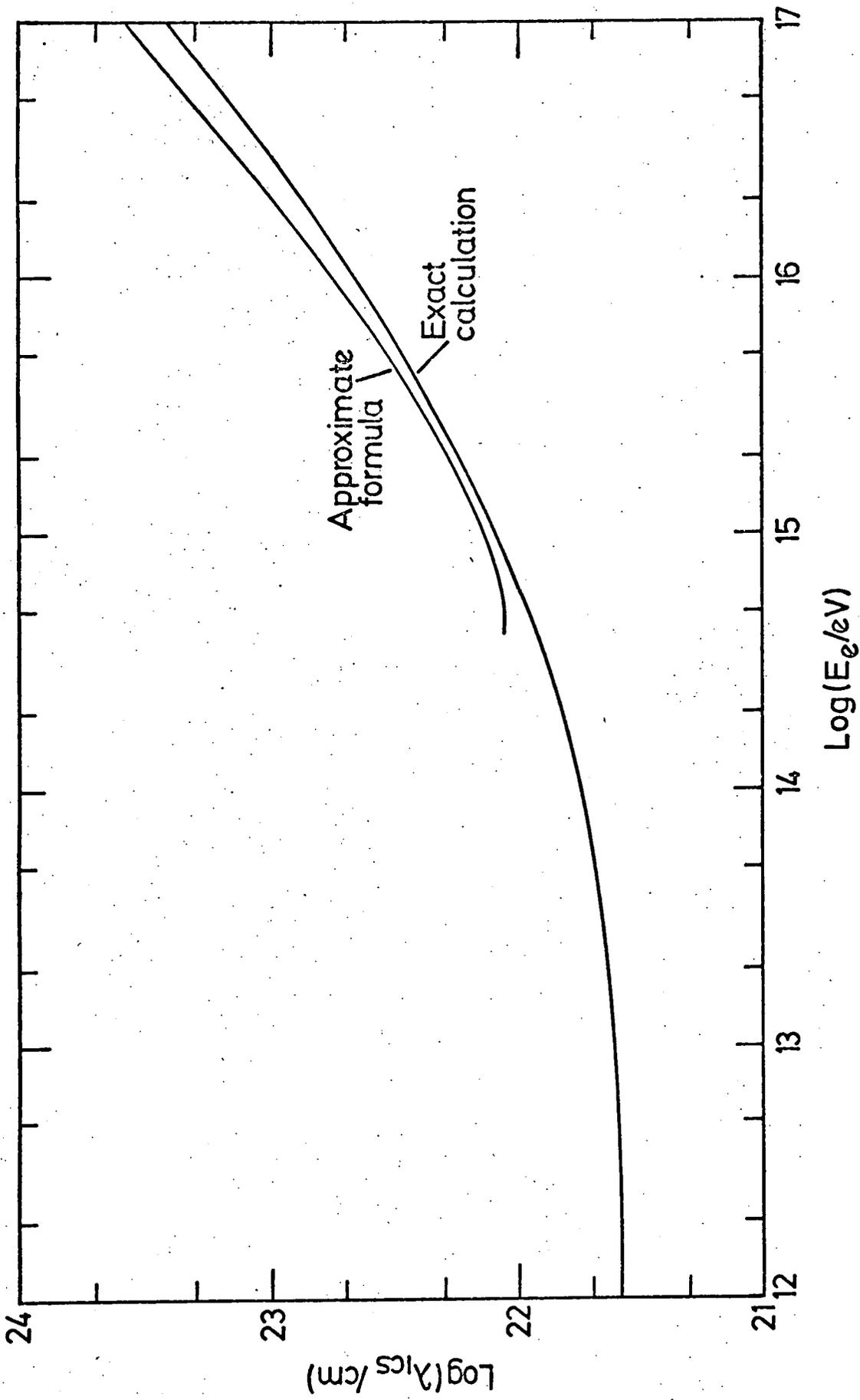
Fig 4-4

Interaction lengths for ICS on Blackbody radiation with T = 2.7 K.

The approximation of eq. (4.24) is also shown.

The results are shown in Fig 4-5, for $E_e = 10^{11} - 10^{17}$ eV, and T = 2.7K.

For comparison, approximations for $\bar{v}_{ICS}$ are also shown. In the low energy

limit, using eqs.(4.19) and (4.25) gives

$$\bar{v}_{ICS} = 3.2\ 10^{-15}\ E_e \qquad \text{for } E_e \text{ in eV, and } T = 2.7K.$$
$$= KE_e \qquad\qquad\qquad\qquad (4.27)$$

This is very close to the accurate calculations for $E_e \lesssim 10^{13}$ eV.

In the high energy limit, it can be shown that (Allcock and Wdowczyk, 1972)

$$\bar{v}_{ICS} = \frac{\ln(2\varepsilon'/m) - 5/6}{\ln(2\varepsilon'/m) + 1/2} \qquad (4.28)$$

This follows from taking the appropriate mean at fixed ε', using eq.(4.6).

For the case of head-on collisions, $\varepsilon' = 2E_e\varepsilon/m_e$, giving $\bar{v}_{ICS} = .52$,

.74 and .86 for $E_e = 10^{15}$, 10^{16} and 10^{17} eV respectively, taking for ε the

mean value given by eq.(4.25). Alternatively, using the value for ε'

obtained by averaging an isotropic laboratory distribution over angles:

$$\langle \varepsilon' \rangle = \frac{\varepsilon \int_0^\pi (1 - \cos\theta)^2 \sin\theta\ d\theta}{\int_0^\pi (1 - \cos\theta)\sin\theta\ d\theta} = \frac{4}{3}\varepsilon$$

gives $\bar{v}_{ICS} = .44, .71$ and $.81$ for the E_e values above. The approximations

agree with the accurate results to within 10% for $E_e > 10^{16}$ eV.
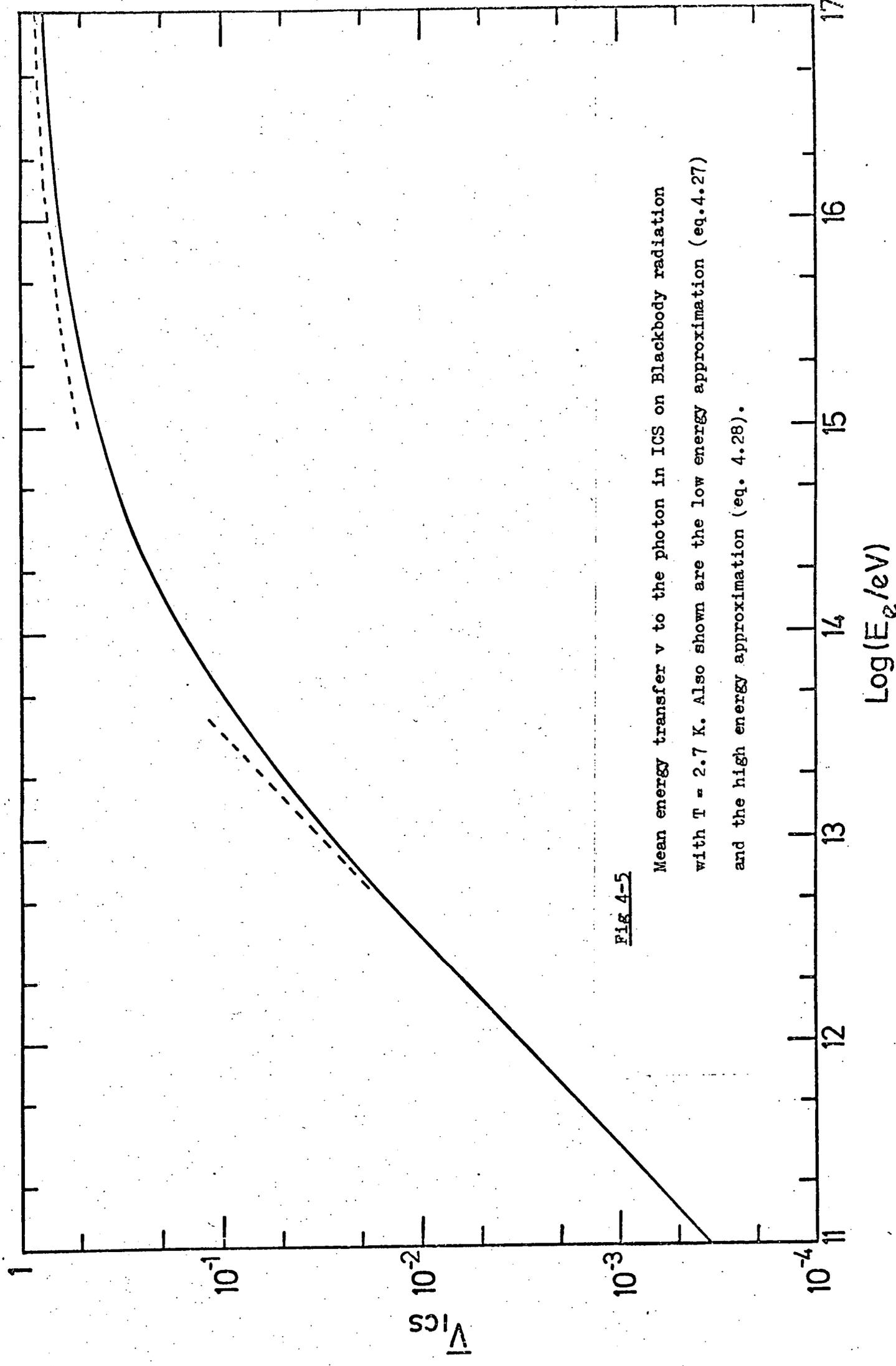
Fig 4-5

Mean energy transfer v to the photon in ICS on Blackbody radiation
with T = 2.7 K. Also shown are the low energy approximation (eq. 4.27)
and the high energy approximation (eq. 4.28).

Chapter 4.   References.

Allcock M C and Wdowczyk J., 1972, Nuovo Cimento $\underline{9}$, 315

Cowsik R., 1973, NASA SP-339, 185

Feenberg E and Primakoff H., 1948, Phys. Rev. $\underline{73}$, 449

Felten J E and Morrison P., 1963, Phys. Rev. Lett $\underline{10}$, 453

1966, Ap. J. $\underline{146}$, 686

Ginzburg V L and Syrovatskii S I., 1964, 'Origin of Cosmic Rays'.

Jauch J M and Rohrlich F., 1955, 'The Theory of Photons and Electrons',

(Addison-Wesley, Camb, Mass)

Chapter 5. Pair-production in photon-photon collisions in a blackbody radiation field.

5.1 Introduction

The importance of the pair-production process $\gamma + \gamma \rightarrow e^+ + e^-$, here-after denoted by PP, was first pointed out by Nikishov (1962), who treated interactions of gamma-rays with the starlight fields in the Galaxy and metagalaxy. Soon after the discovery of the microwave background, Jelley (1966) showed that PP results in severe attenuation of γ-rays of energy above 10^{14} eV over distances of only tens of kiloparsecs. More detailed calculations were carried out by Gould and Schreder (1966,1967a,b), who give analytical expressions for the interaction lengths on a blackbody radiation field. Allcock and Wdowczyk (1972) give expressions for the mean energy of the outgoing electrons for a unique target photon energy in the high energy limit, assuming head on collisions. In the present work, the spectrum of the outgoing electrons for interactions with a blackbody field is required, and to this end the differential reaction-rates are calculated as described in the following Sections.

5.2 Kinematics of PP.

It is convenient to work in terms of center-of-momentum quantities, which will be denoted with an asterix. Consider the collision of two photons of momenta $\underline{p}_1$ and $\underline{p}_2$ and energies E_γ and ε , with $E_\gamma \gg \varepsilon$. Let the angle between the momenta be α in the laboratory frame, (Fig 5-1). In the C.M. frame. the total energy is $2E_e^*$, and the total momentum is zero, so that

$$E_\gamma = 2\gamma_c E_e^* \qquad \text{since } E_\gamma \gg \varepsilon \qquad (5.1)$$

Transforming the electron energy into the laboratory frame,

$$E_e = \gamma_c(E_e^* - p_e^* \cos \theta^*)$$

LAB FRAME
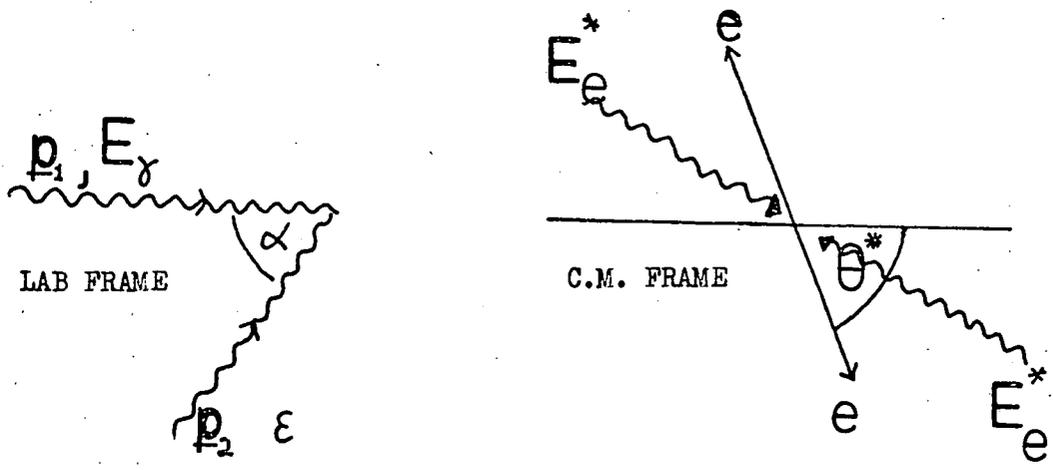
C.M. FRAME

Fig 5-1. Geometry of pair-production in γ-γ collision, illustrating notation used.

$$= \frac{E}{2}\left(1 - \frac{p^*_e}{E^*_e} \cos \theta^*\right) \tag{5.2}$$

where θ^* is the angle between the C.M. direction of motion and the electron momentum in the C.M. frame.

Using the invariant square of the 4-momentum,

$$(2E^*_e)^2 = (E_\gamma + \varepsilon)^2 - (\underline{p}_1 + \underline{p}_2)^2 = 2E_\gamma \varepsilon (1 - \cos\alpha)$$

so that

$$E^*_e = \sqrt{\frac{E_\gamma \varepsilon (1 - \cos\alpha)}{2}} \tag{5.3}$$

For an isotropic photon distribution in the laboratory,

$$P(E^*_e)\, dE^*_e = P(\alpha)\, d\alpha = \tfrac{1}{2} \sin\alpha\, (1 - \cos\alpha)\, d\alpha$$

From eq.(5.3),

$$\frac{dE^*_e}{d\alpha} = -\sqrt{\frac{E_\gamma \varepsilon}{2}} \cdot \tfrac{1}{2}(1 - \cos\alpha)^{-\frac{1}{2}} \sin\alpha$$

$$P(E^*_e) = \sqrt{\frac{2}{E_\gamma \varepsilon}} (1 - \cos\alpha)^{3/2}$$

Substituing from eq.(5.3) we get

$$P(E^*_e) = \frac{4E^{*\,3}_e}{\varepsilon^2 E^2_\gamma} \qquad \text{for } 0 \leqslant E^*_e \leqslant \sqrt{E_\gamma \varepsilon} \tag{5.4}$$

5.3 Differential reaction rates for PP.

The differential cross-section for PP can be derived using covariant quantum electrodynamics (see Jauch and Rohrlich, 1955), and is given by

$$d\sigma = \frac{2\pi r^2_0}{2} \beta \left(\frac{m_e}{E^*_e}\right)^2 \left[\frac{1 - \beta^4 \cos^4\theta^* + 2(m_e/E^*_e)^2 \beta^2 \sin^2\theta^*}{(1 - \beta^2 \cos^2\theta^*)^2}\right] \sin\theta^*\, d\theta^* \tag{5.5}$$

where $\beta = p^*_e/E^*_e$. A factor of 2 has been included since we do not distinguish between electrons and positrons in the present work.

We require the cross-section in terms of the fractional energy transfer to an electron, $v_{PP} = E_e/E_\gamma$. From eq.(5.2),

$$v_{PP} = \tfrac{1}{2}(1 - \beta \cos \theta^*) \tag{5.6}$$

$$\cos \theta^* = 1 - 2v$$

Differentiating eq.(5.6) for constant β

$$dv = \frac{\beta}{2} \sin \theta^* d\theta^*$$

Putting $x = E_e^*/m_e$ gives

$$\frac{d\sigma}{dv} = 2\pi r_o^2 \frac{1}{x^2} \frac{\left(1 - (1-2v)^4 + \frac{2}{x^2}\left[\left(1 - \frac{1}{x^2}\right) - (1-2v)^2\right]\right)}{16v^2(1-v)^2} \tag{5.7}$$

Integration of eq.(5.7) over v gives the total cross-section for fixed E_e^* :

$$\sigma(E_e^*) = \frac{\pi r_o^2}{2}(1-\beta^2)\left[(3-\beta^4)\ln\frac{1+\beta}{1-\beta} - 2\beta(2-\beta^2)\right] \tag{5.8}$$

which agrees with form given by Jauch and Rohrlich (1955).

In the high energy limit, this reduces to

$$\sigma(E_e^*) = \frac{\pi r_o^2}{x}(2\ln 2x - 1) \tag{5.8a}$$

and in the low energy limit to

$$\sigma(E_e^*) = \pi r_o^2 \beta \tag{5.8b}$$

The differential reaction rate $g_{PP}(E_e , E_\gamma) = d/dv \overline{\sigma n}(E_e , E_\gamma)$ is given by

$$g_{PP}(E_e , E_\gamma) = \int_{E_{e\,min}^*}^{\infty} \frac{d\sigma}{dv}(E_e , E_\gamma, E_e^*) n(E_e^*) dE_e^* \tag{5.9}$$

where $n(E_e^*)$ is the distribution of one type of electron (e^+ or e^-) in the C.M. frame. $n(E_e^*)$ can be obtained using eq.(5.4) and $n(\varepsilon) = (1/\pi^2\hbar^3c^3) \varepsilon^2/(\exp(\varepsilon/kT) -1)$:

$$n(E_e^*) = \int_{E_e^{*2}/E_\gamma}^{\infty} P(E_e^* , \varepsilon) n(\varepsilon) d\varepsilon$$

$$= \frac{1}{\pi^2 h^3 c^3} \frac{4E_e^{*3}}{E_\gamma^2} kT \ln(1 - e^{-E_e^{*2}/E_\gamma kT}) \tag{5.10}$$

E_{min}^* is obtained by solving eq.(5.2) for E_e^* with $\cos \theta^* = 1$, giving

$$E_{min}^* = \frac{m_e}{2\sqrt{v(1-v)}}$$

Introducing $y = E_e^{*2}/E_\gamma kT$, $y_m = \dfrac{m_e}{E_\gamma kT.\ 4v(1-v)}$

and substituting in eq.(5.9) gives

$$g_{PP}(E_e,\ E_\gamma) = \frac{2\pi r_o^2 (kT)^3}{\pi^2 h^3 c^3} \cdot 16v(1-v)y_m\left[\left(\frac{1}{4v(1-v)} - \tfrac{1}{2}\right)I_1 + I_2 y_m - I_3 y_m^2\right]$$
(5.11)

where I_1, I_2 and I_3 are given by eq.(4.11) and the constant by eq.(4.12).

The reaction rates for PP were calculated numerically from eq.(5.11) and the results are shown in Fig 5-2 for $E = 10^{14} - 10^{17}$ eV. For y_m large, the terms in I_2 and I_3 cancel, and $I_1 \to e^{-y_m}$ so that

$$g_{PP}(E_e,\ E_\gamma) = 8\pi \frac{r_o^2 (kT)^3}{\pi^2 h^3 c^3} (1 - 2v(1-v))\ y_m e^{-y_m}$$
(5.12)

5.4 Interaction lengths for PP on blackbody radiation.

The interaction length λ_{PP} given by

$$\lambda_{PP}^{-1} = \int_0^1 g_{PP}(E_e,\ E_\gamma)\ dv$$
(5.13)

is shown in Fig 5-3 for $E_e = 7\ 10^{13} - 10^{18}$ eV, and T = 2.7 K. Also shown is the approximation obtained from eq.(5.8), assuming that $\varepsilon = \bar{\varepsilon} = 2.7kT$, N = 400 cm^{-3}, and assuming head-on collisions so that $E_e^* = \sqrt{E_\gamma \varepsilon}$. The error involved in using these approximations leads to values about a factor of 2 above the accurate values.

As in the case of ICS, the interaction length for different T is obtained from

$$\lambda_{PP} = (T_o/T)^3 \lambda_{PP}(ET/T_o,\ T_o)$$
(5.14)

5.5 Mean energy transfer for PP.

The mean fractional energy transfer $\bar{v}_{PP}$ to the more energetic of
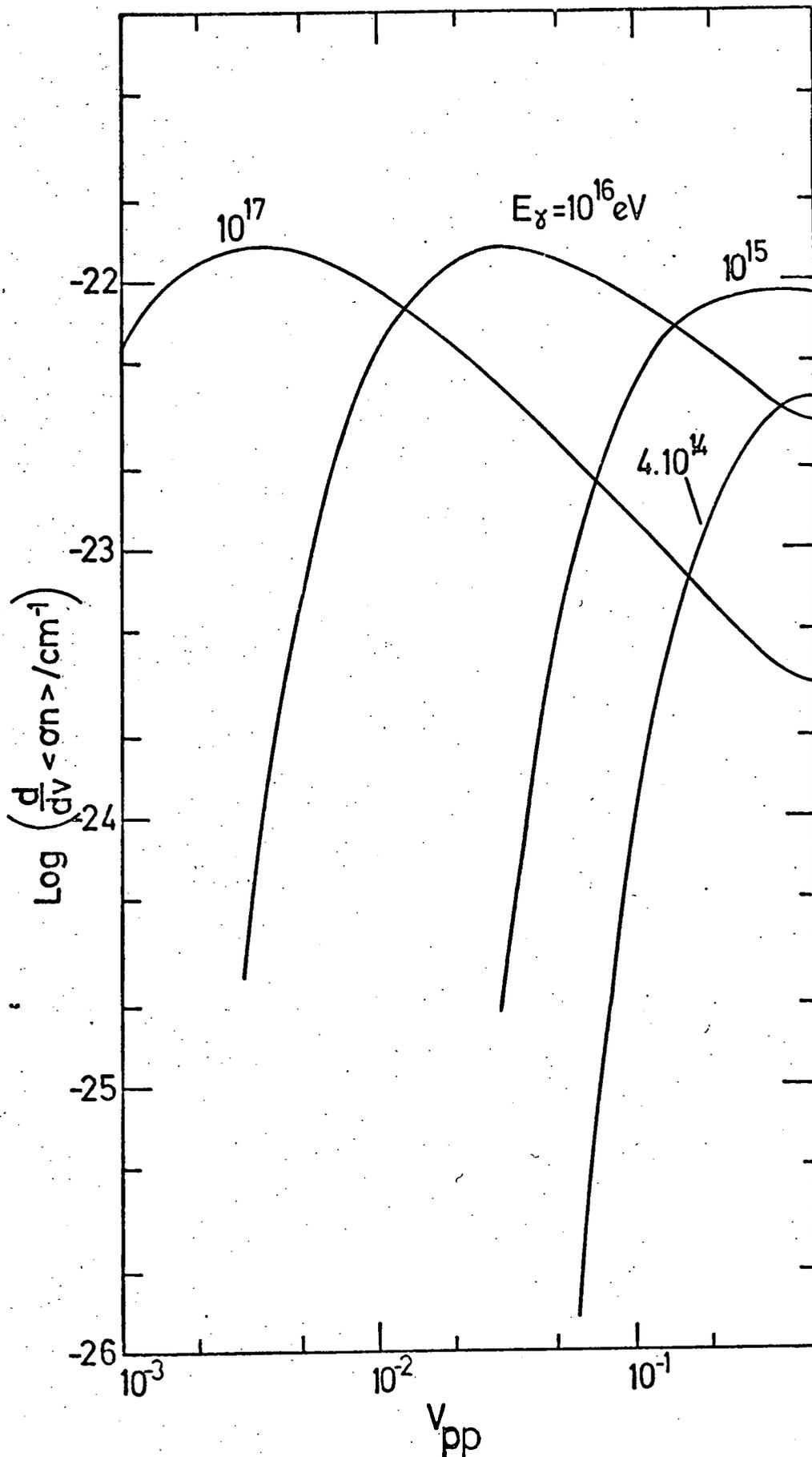
Fig 5-2

Differential reaction rates for the PP process
for various gamma-ray energies, as a function of the
fractional energy tranfer v_{pp} to one of the electrons.
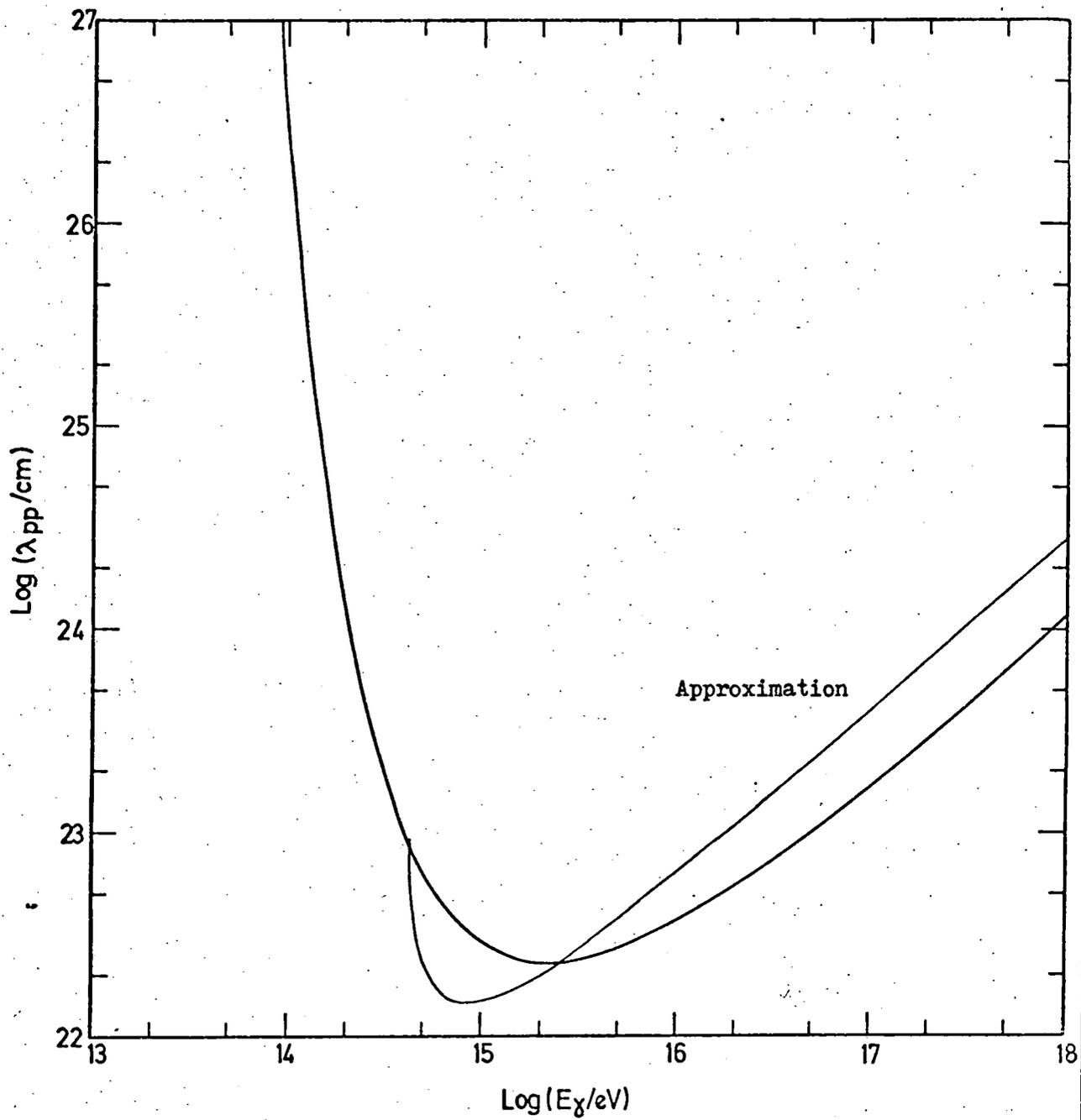
Fig 5-3

Interaction lengths for the PP process on a Blackbody

radiation field with T = 2.7 K. Also shown is the app-

roximation using eq. (5.8) for head-on collsions and

a radiation field with unique energy $2.7kT = 6 \cdot 10^{-4}$ eV.

the particles in the electron-positron pair was calculated from

$$\bar{v}_{PP} = \int_{\frac{1}{2}}^{1} v_{PP}\, g_{PP}(E_e\,,\,E_\gamma)\, dv_{PP} \qquad (5.15)$$

Since g_{PP} is symmetric in v_{PP} and $(1-v_{PP})$, the mean fractional energy transfer to the less energetic particle is $(1 - \bar{v}_{PP})$. Using eq.(5.11) for g_{PP}, the numerical results are shown in Fig 5-4 for $E_e = 7\ 10^{13} - 10^{18}$ eV.

Equation (5.7) can be used to obtain an approximation to $\bar{v}_{PP}$ for unique E_e^* in the high energy limit, the result being (Allcock and Wdowczyk, 1972), for head-on collisions,

$$\bar{v}_{PP} = \frac{1}{2}\left[1 + \frac{2\ln x - \frac{1}{2}}{2\ln x + \ln 4 - 1}\right] \qquad (5.16)$$

The value given by eq.(5.15) is also plotted in Fig 5-4 for the case of head-on collisions with photons of energy 2.7kT.

5.6 PP and ICS treated as a single process.

PP and ICS can be treated together as a single process in which the initial photon produces two photons of lower energy. The mean energy transfer to the higher energy photon is

$$\overline{v_{PP}v_{IC}} = 2\ \frac{\int_{\frac{1}{2}}^{1} v_{PP}\,\bar{v}_{IC}(E_\gamma v_{PP})g_{PP}(E_{\gamma_{PP}},E_\gamma)\, dv_{PP}}{\int_{0}^{1} g_{PP}(E_{\gamma_{PP}},E_\gamma)\, dv_{PP}} \qquad (5.17)$$

Changing the limits in the numerator to 0 and $\frac{1}{2}$ gives the expression for the lower energy photon. The result of a numerical evaluation of eq.(5.17) is shown in Fig 5-5.
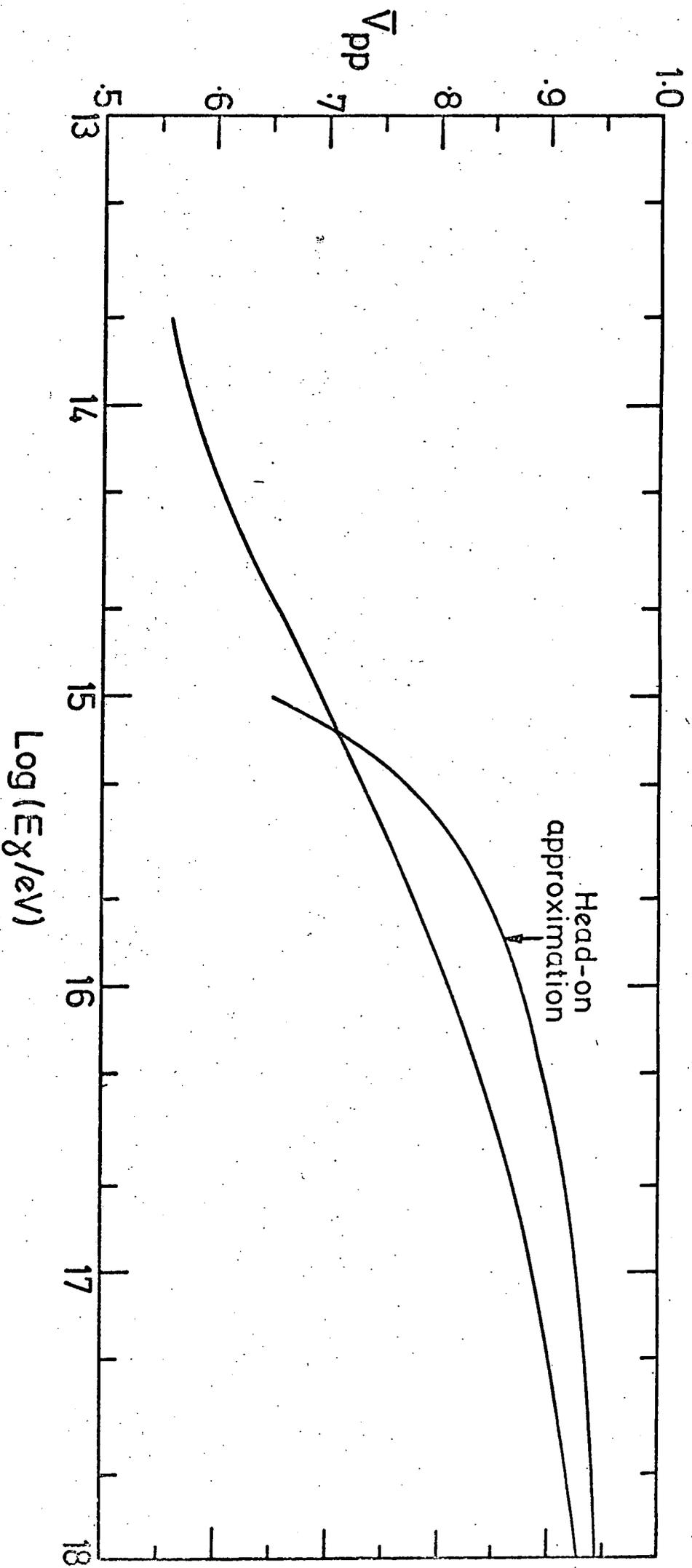
Fig 5-4

Mean energy transfer $\bar{v}_{pp}$ to electrons in the PP process. The curves
are for the more energetic electron. The approximation given by
eq. (5.16) is also shown.
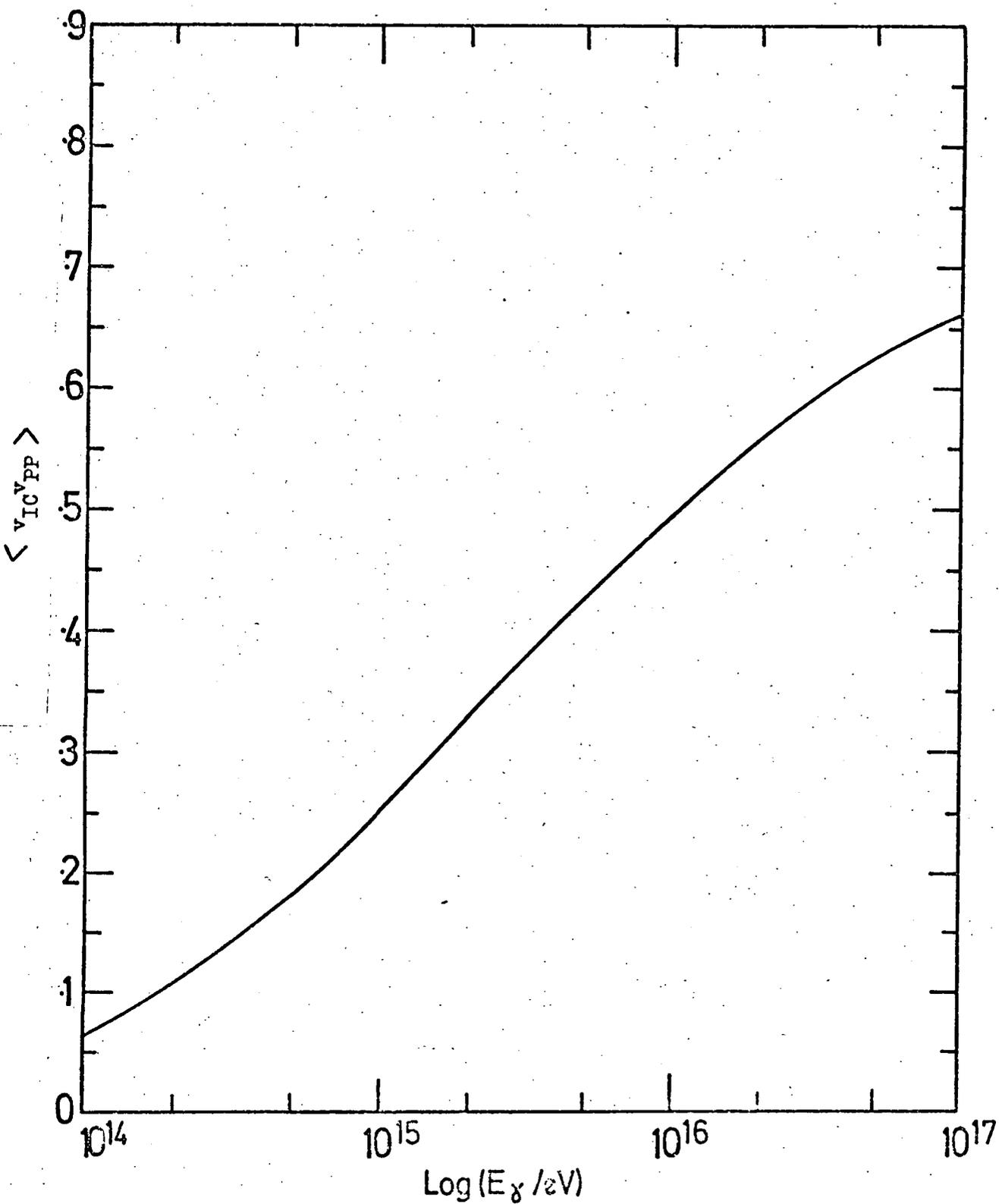
Fig 5-5   The mean fractional energy loss by gamma-rays for combination
of PP and ICS processes. The curve is for the gamma-ray prod-
uced by the higher energy electron of the pair.

Chapter 5   References

Allcock M C and Wdowczyk J., 1972, Nuovo Cimento $\underline{9}$, 315

Gould R J and Schreder G P., 1966, Phys Rev Lett $\underline{16}$, 252

                                     1967a, Phys. Rev. $\underline{155}$, 1404

                                     1967b, Phys. Rev. $\underline{155}$, 1408

Jauch J M and Rohrlich F., 1955, 'The Theory of Photons and Electrons',

    (Addison-Wesley, Camb, Mass)

Jelley J V., 1966, Phys. Rev. Lett. $\underline{16}$, 479

Nikishov A I., 1962, Sov. Phys. JETP, $\underline{14}$, 393

Chapter 6.   The Electromagnetic Background Radiation - a survey

of Observational and Theoretical aspects.

6.1 Introduction.

The previous Chapters have discussed the physics of the interactions
of cosmic-rays and gamma-rays with the electromagnetic radiation fields
which may exist in extragalactic space. It is therefore important to
discuss the observational evidence, where it is available, for such
background radiation, and to examine theoretical ideas on the background
where it has not yet been observed. In fact, evidence for a cosmic
photon flux only exists in the radio and microwave regions of the spect-
rum - shortwards of 1mm only upper limits are available. The radio
background longward of about 10 cm is not of interest in the present
work, so we shall discuss first the microwave region (10 cm - 1mm),
then the far-infrared (around 100 microns), and finally the near infra-
red, optical and ultraviolet bands (10 microns - 100 Å). Experimental
and theoretical fluxes are summarized in Fig 6-1.

6.2   The Microwave Background.

Observations.

The first evidence for a large isotropic microwave flux was found
by Penzias and Wilson (1965), at a wavelength of 7.35 cm. Their result
corresponded to a blackbody temperature of 3.0 ± 1.0 K. Subsequently
many more ground-based experiments have confirmed that the spectrum is
blackbody in form, with T near 2.7K, up to a wavelength of 3.3 mm, roughly
the peak in the Planck spectrum. The departure from the Rayleigh-Jeans
part of the spectrum (for which $i_\nu \propto \nu^2$) is shown in the shortest
wavelength results at 3.3 mm by Boynton et al. (1968) and Millea et al.
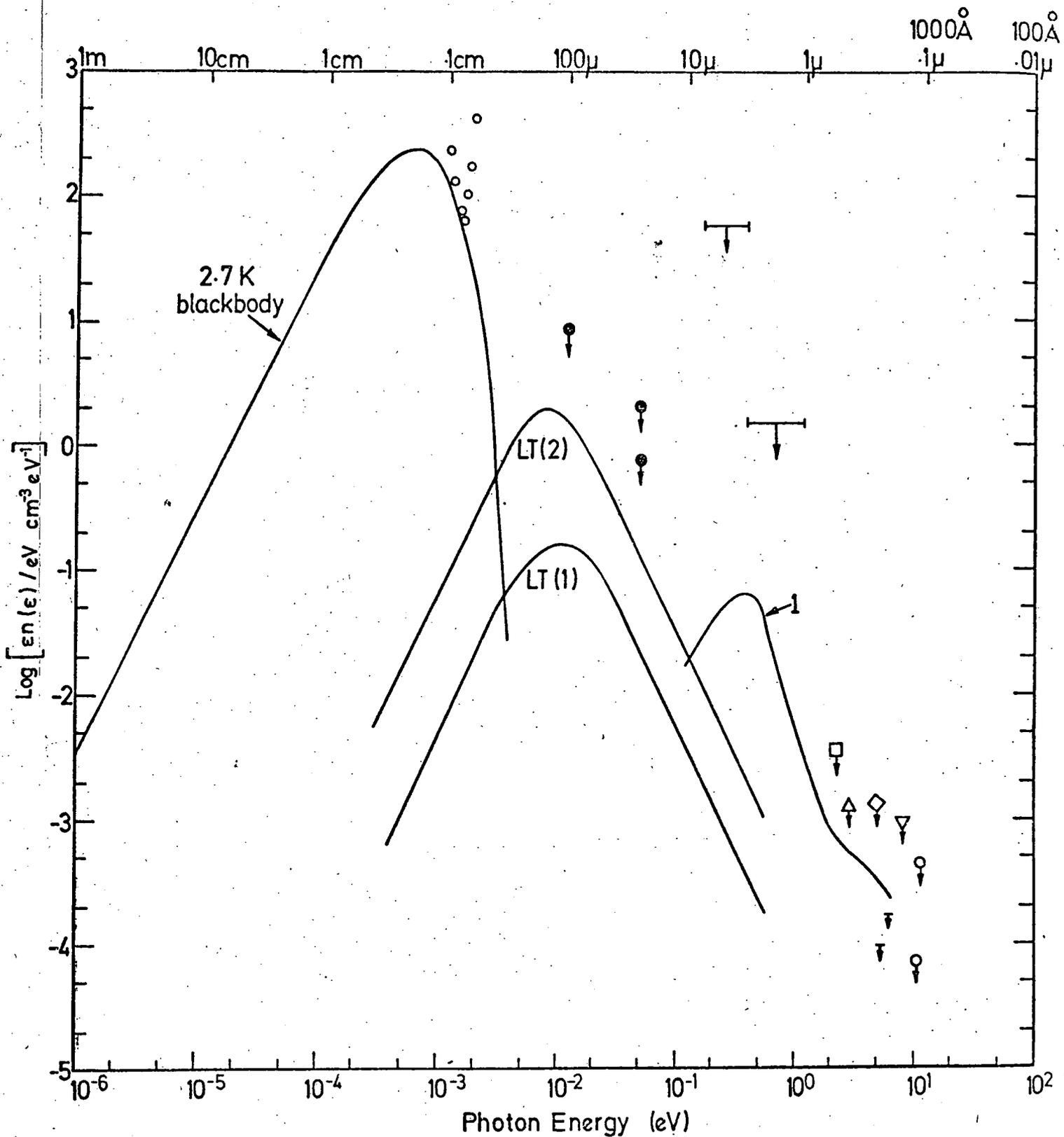
Fig 6-1

Summary of experimental and theoretical fluxes for the integrated back-
ground radiation.

Lillie (1972) Kurt and Sunyaev (1967) Roach and Smith (1968)

Sudbury and Ingham (1970) Harwit et al. (1966) Lillie (1969)

McNutt and Feldman (1970) (see also Peebles 1971) ∇ Hayakawa et al (1969)

LT(1) and LT(2) - possible contributions from Seyfert galaxies,
from Low and Tucker (1968).   1 - model 1 of Tinsley (1973).

A 2.7 K blackbody spectrum is also shown, with recent results by
Robson et al. (1975) in the millimetre band (o o o o).

(1971). At shorter wavelengths, ground-based observations are not poss-
ible because of the absence of sufficiently transparent atmospheric
windows, and it is necessary to use either detectors on balloons and
rockets, or the indirect method of interstellar molecular absorption
lines. Bortolot et al. (1969) obtained T = 2.83 ± 0.15 K at 2.64mm ,
using CN absorption lines in ʃ Ophiuchi. Other results from this method
have so far given only rather high upper limits, but which limit the
possible blackbody temperature to 4.7K at 1.3 mm, 5.4 K at .56 mm and
8.1 K at .36mm (Bortolot et al. 1969).

Direct Helium-cooled-radiometer measurements above the atmos-
phere have been made from rockets (Cornell-NRL group, Pipher et al.
1971, and the LASL group, Blair et al. 1971) and from balloons (MIT
group, Muehlner and Weiss, 1970). Fluxes well above the expected
Planck extrapolation from lower energies were reported by the Cornell
and MIT groups. The situation has been reviewed by Thaddeus (1972). The
MIT group found a high flux near 1 mm suggesting a strong spectral line
feature superimposed on the blackbody radiation, but further balloon
flights failed to confirm this line (Muehlner and Weiss, 1972). The
Cornell experiment gave a flux corresponding to $2 \ 10^3 \ cm^{-3}$ (in the units
of Fig 6-1) in the 1.3 - 0.44 mm band. However, the LASL rocket experi-
ment obtained a result equivalent to a temperature $T = 3.1 \ ^{+0.5}_{-2.0}$ in the 6-
0.8 mm range. This would only be consistent with the Cornell result if
there were a strong background radiation confined to the region 0.44-
0.8 mm. Recent results by Robson et al. (1974) using a balloon-borne
cooled polarizing Michelson interferometer,are consistent with T = 2.7K
in the range 3 - 0.8 mm, and in fact lie very near this curve at 0.8 mm.

At the present time therefore there is good reason to adopt a
2.7K blackbody spectrum at least up to 8mm ($2 \ 10^{-3}$ eV), and no confirm-

ation of reported high fluxes at shorter wavelengths.

Theoretical aspects of the blackbody radiation.

The existence of a blackbody background was first suggested by Gamow (1948) as a consequence of the physical conditions in the hot early universe. At early epochs, the energy density of the universe was dominated by radiation, since radiation density $\rho_r \propto R^{-4}$ whereas matter density $\rho_m \propto R^{-3}$, where R is the scale factor for the universe (see Chapter 2). For this reason, the expansion rate at early epochs is independent of the cosmological parameters (e.g. the matter density), and in fact the radiation temperature T can easily be shown to be $T = 1.5 \; 10^{10} \; t^{-\frac{1}{2}}$. If it is assumed that Helium is primordial (and obsevations of the oldest stars seem to support this view), then it was built up by a series of reactions starting with $n + p \rightarrow d + \gamma$. Above $T = 10^9$ K, the blackbody photons have sufficiently high energy to destroy the deuterium by the reverse of this reaction, so that deuterium (and hence helium) does not accumulate until the temperature drops below this value. The relation between T and t given above shows that this point is reached about 200 seconds after the 'big bang'. Since the present helium abundance is about 30% by mass, a significant part of the total hydrogen content of the universe must have been converted to helium in a time comparable to 10^2 seconds (the reaction rates fall rapidly in the expanding universe, so most of the production occurs soon after the $n(p,d)\gamma$ reaction becomes irreversible). This implies that $\sigma \; n(t) \; vt \sim 1$, where σ is the cross-section for the $n(p,d)\gamma$ reaction, and v is the mean thermal velocity of the nucleons. From this relation , we find $n \sim 10^{18}$ cm^{-3} when t = 200 sec corresponding to $T = 10^9$ K. Then using $n \propto R^{-3} \propto T^3$ we get T = 5K for $n = 10^{-7}$ cm^{-3}, roughly the density of matter observed at the present time. This simple treatment, due to Gamow (1948), gives a temperature close to that observed.

The form of the spectrum is expected to be blackbody because at very early epochs ($T > 10^{10}$ K) all the constituents of the universe (protons, neutrons, electrons, neutrinos and radiation) are in thermal equilibrium. Matter and radiation are coupled by the reaction $e^+ + e^- \rightleftharpoons \gamma + \gamma$ at these temperatures, and by Thompson scattering at lower temperatures until $T \lesssim 3000$ K, when the cosmic plasma recombines to form neutral hydrogen and the coupling ceases. Although the radiation and matter are not in equilibrium during the Thompson scattering phase(the different expansion characteristics mentioned above cause a flow of energy from the radiation to the gas) the departure from an equlibrium spectrum is very small (Peebles, 1971).

6.3 The Far Infrared region ($10\mu - 100\mu$)

Observations of the background in the far IR are confined to upper limits from rocket experiments by McNutt and Feldman (1970) at 100μ and by the same group at 24μ (see Peebles, 1971a). These limits are shown in Fig 6-1. In the absence of observational data, the background in this region must be estimated from our knowledge of the output of discrete sources.

Observations of extragalactic sources have revealed large IR fluxes from the nuclei of Seyfert galaxies and from quasars, the energy output in the IR often exceeding that at all other wavelengths. A typical Seyfert galaxy, NGC 1068, emits about 10^{45} erg s^{-1} in the IR compared to about 10^{41-42} erg s^{-1} in the IR from the nucleus of our own Galaxy. We would therefore expect a significant contribution from Seyferts to the IR background, and possible spectra have been estimated by Low and Tucker (1968). They use the mean emission spectrum from 5 Seyferts observed by Kleinmann and Low (1970), and consider models in which there

is evolution of sources with epoch similar to that of the powerful radio sources (as discussed in Chapter 1) as well as non-evolving cases. Seyferts are taken to constitute 1% of all galaxies, giving a number density of 2 10^{-77} cm^{-3}. The resulting backgrounds for the extreme models are shown in Fig 6-1. Both are well inside the limits set by McNutt and Feldman, but near enough for the limits to be of interest. It is possible that the models give an overestimate of the intensities, since the sample of Seyferts includes NGC 1275 and 3C120, both of which are two orders of magnitude brighter in the radio than most Seyferts and are also the most important contributors to the average IR flux used. However, Low and Tucker suggest that their results may not be unreasonable because (i) all the IR luminosities lie within a factor of 10 of the average and (ii) the radio emission from Seyferts comes mainly from the halo while the IR comes from the nuclear regions, and the two are not necessarily correlated.

6.4 Near-IR, Optical and UV backgrounds.

Observations.

Rocket experiments by Harwit et al. (1966) give upper limits in the 1 - 10 μ range, but these are too high to be of very much interest. In the optical region (3000$\overset{\circ}{A}$ - 10,000$\overset{\circ}{A}$) limits have been obtained in ground-based, rocket and satellite experiments. All require correction for the zodiacal light (sunlight scattered from interplanetary dust) and for Galactic light, and are therefore limited by the accuracy of models for these sources. Roach and Smith (1968) carried out ground-based observations which gave an upper limit after the corrections of 5 tenth-magnitude stars per square degree at 5500$\overset{\circ}{A}$, this being only about 1% of the background from non-cosmic sources. Rocket

results by Lillie (1969) at 4100Å gave a similar limit, as shown in Fig 6-1.

In the UV, the Galactic starlight spectrum falls rapidly, so that the separation of the extragalactic component of the cosmic flux is easier, but solar Lyα re-emitted by hydrogen in the Solar System makes the sky very bright in this region. Hence only upper limits have been obtained. Measurements with gas-filled couters on the USSR spacecraft Venus (Kurt and Sunyaev, 1967) gave limits between 1050 and 1340Å. A rocket experiment by Hayakawa et al.(1969)gave a limit in the 1350-1480Å range. Sudbury and Ingham (1970) mapped the Milky Way at 2500Å using a rocket-borne detector, and also obtained a limit on the starlight background at this wavelength. The most recent results are from the UV telescope on the OAC-2 satellite (Lille, 1972) ; the limits obtained at 2000 and 2360Å are an order of magnitude below those from the earlier rocket experiments.

Beyond the Lyα limit (912Å), which is inaccessible to direct observation because of ionization absorption in interstellar gas, significant limits can nevertheless be obtained from the observation of neutral hydrogen around galaxies. The neutral gaseous disc of M31, which is shielded from the UV background by a layer of ionized gas, can be used to derive an upper limit of $6 \ 10^{-7} \ cm^{-3}$ between 300 and 912Å (Sunyaev, 1969). This is more than two orders of magnitude below the direct observational limits set just below the Lyman limit.

Theoretical predictions in the near-IR, optical and UV.

A rough estimate of the expected energy density of starlight in the optical region from normal galaxies is easily made. The present luminosity of galaxies per unit volume has been calculated by

Oort (1958), van den Bergh (1961), Kiang (1961) and Davidson and Narlikar (1969). All these authors give values agreeing within about 50%, and we will take that from Davidson and Narlikar, viz. $2.8 \ 10^8 L_\odot$ $Mpc^{-3} = 3.2 \ 10^{-32} \ erg \ s^{-1} \ cm^{-3}$. The expected starlight density assuming that galaxies have been emitting for the Hubble time is roughly

$$w_{ph} = \frac{3.2 \ 10^{-32}}{1.6 \ 10^{-12}} \cdot 6 \ 10^{17} sec \sim 10^{-2} \ eV \ cm^{-3}$$

Davidson and Narlikar calculate the value for various cosmological models, and obtain results which are all within a factor of 2 of $3 \ 10^{-3}$ $eV \ cm^{-3}$. Reference to Fig 6-1 shows that this is of the same order as the present upper limits in the optical region.

Any improvement on such estimates must involve models for the evolution of galaxies as well as the cosmological model, the former being the dominating factor. Early calculations by Whitrow and Yallop (1963,1965) used a 6000K emission spectrum, and either no evolution or a time-dependent temperature without any theoretical basis. An attempt to obtain a better estimate was made by Partridge and Peebles (1967), using models of Galactic evolution based on stellar birth-rate functions for our own Galaxy. The models were designed to give a 30% conversion of hydrogen to helium in stars (helium was assumed not to be primordial), and hence the models have very high luminosity in their early stages. The epoch of galaxy formation was taken to be $1.5 \ 10^8$ years on the basis of a gravitational instability model for galaxy formation. This corresponds to redshifts $z \sim 10 - 30$ depending on the cosmological model. It is now generally believed that Helium is primordial in origin, and hence the predictions of this model are probably too high. Fig 6-2 shows the most probable spectrum according to Partridge and Peebles.

The most comprehensive treatment of the problem has been made by Tinsley (1973). She has developed models of the evolution of elliptical
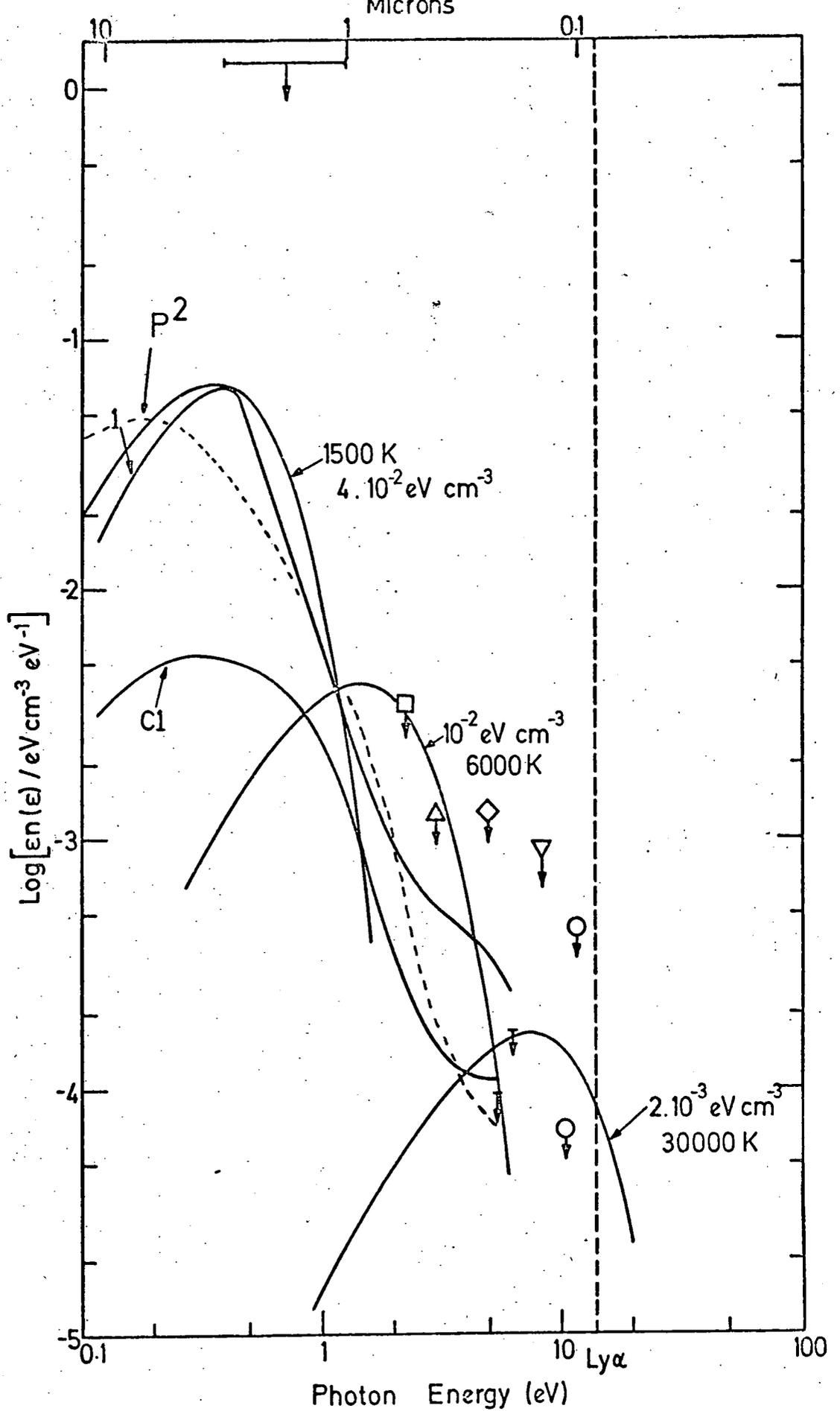
Fig 6-2   Theoretical spectra for starlight background.
Experimental points as in Fig 6-1.

P^2 - predicted spectrum from Partridge and Peebles
(1967), models 2 and 5.

c1,1 - Tinsley (1973) models, without and with
galactic evolution respectively.

and spiral galaxies which give a good representation of their colours and luminosities at the present epoch. The method adopted in computing the integrated background emission was to use the observed spectra for the various types of galaxy at the present time together with the models for evolution in each spectral region. Ground-based observational data on induvidual galaxies are available in the 3400Å -3.4 μ range. Beyond 3.4 μ, a Rayleigh-Jeans extrapolation was used, thus excluding the contribution from bright IR sources. For the 912-3400Å range, recent results from OAO-2 (Code et al. 1972) were used. These indicate large UV fluxes from elliptical galaxies due to the presence of hot, young stars. For E galaxies, the model used gives an initally high luminosity, falling off with a timescale of 10^8 years. The spiral models reach a maximum luminosity at around 10^8 years before starting to fade. Initially the UV component is very strong in all the models due to the young stars which are formed soon after the galaxy condenses. The Sa spiral models are based on M31, and the Sc models on M33. Owing to the dominance of the hot young stars in the initial luminosity function, all the final background spectra resemble a greybody at 1-3 10^4 K redshifted back to z = 0 from the epoch of formation, taken as 1.3 - 2.6 10^8 years.

For comparison, a model (c1) with no evolution was also computed by Tinsley. The evolutionary models show little variation with the cosmological parameters H_o and q_o. Fig 6-2 shows model c1 and model 1, in which H_o = 100 km s^{-1} Mpc^{-1} and q_o = .02, and formation redshifts of 35 for E galaxies and 20 for spirals. Also shown are greybody spectra with T = 1500K, w_{ph} = 4 10^{-2} eV cm^{-3} , T = 6000K, w_{ph} = 10^{-2}

eV cm^{-3}, and T = 30,000K , w_{ph} = 2 10^{-3} eV cm^{-3}. The combination

of the 1500K and 30,000K curves give a reasonable representation of

the Tinsley model 1, and these parameters were adopted for use in the

later treatment of the gamma-ray spectrum. Development of the spectra

with redshift was approximated by redshifting the 1500K spectrum

back from z = 0 in the usual way, while leaving the 30,000K spectrum

constant since it represents the contribution from contemporary hot

stars at any particular time.

Chapter 6. References.

Blair A G et al., 1971, Phys. Rev. Lett. $\underline{27}$, 1154

Bortolot V J Jr, Clauser J F and Thaddeus P., 1969, Phys. Rev. Lett. $\underline{22}$, 307

Boynton P E, Stokes R A, and Wilkinson D T., 1968, Phys. Rev. Lett. $\underline{21}$, 462

Code A D, Welch G A and Page T L., 1972, Scientific Results from the Orbiting Astronomical Observatory, NASA, 541

Davidson W and Narlikar J V, 1969, in 'Astrophysics' reprint volume from Rep. Prog. Phys. (Benjamin) 59

Gamow G., 1948, Phys. Rev. $\underline{74}$, 505

Harwit M, McNutt D P, Shivanandan K and Zajac B J., 1966, Astron. J. $\underline{71}$, 1026

Hayakawa S, Yamashito K and Yohioka S., 1969, Ap. Sp. Sci. $\underline{5}$, 493

Kiang T., 1961, Mon. Not. Roy. Astr. Soc. $\underline{122}$, 263

Kleinmann D E and Low F J, 1970, Ap. J. $\underline{159}$, L165

Kurt B G and Sunyaev R A., 1967, Astron. J. $\underline{44}$, 1157

Lillie C F., 1969, Bull. Amer. Astr. Soc. $\underline{1}$, 132

Lillie C F., 1972, Scientific Results from the Orbiting Astronomical Observatory, NASA,

Low F J and Tucker W H., 1968, Phys. Rev. Lett. $\underline{21}$, 1538

McNutt D P and Feldmann P D, 1970, J. Geophys. Res. $\underline{74}$, 4791

Millea M F, McColl M, Pederson R J and Vernon F L Jr., 1971, Phys. Rev. Lett. $\underline{26}$, 919

Muehlner D and Weiss R., 1972, referred to in Thaddeus (1972)

Oort J H., 1958, 11th Solvay Conf, Brussels (ed. R. Stoops), 163

Partridge R B and Peebles P J E., 1967, Ap. J. $\underline{148}$, 377

Peebles P J E, 1971a, 'Physical Cosmology' (Princeton)

Peebles P J E, 1971b, Comm. Astrophys. Sp. Sci. $\underline{3}$, 20

Penzias A A and Wilson R W., 1965, Ap. J. 142, 419

Pipher J L, Houck J R, Jones B W and Harwit M., 1971, Nature 231, 375

Roach F E and Smith LL., 1968, Geophys. J. 15, 227

Robson E I, Vickers D G, Huizinga J S, Beckmann J E and Clegg P E.,

1974, Nature, in press.

Sudbury G C and Ingham M F., 1970, Nature 226, 526

Sunyaev R A., 1969, Ap. Lett. 3, 33

Thaddeus P., 1972, Ann. Rev. Astr. Astrophys. 10, 305

Tinsley B M., 1973, Astr. Astrophys. 24, 89

Van den Bergh S., 1961, Z. Astrophys. 53, 219

Chapter 7. The Gamma-ray spectrum in the Hillas Model : semianalytical

        solutions.

7.1 Introduction.

The development of the gamma-ray spectrum in the Hillas model

involves an electron-photon cascade in an expanding Universe in which

reaction-rates, interaction lengths and energy transfers are varying

functions of time. It is this variation, due to the changing black-

body radiation temperature, which introduces some complexity into the

calculation of the expected spectrum at the present time. In Chapter 8,

a numerical method is described which explicitly follows the cascade as

function of redshift; however, by making simplifying assumptions, a

reasonable approximation to the spectrum can be obtained, with consequ-

ent better understanding of the important features of its production.

The processes involved in the production of the spectrum are,

firstly, the pair-production of electrons by high energy protons on

the blackbody radiation (PC process), followed by an ICS - PP cascade.

This cascade is maintained by the blackbody radiation until the gamma-

ray energies are no longer high enough for PP on microwave photons;

instead, PP may now occur on the much lower density starlight background

which maintains the cascade until gamma-ray energies fall below about

10^{11} eV. There is thus a buildup of photons with energies $< 10^{11}$ eV

which do not interact again, and these form the final gamma-ray spectrum.

The important features of the various stages will now be discussed ,

leading to the simplifying assumptions which are then used in the

approximate solutions.

7.2 Pair-production by protons in the Blackbody radiation (PC).

This process was treated in detail in Chapter 3. At $z = 0$, the attenuation length for protons well above threshold for PC (i.e. $E_p \sim$ 10^{19}eV) is , from Fig 3-5, about $4 \ 10^{27}$ cm. At any other z, the rate of attenuation is given by $\Delta z = (1/E \ dE/dz)$ where (see Sec 2-3)

$$\Delta z = \left[\frac{cH_o^{-1} \ (1+z)^3}{\lambda_{PC}(1+z)^2(1+2q_o z)^{\frac{1}{2}}} \right]^{-1} = \frac{\lambda_{PC}}{1.9 \ 10^{28} \ (1+z)^{\frac{1}{2}}} \qquad (7.1)$$

for $H_o = 50$ km s^{-1} Mpc^{-1} and $q_o = \frac{1}{2}$. Thus for energies well above threshold, $\Delta z \sim 0.2(1+z)^{-\frac{1}{2}}$, so that attenuation occurs in a small interval of z, and it is a good approximation to assume that all the proton energy is lost to electrons at the same redshift as the protons are produced. At lower energies, the situation is not so simple, since Δz becomes larger, and more of the energy losses occur at smaller z. Since the energy input to protons per logarithmic energy interval is $\propto E^{-(\gamma-2)} = E^{-0.5}$, these lower energy protons will be the major contributors to energy in electron pairs. However, when Δz approaches z_m, the protons lose a large part of their energy by redshifting, so that it does not appear as electron pairs. Fig 7-1 shows Δz as a function of E_p for $z = 0$ and $z = 14$, derived from Fig 2-1 and eq.(7.1). Fig 7-2 shows the same quantity as a function of z for constant E_p, as well as the value $\Delta z = 1+z$ corresponding to redshift losses. It can be seen that whenever the PC losses predominate over redshift losses, Δz falls rapidly with increasing z, and the change in z required for a proton to lose most of its energy is about $\delta z \sim 3$ at most. Since this is small compared to z_m, where most of the energy is injected, it is a good enough approximation to assume all the proton energy loss by PC to occur at the redshift of proton production.
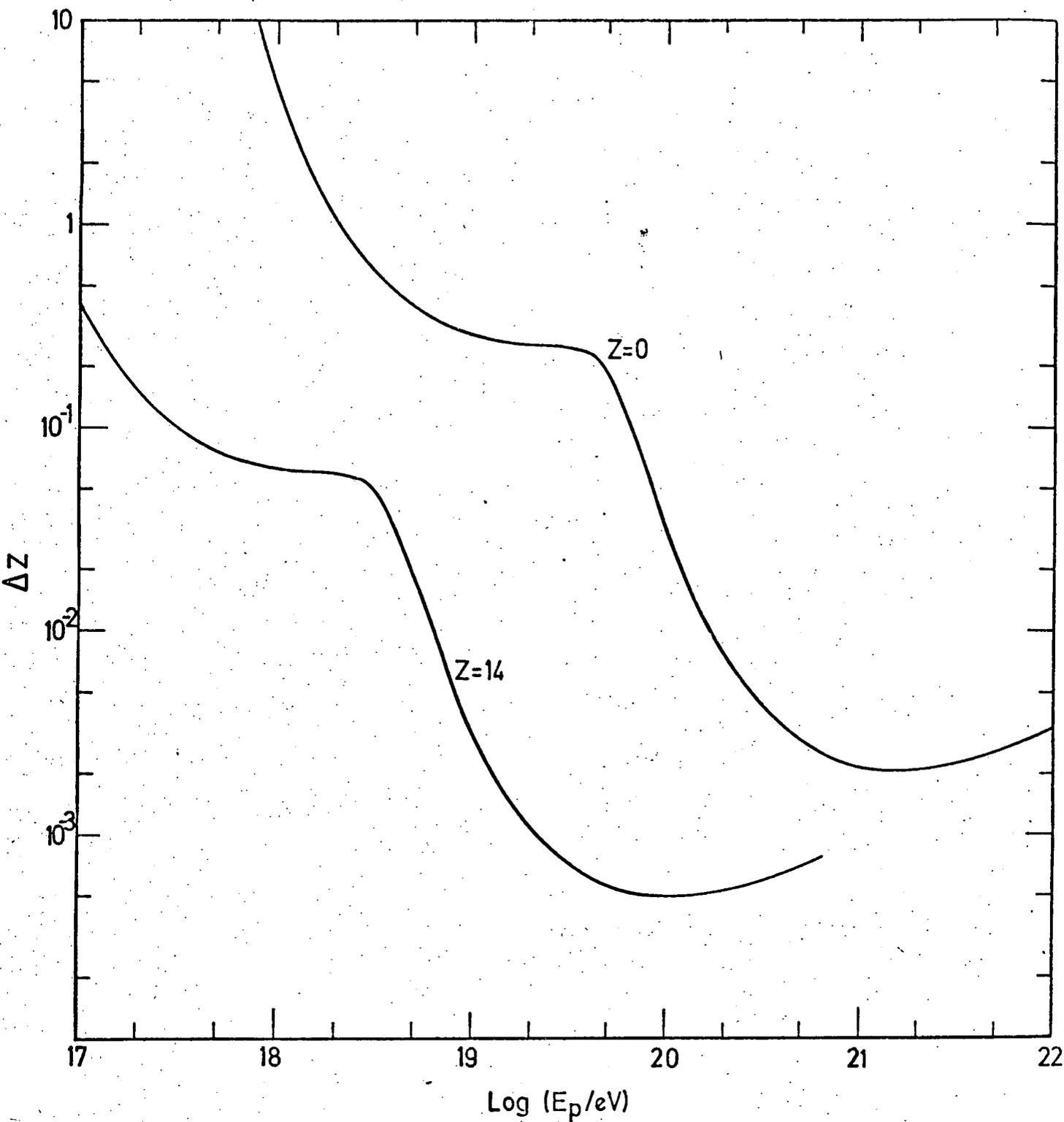
__Fig 7-1__

Proton attenuation lengths expressed in terms of redshift,

$$\Delta z = \left[\frac{1}{E}\frac{dE}{dz}\right]^{-1} \quad , \text{ for the case } H_o = 50 \text{ km s}^{-1} \text{ Mpc}^{-1}, \ q_o = \tfrac{1}{2},$$

and z = 0 and z = 14.

$\Delta z = 1 \div z$

$5.10^{16}\,eV$

$E_p = 10^{17}\,eV$

$10^{18}\,eV$

REDSHIFT Z
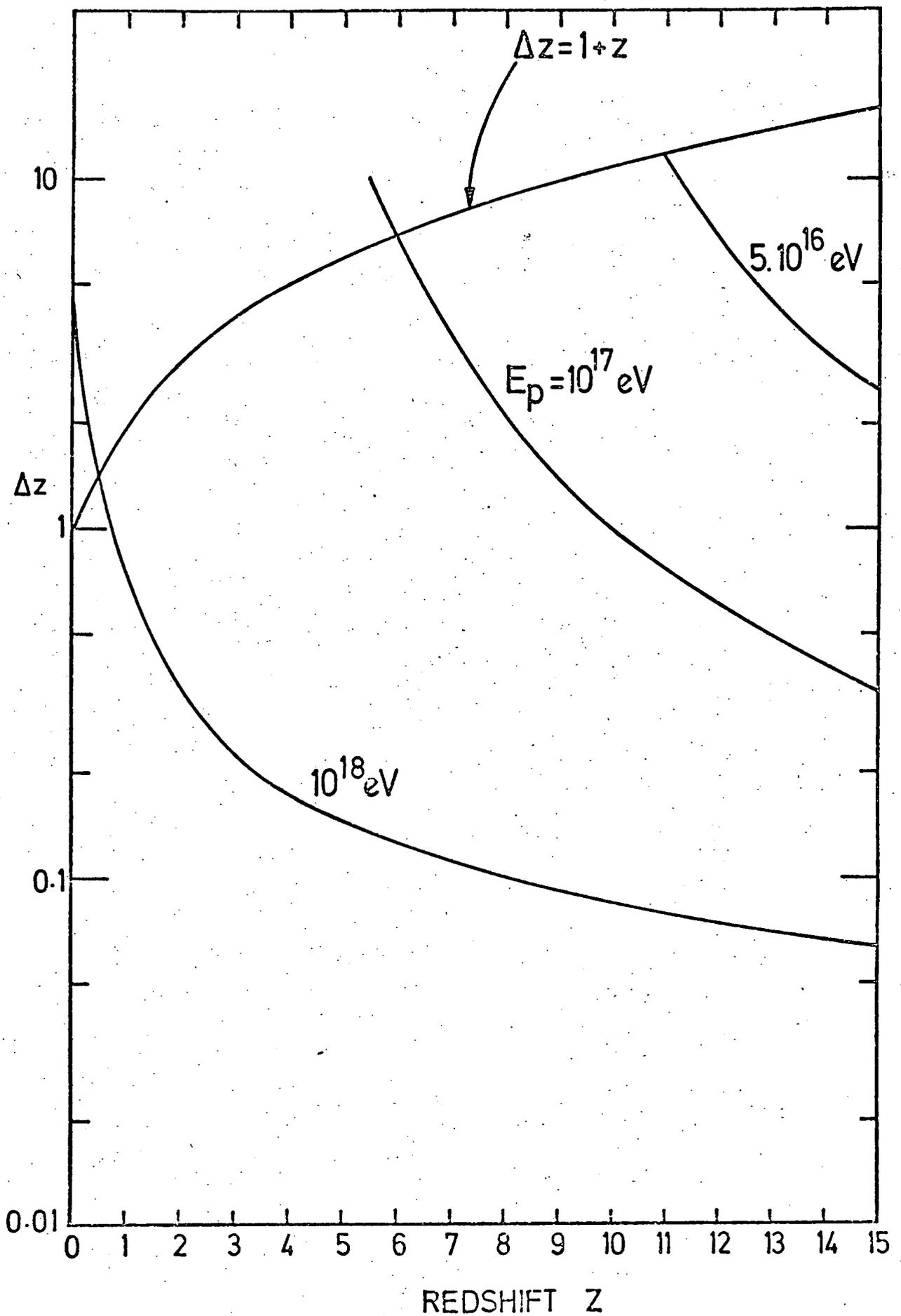
Fig 7-2

Δz as a function of z for various proton energies, for $H_o = 50$ km s^{-1} Mpc^{-1} , $q_o = \frac{1}{2}$.

The energy spectrum of electrons from various proton energies is shown in Figs 3-3 and 3-4. The latter shows how the energy is distributed, as explained in Sec.3-5, and since in these curves there is symmetry about the maxima, the maximum also gives the mean energy of electrons (weighted according to energy content rather than number of electrons). Near the threshold, the mean electron energy is $5\ 10^{14}$ eV for $T = 2.7K$, as expected, since for electrons produced at rest in the proton frame

$$E_e = m_e/M_p \cdot E_p = 10^{18}eV/2000 = 5\ 10^{14}\ eV \qquad (7.2)$$

Since $E_{p,th} \propto (1+z)^{-1}$, $E_e \sim 5\ 10^{14}/(1+z)$ eV near threshold. In the approximate treatment of the spectrum, all electrons were assumed to be produced with $E_e = 10^{15}/(1+z)$ eV. The justification for this procedure is that since the energy input to protons falls off as $E_p^{-0.5}$, most of the electrons will be produced by electrons near or rather above the threshold energy.

7-3 : Inverse Compton Scattering.

The mean energy transfer to photons in ICS on a 2.7K radiation field is shown in Fig 4-5. For other temperatures, the value of $\overline{v}_{ICS}$ is given by

$$\overline{v}_{ICS}\ (E_e\ ,T) = \overline{v}_{ICS}\ (E_e T/T_o\ ,T_o) \qquad (7.3)$$

For $E_e < 10^{13}/(1+z)$, the approximation (from eq.4.27)

$$\overline{v}_{ICS} = 3.2\ 10^{-15}\ (E_e/eV)\ T/T_o \qquad (7.4)$$

is applicable. Above this energy, the approximation becomes inaccurate, and the computed curve of Fig 4-5 must be used.

Reference to Fig 4-4 shows that the interaction length for electrons on the blackbody radiation is always $\ll cH_o^{-1}$ for electrons in the energy range of interest. The same is true of the attenuation lengths Λ_{ICS}. At the high energy end of Fig 4-4, $\Lambda_{ICS} \sim \lambda_{ICS} \ll cH_o^{-1}$.

For the low energy end, consider electrons of energy 10^{10} eV, producing (for z = 0) gamma-rays of energy about $3 \cdot 10^5$ eV, about the lowest energy of interest here. In this case, $\bar{v}_{ICS} = 3.10^{-5}$ and hence $\Lambda_{ICS} = \lambda_{ICS} / \bar{v}_{ICS}$ $\sim 4.10^{21}/3.10^{-5} \sim 10^{26}$ cm , a value still $\ll cH_o^{-1}$. It can therefore always be safely assumed that ICS is a 'point process', i.e., the electron converts all its energy into gamma-rays at the same time as the electron is created.

Spectrum generated by ICS from a single electron.

Since each electron loses effectively all of its energy to gamma-rays in a short time, as shown above, it is convenient to calculate the spectrum of gamma-rays resulting from the conversion of all of the electron energy via ICS. This is easily done provided the energy loss process can be treated as continuous (this is not valid for $E_e > 5 \cdot 10^{14}/(1+z)$, when $\bar{v}_{ICS} > 0.3$). Then by conservation of energy, as the electron loses energy dE_e , the gamma-ray spectrum between E_γ and $E_\gamma + dE_\gamma$ is formed according to

$$dE_e = \frac{4\pi}{c} j(E_\gamma) E_\gamma dE_\gamma$$
$$j(E_\gamma) = \frac{c}{4\pi} \frac{1}{E_\gamma} \frac{dE_e}{dE_\gamma} \qquad (7.5)$$

where $E_\gamma = E_e \bar{v}_{ICS}(E_e)$. Equation (7.5) is conveniently written

$$j(E_\gamma) = \frac{4\pi}{c} \frac{1}{\bar{v}(E_e) E_\gamma} \frac{d \ln E_e}{d \ln E_\gamma} \qquad (7.6)$$

In the low energy approximation, writing $E_\gamma = K E_e^2$ (from eq. 4.27), we have

$$j(E_\gamma) = \frac{c}{4\pi} \frac{E_\gamma^{-3/2}}{2\sqrt{K}} \qquad (7.7)$$

The photon spectrum produced by an electron spectrum $j(E_e)$ is

$$j(E_\gamma) = \frac{j(> E_e)}{\bar{v}_{ICS}(E_e) E_\gamma} \frac{d \ln E_e}{d \ln E_\gamma} \qquad (7.8)$$

where $E_\gamma = E_e \bar{v}_{ICS}(E_e)$ and $j(> E_e)$ is the integral form of $j(E_e)$.

The function $d \ln E_e / d \ln E_\gamma$ is shown in Fig 7-3 for $z = 0$, approximated by two straight lines on a log-linear plot which were found to represent well the values of the derivative obtained from Fig 4-5. At other redshifts, the curve must be read at energy $E_\gamma/(1+z)$.

7.4 Pair-production in photon-photon collisions.(PP)

For this process we must distinguish between interactions with the blackbody radiation and those with starlight photons. The first process has a threshold for gamma-ray energy $10^{14}/(1+z)$, and the interaction length as a function of energy is shown in Fig 5-3. Above the threshold the interaction length is much less than cH_o^{-1}, and therefore it is a good approximation to treat PP on the blackbody radiation as a point process. The variation of mean energy transfer $\bar{v}_{PP}$ to the higher energy electron is shown in Fig 5-4 ; near the threshold the energy of the gamma-ray is divided almost equally between the two electrons. In the approximate treatment, this was assumed to be the case for all gamma-ray energies. The justification for this is that for a steeply falling gamma spectrum, most of the interactions producing a given electron energy will occur near threshold.

The interaction lengths for PP on starlight are subject to the large uncertainties in the spectrum of extragalactic starlight. Theoretical and experimental work on this subject has been discussed in Ch. 6 and Fig 6-2 showns possible spectra for $z = 0$. The corresponding interaction lengths for PP for the various greybody spectra shown in Fig 6-2 to represent the possible starlight spectra, are plotted in Fig 7-4. This was derived from the curve for $T = 2.7K$ shown in Fig 5-3 . There is a large spread in the possible interaction lengths, and also uncert-
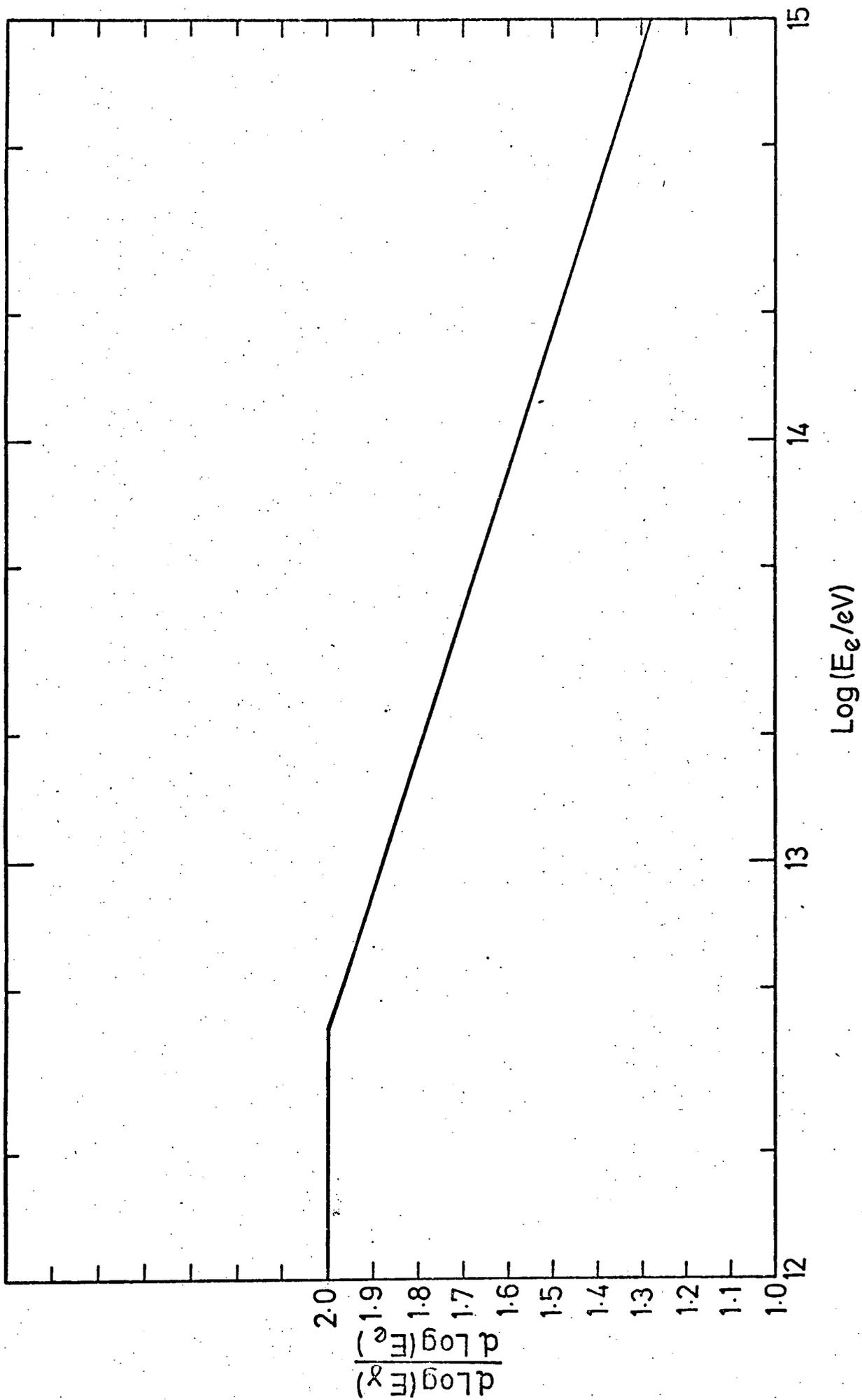
Fig 7-3   The function $\dfrac{d \,(\log \overline{E_e})}{d \,(\log E_\gamma)}$ for ICS, derived from the function $\overline{v}_{ICS}$ given in Fig 4-5.
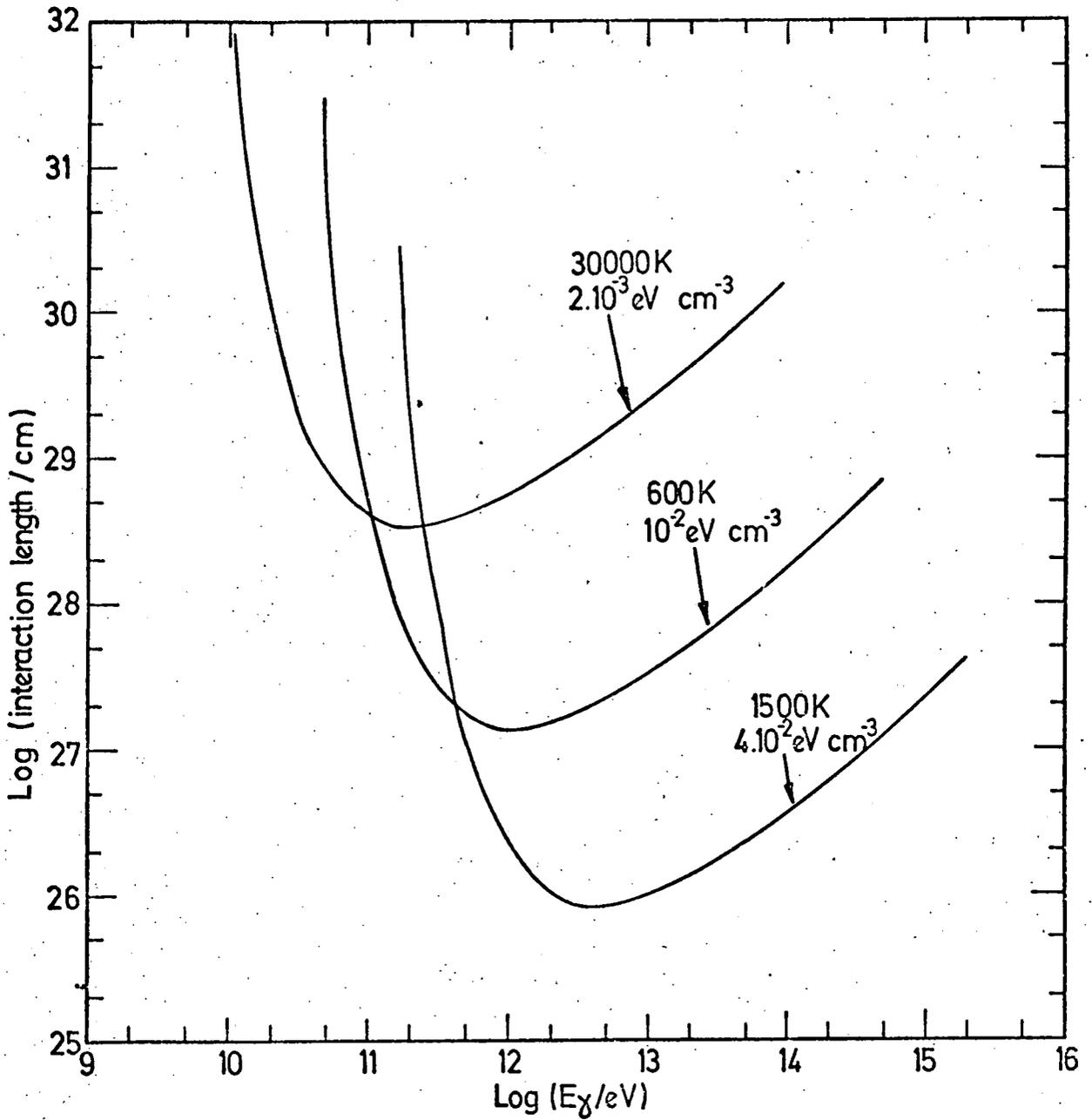
Fig 7-4

Interaction lengths for photons for γ-γ interactions
in the greybody radiation fields shown in Fig 6-2.

ainty in the epoch at which the starlight was produced. If it was emitted at early epochs (z~15) and has a spectrum similar to Tinsley's (1973) model 1, (corresponding roughly to T = 1500K, w = 4.10^{-2} eV cm^{-3} at z = 0), then the interaction length is small enough to allow pair-production by PP to be treated as a 'point process'. If, on the other hand, starlight production occurs later, or has an energy density much less than the Tinsley model 1, then PP on starlight will only occur on scales ~ cH_o^{-1}~10^{28} cm. In view of the uncertainties in the model, two treatments, A and B, representing the extreme situations described above, were developed. Comparison of the resulting spectra of gamma-rays then gives an indication of the sensitivity of the spectrum to the assumptions of the model. These two treatments will now be described in turn.

7.5   Treatment A.

The interaction length for PP on starlight is assumed to be small for all gamma-ray energies greater than a minimum, $E_{\gamma,th}$. Below this energy, it is assumed that no further interactions of photons occur, and energy is lost by redshift only. $E_{\gamma,th}$ was taken as redshift independent, and a value $E_{\gamma,th}$ = 10^{11}eV was taken as representative. Fig 7-4 shows that at this energy, λ_{PP}~10^{28} cm for the 6000K (w = 10^{-2} eV cm^{-3}) starlight field, and falls to a minimum of about 10^{27} cm at higher energies, so that the assumptions described above do approximately represent this starlight model. For lower energy starlight fields, $\lambda_{PP} \gtrsim 10^{28}$ cm for all gamma-ray energies, so that the approximation will not be valid.

The procedure used was as follows:

i)   For each redshift , compute the gamma-ray spectrum $j_H(E)$ generated at this redshift by an electron of energy $10^{15}/(1+z)$ eV by ICS, using equation (7.8).

ii)   The part of $j_H(E)$ with $E_\gamma > E_{\gamma,th}$ undergoes PP on starlight. The

resulting spectrum is calculated from

$$j_{e1}(E_e) = 4j_{\gamma 1}(2E_e) \qquad\qquad E_e > 5 \; 10^{10} \text{ eV.}$$
$$= 0 \qquad\qquad\qquad E_e < 5 \; 10^{10} \text{ eV.} \qquad (7.9)$$

iii) The ICS gamma-ray spectrum from j_{e1} is obtained using eq.(7.8) :

$$j_{\gamma 2} = \frac{j_{e1}(> E_e)}{\overline{v}_{IC}(E_e)E_\gamma} \qquad \frac{d\ln E_e}{d\ln E_\gamma} \qquad\qquad (7.10)$$

where $E_\gamma = \overline{v}_{IC}(E_e)E_e$ for $E_\gamma > \frac{1}{2}E_{\gamma,th} \; \overline{v}_{IC}(\frac{1}{2}E_{\gamma,th})$ (7.11)

and $E_e = \frac{1}{2}E_{\gamma,th}$ for $E < \frac{1}{2}E_{\gamma,th} \; \overline{v}_{IC}(\frac{1}{2}E_{\gamma,th})$

iv) Steps (ii) and (iii) are repeated to obtain $j_{\gamma 3}$, $j_{\gamma 4}$ etc, until no gamma-rays remain with $E > E_{\gamma,th}$. The gamma-ray spectrum formed at z is then the sum $j_\gamma(E_\gamma, z) = \sum_n j_{\gamma,n}(E_\gamma, z)$.

v) The spectrum $\Delta j(E_\gamma, z)$ resulting from the redshifting of the spectrum formed at z back to z = 0 is given by

$$\Delta j_\gamma(E_\gamma, z) = (1+z)^2 j_\gamma(E_\gamma(1+z), z) \qquad\qquad (7.12)$$

for each 10^{15} eV of energy going into gamma-rays at z.

vi) The contributions from all z to the gamma-ray spectrum at z = 0 are summed, after weighting according to a factor giving the amount of energy going into electron pairs by PC per unit z. This energy, $\Delta E(z)$, is proportional to

$$\frac{(1+z)^\beta}{(1+z)^2(1+2q_0 z)^{\frac{1}{2}}} \int_{\frac{E_{p,th}}{1+z}}^{\infty} j(E_p) \left[E_p - \frac{E_{p,th}}{1+z} \right] dE_p \qquad\qquad (7.13)$$

For a power-law spectrum of protons $j(E_p) \propto E_p^{-\gamma}$,

$$\Delta E(z) \propto (1+z)^{\beta+\gamma-2}(1+z)^{-2}(1+2q_0 z)^{-\frac{1}{2}} \qquad\qquad (7.14)$$

Putting $\gamma = 2.5$, $\beta = 4.4$ and $q_0 = \frac{1}{2}$ gives $\Delta E(z) \propto (1+z)^{2.4}$. The final spectrum at z = 0 therefore has the form

$$j(E) = \frac{\int_0^{z_m} (1+z)^{2.4} \Delta j(E_\gamma, z) \, dz}{\int_0^{z_m} (1+z)^{2.4} \, dz} \qquad\qquad (7.15)$$

The spectrum is finally normalized to the total energy flux in gamma-rays, which is determined from the shape of the primary proton spectrum as described in Sec.2-8.

Results of Treatment A.

The procedure outlined above in steps (i)-(iii) was followed for $z = 0$ and $z = 9$. The development of the spectra is shown in Figs 7-5 and 7-6. Summation over $j_{\gamma,n}$ and redshifting to $z = 0$ as described in steps (iv) and (v) resulted in the spectra shown in Fig 7-7.

The following comments may be made on the features of the spectra of Fig 7-7.

1. Electrons are always produced with $E_e > E_{\gamma,th}/2 = 5 \ 10^{10}$ eV. Thus all electrons produce a spectrum of the form given in eq.(7.7) for gamma-ray energies below $5 \ 10^{10} \ \bar{v}_{ICS}(5 \ 10^{10} eV) = 8 \ 10^6$ eV. This result is independent of the reshift of electron production, since the gamma-ray energy after redshifting to $z = 0$ is, using eq.(7.4)

$$E_\gamma = 3.2 \ 10^{-15} E_e^2 \ (1+z)/(1+z) = 3.2 \ 10^{-15} E_e^2 \qquad (7.16)$$

Hence for $E_\gamma < 8 \ 10^6$ eV, the spectrum is a summation of curves of the form given in eq.(7.7), i.e. a power law with index -3/2.

2. The maximum energy in the contribution from z, $\Delta j(E_\gamma, z)$, occurs at $E_{\gamma,th}/(1+z)$, as a consequence of the assumption that gamma-rays interact if $E_\gamma > E_{\gamma,th}$ at z.

3. In the intermediate energy range $E_{\gamma,th}/(1+z) > E_\gamma > 8 \ 10^6$ eV, both the $z = 0$ and $z = 9$ curves are well approximated by a power law of exponent -1.93. Since, therefore, the shape of Δj in this energy range is insensitive to z, the spectrum contributed by any z can be estimated from $\Delta j(E_\gamma, z=0)$. It was found that $\Delta j(E_\gamma, z)$ was very nearly equal to

Fig 7-5 Development of γ-ray spectrum in Treatment A, for $z = 0$. Electrons injected with $E_e = 10^{15}$ eV. The electron and photon spectra are labelled e_1, e_2 and γ_1, γ_2 etc.
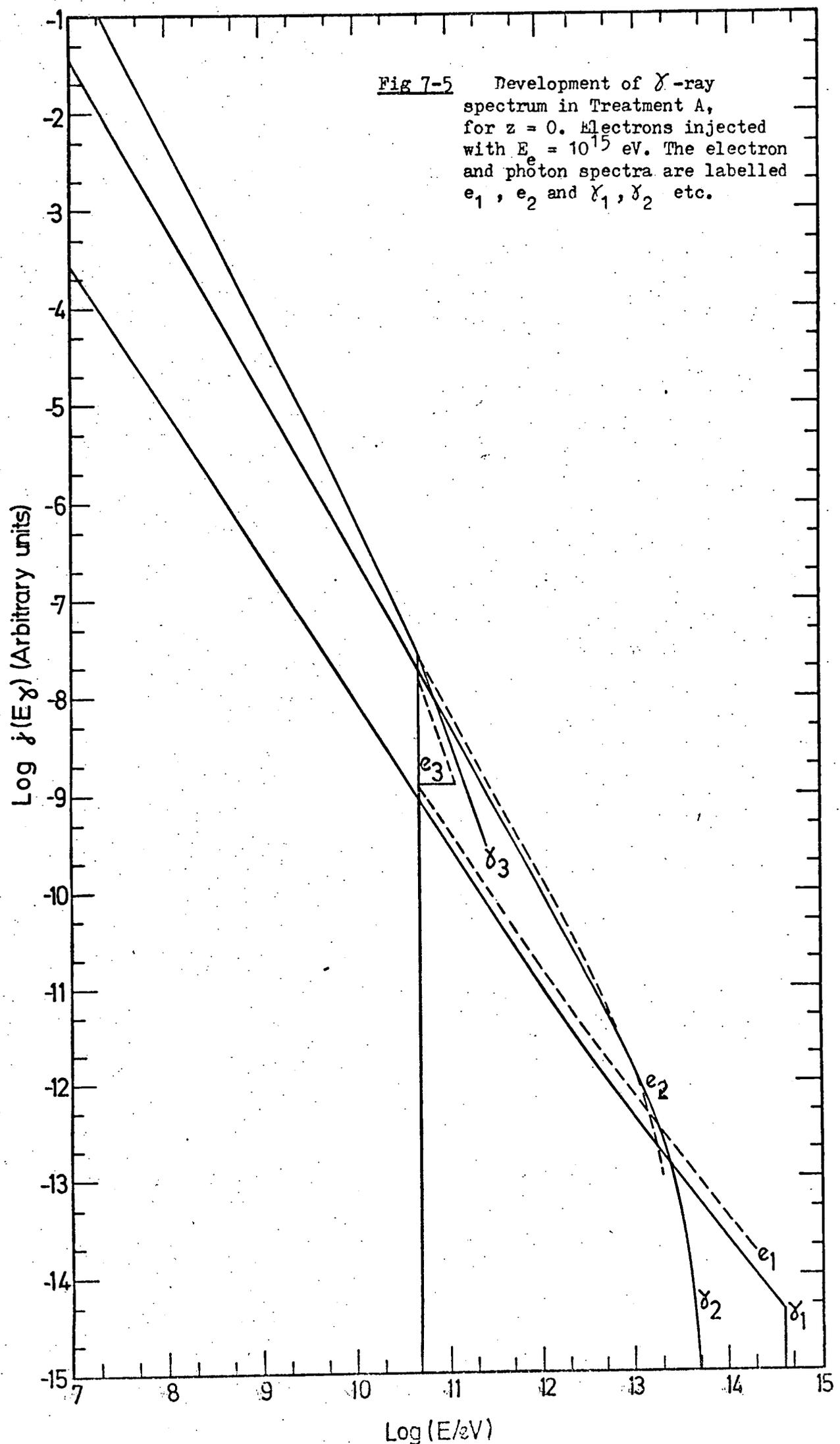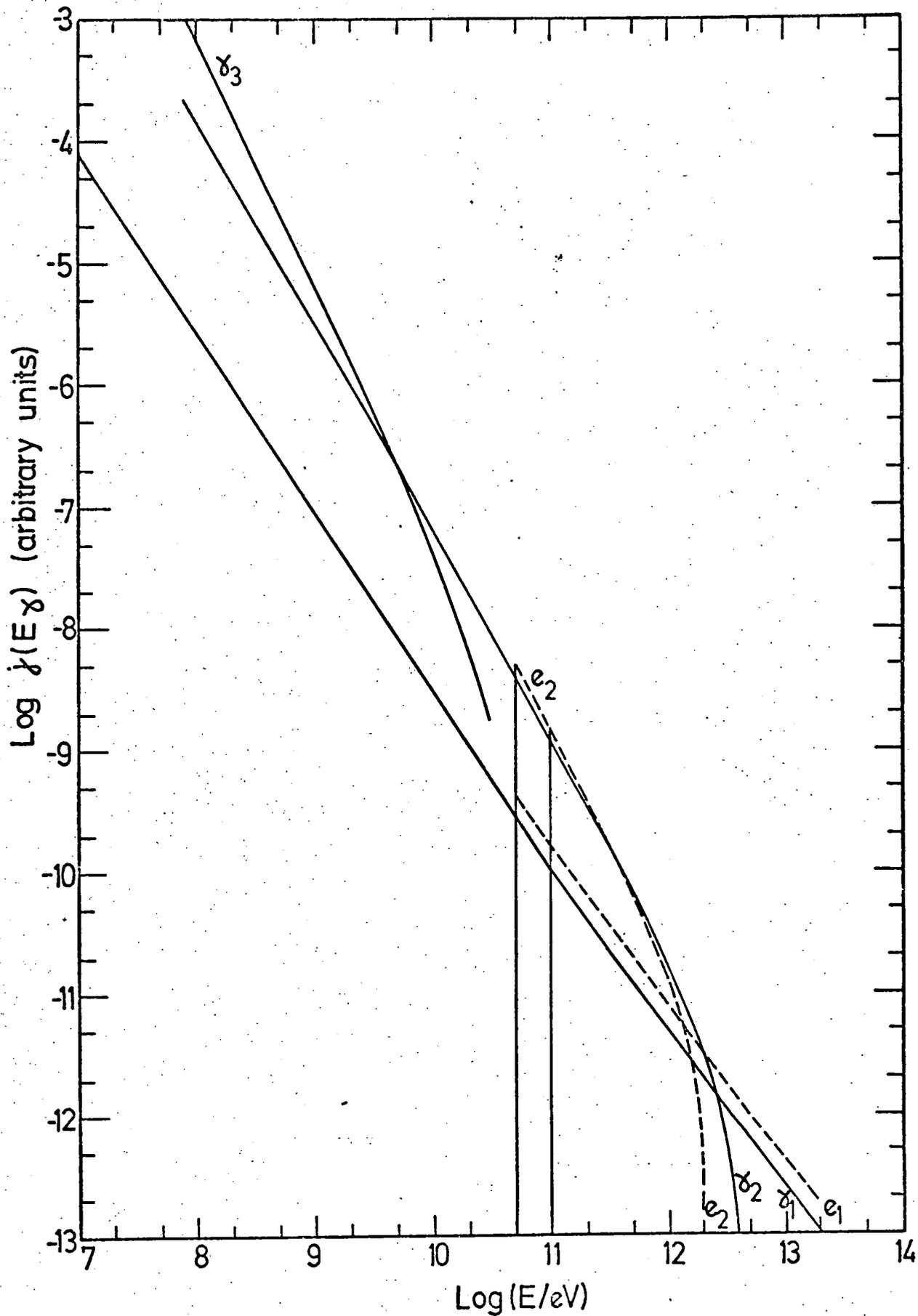
Fig 7-6

As for Fig 7-5, for the case z = 9. Electrons injected with
$E_e = 10^{14}$ eV.
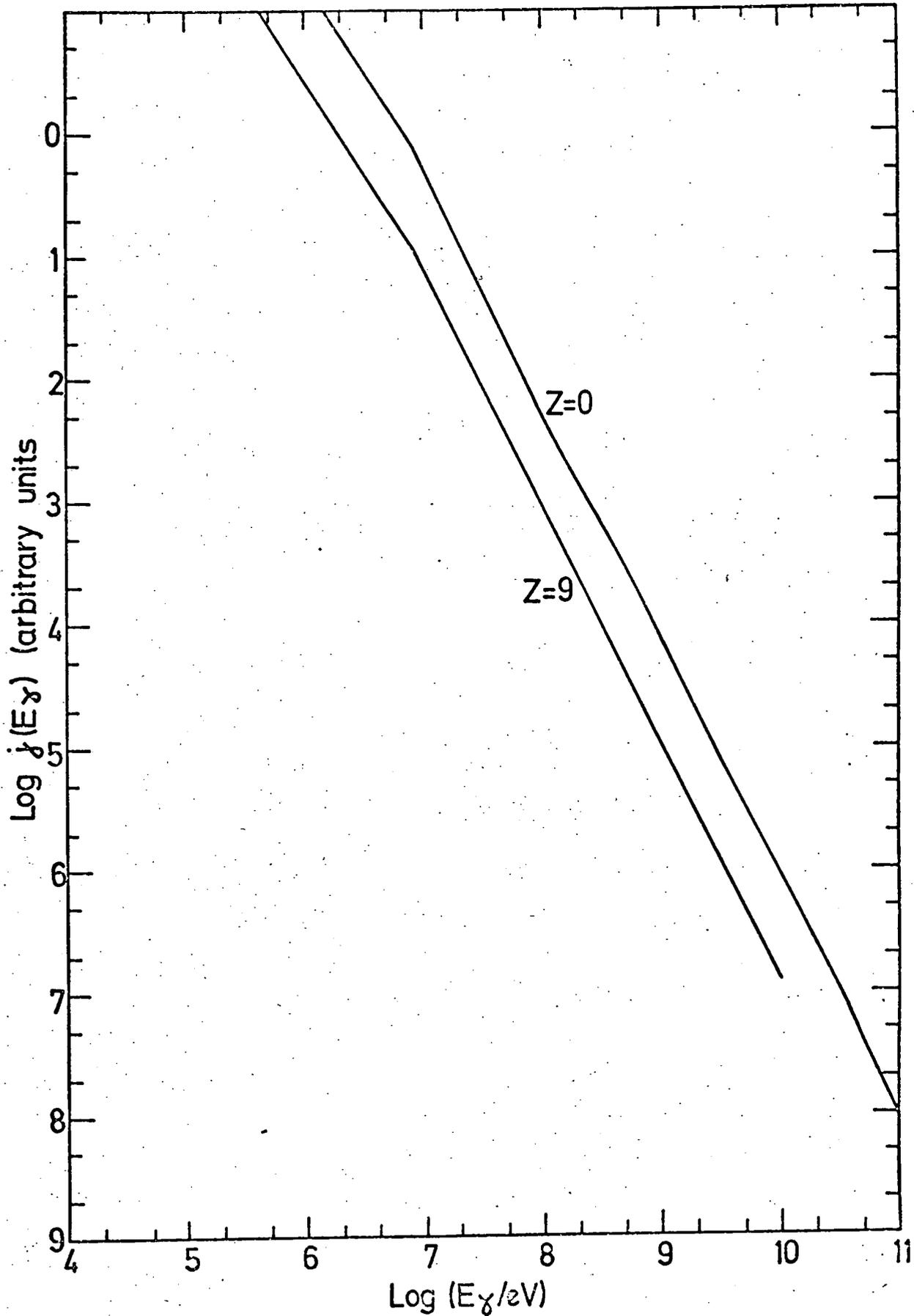
Fig 7-7

The contributions to the gamma-ray spectrum at z = 0
resulting from electron interactions at z = 0 and z = 9.
The spectra are normalized to the same energy input at these
redshifts as explained in the text.

the spectrum obtained by redshifting $\Delta j(E_\gamma ,0)$ from z to 0, by multiplying by $(1+z)^{-0.93}$ (the factor appropriate to a spectral slope -1.93).

Summarizing 2) and 3) above, we have, for $E_\gamma > E_{\gamma,th}/(1+z_m)$

$$\Delta j_\gamma (E ,z) \begin{cases} = \Delta j_\gamma(E_\gamma, 0) \ (1+z)^{-0.93} & E_\gamma < E_{\gamma,th}/(1+z) \\ = 0 & E_\gamma > E_{\gamma,th}/(1+z) \end{cases}$$

and for $E_{\gamma,th} > E_\gamma > 8 \ 10^6 eV$

$$\Delta j_\gamma(E_\gamma ,z) = \Delta j_\gamma(E_\gamma,0) \ (1+z)^{-0.93} \tag{7.17}$$

Hence, from (7.15)

$$\Delta j(E_\gamma z) = \Delta j(E_\gamma ,0) \frac{\int_0^{z_u} (1+z)^{1.47} \, dz}{\int_0^{z_m} (1+z)^{2.4} \, dz} \tag{7.18}$$

where $1+z_u = E_{\gamma,th}/E_\gamma$ for $E_\gamma > E_{\gamma,th}/(1+z_m)$

$z_u = z_m$ for $\dfrac{E_{\gamma,th}}{1+z_m} > E_\gamma \ 8 \ 10^6 eV$

Evaluation of eq.(7.18) gives, for $z_m = 14.3$ (see Chapter 3)

$$j(E_\gamma) \begin{cases} = 0.11 \ j(E_\gamma,0) & \text{for } E_\gamma > 6.5 \ 10^9 eV \\ = 1.3 \ 10^{-4} \ j(E_\gamma ,0) \left[\dfrac{E_{,th}}{E_\gamma}^{2.47} -1 \right] & \text{for } 6.5 \ 10^9 > E_\gamma > 8 \ 10^6 eV \end{cases} \tag{7.19}$$

For $E_\gamma < 8.10^6$ eV, a spectrum of slope -3/2 can be fitted to match the value given by eq.(7.19) at this energy.

The spectrum was finally normalized to the total energy flux determined from the proton spectrum in Sec 2-8, $w = 1.9 \ 10^5$ eV cm^{-2}s^{-1} sr^{-1}. Fig 7-8 shows the resulting spectrum.

7.6 The Gamma-ray spectrum: Treatment B.

In this approximation, it is assumed that the starlight density

Fig 7-8 The γ-ray spectrum from Treatment B, for different values of $E_{\gamma,max}$. The total spectrum from treatment A is also shown.

(B)

$E_{\gamma\,max}=10^8\,eV$

" $=5.10^8\,eV$

" $=10^9\,eV$

(A)

$\mathrm{Log}(j(E_\gamma)/cm^{-2}s^{-1}sr^{-1}eV^{-1})$

$\mathrm{Log}(E_\gamma/eV)$
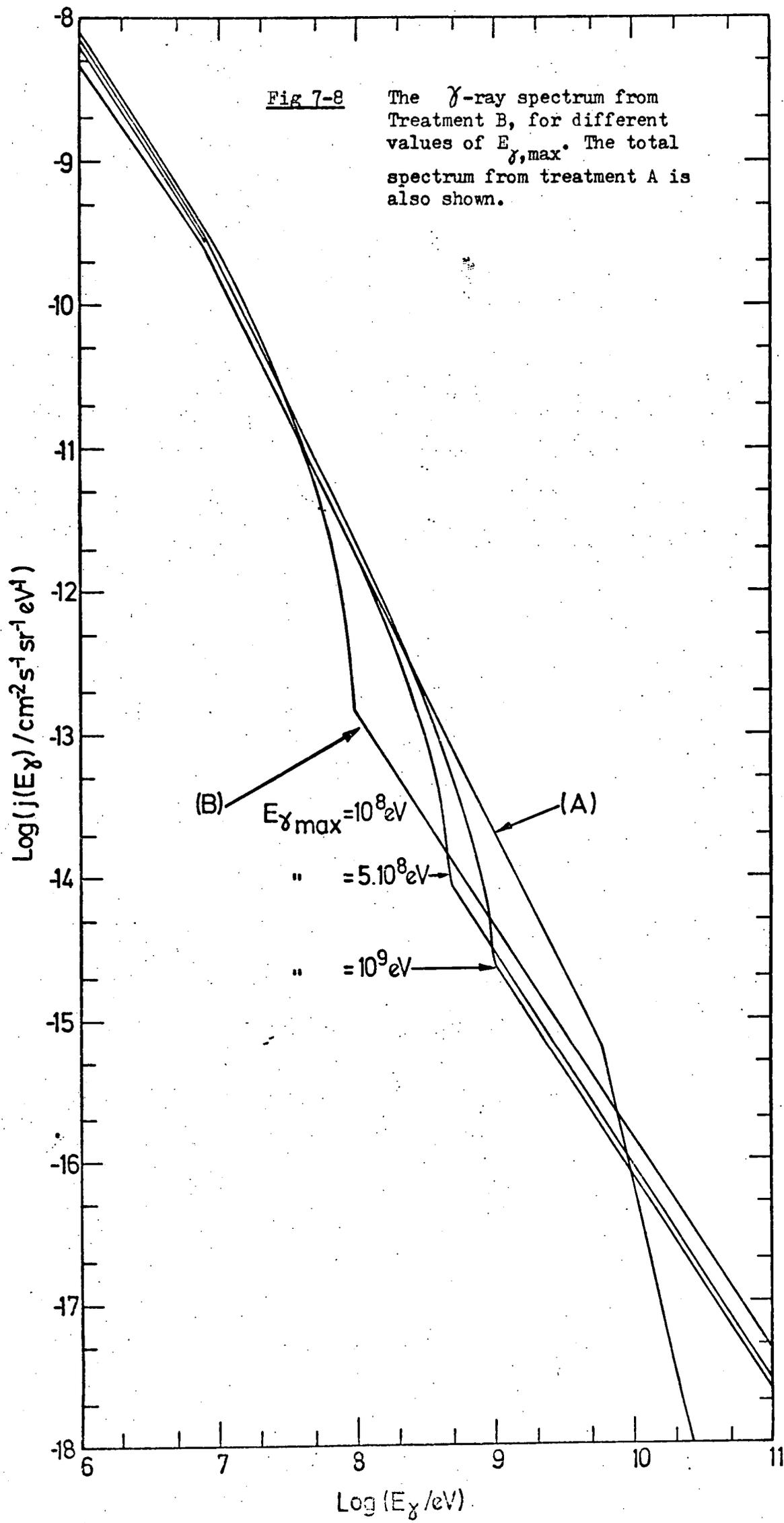
density is low enough that PP interactions of gamma-rays with starlight only occur on distance scales of order cH_o^{-1} ; for simplicity, these interactions are assumed to occur at z = 0, and, as in Treatment A, a threshold energy $E_{\gamma,th}$ is estimated below which no PP interactions are allowed. Unlike Treatment A, all the electrons from PC are assumed to be injected at z = z_m ; this is a good approximation for most of the gamma-ray spectrum, since the output from sources according to the model is strongly peaked at z_m . On the other hand, the high energy end of the gamma-ray spectrum ($E_\gamma > 10^9$ eV), which originates mainly at low z in Treatment A, is underestimated in this treatment.

The stages in the calculation are as follows:

(i) Pair-production by protons on the Blackbody radiation (PC) occurs at z_m to produce electrons of energy roughly $5 \cdot 10^{14}/(1 + z_m)$ eV.

(ii) These electrons produce a gamma-ray spectrum by ICS with a maximum energy (at z_m) of $1.5 \cdot 10^{14}$ eV/$(1+z_m)$, using Fig 4-5. The form of the spectrum is given by eq.(7.8). The PP interaction length for the 2.7K radiation increases very rapidly below $1.4 \cdot 10^{14}/(1+z)$ eV, so that this interaction is effectively bypassed in this treatment.

(iii) The first generation of gamma-rays does not, according to the assumption stated above, interact with the starlight background until z = 0. The gamma-ray spectrum is therefore redshifted so that its maximum energy is $1.5 \cdot 10^{14}/(1+z_m)^2 \sim 7 \cdot 10^{11}$ eV. It is clear that, taking $E_{\gamma,th} = 10^{11}$ eV, only one cycle of PP (on starlight) + ICS is required to reduce the energy of all gamma-rays to less than $E_{\gamma,th}$.

(iv) The gamma-rays with $E_\gamma > E_{\gamma,th}$ produce an electron spectrum of the form $AE_e^{-3/2}$, using eq.(7.7) for the gamma-ray spectrum and assuming that the PP process on starlight divides the gamma-ray energy equally between the electron and positron. The maximum energy of this electron spectrum is, using the result of (iii) above, $E_{e,max} = 7 \cdot 10^{11}/2 = 3.5 \cdot 10^{11}$ eV. The minimum energy electrons, from gamma-rays at the minimum energy

$E_{\gamma,th}$ for PP, have $E_{e,min} = 5 \ 10^{10}$ eV.

(v) The electron spectrum formed in stage (iv) interacts by ICS to give the observed gamma-ray spectrum at $z = 0$. The form of the spectrum is

$$j(E_\gamma) = AE_\gamma^{-3/2} \int_{E_{e,1}}^{E_{e,max}} E_e^{-3/2} \, dE_e \qquad (7.20)$$

where , using eq.(4.27),

$$E_{e,1} = \begin{cases} \sqrt{\dfrac{E_\gamma}{K}} & \text{for } KE_{e,max}^2 > E_\gamma > KE_{e,min}^2 \\[2ex] E_{e,min} & \text{for } E_\gamma < KE_{e,min}^2 \end{cases} \qquad (7.21)$$

Introducing $E_{\gamma,min} = KE_{e,min}^2 \sim 8 \ 10^6$ eV , $E_{\gamma,max} = KE_{e,max}^2 \sim 4 \ 10^8$ eV , eq.(7.20) gives

$$j(E_\gamma) = AK^{\frac{1}{4}} E_\gamma^{-7/4} \left[1 - \left(\frac{E_\gamma}{E_{\gamma,max}} \right)^{\frac{1}{4}} \right] \qquad \text{for } E_{\gamma,max} > E_\gamma > E_{\gamma,min} \qquad (7.22)$$

$$= AK^{\frac{1}{4}} E_\gamma^{-3/2} E_{\gamma,min}^{-\frac{1}{4}} \left[1 - \left(\frac{E_{\gamma,min}}{E_{\gamma,max}} \right)^{\frac{1}{4}} \right] \qquad \text{for } E_\gamma < E_{\gamma,min}$$

The spectrum must now be normalized to the total energy flux w, determined in Chapter 3. Writing $R = E_{\gamma,min}/E_{\gamma,max}$,the energy fluxes in the spectra of eq.(7.22) are found to be

$$w_1 = 2AK^{\frac{1}{4}} E_{\gamma,max}^{\frac{1}{4}} (1 - R^{\frac{1}{4}})^2 \qquad (7.23)$$

$$w_2 = 2AK^{\frac{1}{4}} E_{\gamma,max}^{\frac{1}{4}} (R^{\frac{1}{4}} - R^{\frac{1}{2}})$$

Thus the total energy in the spectrum which has been produced via the PP process is

$$w_{PP} = w_1 + w_2 = 2AK^{\frac{1}{4}} E_{\gamma,max}^{\frac{1}{4}} (1 - R^{\frac{1}{4}}) \qquad (7.24)$$

The fraction of the total energy which undergoes PP is given by

$$f = \frac{(2E_{e,max})^{\frac{1}{2}} - E_{\gamma,th}^{\frac{1}{2}}}{(2E_{e,max})^{\frac{1}{2}}} = 1 - \frac{K^{\frac{1}{4}}}{\sqrt{2}} \frac{E_\gamma^{\frac{1}{2}}}{E_{\gamma,max}^{\frac{1}{4}}}$$

$$= 1 - 53/E_{\gamma,max}^{\frac{1}{4}} \qquad (7.25)$$

for $E_{\gamma,max}$ in eV. Since $w_{PP} = fw$, the spectrum of eq.(7.22) becomes

$$
j(E_\gamma) \begin{cases} = \dfrac{w}{2} \ \dfrac{E_{\gamma,max}^{-\frac{1}{4}}}{(1 - R^{\frac{1}{4}})} \left[1 - \left(\dfrac{E_\gamma}{E_{\gamma,max}} \right)^{\frac{1}{4}} \right] E_\gamma^{-7/4} & E_{\gamma,max} > E > E_{\gamma,min} \\ & \quad (7.26) \\ = \dfrac{w}{2} \ E_{\gamma,max}^{-\frac{1}{4}} \ E_{\gamma,min}^{-\frac{1}{4}} \ E_\gamma^{-3/2} & E < E_{\gamma,min} \end{cases}
$$

vi) The part of the spectrum for which no PP has occured must also be added. This has a spectrum of the form $E_\gamma^{-3/2}$ up to $E_{\gamma,th}$; and total energy $w(1 - f)$. The normalized spectrum is then

$$
j(E_\gamma) = \frac{w(1 - f)}{2E_{\gamma,th}^{\frac{1}{2}}} \ E_\gamma^{-3/2} \qquad\qquad (7.27)
$$

In order to evaluate expressions 7.26 and 7.27, values for $E_{\gamma,min}$ and $E_{\gamma,max}$ are required. The value $E_{\gamma,min} \sim 8 \ 10^6$ eV calculated above is adequate, since the spectrum does not depend critically on this parameter. However, the shape of the spectrum near 10^8 eV is sensitive to $E_{\gamma,max}$, and there is no simple way of determining the best value for this parameter apart from the rough estimate in (v) above (eq.7.20). It will in any case depend on the uncertain density of starlight photons. Therefore $E_{\gamma,max}$ was taken as a free parameter and the spectrum calculated for $E_{\gamma,max} = 10^8$, $5 \ 10^8$ and 10^9 eV, to determine the effect of variation around the value estimated in (v). The resulting spectra are shown in Fig 7-8. Since, as mentioned at the beginning of this Section, this treatment underestimates the high energy end of the spectrum, the shape predicted near $E_{\gamma,max}$ is not of significance.

7.7 Discussion and comparison with observations.

The experimental data on the gamma-ray background are reviewed in Chapter 9. Fig 7-9 shows a comparison between the data and the spectra derived here. It is apparent that there is a good possibility of agreement between the theory and observation, since all the

Fig 7-9

Comparison of theoretical spectra of this Chapter with observations. Key to data given in Fig 9-1.
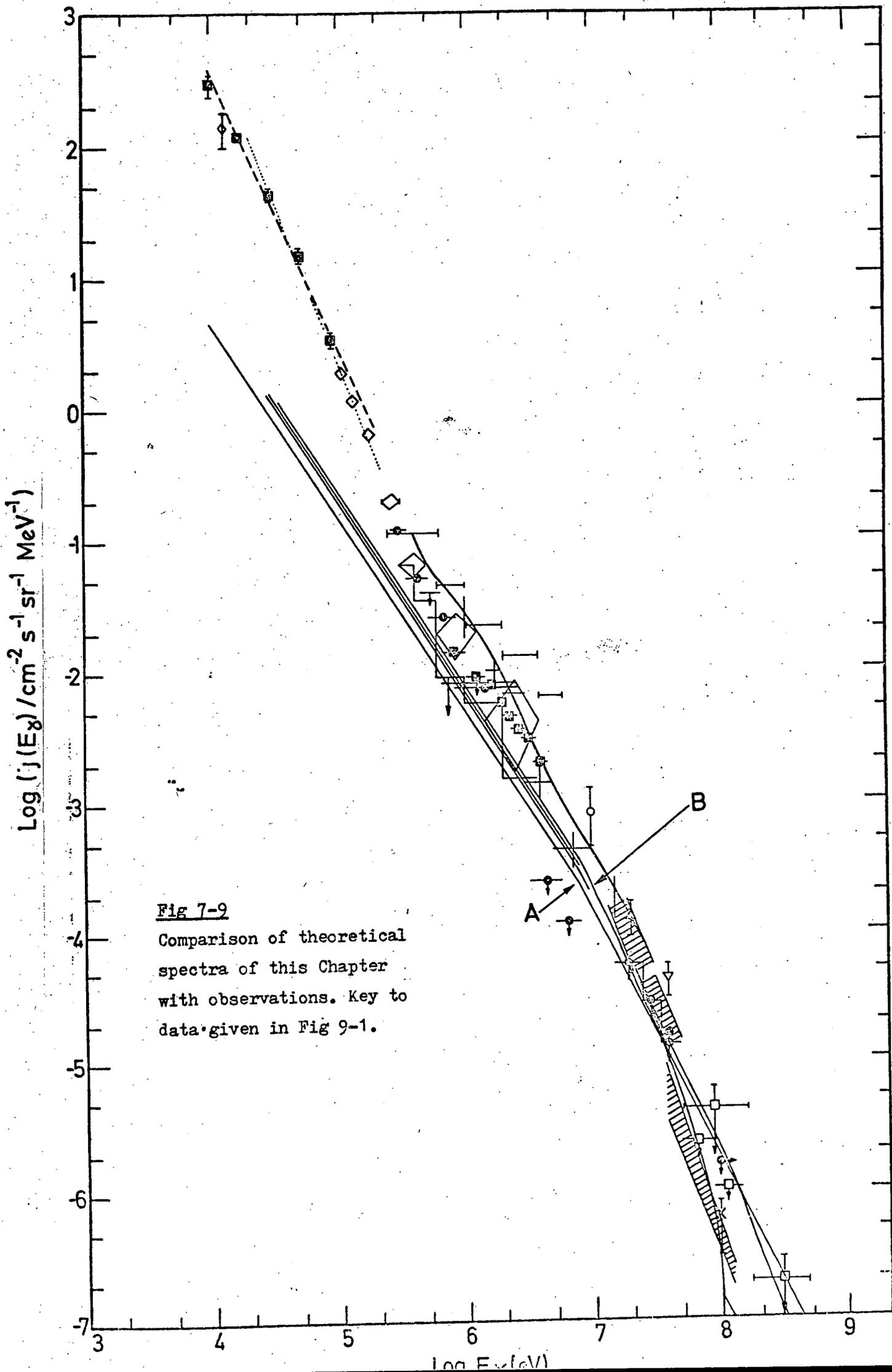
approximations lead to spectra which lie fairly close to the observational points in the 1-100 MeV range.

Probably the most important source of error in the calculations described in this Chapter is the use of mean values for the energy tranfer in PC,PP and ICS processes. Reference to Figs 3-4,4-3,4-4 and 5-2 shown that in each of these processes, the energy is distributed over a wide range (typically a factor 10 on each side of the mean). As a result, more energy will be distributed in the high energy end of the spectrum than is found in the simple treatments.

To remove the ambiguities, and having shown that approximate treatments give a spectrum remarkably close to the observations, (especially because the normalization of the spectrum is derived independently from the properties of the primary cosmic-ray spectrum), it was decided to refine the calculations to give a truer representation of the processes involved. This involves the use of the proper energy distribution functions calculated in the previous Chapters, and a more rigorous approach to the development of the spectrum as a function of z. These calculations are described in Chapter 8.

Chapter 8   Numerical approach to the Gamma-ray spectrum on the
                   Hillas model.

8.1 Introduction.

In the approximate treatments of the gamma-ray spectrum described
in the previous Chapter, it was necessary to make many simplifying
assumptions about the processes involved in order to render the problem
tractable. Thus, the initial production of electrons by the PC process
was taken to give electrons of unique energy at any redshift, and the
ICS spectra were derived using the mean values for energy transfer.
Pair-production in photon-photon collisions (PP process) was treated
by dividing the gamma-ray energy equally between the two electrons.
The main difficulty was in the interactions between gamma-rays and the
starlight background; it was necessary to assume that some $E_{\gamma,th}$ could
be chosen so that gamma-rays interact only for $E_\gamma > E_{\gamma,th}$, and to con-
sider this process as occuring either at the redshift of electron prod-
uction, or alternatively, at $z = 0$. No attempt was made to include the
effect of a cosmologically varying starlight spectrum, although from the
discussion of Chapter 6, a realistic model involves such a variation.

The calculations described in this Chapter are an attempt to
follow the development of the gamma-ray spectrum explicitly; as far as
possible approximations have been avoided in order to derive a reliable
result.

8.2 Outline description of techniques.

The basis of the method is the division of the interval of red-
shift $z = 0 - z_m$ into a number of sub-intervals δz, over which the
blackbody temperature T and the starlight density are nearly constant.

Fig 8-1. Summary of Development of γ-ray spectrum from z to $z - \Delta z$
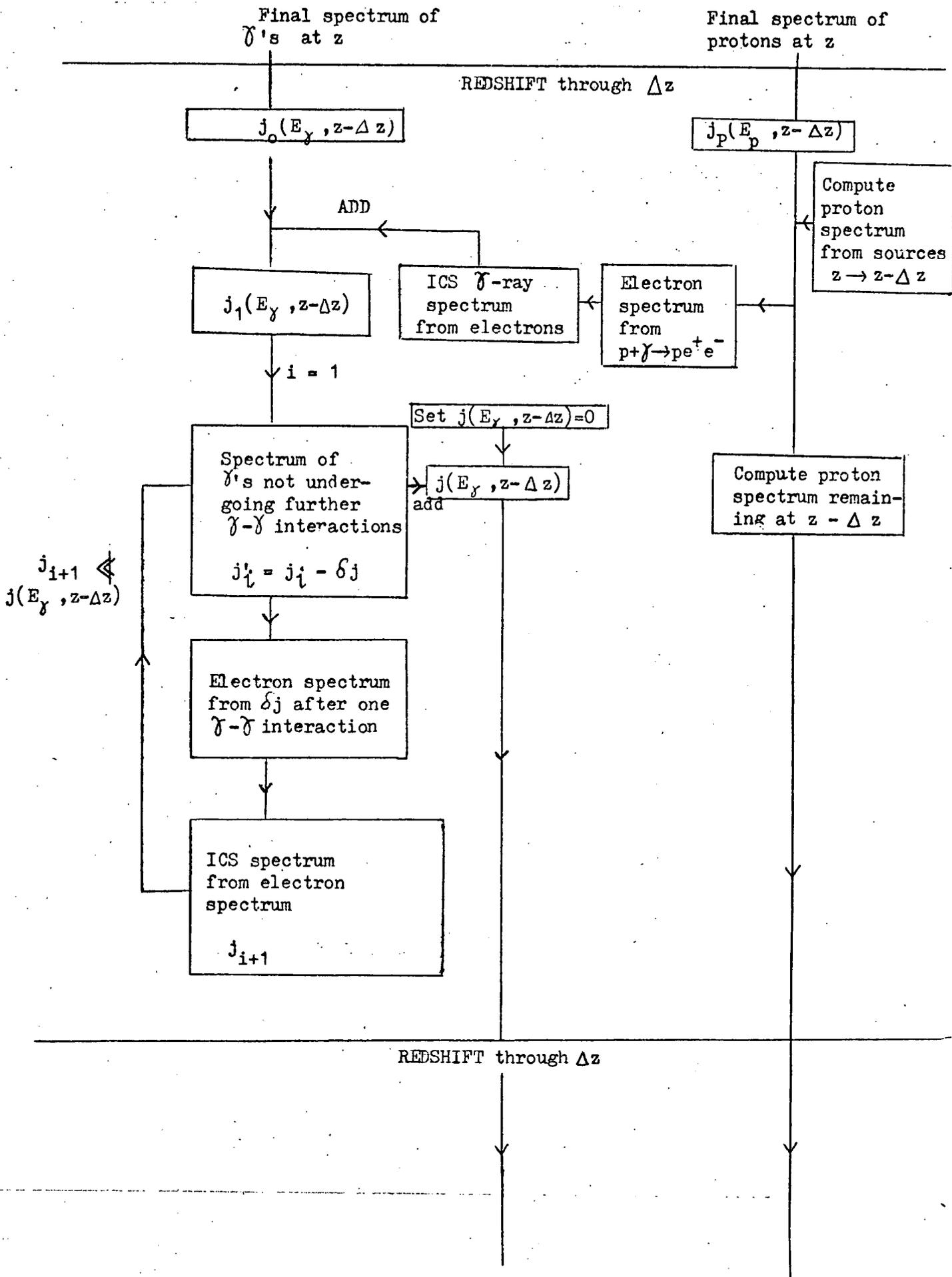
The change in the gamma-ray spectrum over δz is computed as indicated in Fig 8-1, which summarizes the description which now follows.

At the start of each new z interval $(z \to z - \delta z)$, the spectrum of protons at the start of the interval is taken to be the sum of the newly produced protons from sources over z, and the protons remaining from the previous interval. The electron spectrum from the PC process over δz is computed, together with the proton spectrum remaining at the end, i.e. at $z - \delta z$. The approximation made here is the replacement of a continuous injection of protons over δz by injection at the start of the interval. The error introduced by this procedure is small provided T is nearly constant over the interval.

The gamma-ray spectrum from the ICS of these first generation electrons is computed, and added to the gamma-ray spectrum carried over from the previous interval. This is a 'point process' as discussed in Chapter 7, so that this spectrum, which will be denoted $j_1(E_\gamma, z)$, is effectively formed at z. The propagation of j_1 to $z - \delta z$ is now followed.

The effect of the PP process on j_1 is calculated as follows. First, the part of the spectrum which does not interact by this process within δz is subtracted from j_1. Denote this non-interacting component by $\delta j_1(E_\gamma, z)$. Then

$$\delta j_1(E_\gamma, z) = j_1(E_\gamma, z) \exp - \left[\frac{\delta z}{\lambda_{PP}} \frac{dx}{dz} \right] \qquad (8.1)$$

where λ_{PP} is the PP interaction length on the blackbody and starlight background. The gamma-ray spectrum at $z - \delta z$, $j_1(E_\gamma, z-\delta z)$ is incremented by δj_1. The remaining part of the spectrum is denoted j_1' ($= j_1 - \delta j_1$). The PP electron spectrum from j_1' is then derived, and the ICS gamma-ray

spectrum from these electrons, $j_2(E_\gamma, z)$, is obtained. The result of subsequent PP - ICS cycles is then determined by a repeat of the procedures above, to obtain $j_3(E_\gamma, z)$ etc. After several of these cycles, most of the energy is transferred to the new redshift, i.e., $j_i(E_\gamma, z) \ll \sum_i j_i(E_\gamma, z - \delta z)$. When this condition is met, the propagation of the spectrum to $z - \delta z$ is regarded as complete. The whole procedure can now be repeated for the next z interval. The final spect- is obtained when z = 0 is reached.

8.3 Details of computational techniques.

The calculations were carried out on a computer, so that a suitable method for representing the various spectra was required. The energy range of interest ($10^5 - 10^{17}$ eV) was divided up into n bins of range $E_k - E_{k+1}$, such that there were between 5 and 20 bins per decade of energy. The spectrum is represented by n quantities N^k proportional to the total flux of particles within the k'th bin. A convention of decreasing energy with increasing k was found to be convenient so that particles move to bins of increasing k as the spectra develop. For the purpose of calculation, the particles were assumed to be uniformly distributed within the energy bins. The spectra can then be developed by operating on the N^k with matrices appropriate to the various processes. The details of this procedure will now be described.

(i) ICS process.

The electron and gamma-ray spectra are represented as described above by the vectors N_e^k and N_γ^k respectively. Matrices M_{ICE}^{kl} and M_{ICP}^{kl} are defined such that

$$\Delta N_e^{kl} = M_{ICE}^{kl} N_e^k \qquad l > k \quad (E_l < E_k)$$

$$\Delta N_\gamma^{kl} = M_{ICP}^{kl} N_e^k \qquad l > k \tag{8.2}$$

where ΔN_e^{kl} and ΔN_γ^{kl} are the increments to N_e^1 and N_γ^1 consequent on the removal of all the electrons from the k'th bin by ICS. Hence, by definition, $M_{ICE}^{kk} = 0$.

The definition of the matrices given above is convenient in that it allows the complete conversion of an electron spectrum into a gamma-ray spectrum in approximately $\frac{1}{2}n^2$ steps of the form:

for all k from 1 to n :

(i) for $l > k$, replace N_e^1 by $N_e^1 + \Delta N_e^{kl}$.

(ii) for $l \geqslant k$, replace N_γ^1 by $N_\gamma + \Delta N^{kl}$.

(iii) set $N_e^k = 0$.

The calculation of the matrix elements will now be described. First the quantities Q_{ICP}^{kl} calculated from

$$ Q_{ICP}^{kl} = \frac{1}{E_k - E_{k+1}} \int_{E_e=E_{k+1}}^{E_e=E_k} \int_{E_\gamma=E_{l+1}}^{E_\gamma=E_l} P_{IC}(E_\gamma, E_e)\, dE_e dE_\gamma \quad (8.3) $$

Q_{ICP}^{kl} is the probability for an electron in the k'th bin producing a gamma-ray in the l'th bin in one ICS interaction. $P_{IC}(E_\gamma, E_e)$ is the differential probability spectrum for gamma-rays from one electron of energy E_e , given by

$$ P_{IC}(E_\gamma, E_e) = \frac{g_{IC}(E_\gamma, E_e)}{\int_0^{E_e} g_{IC}(E_\gamma, E_e) dE_\gamma} \quad (8.4) $$

where g_{IC} is the differential reaction rate for ICS defined in Chapter 4.

Similarly, for the electron distribution from one ICS interaction, we calculate Q_{ICE}^{kl} from

$$ Q_{ICE}^{kl} = \frac{1}{E_k - E_{k+1}} \int_{E_e=E_{k+1}}^{E_e=E_k} \int_{E_e'=E_{l+1}}^{E_e'=E_l} P_{IC}(E_e', E_e)\, dE_e\, dE_e' \quad (8.4a) $$

The quantity Q_{ICE}^{kk} is the probability of an electron remaining in the same bin after ICS, and can be used to obtain M_{ICE}^{kl} and M_{ICP}^{kl}. Provided we can ignore the redistribution of electrons within the k'th bin, the effect of repeated ICS interactions is to reduce the contents of this bin by the factor Q_{ICE}^{kk} each time. Since $N_e^k(1 - Q_{ICE}^{kk})$ electrons leaving bin k produce $N_e^k Q_{ICP}^{kl}$ gamma-rays in the l'th energy bin, it follows that

$$\left.\begin{array}{l} M_{ICE}^{kl} = Q_{ICE}^{kl} \\ M_{ICP}^{kl} = Q_{ICP}^{kl} \end{array}\right\} \times (1 - Q_{ICE}^{kk})^{-1} \qquad (8.5)$$

This method was used for ICS from electrons with energies above $\dfrac{1.5 \ 10^{14}}{1+z}$ eV for which Q_{ICE}^{kk} is not too near 1, so that eq.(8.5) gives a reliable result. For lower electron energies, where the energy loss on each interaction is small and $Q_{ICE}^{kk} \sim 1$, a slightly different procedure is used. The electron energy loss is assumed to be continuous, and instead of computing the new electron distribution when all electrons are removed from the k'th bin in a definite number of ICS interactions, the electrons are redistributed uniformly in the (k+1)'th bin. The number of interactions is therefore not defined, but the total energy transfer to gamma-rays is known, and is equal to $\frac{1}{2}(E_k - E_{k+2})$, per electron. The quantity Q_{ICP}^{kl} is defined as before. We then have

$$\begin{array}{ll} M_{ICE}^{kk} = 0 \\ M_{ICE}^{k,k+1} = 1 \\ M_{ICE}^{kl} = 0 & l > k+1 \qquad (8.6) \\ M_{ICP}^{kl} = Q_{ICP}^{kl} \cdot \frac{1}{2}(E_k - E_{k+2}) / E_{trans} \end{array}$$

where $E_{trans} = \displaystyle\sum_{l=k}^{l=n} Q_{ICP}^{kl}(E_l + E_{l+1})/2$ is the energy transfer to gamma-rays in one ICS interaction.

This method is only suitable when the mean fractional energy loss of an electron in one collision is small, and the changeover between

the two methods is made when this fractional energy loss is about 0.2. At this energy, provided the bin-width is small enough, both methods are suitable.

(ii) Photon-photon interactions (PP process).

This process is easier to treat than ICS, since only one interaction per gamma-ray converts the spectrum totally into electrons. The relations used are (cf.Sec 8-2)

$$\Delta'N_{\gamma}^{k} = N_{\gamma}^{k} \exp\left(-\frac{\delta z}{\overline{\lambda}_{PP}} \frac{dx}{dz} \right)$$

$$\Delta N_{e}^{kl} = M_{PP}^{kl} N_{\gamma}^{l} \left(1 - \exp\left(-\frac{\delta z}{\overline{\lambda}_{PP}} \frac{dx}{dz} \right) \right) \qquad (8.7)$$

where $\Delta'N_{\gamma}^{k}$ is the increment to the gamma-ray spectrum at $z-\delta z$ from gamma-rays not interacting within δz, ΔN_{γ}^{kl} is the increment to the l'th bin of the electron spectrum from those gamma-rays which do interact within δz. M_{PP}^{kl} is the probability of an electron being produced in bin 1 from a gamma-ray in bin k, given that the interaction does occur. $\overline{\lambda}_{PP}$ is the PP interaction length at the mean energy of the k'th bin.

(iii) Redshift energy losses.

These losses occur continuously throughout the various stages of the cascade development, and are independent of whether the energy is in electrons or photons. The method used here for representing the energy spectra allows a simple procedure to include the effect of red-shifting; the energies E_{k} defining the bins are allowed to vary with z according to $E_{k}(z) = E_{k}(0) (1+z)$. In this way all particles are red-shifted by the correct amount as the spectrum develops.

(iv) The proton spectrum and the PC process.

Fig 8-2   Summary of Development of Electron Injection Spectrum.

$N_p^k(z_1)$

$z = z_1$
$k_1 = 1$

Proton input from
sources in (z_1, z_2)

ADD

$N_p^k(z) \ll$
$N_p^k(z_1)$
$(k_1 \leqslant k \leqslant k_2)$

$\left.\begin{array}{l} \delta z = \frac{1}{2}\lambda_a(E_p^{k1})\frac{dz}{dx} \\ \\ z - z_2 \end{array}\right\}$ lesser of

Choose k_2 such that $k_2 > k_1$
and $\lambda_a(E_p^{k2}) < 2\lambda_a(E_p^{k1})$

Compute electron
injection spectrum in
$(z, z - \delta z)$
$\Delta N_e^l = \sum M_{PC}^{kl} N_p^k \delta z$

ADD

Total
electron
injection
in (z_1, z_2)

Increment $N_p^l(z - \delta z)$ by
$N_p^k(z)$ where

$E_p^{l+1} < \overline{E}_p^k - \Delta E_p^k < E_p^l$

$E_p^k = \frac{dE}{dz}(\overline{E}_p^k)\,\delta z$

$\overline{E}_p^k = \dfrac{E_p^k + E_p^{k+1}}{2}$

$z \rightarrow z - \delta z$

$z < z_2$

$z = z_2$

$N_p^k(z_2)$
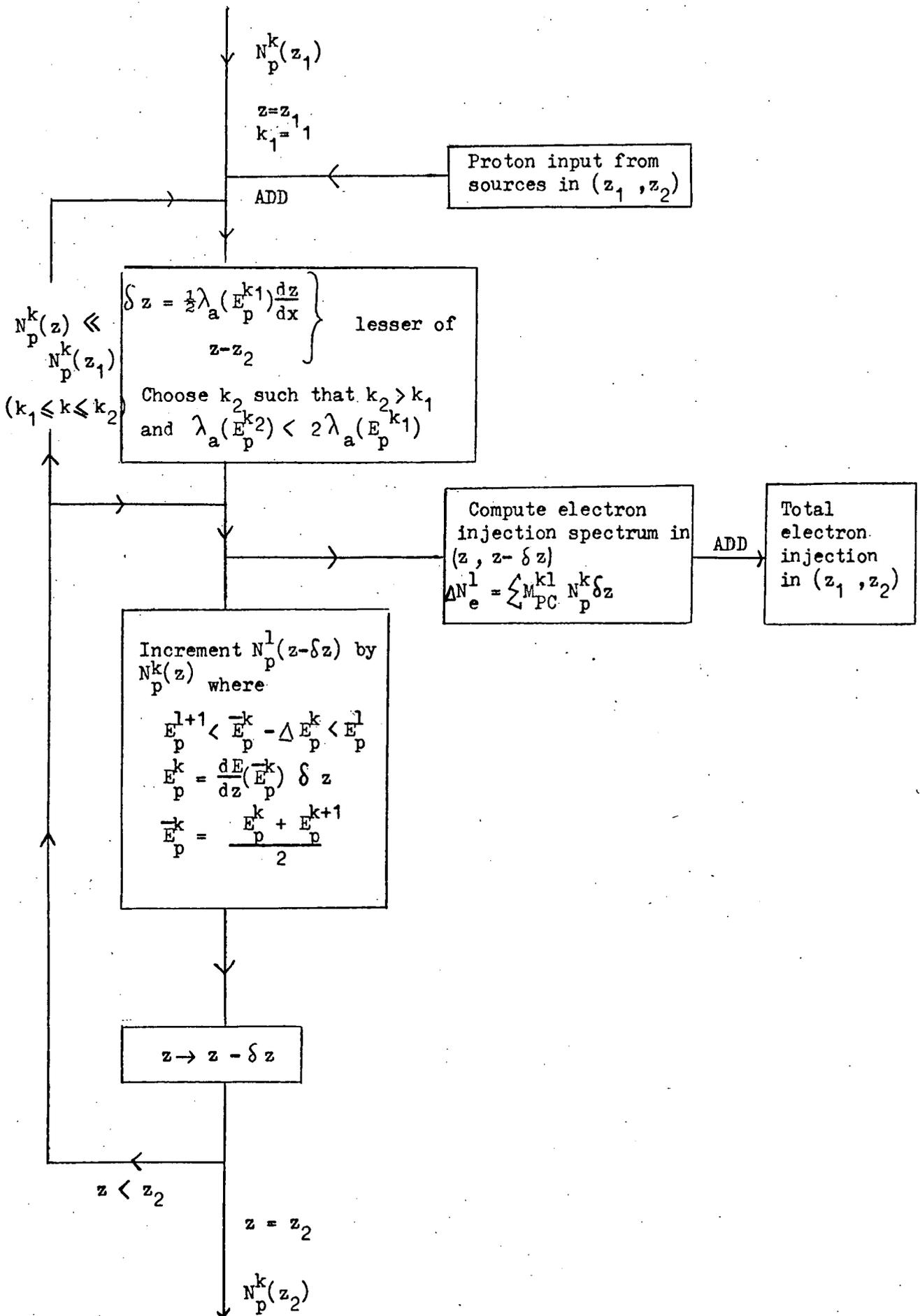
The proton spectrum was followed explicitly as a function of redshift, so that the electron spectrum injected in each redshift interval could be calculated. The large variation in the rate of energy loss by the PC process necessitates the further division of δz into smaller intervals appropriate to the different energy ranges.

The proton energy range of interest ($10^{15} - 10^{20}$ eV) was divided logarithmically into m bins such that the k'th bin spanned the range $E_p^k - E_p^{k+1}$ and contained N_p^k protons. (As before, the convention of increasing k with decreasing energy was adopted). A flowchart for the method adopted to develop the proton spectrum from some z_1 to $z_2 = z_1 - \delta z$ is given in Fig 8-2.

The source-generated protons for the interval (z_1, z_2) are assumed to be injected at z_1, as explained in Sec 8-2. The injected proton spectrum is added to that remaining from the previous z interval. The resulting proton spectrum is then followed through the series of subdivisions $\delta'z$, chosen according to

$$\delta'z = \text{greater of} \begin{cases} \frac{1}{2}\lambda_{PC}(E_p^{k1})dz/dx \\ z - z_2 \end{cases} \quad (8.8)$$

where E_p^{k1} is the highest proton energy present in the spectrum in significant amount. A second energy E_p^{k2} is also chosen such that E_p^{k2} is the lowest energy for which

$$\lambda_{PC}(E_p^{k2}) < 2\lambda_{PC}(E_p^{k1}) \quad (8.9)$$

The proton spectrum is now developed through successive intervals $\delta'z$ until the bins between E_p^{k1} and E_p^{k2} have been depleted (i.e. contain a negligible fraction of the particles they contained at z_1). The development through $\delta'z$ is carried out by calculating the energy loss for protons at the mean energy of the bin, and tranferring the contents of

each bin to the new bin appropriate after the energy loss. Thus $N_p^l(z - \delta'z)$ is incremented by $N_p^k(z)$, where

$$E_p^{l+1} < (\overline{E}_p^k - \Delta E_p^k) < E_p^l$$

$$\overline{E}_p^k = (E_p^k + E_p^{k+1})/2 \qquad\qquad (8.10)$$

$$\Delta \overline{E}_p^k = \frac{dE}{dz}(\overline{E}_p^k)\, \delta'z$$

When the bins $k1 \to k2$ are depleted, a new $\delta'z$ is chosen appropriate to the highest energy now present, and the process is repeated until z_2 is reached. The energy loss term dE/dz here includes redshift, PC and photomeson energy losses.

At each step $\delta'z$, the injected electron spectrum ΔN_e^l is also calculated from

$$\Delta N_e^l = M_{PCE}^{kl}\, N_p^k\, \delta'z \qquad\qquad (8.11)$$

where

$$M_{PCE}^{kl} = P_{PCE}(\overline{E}_e^l, \overline{E}_p^k)\, \Delta E_e^l \qquad\qquad (8.12)$$

P_{PCE} is related to the reaction rate g_{PC} defined in Chapter 3 by

$$P_{PCE} = g_{PC}\, dx/dz . \qquad\qquad (8.13)$$

The procedure described above was designed to give a reasonably accurate result for the electron injection spectrum without involving long computation times. The method does not produce an accurate final proton spectrum, because the errors in each step are cumulative; however this is not important for the electron spectrum since most of the energy injected into electrons from a given proton occurs while the proton energy is comparable to its initial energy. Accurate methods for calculating the proton spectrum were described in Chapter 2.

8-4   The Gamma-ray spectrum : results of computations.

The gamma-ray spectrum was computed using the techniques described above for the following model parameters:

(a) a greybody starlight spectrum with T_s = 1500 K and energy density w_s = 4 10^{-2} eV cm^{-3} at z = 0, and undergoing redshift back to z_m ; also a UV spectrum with T_{UV} = 3 10^4 K and energy 2 10^{-3} eV cm^{-3}, assumed not to vary with z. As discussed in Chapter 6, the former spectrum gives a reasonably good representation of the Tinsley model 1 spectrum shown in Fig 6-1, and the latter the unredshifted contribution from young stellar populations at small z. The cosmological parameters were taken as for the 'standard model' of Chapter 2, i.e., H_0 = 50 km s^{-1} Mpc^{-1} and $q_0 = \frac{1}{2}$.

(b) As for (a), but with q_0 = .02.

(c) A greybody starlight spectrum with T_s = 6000K and w_s= 10^{-2} eV cm^{-3}.

The starlight was assumed not to vary with epoch. As before, H_0=50,q_0=$\frac{1}{2}$.

(d) As for (c), but with w_s = 10^{-1} eV cm^{-3}.

Figs 8-3 to 8-6 illustrate the development of the gamma-ray spectrum in the four cases. The spectrum for each z is shown as it is at the end of a redshift interval δz, before injection of further electrons by the PC process. The spectra are shown in the form $E_\gamma^2 \, j(E_\gamma)$ in order to indicate the energy distribution. Fig 8-7 compares the final spectra obtained for each case, normalized to the total energy flux calculated in Ch. 2.

The normalized spectra from cases (a) and (b) are almost identical, showing that the value for q_0 used has very little effect on the spectrum, within the range .02 - .5 . The principal difference between the cases (a),(b) and (c),(d) is in the energy remaining in the 10^9 - 10^{10} eV range; in the former cases, most of the energy is tranferred to gamma-rays below 10^7 eV, while the latter models have a spectrum which does not

The figure shows a plot with the y-axis labeled $\log\,[E_\gamma^2\, j(E_\gamma)]$ arbitrary units (ranging from -4 to above 1) and the x-axis labeled $\mathrm{Log}\,(E_\gamma/eV)$ (ranging from 5 to 11). Curves are labeled $10{\cdot}0$, $11{\cdot}7$, $13{\cdot}3$, $1{\cdot}67$, and $0{\cdot}0$.

Parameters shown in the figure:

$$T_s = 1500(1+z)\ \mathrm{K}$$
$$w_s = 4.\ 10^{-2}(1+z)^4\ \mathrm{eV\ cm}^{-3}$$
$$T_{UV} = 3.\ 10^4\ \mathrm{K}$$
$$w_{UV} = 2.\ 10^{-3}\ \mathrm{eV\ cm}^{-3}$$
$$q_o = 0.5$$
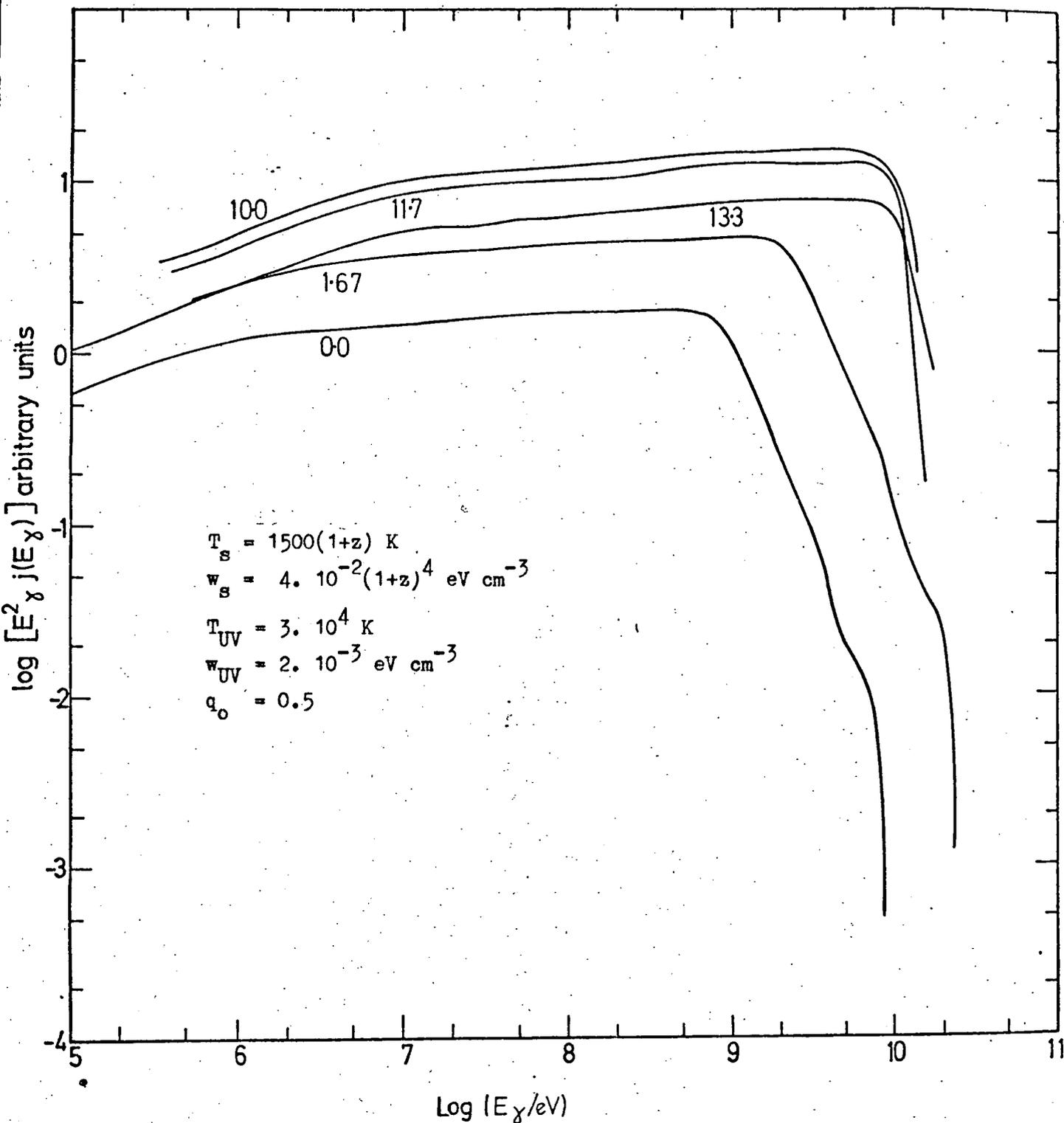
Fig 8-3

Development of gamma-ray spectrum using numerical techniques
described in this chapter. Numbers on curves refer to the red-
shift. The parameters are those of model (a).
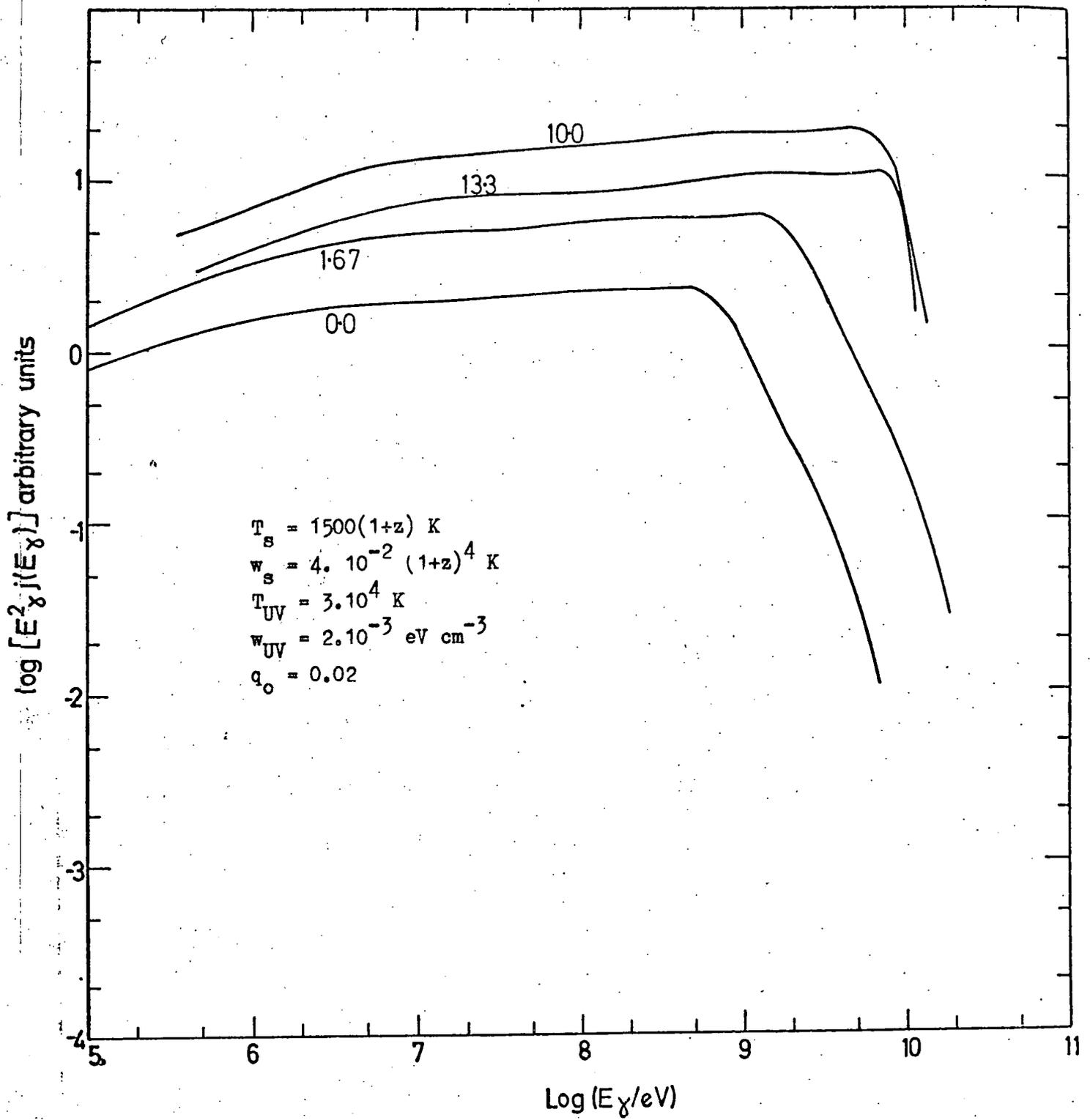
Fig 8-4

Development of gamma-ray spectrum, model (b)
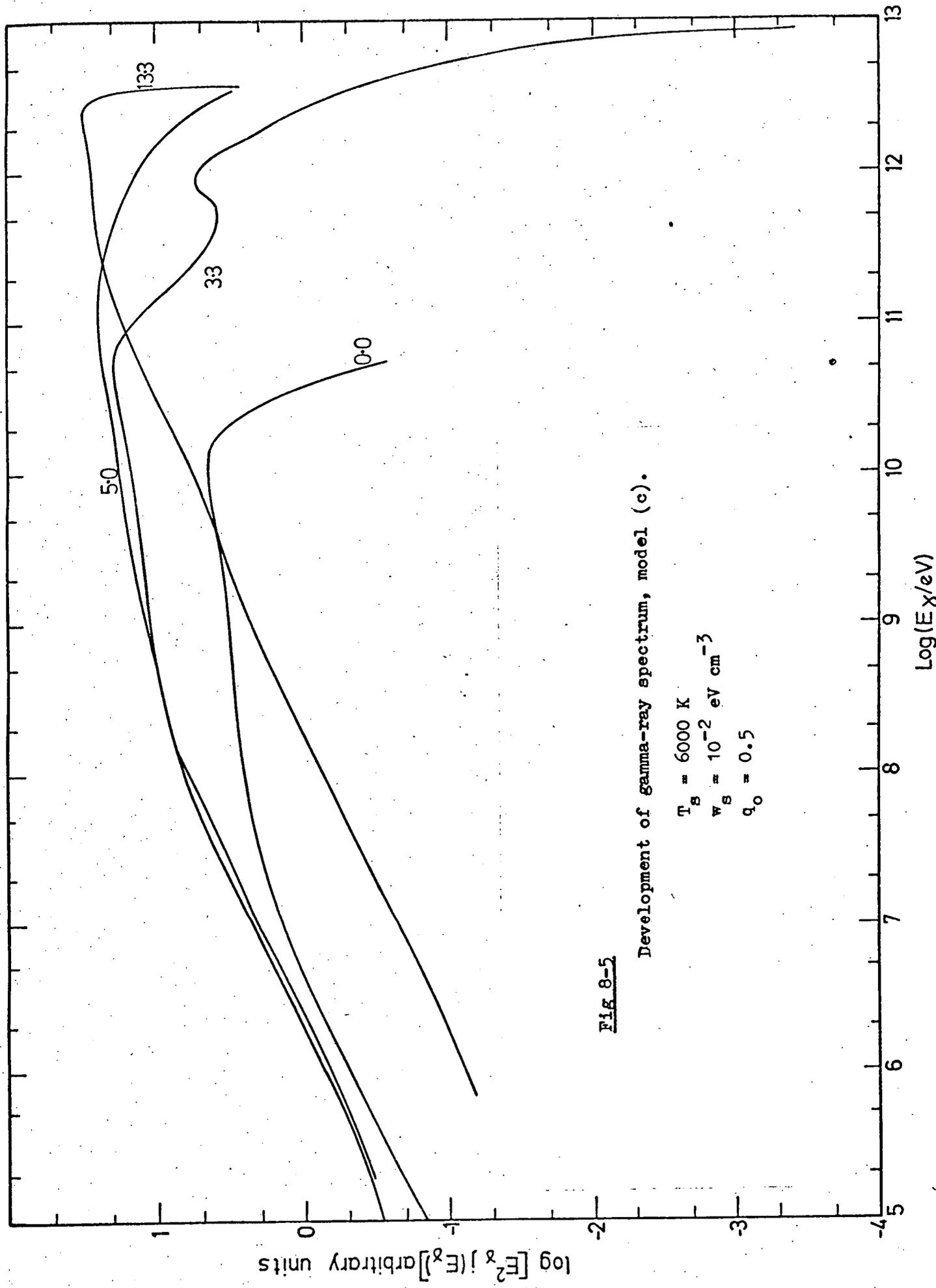
Fig 8-5

Development of gamma-ray spectrum, model (c).

$T_g = 6000$ K

$w_s = 10^{-2}$ eV cm^{-3}

$q_o = 0.5$

Log(E_γ/eV)

log $[E_\gamma^2 j(E_\gamma)]$ arbitrary units

Fig 8-6

Development of gamma-ray spectrum, model (d).

$T_s = 6000$ K

$w_s = 10^{-1}$ eV cm^{-3}

$q_o = 0.5$

Log (E_γ/eV)

log [E_γ^2 j(E_γ)] arbitrary units
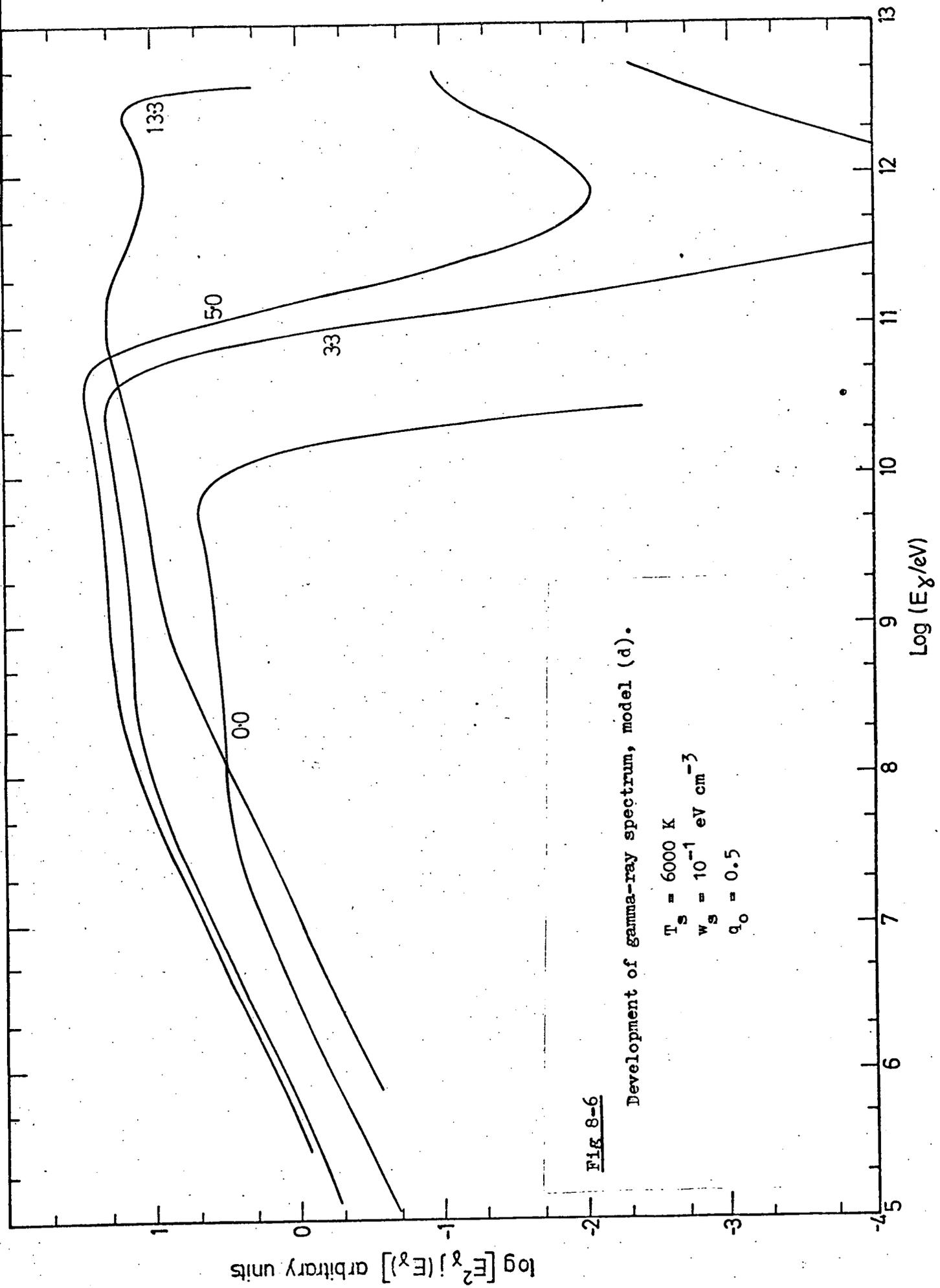
Fig 8-7

Spectra from models a-d, normalized to the total energy determined from the primary proton spectrum. Spectra a and b are very similar and only (a) is shown.

cut off before 10^{10} eV, and consequently lower fluxes in the range below 10^7 eV. The difference is a result of the high temperature starlight fields which occur for large z in models (a) and (b), and the effect of these is shown in Figs8-3 and 8-4 as a sharp cutoff in the spectrum above 10^{10} eV for $z \sim z_m$, followed by redshifting off the cutoff to about 10^9 eV. Case(c), with the lower starlight density, cuts off at a slightly higher energy ($\sim 4 \ 10^{10}$ eV) than (d).

The models described above would appear to represent extremes in what is reasonable to assume about the starlight spectrum during differnet epochs. Case(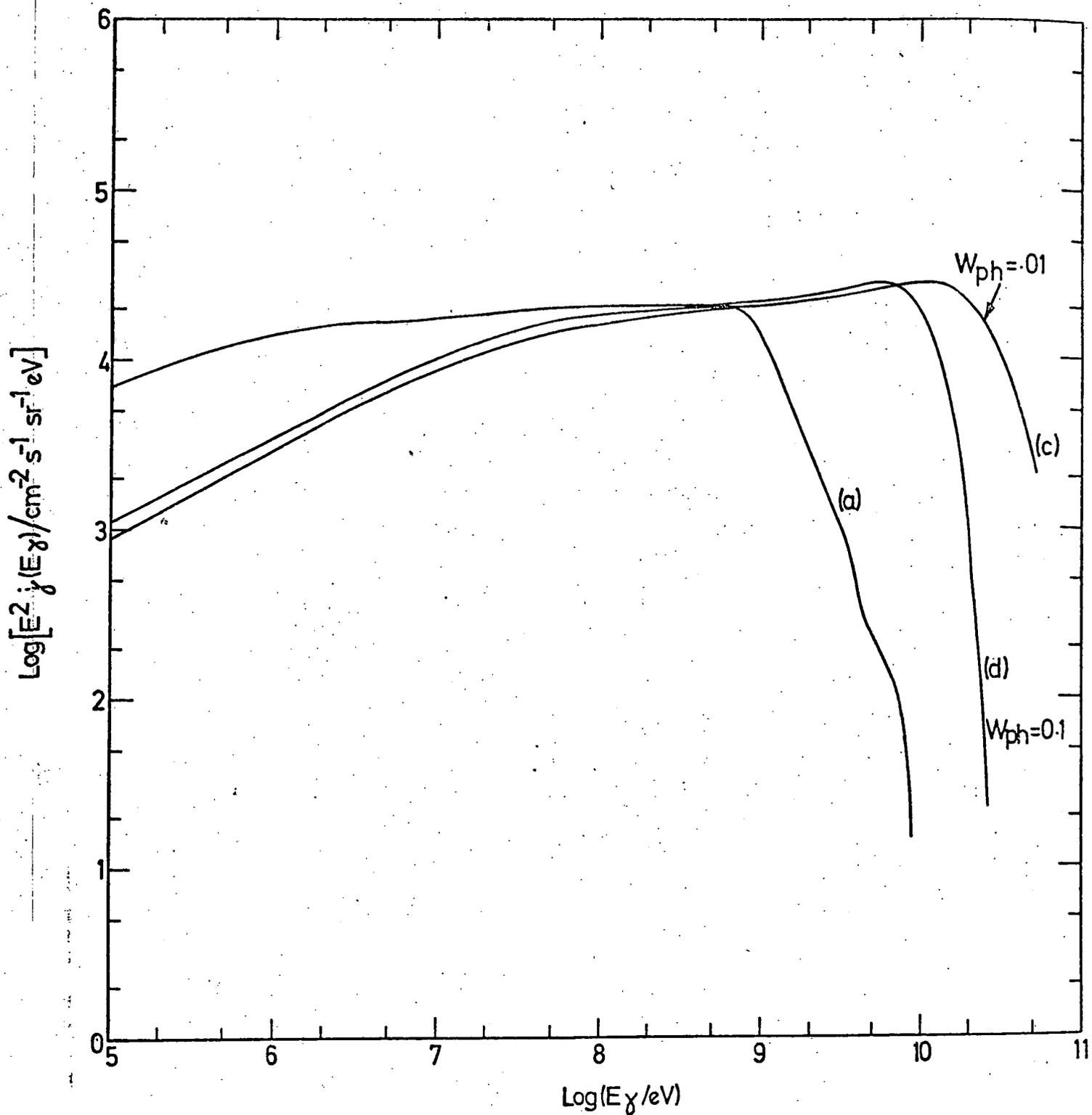a), corresponding to the galaxy evolution models of Tinsley (1973), is perhaps the most plausible of the models. Here, interactions with starlight occur on scales small compared to the Hubble distance. Cases (c) and (d) illustrate the result of a starlight spectrum of lower temperature which does not vary with epoch.

8.5 Comparison with approximate treatments of cascade.

Fig 8-8 compares the spectra obtained in this Chapter with the approximate solutions of Chapter 7. The curve for treatment A is a fairly good approximation to the constant high density starlight case of curve (d). This is as would be expected since treatment A assumes a high enough starlight density for PP on starlight to be a 'point' process, and uses parameters appropriate to a 6000 K greybody spectrum like that assumed for curve (d). The nearest equivalent in the approximate solutions to the low density starlight case of curve (c) is treatment B. As remarked in Chapter 7, the sharp dip predicted in this treatment above the energy $E_{\gamma,max}$ is unrealistic owing to the energy spread in the PP and ICS processes, which was ignored in this method. The curve with $E_{\gamma,max} = 10^9$ eV comes nearest to curve (c) at least in the low energy
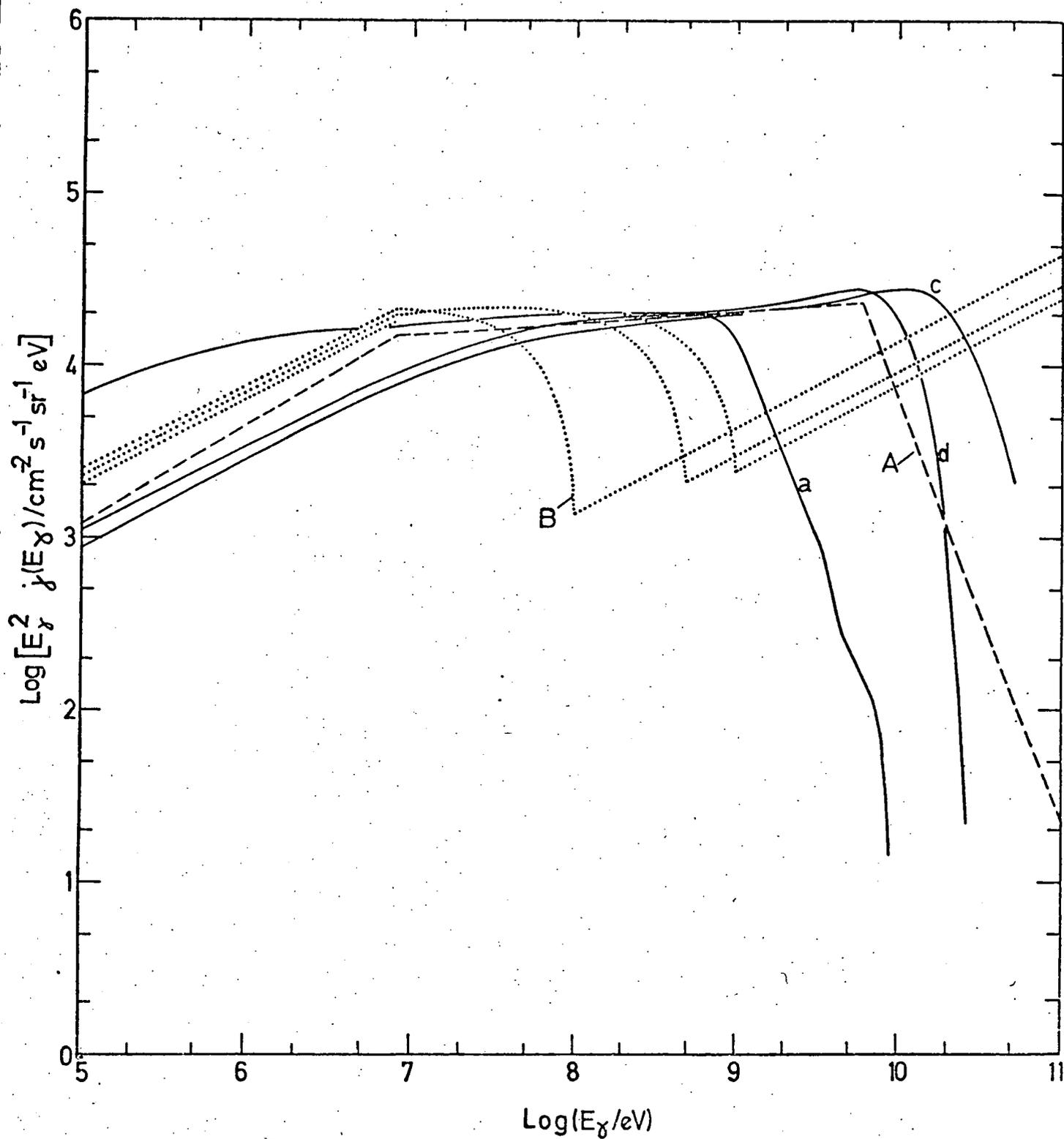
Fig 8-8

Comparison of gamma-ray spectra on models a - d with those

obtained in Chapter 7 by approximate treatments A and B. Normali-

zation is to the same total energy in each case.

range, and the curves are within a factor of 2 up to $4 \cdot 10^8$ eV.

The approximate treatments do not attempt to include the effects of varying the starlight density with epoch; hence none of the approximate solutions can be compared with curves (a) and (b), in which starlight is assumed to increase with z in energy and density.

8.6 Discussion.

The numerical treatment of the gamma-ray spectrum described in this Chapter is found to confirm the general features of the spectrum given by the approximations of Chapter 7. In the energy range 10^7 - 10^8 eV, all the models (except treatment B with $E_{\gamma,max} = 10^8$ eV) give similar spectra, so that this energy range provides a good test of the model independent of the details of a particular version. Data above 10^8 eV are not at present available. Below 10^7 eV, models (c) and (d) predict a slope -1.5, whereas models (a) and (b) give a slope nearer -2 and consequently much higher fluxes in the range below 1 MeV. This part of the spectrum is therefore dependent on the model details, and not so well suited for a general test of the model.

Chapter 9. <u>Review of Observational data on the Gamma-ray Background</u>
<u>and comparison with the models.</u>

9.1 Introduction

The first definite evidence for the existence of a cosmic background of gamma-rays came from the Ranger III and V moon-probes (Arnold et al., 1962), which carried scintillation counters designed to detect gamma-rays near 1 MeV. Upper limits to the flux in the 100 MeV region were also obtained at this time by the Explorer XI satellite (Kraushaar and Clark, 1962); but the low fluxes at these energies prevented the identification of a definite cosmic flux until the development of the gamma-ray telescope on the OSO-III satellite (Clark et al.,1968) and later the SAS-II experiment (Fichtel et al., 1974).

A large number of experiments, from balloons, satellites and other spacecraft, have been carried out to determine the form of the gamma-ray background spectrum. In the following sections, a short account of the techniques involved in gamma-ray astronomy is given, followed by a description and discussion of the problems peculiar to the experiments from which data has been taken. The sections are divided according to whether experiments are from balloon or spacecraft, and have energy ranges above of below about 30 MeV. A short account of the X-ray region is also included.

9.2 Gamma-ray astronomy techniques

Gamma-rays are detected via the electrons produced in interactions with matter, by the photoelectric effect, Compton effect or pair-production. In the 1-10 MeV range, the Compton effect dominates, while pair-production becomes the most important above this energy. The electrons are detected

by scintillation counters (consisting of fluorescent translucent material viewed by photomultipliers) , Cerenkov counters, spark chambers, and most recently, solid-state detectors. In balloon experiments, the use of nuclear emulsions is also possible, as in the NRL detector (Share et al. 1974). A large-Z material, e.g. lead or tungsten, is normally used for the conversion of the gamma-ray to electrons.

The most frequently used detector in both balloon and space experiments has been the Thallium-doped NaI scintillator, which gives an energy-loss spectrum from a pulse-height analysis of photomultiplier signals. The main disadvantage is the lack of directionality, since collimation of gamma-rays is difficult owing to the problem of absorbing the shower produced in the shielding material. Much better angular resolution can be obtained by the use of the double-Compton telescope (Schonfelder et al, 1973) in which two widely spaced scintillators are used to define a small solid angle for the Compton-produced electrons. However, the used of this technique severely limits the quality of the statistics which can be obtained.

In the energy range above 10MeV, spark-chambers give good angular resolution (better than 5°) and a more certain identification of gamma-ray events, since a 'picture' of the event is produced. The energy is determined from a study of the Compton interactions of the electrons in the chamber.

Further discussion of the techniques mentioned above will be found in the sections on the particular experiments below.

9.3   Gamma-ray experiments from balloon altitudes.

9.3.1 General

Experiments designed to determine the diffuse gamma-ray spectrum using balloon-borne detectors have been developed for a variety of techniques. The most important problem common to all is the large atmospheric gamma-ray albedo present in the electron-photon cascades initiated by primary cosmic-ray particles. Discrimination against charged particles is generally by means of a plastic-scintillator anticoincidence shield surrounding the detector. However, gamma-ray events may be simulated in various ways by charged particles, depending on the type of detector in use (see discussion of induvidual experiments).

The usual method for removing the atmospheric background is to extrapolate the gamma-ray intensity versus atmospheric depth curve back to zero depth, either assuming this to be linear on a log-log scale, or using a function of the form $At + Be^{-\lambda t}$ (t = atmospheric depth in gm cm^{-2}), which is appropriate when large depths are included and absorption of the primary gamma-rays is significant.

The interpretation of the flattening of the intensity-depth curve (the 'growth' curve) at small depths may be invalid for energies below a few MeV. Calculations by Danjo (1972) on the expected growth curve, taking into account photoelectric effect, Compton effect and pair-production in the atmosphere show that at small depths there is a buildup of contributions from upward-moving photons generated at larger depths, and this leads to a flattening of the curve. Of course, this will only apply to detectors incapable of discriminating against upward-moving photons, i.e. those using scintillators only. The results of Damle et al. (1972), using a NaI(Tl)

scintillator, and Vedrenne et al.(1971) using an organic scintillator, are possibly subject to this effect. (See discussion by Pal,1972). In the Vedrenne experiment, the neutron component of the atmospheric particle flux was used to extrapolate the growth curve, on the assumption that atmospheric neutrons and gamma-rays develop in the same way. However the different modes of propagation of neutrons and gamma-rays may invalidate this assumption for neutrons measured above a threshold near their production energy of ~1 MeV (Pal, 1972).

The development of spark-chamber techniques has led to improved event identification and angular resolution, and especially the means of accepting only downward-moving gamma-rays at small angles to the zenith. This reduces the growth-curve extrapolation problems mentioned above. A gamma-ray is identified with a well-defined inverted-V event originating in the converter, and problems can arise in the discrimination against simulated inverted-V events due to charged particles - for example in the Share et al. experiment (1974), more than half of the events were of this type.

The double-Compton telescope used by the MPI group (Schonfelder and Lichti 1974) is also capable of fair angular resolution (about $20°$) and also up-down discrimination from the time-of-flight measurement. It was claimed to be immune from locally-produced background, but gamma-rays produced by albedo neutrons reacting in the upper detector later proved to be an important contributor to the count rate.

We now turn to an individual discussion of the major balloon experiments. The main features of each experiment are summarized in Table 9-1, to which reference should be made in conjunction with each section. All observational results discussed are plotted in Fig 9-1.

<u>Fig 9-1</u>   <u>Observations of the Gamma-Ray Background.</u>

KEY

Trombka et al. (1973)

Vette et al. (1970)

Golenetskii et al. (1971)

Vedrenne et al. (1971)

Schonfelder and Lichti (1974)

Kuo et al. (1973)

Agrinier et al. (1974)

Share et al. (1974)

Mayer-Hasselwander et al. (1972)

Herterich et al. (1973)

Hopper et al. (1973)

Bratolubova-Tsuludidze et al. (1970)

Kraushaar et al (1972)

Galper et al. (1973)

Daniel et al. (1972)

Dennis et al. (1973)

Schwarz and Gursky (1973)

Fukada et al. (1975)

Gorenstein et al. (1969)

Bleeker and Deerenberg (1970)
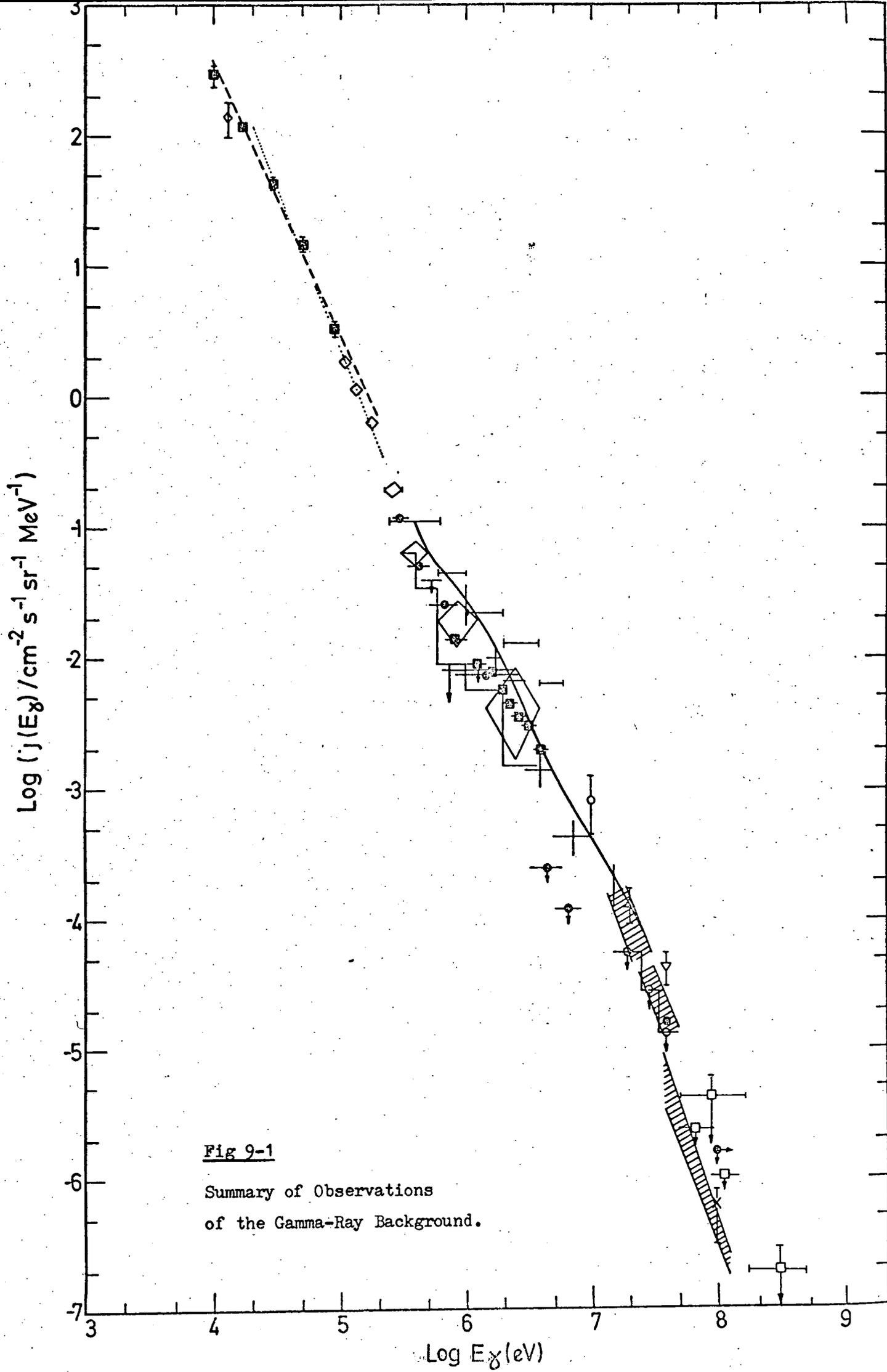
Fichtel et al. (1974)

Fig 9-1

Summary of Observations
of the Gamma-Ray Background.

9.3.2 Description of balloon experiments.

1) Share et al. (1974)

This is the only experiment incorporating a nuclear emulsion stack, as well as a spark chamber, to help identify gamma-ray events. The emulsion is also the converter, producing electron pairs which can be photographed in the spark-chamber. Events appearing in photographs as downward-moving pairs are traced back to their origins in the emulsion, allowing good identification and an energy resolution of 25%. The rate of gamma-ray events was determined between depths of 55 and 3 gm cm^{-2}, and a linear extrapolation made to the top of the atmosphere. A 3.8 σ residual flux was found.

Two important sources of events which can simulate gamma-rays had to be considered. These result from upward-moving electrons which are scattered backwards in the emulsion, producing inverted-V tracks. The electrons can come either directly from the atmosphere through a gap in the telescope geometry, or from conversion of upward-moving atmospheric albedo gamma-rays converting in the Plexiglas Cerenkov counter. The two effects account for more than half of the residual inverted-V events.

The presence of these electron-generated events restricted the results to upper limits. These limits, however, at 20, 30 and 40 MeV, fall more than a factor of 2 below the Apollo-15 results (see later section) in the same energy region, and may indicate the latter experiment was sensitive to charged particles. A strong East-West effect (a factor of 1.4) was found at ceiling depth, probably a result of charged-particle interactions in the material overlaying the instrument,

or to the Galactic plane.

2) Mayer-Hasselwander et al. (1972); Herterich et al.(1973).

This experiment used a 13-gap wire spark chamber on three flights. Visual inspection of all events was performed, only pair-events showing two tracks in at least two projections being classified as gamma-rays. Extrapolation to the top of the atmosphere was made using a fit to a linear-plus-exponential function (see Sec 9.3.1). The spark chamber had not been calibrated by accelerator when the results were first presented (Mayer-Hasselwander et al. 1972). Calibrations were later made, including use of a DESY tagged gamma-ray beam with the chamber on a co-ordinate table allowing gamma-rays to injected at all orientations.

These results were the first to indicate a gamma-ray background in the 30-50 MeV range about a factor 10 above the extrapolated X-ray background, which appears to have been confirmed by later work, including the Apollo-15 results.

3) Agrinier et al. (1973)

A 13-plate spark chamber telescope was flown in France and Brazil to obtain different geomagnetic cutoffs, as shown in Table 9-1. Events recognizable as downward-moving electron pairs were counted without gamma-ray direction reconstruction, giving an acceptance angle of 20°. Curves of growth were obtained with a ratio of slopes at the two cutoff rigidities agreeing well with the results of Share et al. (1974), which involved almost the same cutoff rigidities. Extrapolation to zero depth gave a 3.6σ excess at the top of the atmosphere for the 11.5GV result.

The geometrical factor for an isotropic gamma-ray flux had to be

estimated using the computed atmospheric spectrum of Beuerman(1971), since the experiment was only calibrated for axial incidence. The final result was computed assuming a spectral shape E^{-2} for the cosmic background. It should be regarded an an upper limit, since the authors give three effects which lead to overestimation of the flux. These are, an under-estimate of the geometrical factor at low energies, a possible contribution from the Galactic disc, and possible local production of gamma-rays in the detector.

4) Kuo et al. (1973)

The spark chamber used in this experiment consisted of an upper chamber with thin Al plates for track definition, and a lower chamber with increasingly thick Al plates for energy determination. The main background was due to upward-moving electron scattered back in the chamber. The wide opening angle characteristic of such simulated pair-events enabled them to be eliminated by accepting only events with an opening angle less than 76°, with no significant effect on the number of real pair-events.

The gamma-ray flux for zenith angles less than 60° at 10 MeV and depth 3 gm cm^{-2} was compared with the atmospheric flux estimated from other experiments at the same rigidity cutoff. An extraterrestrial component was indicated by the presence of an excess in each case, although the actual value varied widely. The final quoted spectrum was obtained using the mean of all the atmospheric flux estimates, giving a value which is a factor 2 above the Apollo-15 value at 10MeV, but consistent within the quoted errors.

5) Hopper et al.(1973)

This experiment was intended to check the results of the MPI group (Mayer-Hasselwander et al. 1972, discussed above), by flying spark chambers designed for the same energy region at higher altitude and higher cutoff rigidity. The higher altitude reduced the atmospheric background by a factor of more than 2 over the MPI experiment. Only upper limits were obtained however, the extrapolation to the top of the atmosphere being consistent with zero intercept. The upper limits are slightly below the MPI maximum value at 40 MeV, and consistent with the SAS-II result at 100 MeV, although too high too be of much interest in this region.

The following experiments were designed to investigate the energy range 0.1 - 10 MeV

6) Vedrenne et al. (1971)

The detector was flown at three different latitudes in order to estimate the atmospheric background (see Table 9-1). This was necessary because the organic stilbene detector was almost omnidirectional, and no pictorial information was obtained. The main interaction process in the detector was the Compton effect: thus both the gamma-ray and neutron specctra could be obtained using pulse-shape discrimination. The ratio of gamma-rays to neutrons was found to increase with decreasing geomagnetic latitude (and hence increasing cutoff rigidity); this was attributed to an extraterrestrial gamma-ray component. The form of the atmospheric gamma-ray spectrum at latitude 10° N was taken as that from the France and USSR flights, which both gave $E^{-1.5}$ spectra, and the absolute normalization was obtained from the neutron spectrum assuming that neutrons and gamma-rays show the same development with depth. This assumption has been challenged by Pal (1972) as mentioned in Sec 9.3.1.

The results agree quite well with the Apollo-15 curve below 1.5 MeV; the two points below this energy fall a factor of three below this curve.

7) Damle et al. (1972).

A collimated NaI(Tl) scintillator measured the growth curve up to 6 gm cm^{-2} depth. A radioactive source provided in-flight calibration at 2.68 MeV. The growth curve extrapolated to the top of the atmosphere showed an excess which appeared to be independent of the pointing of the telescope towards the Galactic Center or at right angles to the Galactic Plane. This was claimed as evidence for an extragalactic origin for the flux. No actual vales were given.

8) Daniel et al. (1972).

This experiment was designed to check the results of the ERS-18 satellite (Vette et al. 1970, see later discussion), particularly the high flux values above 1 MeV. The detector system was very similar to that on ERS-18, so that direct comparison of energy loss spectra was possible. The total count rate above 1 MeV at 4.7 gm cm^{-2} depth was significantly less than that from ERS-18, confirming the conclusion of Golenetskii et al. (1971) from the Cosmos 135 and 163 experiments (see Section on satellites), that the ERS-18 detector was seriously affected by nuclear spallation induced by cosmic-rays. Since most of the gamma-rays at the depth of the Daniel et al. experiment are atmospheric, the upper limit to the cosmic gamma-ray flux (obtained assuming a power law dependence of atmospheric flux on depth) is much lower than this total count rate, and is a factor of 4 below the Apollo-15 values at 7 MeV. The calculations of Danjo (1972) would suggest that even these low values are overestimated (see Section 9.3.1 above). However, other experiments have not confirmed that the flux above 1 MeV is as low as claimed here.

9) <u>Schonfelder and Lichti (1974)</u>.

A double-Compton telescope was used in this experiment, in an attempt to reduce the background effects, including locally produced radioactivity , and to give some directionality in the energy range 1-10MeV , other detectors in this energy region being mainly omnidirectional. The total energy of the gamma-ray is estimated from the energy losses E_e' and E_e'' of the Compton electrons produced in the two detectors. A time-of-flight measurement discriminates against upward-moving gamma-rays. The scattering angle $\emptyset$ at the first Compton interaction can be estimated from E_e' and E_e'' , and by requiring this angle to be less than 30^0 an effective aperture with full width at half maximum of 20^0 at 2.75 MeV was obtained.

The growth curve was determined up to a depth of 2.45 gm cm^{-2}, and the gamma-ray excess at the top of the atmosphere estimated using a fit to a linear-plus-exponential function. The statistical errors in this type of experiment are quite large because of the small number of events falling in the narrow acceptance angle. From the angular distribution in celestial co-ordinates, at least four-fifths of the emission appeared to be of extragalactic origin.

An additional source of background was found to be atmospheric albedo neutrons undergoing inelastic gamma-ray producing interactions with carbon in the upper detector. This led to a reduction in the derived extraterrestrial spectrum by 14% below 3 MeV and by 50% for 3-10 MeV.

Table 9.1 Balloon observations of the Gamma-Ray Background.

	Ref.	Energy	Location	Vertical cutoff	Ceiling depth ($g\ cm^{-2}$)	Detector	Ang.Res.
1.	Share et al. (1974) NRL	10MeV	Argentina Texas	11.5 GV 4.5	2.5 5.0	Emulsion +spark chamber	1°
2.	Mayer-Hassel-wander et al. (1972) Herterich et al. (1973) MPI Munich	30-50 MeV		4.5 GV	1.7-2.2	Spark chamber	
3.	Agrinier et al.(1973) France-Italy -Brasil	20 MeV	France Brasil Brasil	5.4 GV 12. GV 12. GV	2.0 2.3 5.5	Spark chamber	20° accept-ance
4.	Kuo et al. (1973) Case-Western	10 MeV	Palestine (Texas)	4.5 GV	3.0	Spark chamber	
5.	Hopper et al. (1973) Case-Western-Melbourne	30 MeV	Queens-land	8.8 GV	1.	Spark chamber	
6.	Vedrenne et al.(1971) Toulouse	0.7-4.5 MeV	Guiana France USSR		4. 3.5 4.	Stilbene scint-illator	Omni-direct-ional
7.	Damle et al. (1972) TATA Inst.	0.25-4.2 MeV	Hyderabad		6.	NaI(Tl) scinti-llator (collim-ated).	55° FWHM
8.	Daniel et al. (1972)	0.1-8.5 MeV	Hyderabad		4.7	NaI(Tl) scinti-llator.	Omni-direct-ional
9.	Schonfelder and Lichti (1974) MPI Munich	1.5-10 MeV	Palestine (Texas)	4.5 GV	2.5 10.	Double Compton telescope	20°
10.	Tanaka (1974) Nagoya	0.1-7.5 MeV	Hyderabad		4.3	NaI(Tl) scinti-llator in active shield.	2π

9.4 Gamma-ray Observations from Spacecraft.

9.4.1 General.

The main problem associated with balloon-borne gamma-ray experiments, the atmospheric background, can only be satisfactorily resolved by taking detectors right out of the atmosphere, either on satellites or on space-probes.

In satellite experiments, close Earth orbits ($\sim$ 500 km above the Earth's surface) are generally preferred since they avoid the high particle fluxes associated with the trapped radiation belts situated at a few Earth radii. As with balloon work, directional detectors are better for distinguishing the cosmic gamma-ray component; some experiments have used omnidirectional detectors which are sensitive to background from Earth albedo gamma-rays (e.g. the Cosmos 135 and 163 experiments, Golenetskii et al.,1971, and Cosmos 461, Mazets et al., 1974). In this case, attempts are made to use the variation in the terrestrial component with cutoff rigidity to subtract the background.

Contamination by gamma-rays originating in material near the detector, and from spallation products of cosmic-ray interactions in the detector (occuring around 1 MeV), must be allowed for. The latter is a particular cause of difficulty in the interpretation of experiments in which a scintillator is carried through the radiation belts (e.g. Vette et al., the ERS-18 experiment, and Apollo-15, Trombka et al., 1973).

In the following sections, the main satellite experiments to date are described, and the problems associated with each are discussed. The main features of each experiment are summarized in Table 9-2.

9.4.2   Description of Satellite and Space-probe experiments.

The following experiments operated in the energy range 0.5 - 30 MeV:

1) Arnold et al.,(1962); Mezger et al., (1964).

These pioneering investigations on the Ranger III and V moon probes were the first to give definite evidence of a cosmic gamma-ray flux around 1 MeV. The scintillator was mounted on a six-foot boom to avoid contamination from gamma-rays from the spacecraft. The instrumental response was not unfolded in the spectrum quoted in Mezger (1964).

2) Vette et al. (1970).

The energy-loss spectrum for an omnidirectional NaI(Tl) detector at energies around 1 MeV was measured. The ERS-18 satellite was in a high orbit, and therefore encountered the trapped radiation belts. The results show a marked flattening of the spectrum above 1 MeV, which may be the consequence of the decay of long-lived (half-life of order days) isotopes formed as spallation products of cosmic-ray interactions with I^{127} in the detector. Such events will not trigger the anticoincidence system of the telescope. The problem has been discussed by Dyer and Morfill(1971), Fishman (1972,1973) and Golenetskii (1971).

Other experiments using the same type of detector have overcome this problem either by operating near the geomagnetic equator where the cosmic-ray intensity drops by an order of magnitude (e.g. Cosmos 135 and 163, Golenetskii et al. (1971)), or by attempting to predict the induced radioactivity and subtracting the gamma-ray lines from the spectrum (e.g. the Apollo-15 experiment, Trombka et al. 1973).

3) Trombka et al. (1973).

The Apollo-15 and 16 moon missions carried NaI(Tl) detectors very similar to those used by the ERS-18 and Ranger III and V experiments. The instrument was mounted on a boom extendable up to 7.6m from the spacecraft, to allow an assessment of the spacecraft-generated background. The observation that the gamma-ray intensity varies by a factor of 5 while the spacecraft solid angle at the detector varied by a factor of 20 showed that most of the counts were not of local origin when the boom was fully extended.

Conversion from the energy-loss spectrum to the photon spectrum was made using a matrix inversion technique with a measured response library for the detector. The gamma-ray lines (appearing as discontinuities in the spectrum) were removed by requiring a smooth variation of the spectrum - resulting in the removal of about 17% of the counts in the 0.6 - 3.5 MeV range. (Of course, any cosmic gamma-ray lines are also removed by this technique). The main lines removed were at 0.51 MeV (positron annihilation), 0.63 and 0.69 MeV (proton-induced $I^{124,126}$ in the crystal), 1.47 MeV (natural K^{40} in the spacecraft) and 2.6 MeV (Thorium in the spacecraft).

The most difficult correction was that for the radioactive spallation continuum. The method adopted was to subtract a spectrum of the shape calculated by Fishman (1972) and Dyer and Morfill (1971), varying the normalization of the subtracted spectrum until the remaining spectrum was smooth over the 0.6 - 3.5 MeV range. An experimental determination of the spallation continuum was also made by flying an identical crystal on the Apollo-17 mission, and measuring the gamma-ray intensity in the crystal for a period starting $1\frac{1}{2}$ hours after ther recovery of the space-

craft. The result was consistent with that obtained from Apollo-15 as described above when account was taken of the different exposure profiles for Apollo-15 and 17 (the latter encountered the radiation belts twice before the measurements were started; also the detector environment was different).

The final spectrum obtained indicates a flattening over a power-law extrapolation of the X-ray region above 1 MeV, but only about half the effect claimed by Vette et al. (1970).

4) Golenetskii et al. (1971)

These experiments on Cosmos 135 and 163 used an omnidirectional NaI(Tl) detector and were designed to study the gamma-ray flux over a wide range of geomagnetic latitude at close-Earth altitudes. As in all experiments using omnidirectional detectors, the removal of the upward atmospheric gamma-ray flux is the main problem. To reduce the effect of induced radioactivity, the data used were mainly obtained between the launch and the first passage through the South Atlantic Anomaly (where trapped particle fluxes are high).

The 0.511 MeV positron annihilation line was monitored together with the continuum flux, and the ratio $n_{0.5}/n_{0.4-2.5}$ was found to be nearly constant with cutoff rigidity (evaluated at the projection of the satellite's position onto the Earth's surface), confirming a common origin for both these gamma-ray components (i.e. the electron-positron cascades from primary cosmic-ray protons). To evaluate the cosmic component of gamma-rays n_c , the atmospheric rate n_a was assumed to follow a power law in rigidity R, so that the total rate $n = n_c + n_a^o R^{-\alpha}$. Different assumed values of α lead to different estimates of n_c ; the best value was deduced by plotting

the ratio $n_{0.5}/(n-n_c)$ against R; for $\alpha=1$, the ratio is independent of R, as it should be, so this value was adopted. In the geomagnetic equatorial region, the cosmic contribution to the gamma-ray flux was less than 25%. All cosmic fluxes were given as upper limits only.

The limits found were lower than the ERS-18 results by a factor of about 3 above 1 MeV, and are consistent with a power-law extrapolation of the X-ray spectrum with slope -2.3 to -2.5, and do not show even the milder flattening observed by Apollo-15. The authors attribute the higher fluxes from the ERS-18 work to spallation effects; the low cosmic-ray intensity in the geomagnetic equatorial region near the Earth reduces this problem in the Cosmos experiments.

5) Mazets et al (1974)

Designed as a development of the Cosmos experiments described above, the Cosmos-461 detector was also flown in a close Earth orbit below the radiation belts to avoid contamination of the crystal, and only the first few hours of data were used, to eliminate the effects of induced radioactivity. Results very similar to those from Apollo-15 were obtained, with a flattening of the spectrum above 1 MeV. The absolute intensities above 1MeV were a factor of about 1.5 below the Apollo-15 results.

The remaining experiments to be described are concerned with the energy range above 30 MeV

6) Kraushaar and Clark (1962); Kraushaar et al. (1965).

The first satellite experiment designed to detect a cosmic gamma-

ray flux above 100MeV, the Explorer XI satellite used a CsI/NaI
detector in a sandwich configuration for energy estimation. Calibra-
tion was by pion-decay gamma-rays from an MIT synchrotron and a tagged
photon beam at Caltech. The technique used for the exposure correction,
adopted also in the later OSO-III experiments by this group, was to
generate random artificial events during the ON periods of the detec-
tor, with a mean interval of 20 sec., five times the true counting rate.
Then the number of artificial events recorded in particular time inter-
vals measures the exposure within these intervals. Although a definite
cosmic gamma-ray flux was not claimed, a useful upper limit on the
whole-sky average was obtained.

7) Kraushaar et al. (1972).

The Third Orbiting Solar Observatory, OSO-III, which operated for
16 months in 1967-8, carried a gamma-ray telescope designed as a succ-
essor to the Explorer XI detector. A very high rejection efficiency
for charged particles was obtained. Calibration again used the Caltech
tagged gamma-ray beam, and an in-flight measurement of the terrestrial
gamma-ray flux, on comparison with the Explorer XI results, revealed a
calibration error which was later corrected. The response function of
the detector was found to be adequately represented by a function of
the form $a(E,\theta) = Af(E)\exp(-(\theta/15^\circ)^2)$, where θ is the angle made by the
gamma-ray with the axis of the telescope. However, the nadir intensity
of atmospheric gamma-rays determined by OSO-III was almost a factor
of 2 higher than the value from a balloon flight by Fichtel et al.(1969).
The reason for this discrepancy was not apparent.

The improved angular resolution (about 30°) of this experiment,
and the whole-sky coverage obtained during the period of observation,

allowed an interpretation in terms of the Galactic and isotropic components to be attempted. In order to separate out the isotropic flux, the region of the sky away from the Galactic centre (in fact with $30^{\circ} < 1 < 300^{\circ}$) was divided into two areas with $|b| < 30^{\circ}$ and $|b| > 30^{\circ}$. Then using the integrated neutral hydrogen column densities for the Galaxy (from Daltabuit and Meyer, 1972) together with the exposure corrections (derived from artificial event generation as for the Explorer XI experiment), the total gamma-ray flux expected in the two areas was expressed as the weighted mean of Galactic and isotropic components. This gave two simultaneous equations which were solved to give the separate components.

A finite flux of isotropic gamm-rays was claimed, being a factor 10 below the upper limit set by Explorer XI. The OSO-III result remained the principal experimental datum for energies above 100 MeV until the advent of the SAS-II satellite in 1972.

8) Valentine et al. (1970).

A scintillator-Cerenkov particle telescope operated by the University of Rochester was also carried on OSO-III. Interpreted as an isotropic flux, the result obtained for energies above 100 MeV was more than a factor 3 above the final OSO-III value. However, their low angular resolution did not allow the Galactic component to be separated. Also, an inefficiency in the anticoincidence system complicated the are analysis of the results.

9) Fichtel et al. (1974).

The second spark-chamber gamma-ray telescope in space was carried

on the satellite SAS-II, which operated for eight months during 1972-3. (The first appears to have been on Cosmos-264, see Galper et al.(1970) and note below). The magnetic core spark-chamber consisted of an upper chamber with 16 modules separated by thin tungsten plates (.03 radiation lengths) in which pair-production occurs with known efficiency, and a further set of 16 modules below a set of four central plastic scintillators, which form anticoincidence systems with four directional Cerenkov detectors below the lower chamber. A plastic scintillator dome surrounds the whole telescope to give anticoincidence discrimination against charged particles, except those travelling upwards, for which discrimination is made by coating the top of the Cerenkov radiators black, thereby absorbing the Cerenkov light from such particles and preventing activation of the coincidence systems. The threshold for the telescope was 30 MeV, and energies up to 200 MeV could be determined, as well as the integral flux above 200 MeV.

Events were examined visually and selected on the basis of a set of rules designed to discriminate against non-cosmic gamma-rays. The energies were determined using the multiple scattering of the pair electrons in the tungsten plates, using techniques developed by Pinkau (1966). Calibration was done using gamma-ray beams at the National Bureau of Standards, and at DESY, Hamburg.

The gamma-ray background was determined as the mean for six directions with $|b|>30^\circ$, only gamma-rays within 25° of the detector axis being accepted. These regions were found to have uniform intensity within the experimental statistics. The spectrum was found to be steeper than determined in earlier balloon experiments with a similar detector, (Fichtel et al, 1969,1972), having a differential slope -2.4 ± 0.2.

The only non-cosmic background originates in the 0.15 g cm^{-2} of material

around the detector, and this is probably an order of magnitude below the cosmic flux. The SAS-II results are slightly lower than the OSO-III values, but agree within the expected errors and allowing for the fact that the OSO-III result may contain some Galactic contribution due to the lower resolution. The fluxes are consistent with the upper limits from other experiments, but conflict with the high 40 MeV flux reported by Herterich et al. (1973) (see section on balloon experiments above).

10) Bratolubova-Tsulukidze et al. (1969).

This paper reported results from the satellites Proton-2 and Cosmos-208. Only upper limits were obtained, including results for energies above 500 MeV. The contribution from charged particles was undetermined.

11) Galper et al. (1973) ; Volobuev et al. (1969).

The first satellite-borne gamma-ray spark chamber was in operation in 1969 on Cosmos-264. The upper limit obtained for the diffuse flux above 100 Mev is consistent with the SAS-II value, being a factor of 7 above the finite flux found by Fichtel et al. (1974).

Table 9.2   Satellite observations of the Gamma-Ray Background.

	Ref.	Energy	Spacecraft	Detector
1.	Arnold et al. (1962) Mezger et al. (1964)	0.7-4.4 MeV	Ranger 3,5 moonprobes	CsI(Tl) scintillator on 6 foot boom. 32 channel PHA
2.	Vette et al. (1970) GSFC USCD	0.25-6 MeV	ERS-18 15,000 - 117,500 km	NaI(Tl) omnidirectional 6 channel PHA
3.	Trombka et al. (1973) GSFC,USCD, JPL,LASRL	0.3-27 MeV	Apollo 15,16	NaI(Tl) omnidirectional on boom out to 7.5 m from Service Module. 511 channel PHA
4.	Golenetskii et al.(1971) A.F.Ioffe Inst Leningrad	0.3-3.7 MeV	Cosmos 135 Cosmos 163 250-660 km	NaI(Tl) omnidirectional 64 channel PHA
5.	Mazetz et al. (1974) A.F.Ioffe Inst Leningrad	28keV- 4.4 MeV	Cosmos 461 500 km	NaI(Tl) omnidirectional on boom. Development of Cosmos 135,163 detectors
6.	Kraushaar and Clark(1962) Kraushaar et al (1965) MIT	> 100 MeV	Explorer XI 480-1800 km	Sandwich CsI+NaI converter Cerenkov counter
7.	Kraushaar et al (1972) MIT	>100 MeV	OSO-III	CsI converter Lucite Cerenkov counter NaI(Tl) sandwich energy discriminator
8.	Valentine et al (1970) Rochester N.Y.	>100 MeV	OSO-III	Pb converter Lucite Cerenkov counter
9.	Fichtel et al. (1974) GSFC	35 MeV -200 MeV	SAS-II 440-610 km	32 gap Sparkchamber Cerenkov counter
10.	Bratolubova- Tsuludidze et al. (1970) Moscow	50 - 1500 MeV	PROTON-2 Cosmos-208	Scintillation counter Cerenkov detector
11.	Galper et al. (1973) Volobuev et al. (1970) Moscow	> 100 MeV	Cosmos-264 270 km	Spark chamber, 4 gap Pb converter

9.5 Review of experimental data on the X-ray Background.

The models described in the present work are not intended to provide an explanation of the X-ray background as well as the gamma-ray background, but for completeness some discussion of the region 10keV - 1 MeV is included here. Fig 9-1 includes the results discussed.

The X-ray background has been the subject of a large number of experiments from balloons, rockets and satellites. The agreement between different results in absolute flux is good enough (generally within 50%) to be reasonably confident about the general nature of the spectrum in this range, though arguments continue as to the exact spectral shape.

X-ray experiments are subject to similar problems as for gamma-rays (with the exception of statistics, which are generally ample in the X-ray region). Detectors are usually NaI(Tl) or CsI(Tl) scintillators. Balloon experiments require the subtraction of large atmospheric fluxes, while satellites encountering the radiation-belts of the Earth are contaminated with radioactive isotopes which subsequently decay inside the anticoincidence systems and simulate X-rays. Schwartz and Gursky (1973) have summarized what is in their opinion the most reliable data, and this, together with more recent results from OSO-V, will be discussed here.

The experiments selected operated either over different geomagnetic latitudes, or used direct methods of discriminating against electron-induced counts. The balloon experiment of Bleeker and Deerenberg (1970) used a NaI(Tl) scintillator at geomagnetic latitudes 20°, 40° and 50°, and investigated the energy range 20 - 220 keV. A shield

was used to give some directionality, the full width at half maximum being 35°. The cosmic-ray induced background was determined by running with the telescope aperture closed. A power-law form of the depth-intensity curve was used for extrapolation to the top of the atmosphere.

The ASE rocket experiment of Gorenstein et al (1969) determined the cosmic flux in the 1-13 keV range using a proportional counter and a methane-filled anticoincidence counter. Rocket experiments have the advantage of operating above the atmosphere but below the radiation belts, and Schwartz and Gursky (1973) consider that this experiment should be uniquely free from charged particle contamination.

The USCD detector on OSO-III (Schwartz et al. 1970) used concentric cylindrical NaI and CsI counters in anticoincidence to give a resolution of 11.5°. The energy range was 7.7 - 113keV. The geomagnetic latitude variations were used to eliminate the electron contamination events (about 80 % of the data). Induced radioactivity from passage through the South Atlantic Anomaly, in the form of Na^{24} which decays to Mg^{24} with a half-life of 15 hours, was the second largest correction. However, results from OSO-V (Dennis et al. 1973), using a similar detector, suggest that the assumption that Na^{24} decay dominates the spallation background may be erroneous, and that several other products are of equal importance. This later experiment has an increase of statistics of 2 orders of magnitude over OSO-III, and allowed the subtraction of a large amount of the non-cosmic background on the basis of short-term variations. The corrected results agree well with those of OSO-III, but the authors consider this fortuitous because of the reservations about the OSO-III radioactivity corrections mentioned above. The OSO-V results fit rather well onto a power-law curve of slope -2.08 $\pm$ .2 for the energy range 14 - 200 keV.

9.6 Comparison of models with experimental data.

In Chapter 7 it was shown that simple treatments of the model for the gamma-ray background discussed therein led to spectra in reasonable agreement with the data, but a more detailed comparison was not possible because of the uncertain accuracy of the treatments used. Chapter 8 showed how numerical techniques were applied to obtain reliable predictions from the model, and compared these with the previous analytical treatments. Here the data reviewed in this Chapter will be used to assess the viability of the model.

Fig 9-2 shows the observations and spectra for models (a) and (c) of Chapter 8. As pointed out in Ch. 8, in the energy range where observations are available (ie, below 100MeV), there is little difference between the predictions of models (a) and (b), and between (c) and (d), so that only (a) and (c) are shown in Fig 9-2. The uncertainty in the energy normalization determined in Ch. 2 from the primary proton spectrum means that the predicted spectra can be moved a factor of 2 up or down.

The following points can be noted:

(i) In both models shown, the overall agreement in the 10^6 - 10^8 eV range is good, in view of the fact that the normalization is derived from the primary proton spectrum.

(ii) Neither model can reproduce the spectrum in the range below 10^5 eV, and a separate mechanism (e.g. plasma bremsstrahlung) must be invoked.

(iii) In the range 10^5 -10^6 eV, the model with increasing starlight density in the past, model (a), agrees well with the data, while the constant starlight model (c) falls below the observations in this range. This is satisfactory since the Tinsley starlight spectrum of model (a)
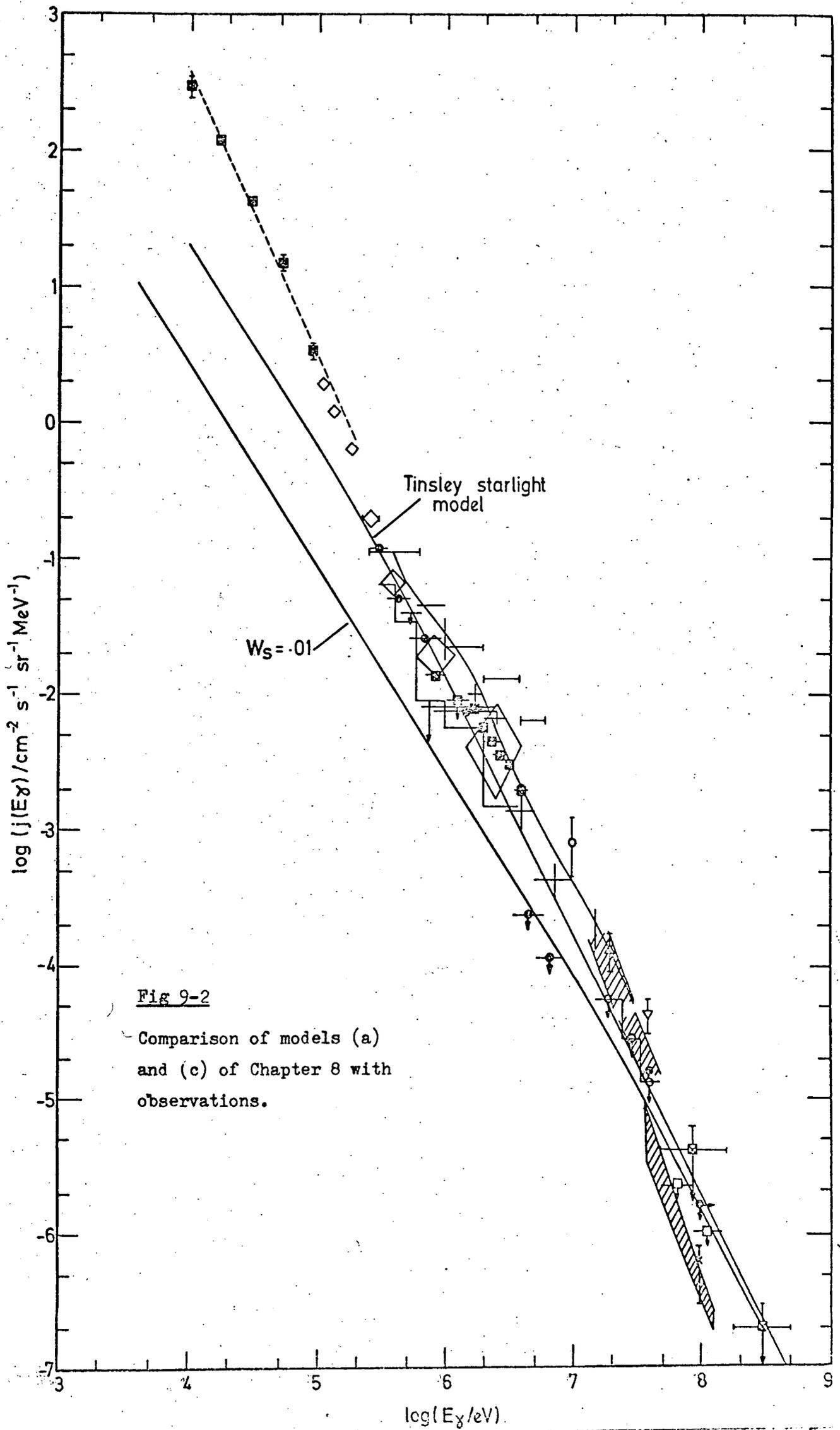
Fig 9-2

Comparison of models (a)
and (c) of Chapter 8 with
observations.

is almost certainly the more realistic of the two.

(iv) Agreement in the 10^6 - 10^7 eV range in satisfactory for both models. The existence of a 'hump' in this region is not predicted, but as discussed in the review of observations above, there is still considerable disagreement as to the size and even the existence of such a 'hump' (e.g. Daniel et al. 1972 find upper limits in this region considerably lower than the fluxes reported by other experiments). Other theories of the gamma-ray background which attempt to explain the 'hump' have been mentioned in Sec 1.5.

(v) Above 10^7 eV, both models predict a spectrum of the form E^{-2} approximately, while the observations of Fichtel et al. (1974) from the SAS-II satellite suggest E^{-3}, and are in agreement with the OSO-III result at 100MeV. Since this region of the spectrum is fairly independent of the starlight spectrum assumed (as discussed in Chapter 8), it provides a critical test for the model. If indeed the spectrum is confirmed to have the steeper slope, this would constitute a disproof of the theory in its present form. However, it would be wise to await confirmation of the experimental data in this region before stating categorically that the model is untenable. There seems to be no way in which the model could be modified to give a steeper slope, since very high UV and X-ray background fluxes would be required to allow the necessary γ-γ interactions to occur, and such backgrounds would conflict with observational limits.

9.7 Conclusions

The original motivation for studying the gamma-ray spectrum from the Hillas model of the CR primary spectrum was to try to determine whether it was consistent with the observed fluxes of gamma-rays, and thus possibly to disprove the model (independent of tests involving gamma-rays from CR-gas interactions, which depend on assumptions

about gas density, and in any case do not apply if we assume a Hillas

type origin only for CR energies above say 10^{12} eV). When simple

treatments showed a remarkable similarity between the predicted

and observed gamma-ray spectra, a more detailed treatment was promp-

ted in an effort to obtain a definitive comparison with observation

to be made. Using a plausible model for the starlight background

radiation, a rather good overall fit in the $10^5 - 10^8$ eV range was

obtained, although the theory does not predict the steepening in the

$10^7 - 10^8$ eV observed by the SAS-II experiment. Nevertheless, the

agreement in general shape and absolute intensity is sufficiently

remarkable to suggest that the model should be considered a serious

contender for the explanation of the gamma-ray background, and which

moreover provides a useful unification of the gamma-ray and cosmic-

ray primary spectra.

Chapter 9   References

Agrinier B, Forichon M, Leray J P, Parlier B, Montmerle T, Boella G,

    Maraschi L, Sacco B, Scarsi L, Da Costa J M and Palmiera R. 1973,

    Proc 13th Int. Conf. Cosmic Rays, Denver, 1, 8.

Arnold J R, Metzger A E, Anderson E C and van Dilla M A.,1962, J.

    Geophys. Res. 67, 4878

Beuermann K P,. 1971, J. Geophys. Res. 76, 4291

Bleeker J A M and Deerenberg A J M., 1970, Ap.J. 159, 215

Bratolubova-Tsuludidze L I, Grigorov N L, Kalinkin L F, Melioransky A S,

    Pryakhin E A, Savenko I A and Yufarkin V Ya., Acta Phys. 29,

    Supp. 1, 123 (1970)

Clark G W, Garmire G P and Kraushaar W L., 1968, Ap. J Lett 153 L 203

Daltabuit E and Meyer S., 1972, Astr. Ap. 20, 415

Damle S V, Daniel R R, Joseph G and Lavakare P J., 1972, Nature 235, 319

Daniel RR, Joseph G and Lavakare P J., 1972, Ap. Sp. Sci 18, 462

Danjo A., 1972, IAU Symposium 55 on Non-Solar X- and Gamma-Ray Astronomy.

Dennis B R, Suri A N and Frost K J.,1973, Ap. J. 186, 97

Dyer C S and Morfill G E., 1971, Ap. Sp. Sci. 14 243

Fichtel C E, Kniffen D A and Ogelmann H B., 1969, Ap. J. 158, 193

Fichtel C E, Hartmann R C, Kniffen D A and Sommer M., 1972, Ap. J.

    171, 31

Fichtel C E, Hartman R C, Kniffen D A, Thompson D J, Bignami G F,

    Ogelman H, Ozel M F and Tumer T., 1974, GSFC X-662-74-304

Fishman G J., 1972, Ap. J. 171, 163

Fukada Y, Hayakawa S, Kashara I, Makino F and Tanaka Y., 1975,

    Nature 254, 398

Galper A M, Kirillov-Ugryumov V G, Luchkov B I and Ozerov Y V.,

    1973, Proc. 13th Int. Conf. Cosmic Rays, Denver, 1, 450

Gorenstein P, Kellogg E M and Gursky H., 1969, Ap. J. 156, 315

Golenetskii S V, Mazets E P, Il'insky V N, Aptekhar R L, Bredov MM, Gur'yan Y A and Panov V N., Astrophys. Lett. 9, 69 (1971)

Herterich W, Pinkau K, Rothermel H and Sommer M, 1973, Proc. 13th Int. Conf. Cosmic. Rays, Denver, 1, 21.

Hopper V D, Mace O B, Thomas J A, Albats P, Frye G B, Thompson G B, and Staib, J A., 1973, Ap. J. 186, L55

Kraushaar W L and Clark G W., 1962, Phys. Rev. Lett. 8 106

Kraushaar W L, Clark G W, Garmire G P, Helmken H, Higbie P and Agogino M., 1965, Ap. J. 141, 845

Kraushaar W L, Clark G W, Garmire G P, Borken R, Higbie P, Leong C and Thorsos T., 1972, Ap. J. 177, 341

Kuo F S, Frye G M and Zych A D., 1973, Ap. J. 186, L 51

Mayer-Hasselwander H A, Pffermann E, Pinkau K, Rothermel H and Sommer K., Ap. J. 175, L23 (1972)

Mazets E P, Golenetskii S V, Il'inskii V N, Gur'yan Yu A and Kharitonova T V., 1974, JETP Lett. 20, 32

Metzger A E, Anderson E C, van Dilla M A and Arnold J R., 1964, Nature 204, 766

Pal Y., 1972, IAU Symposium 55 on Non-solar X- and gamma-ray astronomy.

Pinkau K., 1966, Zeit. für Physik, 96, 163

Schonfelder V, Hirner A and Schneider K., 1973, Nuc. Inst. Meth. 107, 385

Schonfelder V and Lichti G., 1974, Ap. J. 191, L1

Schwarz D and Gursky H., 1973, NASA SP-339, 15

Schwarz D A, Hudson H S and Peterson L E., 1970, Ap. J. 162, 431

Share G H, Kinzer R L and Seeman N., 1974, Ap. J. 187, 511

Tanaka Y., 1974, 9th ESLAB Symposium on the Context and Status of Gamma-Ray Astronomy, Frascati, 117.

Trombka J I, Metzger A E, Arnold J R, Matteson J L, Reedy R C and Peterson L E., 1973, Ap. J. 181, 737

Valentine D, Kaplan M F and Badhwar G., 1970, Acta Physica Hungaricae 29, Supp1, 101

Vedrenne G E, Albernhe F, Martin I and Talon R., 1971, Astron. Astrophys. 15, 50

Vette J I, Gruber D, Matteson J L and Peterson L E., 1970, Ap. J. 160, L161

Volobuev S A, Galper A M, Kirillov-Ugryumov V G, Luchkov B I, Ozerov Yu. V, Rosenthal I L, Shermanzon E M, Grigorov N L, Kalinkin L F, Melioransky A S, Savenko I A and Shashko G A., 1970, Acta Physica Hungaricae 29, Supp 1, 127

Acknowledgements.